

EXCITONICS OF COLLOIDAL NANOCRYSTALS FOR NEXT-GENERATION OPTOELECTRONICS

A DISSERTATION SUBMITTED TO
THE GRADUATE SCHOOL OF ENGINEERING AND SCIENCE
OF BILKENT UNIVERSITY
IN PARTIAL FULFILLMENT OF THE REQUIREMENTS FOR
THE DEGREE OF
DOCTOR OF PHILOSOPHY
IN
ELECTRICAL AND ELECTRONICS ENGINEERING

By
Burak Güzeltürk
May 2016

EXCITONICS OF COLLOIDAL NANOCRYSTALS FOR NEXT-
GENERATION OPTOELECTRONICS

By Burak Güzeltürk

May 2016

We certify that we have read this dissertation and that in our opinion it is fully adequate, in scope and in quality, as a dissertation for the degree of Doctor of Philosophy.

Hilmi Volkan Demir(Advisor)

Ayhan Altıntaş

Mehmet Z. Baykara

Alphan Sennaroğlu

Raşit Turan

Approved for the Graduate School of Engineering and Science:

Levent Onural
Director of the Graduate School

ABSTRACT

EXCITONICS OF COLLOIDAL NANOCRYSTALS FOR NEXT-GENERATION OPTOELECTRONICS

Burak Güzeltürk

Ph.D. in Electrical and Electronics Engineering

Advisor: Hilmi Volkan Demir

May 2016

Owing to the tremendous progress in the past decade, semiconductor nanocrystals that are grown by low-temperature solution-phase epitaxy have evolved into highly promising material systems for optoelectronics with ever increasing interest from the industry. However, fundamental challenges exist in conventional nanocrystals hampering their energy-efficient optoelectronic devices. In this thesis, we addressed important scientific problems and overcome various technological hurdles through optical physics discoveries and innovative nanomaterial processing. Specifically, we have proposed, designed and developed next generation of nanocrystals that exhibit superior optical and material properties than those of the conventional nanocrystals. Mastering intra- and inter-particle excitonic processes in these nanocrystals and their hybrids empowered us to control and tailor the desired photonic response. Our key achievements include demonstration of record high modal gain coefficients and giant nonlinear absorption cross-section in atomically-flat nanocrystals, ultralow-threshold all-solution processed quantum dot lasers and unprecedentedly strong exciton transport in self-assembled nanocrystals.

Keywords: Colloidal quantum dots, semiconductor nanocrystals, nanoplatelets, exciton, nonradiative energy transfer, optoelectronics, laser, optical gain, light-emitting diode, solar cell, light-harvesting.

ÖZET

YENİ NESİL OPTOELEKTRONİK TEKNOLOJİLERİ İÇİN KOLOİDAL NANOKRİSTALLERİN EKSİTONİK ÖZELLİKLERİNİN ANLAŞILMASI

Burak Güzeltürk

Elektrik ve Elektronik Mühendisliği, Doktora

Tez Danışmanı: Hilmi Volkan Demir

Mayıs 2016

Düşük sıcaklıkta sıvı ortamda üretilen yarı iletken nanokristaller son yirmi yılda gösterilen büyük gelişim sayesinde optoeletronik teknolojileri için büyük umutlar vaad etmektedir. Günümüzde bu malzemeler endüstri tarafından yoğun ilgi görmektedir. Buna rağmen, klasik tipteki nanokristaller sınırlı optik özellikleri nedeniyle çok verimli optoelektronik aygıtlar için uygun değildir. Tez kapsamında nanokristallerin optoelektronik aygıtlardaki performansını sınırlayan temel sıkıntıları çözmek için klasik nanokristallere kıyasla üstün özellikler sergileyen yeni nesil nanokristaller önerilmiş, tasarlanmış ve geliştirilmiştir. Ayrıca bu nanokristallerin sahip olduğu üstün optik ve eksitonik özellikler sistematik araştırmalar ile açığa çıkartılmıştır. Bu nanokristallerin kendi içindeki ve bir-biri arasındaki eksitonik etkileri detaylı bir şekilde çalışılmış ve istenilen fotonik özelliklerin elde edilmesi sağlanmıştır. Tez kapsamında atomik seviyede düz nanolevhaların kullanılmasıyla rekor seviyede yüksek optik kazanç katsayısı elde edilmiş, devasa seviyede doğrusal olmayan optik soğurma katsayıları tespit edilmiş, çok düşük eşik değerlerde ışıyan kuvantum noktacık lazerleri üretilmiş ve emsali görülmemiş seviyede çok verimli ışımasız enerji transferi yapan nanolevha filmleri geliştirilmiştir.

Anahtar sözcükler: Koloidal kuvantum noktacık, yarıiletken nanokristal, nanolevha, eksiton, ışımasız enerji transferi, optoelektronik, lazer, optik kazanç, ışık yayan diyot, güneş pili, ışık hasatı.

Acknowledgement

First of all, I would like to thank my advisor Prof. Hilmi Volkan Demir, who has been a great role model and inexhaustible source of motivation. I would like to express my deepest gratitude to him for always sharing his vision with a positive attitude, which was invaluable to me.

I would like to thank my thesis monitoring committee members Prof. Ayhan Altintas and Asst. Prof. Mehmet Z. Baykara for their support and valuable discussions. I would like to sincerely thank my jury members Prof. Alphan Senaroglu, Prof. Rasit Turan, Assoc. Prof. Hakan Altan and Asst. Prof. Giovanni Volpe for serving in my PhD jury and for their comments and suggestions. I would like to also thank Prof. Orhan Aytur and Prof. Donus Tuncel for their support.

I would like to thank all of my past and present office and group mates, who made our days and nights enjoyable. Special thanks go to Sedat and Evren for being good role models; Tuncay and Asli for their support; Emre, Pedro and Murat for always being elder brothers; Yusuf, Kivanc, Can, Aydan, Shahab, Fatih, Onur, Zafer, Halil, Ibrahim, Talha and Zeliha for their friendship and having great fun together; Ali Nail, Veli Tayfun and Fatih Bilge for years long friendship; UNAM friends Ahmet Emin, Sami, Amir, Nuray, Gozde and Gamze for sharing fun.

During this thesis, I have been lucky to collaborate with many labs all around the world. I would like to thank Dr. Jihyun Bae and Dr. Jong-Jin Park from Samsung Advanced Institute of Technology for having me at SAIT for internship; Prof. Peter Skabara and Dr. Alex Kanibolotsky from University of Strathclyde for a fruitful collaboration; Prof. Govorov from University of Ohio and Prof. Martin Dawson from University of Strathclyde for their academic support; Gordon, Marcus, Christin, Andre from Prof. Eychmueller group at TU Dresden for having fun together and nice collaboration; Prof. Oliver Schmidt at Leibniz Institute for Solid State and Materials Research Dresden for hosting my Green Talents research stay; Prof. Karl Leo from Institut fur Angewandte Photophysik at TU Dresden, Dr. Florian Menk and Prof. Rudolf Zentel from Johannes Gutenberg University of Mainz for fruitful collaborations; LUMINOUS! members and Prof.

Cuong Dang from NTU for their support and hosting me twice in Singapore; Prof. Tim Lian from Emory University for his experimental support; Prof. Ulrike Woggon from TU Berlin for our joint project; Prof. Niyazi Sedar Sariciftci at Linz Institute of Organic Solar Cells for hosting us in his lab.

I would like to acknowledge and thank all of the past and present Demir group members: Nima Taghipour, Didem Dede, Yasemin Coskun, Togay Amirahmadov, Refik Sina Toru, Mustafa Akn Sefunc, Onur Akin, Sayim Gokyar, Ozan Yerli, Akbar Alipour, Hatice Ertugrul, Cuneyt Eroglu, Ozge Ilkem Ozel, Neslihan Cicek, Gulis Zengin, Ozgun Akyuz, Emre Unal, Dr. Emre Sari, Dr. Gokce Kucukayan-Dogu, Dr. Vijay Kumar Sharma, Dr. Manoj Sharma and Dr. Savas Delikanli, Dr. Murat Soganci, Dr. Urartu Ozgur Safak Seker.

I would like to thank all of the technical and administrative staff at UNAM, Advanced Research Labs and EEE Department and Muruvet Parlakay who made our lives easier.

I would like to acknowledge support from the fellowships and awards; IEEE Photonics Society Graduate Student Fellowship Award by the IEEE Photonics Society, Photonics21 Student Innovation Award by The European Technology Platform Photonics21, Green Talents Award by Federal Ministry of Education and Research (BMBF) of Germany, SPIE - Optics and Photonics Education Scholarship Award by the SPIE.

I would like to give my special thanks to Pelin Kubra Isgor, who has been patient, warm and supportive. She helped me in many ways to make my life better. Finally, my most sincere thanks go to my family, my father Halit and my mother Nesrin. All these years, they have been endlessly supportive and have always given me their love and care.

Contents

Chapter 1	1
Introduction	1
1.1 Organization of the thesis	4
Chapter 2	6
Scientific Background	6
2.1 Colloidal semiconductor nanocrystals	6
2.1.1 Shape control and composition tuning	7
2.1.2 Atomically flat colloidal nanocrystals: nanoplatelets	9
2.2 Optical properties of colloidal nanocrystals	18
2.3 Excitonics of the nanocrystals	25
2.3.1 Journey of an exciton: essential excitonic processes	25
2.4 Optical gain in colloidal nanocrystals	33
2.4.1 Optical gain: basics	33
2.4.2 Optical gain systems in colloidal nanocrystals	43
Chapter 3	49
Experimental Methods	49
3.1 Steady state and time-resolved fluorescence spectroscopy	49

3.2 Measuring optical gain properties	56
Chapter 4	65
Harnessing Exciton Transfer at the Nanoscale in Designer Nanocrystal Assemblies	65
4.1 Introduction to harnessing exciton transfer	65
4.2 Ultraefficient exciton transfer in nanoplatelet assemblies for long-range exciton diffusion	68
4.2.1 Motivation	69
4.2.2 Experimental	70
4.2.3 Results and discussion	70
4.2.4 Summary	89
4.3 Nonradiative energy transfer in nanoplatelet films	90
4.3.1 Motivation	90
4.3.2 Experimental	91
4.3.3 Results and discussion	92
4.3.4 Summary	106
4.4 Conjugated polymer - nanoplatelet hybrids for efficient exciton dissociation	107
4.4.1 Motivation	107
4.4.2 Experimental	109
4.4.3 Results and discussion	111
4.4.4 Summary	130
4.5 Efficient exciton transfer in quantum dot – nanoplatelet solids for sensitive temperature probing	132
4.5.1 Motivation	132
4.5.2 Experimental	133
4.5.3 Results and discussion	135
4.5.4 Summary	153

4.6 Summary of the chapter	154
Chapter 5	157
Excitonic Light-Generation Using Colloidal Nanocrystals	157
5.1 Introduction to excitonic light-generation	157
5.2 Singlet- and triplet-state harvesting via energy transfer from phosphorescent molecules	161
5.2.1 Motivation	161
5.2.2 Results and discussion	162
5.2.3 Summary	174
5.3 Excitonic light-emitting diodes: energy transfer enabled electroluminescence from the quantum dots	175
5.3.1 Motivation	175
5.3.2 Experimental	176
5.3.3 Results and discussion	177
5.3.4 Summary	187
5.4 Summary of the chapter	187
Chapter 6	188
Optical Gain in Colloidal Semiconductor Nanocrystals	188
6.1 Introduction to colloidal gain	188
6.2 Efficient optical gain in blue-emitting quantum dots	193
6.2.1 Motivation	193
6.2.2 Results and discussion	194
6.2.3 Summary	202
6.3 All-colloidal quantum dot lasers	203
6.3.1 Motivation	203
6.3.2 Experimental	204

6.3.3 Results and discussion	206
6.3.4 Summary	224
6.4 Optical gain and lasing in colloidal nanoplatelets	226
6.4.1 Motivation	226
6.4.2 Experimental	227
6.4.3 Results and discussion	228
6.4.4 Summary	237
6.5 Lateral area dependent spontaneous and stimulated emission properties in colloidal nanoplatelets	238
6.5.1 Motivation	238
6.5.2 Experimental	239
6.5.3 Results and discussion	240
6.5.4 Summary	257
6.6 Summary of the chapter	258
Chapter 7	260
Conclusions and Perspectives	260
7.1 General conclusions	260
7.2 Future outlook	262
7.2.1 Optical gain and lasing	262
7.2.2 Nanocrystals for light-harvesting and light-generation	267
7.3 Contributions of this thesis to the literature and patents	270
Bibliography	274

List of Figures

Figure 2.1. A schematic representation of a CdSe nanoplatelet having four CdSe monolayers with an additional Cd layer.	10
Figure 2.2. High-angle annular dark-field scanning transmission electron microscopy (HAADF-STEM) images of 4 monolayer thick CdSe nanoplatelets (vertical thickness ~ 1.2 nm) with different lateral extents: (a) 15 by 15 nm, (b) 35 by 10 nm.	11
Figure 2.3. High resolution transmission electron microscopy (TEM) images of (a) 4 monolayer thick CdSe nanoplatelet having a fixed vertical thickness of ~ 1.2 nm, (b) CdSe-core/CdSe-shell nanoplatelet having a fixed vertical thickness of ~ 2.7 nm. Green shaded area is drawn as an overlayer to highlight the vertical thickness of the nanoplatelets since they do not perfectly stand upright on the TEM grid.	11
Figure 2.4. (a) Colloidal quantum dots having size polydispersity results in inhomogeneous broadening of their emission spectrum in their ensembles. (b) Colloidal nanoplatelets having magic-sized vertical thickness and large lateral sizes (larger than the exciton Bohr radius) do not exhibit inhomogeneous broadening in their ensembles.	13
Figure 2.5. Photoluminescence emission spectra of 3, 4 and 5 ML thick CdSe nanoplatelets. 3, 4 and 5 ML CdSe nanoplatelets have their peak emission at 463, 513 and 551 nm, respectively. Full-width at half-maximum of the emission is $\sim 8-10$ nm (35 - 40 meV) at room temperature.	14
Figure 2.6. (a) Optical absorption spectrum of a 4 ML thick CdSe nanoplatelet in its solution state (dissolved in hexane). (b) Step-like density of states in the nanoplatelets,	

resembling quantum wells, with additional excitonic features arising from the six-fold degenerate valence band of the CdSe (heavy hole, light hole and split-off states).....	15
Figure 2.7. Heterostructured nanoplatelets: core/crown (lateral extension), core/shell (vertical coating) and core/crown/shell architectures.	17
Figure 2.8. Evolution of the quantum confined energy levels for the electron and hole. Quantum confinement leads to a larger effective bandgap than that of the bulk form of the material.	20
Figure 2.9. E-k diagram for (a) a bulk semiconductor, (b) a quantum dot without considering exciton effect, and (c) a quantum dot considering exciton effect.....	22
Figure 2.10. (a) Atomic-like electronic states in a spherical CdSe quantum dot, (b) exciton manifold formed by the first four energy states. (c) Steady state optical absorption spectrum demonstrating the first four allowed transitions. The transitions are not sharp since measurement is made at room temperature Homogenous and inhomogeneous broadening overall broadens these atomic-like transitions. From V. I. Klimov, "Spectral and Dynamical Properties of Multiexcitons in Semiconductor Nanocrystals," Annual Review of Physical Chemistry 58, 635-673 (2007).....	23
Figure 2.11. Essential excitonic processes are schematically illustrated: (a) Exciton formation via optical excitation or electrical charge injection, (b) radiative and nonradiative recombination, (c) exciton diffusion, (d) exciton dissociation, and (e) excitation energy transfer (FRET and Dexter energy transfer mechanisms). (HOMO: highest occupied molecular orbital level, LUMO: lowest occupied molecular orbital level, $ X_1\rangle$ represents the band edge exciton state, $ g\rangle$ is the ground state.).....	28
Figure 2.12. Basic optical processes in a two-level atomic system: (a) spontaneous emission, (b) stimulated emission and (c) absorption.	33
Figure 2.13. Photon flux entering a medium at $z = 0$ and the medium length is Δz . The increase of the flux indicates the dominant net optical gain in the system. If flux does not change at all, the medium is in transparency condition (equal amount of absorption and stimulated emission), whereas if flux decreases as light propagates, this indicates the presence of dominant absorption process.	37
Figure 2.14. Schematic of a waveguide having a gain material within. The end mirror reflectivities of the waveguide are R_1 and R_2 . There is also intrinsic waveguide loss (α_{loss}) due to the scattering or intrinsic absorption losses.	39

Figure 2.15. Commonly considered gain systems: (a) two-level system, where net gain is not possible, (b) three-level system and (c) four-level system. 40

Figure 2.16. Gain coefficients in a four-level and three-level gain systems having the same stimulated emission cross-section, optical confinement factor and spontaneous emission lifetime. Four-level gain system acts as a “thresholdless” laser, whereas three-level gain medium requires a threshold pump rate to achieve net gain. 42

Figure 2.17. (a) Calculated gain spectra for GaInAs/InP quantum dot (10 nm × 10 nm × 10 nm), quantum wire (10 nm × 10 nm), quantum well (10 nm) and bulk at room temperature. (b) Calculated maximum gain as a function of the injection current density for the same material system with varying quantum confinement dimensionality. [1986] IEEE reprinted, with permission, from [M. Asada, Y. Miyamoto, Y. Suematsu, Gain and the threshold of three-dimensional quantum-box lasers, IEEE Journal of Quantum Electronics, and Sep/1986.]..... 44

Figure 2.18. Quantum dots in three different states: (a) Ground state ($|0\rangle$), (b) single exciton state ($|X\rangle$) and (c) biexciton state ($|XX\rangle$). (a) ground-state quantum dot has net absorption, while (b) quantum dot in $|X\rangle$ state leads to transparency. (c) $|XX\rangle$ state can provide net gain. 45

Figure 2.19. (a) Radiative emission of a biexciton state. (b) Nonradiative Auger recombination of a biexciton state. The recombination energy of the exciton is given to a third particle, i.e., electron or hole, to produce a hot carrier, which then relaxes to band-edge via interacting with phonons (lattice vibrations). Thus, energy is lost into heat..... 46

Figure 2.20. Optical gain model in conventional colloidal nanocrystals. (a) Exciton manifold for the $|0\rangle$, $|X\rangle$ and $|XX\rangle$ states and their transitions (black: upward for absorption, red: downward for radiative emission). (b) Electronic picture of the optical gain. $|X\rangle$ is optically transparent. $|XX\rangle$ state can achieve net gain, while $|0\rangle$ has net absorption. N_{XX} should overcome N_0 to realize population inversion..... 47

Figure 2.21 Occurrence probabilities of the number of excitons (e.g., 0, 1 and 2) per quantum dot when the average number of excitons is $\langle N \rangle$ 1.15. This excitation level induces the transparency since the population difference $N = N_{XX} - N_0 \approx 0$ 48

Figure 3.1. (a) Schematic diagram of an experimental setup that can be used to perform steady state linear absorption spectroscopy. (a) An exemplary absorbance data of a four monolayer thick CdSe nanoplatelet in hexane.	51
Figure 3.2. (a) Schematic diagram of the experimental setup to measure steady state photoluminescence spectrum. (a) An exemplary photoluminescence spectrum of a four monolayer thick CdSe nanoplatelet in hexane.	52
Figure 3.3. (a) Schematic diagram of the experimental setup for steady state photoluminescence excitation spectroscopy. (a) An exemplary excitation spectrum of a four monolayer thick CdSe nanoplatelets in hexane.	53
Figure 3.4. (a) Schematic diagram explaining the working principle of time-correlated single photon counting technique for time-resolved fluorescence spectroscopy. (b) Exemplary fluorescence decay curve measured at the peak emission wavelength of a four monolayer CdSe nanoplatelet (black curve) together with the instrument response function (IRF) (red curve). The inset shows the decay curve and the IRF in an early time window.	55
Figure 3.5. (a) Schematic diagram of the experimental setup to measure amplified spontaneous emission under single-photon absorption pumping (pump laser 400 nm, 120 fs, 1 kHz repetition rate). (b) Exemplary emission spectra from a four monolayer thick CdSe nanoplatelet film showing the transition from spontaneous emission into amplified spontaneous emission as the pump intensity is gradually increased.	58
Figure 3.6. (a) Schematic diagram of the experimental setup to measure amplified spontaneous emission under two-photon absorption pumping (pump laser 800 nm, 120 fs, 1 kHz repetition rate). (b) Exemplary input-output plot from a four monolayer thick CdSe nanoplatelet film showing the transition from spontaneous emission into amplified spontaneous emission as a function of the pump intensity. The threshold for optical gain can be also characterized from this plot.	58
Figure 3.7. Solid film of a colloidal nanoplatelet (heterostructured CdSe/CdTe core/crown architecture) film encapsulated with a cover glass and epoxy. The sample is excited in stripe geometry with a femtosecond laser. Emission from the sample (a) below and (b) above the amplified spontaneous emission threshold.	59

Figure 3.8. CdSe/CdS core/shell quantum dots spin-coated on quartz substrate excited with a pump intensity above the amplified spontaneous emission threshold.	60
Figure 3.9. (a) Schematic diagram of the experimental setup to perform variable stripe length (VSL) method for the measurement of net modal gain coefficients. (b) Exemplary data for the variable stripe length measurement.	61
Figure 3.10. (a) Schematic diagram of the experimental setup for open aperture z-scan technique. (b) Exemplary transmittance data for a four monolayer CdSe nanoplatelet in toluene as the sample is translated through the focus of 800 nm femtosecond Gaussian laser beam.	63
Figure 3.11. Open aperture z-scan setup to measure the nonlinear absorption cross-section constructed and used for this thesis work.	63
Figure 4.1. (a) Absorbance (dashed line) and photoluminescence (solid line) spectrum, (b) transmission electron microscopy images of the 4 ML CdSe NPLs. Reprinted (or Adapted) with permission from [19]. Copyright 2014 American Chemical Society....	72
Figure 4.2. TEM images of the highly stacked NPLs. The scale bar is (a) 400 nm and (b) 100 nm. Column-like ordered stacking of the NPLs is clearly visible. Reprinted (or Adapted) with permission from [19]. Copyright 2014 American Chemical Society....	73
Figure 4.3. High-angle annular dark-field (HAADF) TEM images of the NPLs with (a) no ethanol, a total of (b) 55 μ L, (c) 135 μ L, and (d) 455 μ L ethanol added. The scale bars are 100 nm. As the total added ethanol amount is increased gradually, longer column-like stacks of the NPLs are formed. On each image, cartoon like depiction of the evolution of the stacking in NPLs is presented by yellow-colored NPLs. Reprinted (or Adapted) with permission from [19]. Copyright 2014 American Chemical Society.	74
Figure 4.4. (a) Time resolved photoluminescence decays together with their multi-exponential fits. Inset shows the same photoluminescence decay curves in a shorter time window. (b) Steady state photoluminescence intensity of the NPLs while ethanol is added gradually to the solution of the NPLs. Inset shows the peak emission wavelength and photoluminescence FWHM of the NPLs as a function of the total added amount of ethanol. (c) Amplitude averaged photoluminescence lifetimes of the NPLs shown by black dots as a function of the total added ethanol amount. Blue stars	

show the modeled photoluminescence lifetimes of the NPLs for 0, 55, 135 and 455 μL ethanol added cases. The inset shows the average photoluminescence lifetimes of the NPLs in PBMA host matrix given for different NPL/PBMA volume ratios. Transition from non-stacking to stacking in the photoluminescence decay kinetics of the NPLs is observed without using any ethanol. As the NPL/PBMA volume ratio is gradually increased, phase segregation occurs that result in stacking. This increases the total decay rate of the NPLs. (d) Photoluminescence QY of the NPLs as a function of total added ethanol amount measured directly from steady state photoluminescence measurements and calculated semi-empirically from the photoluminescence lifetimes assuming the radiative recombination does not change. Reprinted (or Adapted) with permission from [19]. Copyright 2014 American Chemical Society. 75

Figure 4.5. Amplitude averaged photoluminescence lifetime of the NPLs as a function of wavelength measured for (a) 0 μL , (b) 50 μL and (c) 455 μL ethanol addition. Reprinted (or Adapted) with permission from [19]. Copyright 2014 American Chemical Society. 77

Figure 4.6. Photoluminescence lifetime components (a) τ_1 , (b) τ_2 , (c) τ_3 and (d) τ_4 , along with their contribution to the overall emission (a) $A_1\tau_1$, (b) $A_2\tau_2$, (c) $A_3\tau_3$ and (d) $A_4\tau_4$, respectively. Reprinted (or Adapted) with permission from [19]. Copyright 2014 American Chemical Society. 78

Figure 4.7. Photoluminescence decays of the NPLs in PBMA polymer host matrix in drop-casted solid thin film samples having different NPL/PBMA volume ratio. In the case of the smallest NPL/PBMA volume ratio, NPLs are well-separated in the polymer matrix as observed by their slower photoluminescence decay kinetics. As the NPL/PBMA volume ratio is increased, the photoluminescence decays become faster due to stacking of the NPLs via phase segregation in the polymer matrix. Reprinted (or Adapted) with permission from [19]. Copyright 2014 American Chemical Society.... 80

Figure 4.8. Schematic depicting the ultra-long range exciton transfer in the stacked NPL assemblies via exciton hopping through homo-FRET. The non-emissive NPL in the stack causes trapping with the assistance of long-range exciton migration causing nonradiative recombination of the excitons that quenches the photoluminescence emission of the NPLs in the stack. Reprinted (or Adapted) with permission from [19]. Copyright 2014 American Chemical Society. 83

Figure 4.9. a) A sample NPL stack with 20 NPLs. The shaded spots schematically represent the defected NPLs. b) Exciton dynamics acting on the NPL located in the i^{th} index of a stack array. The recombination and other energy transfer processes related to $(i-1)^{\text{th}}$ and $(i+1)^{\text{th}}$ NPLs are not shown. Reprinted (or Adapted) with permission from [19]. Copyright 2014 American Chemical Society..... 84

Figure 4.10. Distribution of stack size for the nanoplatelet solution mixed with a) 55 μL , b) 135 μL and c) 455 μL ethanol. Reprinted (or Adapted) with permission from [19]. Copyright 2014 American Chemical Society..... 84

Figure 4.11. Absorption (dashed lines) and photoluminescence (solid lines) of the 4 ML (cyan) and 5 ML (red) NPLs. Reprinted with permission from The Royal Society of Chemistry [68]. Copyright 2015 The Royal Society of Chemistry. 94

Figure 4.12. HAADF-TEM images of the NPLs of (a) 4 ML having the average size of 23.57 nm (\pm 2.90 nm) by 12.17 nm (\pm 1.94 nm) and (b) 5 ML having the average size of 26.32 nm (\pm 2.55 nm) by 9.04 nm (\pm 1.41 nm). Stacking of the NPLs is clearly visible in both NPL populations. The scale bars are 100 nm. Reprinted with permission from The Royal Society of Chemistry [68]. Copyright 2015 The Royal Society of Chemistry..... 95

Figure 4.13. Confocal images of the mixed solid films of the 4 and 5 ML NPLs. The collection window is (a) 505-530 nm matching only the emission of 4 ML NPLs, (b) 560-615 nm matching only with the emission of 5 ML NPLs. In both images, artificial coloring is used to represent the emission intensity. The scale bar is 100 μm . Reprinted with permission from The Royal Society of Chemistry [68]. Copyright 2015 The Royal Society of Chemistry..... 96

Figure 4.14. Time resolved fluorescence spectroscopy of the (a) 4 ML and (b) 5 ML NPLs in their solid thin films. Reprinted with permission from The Royal Society of Chemistry [68]. Copyright 2015 The Royal Society of Chemistry. 97

Figure 4.15. (a) Photoluminescence excitation spectra of the 4 and 5 ML NPLs featuring the electron/light-hole and continuum bands. (b) Enhancement of the 5 ML NPL PLE owing to the NRET from the 4 ML NPLs. Reprinted with permission from The Royal Society of Chemistry [68]. Copyright 2015 The Royal Society of Chemistry..... 100

Figure 4.16. Enhancement of the acceptor NPL emission excitation exhibiting spectral features resembling the spectral PLE features of the donor NPLs. At small A:D ratios, the dominant excitation mechanism of the acceptor NPLs is through NRET, whereas at large A:D ratios the acceptor NPLs are dominantly excited through direct absorption of the pump photons. Reprinted with permission from The Royal Society of Chemistry [68]. Copyright 2015 The Royal Society of Chemistry.	102
Figure 4.17. NRET efficiency as a function of A:D ratio. Reprinted with permission from The Royal Society of Chemistry [68]. Copyright 2015 The Royal Society of Chemistry.	104
Figure 4.18. HAADF-TEM images of mixed NPL populations incorporating 2-3% 4 ML NPLs while the rest of the NPLs are 5 ML. 4 ML NPLs have the square-like shape with an average size of 10.81 nm (\pm 0.53 nm) and 5 ML NPLs have the rectangle-like shape with an average size of 43.67 nm (\pm 3.31 nm) and 12.94 nm (\pm 1.51 nm). Reprinted with permission from The Royal Society of Chemistry [68]. Copyright 2015 The Royal Society of Chemistry.	105
Figure 4.19. HAADF-TEM image of the mixed NPL assembly (without size selective precipitation) of square-like 4 ML NPLs and rectangle-like 5 ML NPLs. Schematic of the NRET as limited by the nanoscale phase segregation between the NPLs of different populations. Reprinted with permission from The Royal Society of Chemistry [68]. Copyright 2015 The Royal Society of Chemistry.	106
Figure 4.20. General reaction scheme for the incorporation of anchor groups into the block copolymer containing a conjugated DEH-PPV block and assignment of the polymers P1 and P2a-c . Reprinted (or Adapted) with permission from [185]. Copyright 2014 American Chemical Society.	112
Figure 4.21. (a) FTIR spectra verifying the success of the post-polymerization modification and (b) ^{19}F -NMR spectra of polymers P1 and P2a . While the signals of the reactive ester occur in the ^{19}F -NMR spectrum of precursor polymer P1, full conversion of the post-polymerization modification is evidenced by the absence of any signals in the spectrum of polymer P2a. Reprinted (or Adapted) with permission from [185]. Copyright 2014 American Chemical Society.	114
Figure 4.22. (a) FTIR spectra verifying the success of the post-polymerization modification and (b) ^{19}F -NMR spectra of polymers P1 and P2b . While signals of the	

reactive ester occur in the ^{19}F -NMR spectrum of precursor polymer **P1**, full conversion of the post-polymerization modification is evidenced by the absence of any signals in the spectrum of polymer **P2b**. Reprinted (or Adapted) with permission from [185]. Copyright 2014 American Chemical Society. 114

Figure 4.23. (a) FTIR spectra verifying the successful post-polymerization modification (transferring **P1** to **P2c**) and (b) ^{19}F -NMR spectra of polymers **P1** and **P2c**. While signals of the reactive ester occur in the ^{19}F -NMR spectrum of precursor polymer **P1**, no signals occur in the spectrum of **P2c** which verify full conversion of the post-polymerization modification. Reprinted (or Adapted) with permission from [185]. Copyright 2014 American Chemical Society. 115

Figure 4.24. 400 MHz ^1H -NMR spectra of the precursor polymer **P1** and polymer **P2a** carrying a sulfide anchor group (in CDCl_3). After post-polymerization modification signals of the anchor group are detected in the spectrum. Reprinted (or Adapted) with permission from [185]. Copyright 2014 American Chemical Society. 115

Figure 4.25. 400 MHz ^1H -NMR spectra of the precursor polymer **P1** and polymer **P2b** carrying an amino anchor group (in CDCl_3). After post-polymerization modification signals of the anchor group are detected in the spectrum. Reprinted (or Adapted) with permission from [185]. Copyright 2014 American Chemical Society. 116

Figure 4.26. 400 MHz ^1H -NMR spectra of the precursor polymer **P1** and polymer **P2c** carrying an amino anchor group (in CDCl_3). After post-polymerization modification signals of the anchor group are detected in the spectrum. Reprinted (or Adapted) with permission from [185]. Copyright 2014 American Chemical Society. 117

Figure 4.27. Absorbance (solid) and photoluminescence (dotted) of (a) 4 monolayer thick CdSe nanoplatelets, and (b) conjugated polymers **P1** and **P2a-c**. Inset in (a) shows the HAADF-STEM image of the CdSe nanoplatelets, the scale bar is 50 nm. Reprinted (or Adapted) with permission from [185]. Copyright 2014 American Chemical Society. 118

Figure 4.28. Steady-state photoluminescence spectra of the hybrids as the polymer were added step by step in the case of (a) NPL-**P2a**, (b) NPL-**P2b** and (c) NPL-**P1** samples. The excitation wavelength for all cases was 375 nm. The insets in (a) and (b) show the NPL emission after spectral shape of the polymer emission has been subtracted. (d) Evolution of the NPL emission as a function of the added polymer

amount for three different cases. Reprinted (or Adapted) with permission from [185]. Copyright 2014 American Chemical Society.	121
Figure 4.29. (a) Emission of the only polymer P2a and NPL + P2a for 5.2 nmol (top) and 2.6 nmol (bottom) polymer amounts. The excitation wavelength for all cases is 375 nm. (b) Emission intensity change in the polymers P2a and P2b in the presence of the NPLs as compared to bare polymer emission. Reprinted (or Adapted) with permission from [185]. Copyright 2014 American Chemical Society.	122
Figure 4.30. (a) Excitation spectra of the NPL emission for three different samples: only NPL (green), NPL + 1.4 nmol P2a (dark blue) and NPL + 2.8 nmol P2a (light blue). Excitation of the NPL emission is estimated by considering absorption of the excitation light by the P2a for two different cases (dotted curves). (b) Excitation spectra of the P2a for only 5.6 nmol P2a (red dotted curve) and NPL + 5.6 nmol P2a (red solid curve) samples. Also, excitation of the P2a emission is estimated by considering absorption of the excitation light by the NPLs (black solid curve). (c) Excitation spectra of the P1 for only 5.2 nmol P1 (orange dotted curve) and NPL + 5.2 nmol P1 (orange solid curve) samples. Also, excitation of the P1 emission is estimated by considering absorption of the excitation light by the NPLs (black solid curve). (d) Energy bands of the NPLs and polymers exhibiting a staggered (Type II) band alignment favoring exciton dissociation. Reprinted (or Adapted) with permission from [185]. Copyright 2014 American Chemical Society.	125
Figure 4.31. (a) Quenching of the NPL's excitation spectra in the NPL+1.4 nmol P2a and NPL+2.8 nmol P2a samples with respect to NPL-only sample. (b) Quenching of the P2a 's excitation spectra in the NPL+5.6 nmol P2a sample with respect to P2a - only sample. Reprinted (or Adapted) with permission from [185]. Copyright 2014 American Chemical Society.	126
Figure 4.32. Cyclic voltammetry measurement of precursor polymer P1 measured in a 0.1 M solution of TBAPF6 in anhydrous acetonitrile versus Fc/Fc+. Reprinted (or Adapted) with permission from [185]. Copyright 2014 American Chemical Society.	127
Figure 4.33. Emission spectra of the only NPL, NPL + 9 nmol P2b and NPL + 9 nmol P2c samples. The inset shows the NPL emission after spectral profile of the polymer emission is subtracted. The emission quenching is larger for P2b than P2c since P2b	

has a shorter anchor ligand. Reprinted (or Adapted) with permission from [185]. Copyright 2014 American Chemical Society.	129
Figure 4.34. HAADF-STEM images of (a) only NPLs and (b) NPL-P2a hybrids. The insets show zoomed-in images with scale bar of 100 nm. Reprinted (or Adapted) with permission from [185]. Copyright 2014 American Chemical Society.	130
Figure 4.35. Absorption and photoluminescence spectra of (a) the blue-emitting CdZnS/ZnS core/shell QDs and (b) the green-emitting 4ML CdSe NPLs, which are dissolved in hexane at room temperature. High-angle annular dark-field scanning transmission electron microscopy (HAADF-STEM) images of (c) the donor-QDs having 9.3 ± 1.2 nm and (d) the acceptor-NPLs having 12.8 ± 1.9 nm by 10.5 ± 1.5 nm mean sizes. The inset in (c) shows the transmission electron microscopy (TEM) image of a CdZnS/ZnS core/shell QDs. Reprinted by permission from Wiley [110], Copyright 2015 Wiley-VCH Verlag GmbH & Co. KGaA, Weinheim.....	137
Figure 4.36. Scanning electron microscopy (SEM) images of the hybrid solid thin films of the donor QDs (bright ones) and the acceptor NPLs having 0.01 D/A molar ratio for (a) 500 nm and (b) 100 nm scale bars. The yellow and blue arrows given in (b) point at the QDs and the NPLs, respectively. Reprinted by permission from Wiley [110], Copyright 2015 Wiley-VCH Verlag GmbH & Co. KGaA, Weinheim.	138
Figure 4.37. Steady-state PL spectra of the solid films of only-donor (blue line), only- acceptor (green line) and donor-acceptor having D/A= 0.10 (red line) cases. Reprinted by permission from Wiley [110], Copyright 2015 Wiley-VCH Verlag GmbH & Co. KGaA, Weinheim.	139
Figure 4.38. Time-resolved fluorescence decay curves of the solid thin film samples including donor-only, acceptor-only and hybrid cases with varying D/A molar ratios measured (a) at the donor band-edge emission wavelength (453 nm) and (b) at the acceptor band-edge emission wavelength (513 nm). The insets show the zoom-in of the same decay curves and the impulse response function (IRF). Reprinted by permission from Wiley [110], Copyright 2015 Wiley-VCH Verlag GmbH & Co. KGaA, Weinheim.....	141
Figure 4.39. Evolution of the nonradiative energy transfer (NRET) efficiency as a function of the donor QDs to acceptor NPLs (D/A) molar ratios. The dash-dot lines are	

a guide for the eyes. Reprinted by permission from Wiley [110], Copyright 2015 Wiley-VCH Verlag GmbH & Co. KGaA, Weinheim.	145
Figure 4.40. (a) Photoluminescence excitation (PLE) spectra of the only-donor QDs (blue-line) and the only-acceptor NPLs (green-line) measured at their emission peak wavelengths (453 and 513 nm, respectively). (b) Excitation spectra of the samples having different D/A ratio normalized at the e-lh transition peak wavelength (480 nm). The inset shows the enhancement in the excitation spectra of the hybrid donor-acceptor samples due to the NRET from donor QDs. Reprinted by permission from Wiley [110], Copyright 2015 Wiley-VCH Verlag GmbH & Co. KGaA, Weinheim.	147
Figure 4.41. Time-resolved fluorescence decay curves of the solid thin film samples including (a) the donor-only, (b) the acceptor-only, and the blended case of donor and acceptor for D/A=0.01 molar ratio measured (c) at the donor band-edge emission wavelength (453 nm) and (d) at the acceptor band-edge emission wavelength (513 nm). The dashed arrows show the direction of decreasing temperature. The insets show the zoom-in for the early phase, along with the impulse response function (IRF). Reprinted by permission from Wiley [110], Copyright 2015 Wiley-VCH Verlag GmbH & Co. KGaA, Weinheim.	148
Figure 4.42. (a) Evolution of the NRET efficiency (η_{NRET}) for D/A=0.01 ratio as a function of the temperature. The dash-dot lines show the linear fitting curve with 0.032 of slope. (b) Enhancement in η_{NRET} corresponding based on the experimental data (blue-circle) and the calculated results using the shift in spectral overlap between the PL spectrum of donor and the absorption spectrum of acceptor (black-diamond) and those using both the shift in spectral overlap and the change in PL QY with decreasing temperature. Reprinted by permission from Wiley [110], Copyright 2015 Wiley-VCH Verlag GmbH & Co. KGaA, Weinheim.	150
Figure 4.43. (a) Temperature dependent 1-T (transmission) spectra for the acceptor-only case. (b) Photoluminescence (PL) spectra of the donor-only case at different temperatures.	151

Figure 5.1. (a) Representative schematic of the organic-inorganic exciton transferring thin film. (b) Fluorescence of TCTA (violet), Flrpic (cyan) and QDs (red) along with

the absorbance of QDs (red-dashed). Reprinted (or Adapted) with permission from [190]. Copyright 2014 American Chemical Society.....	164
Figure 5.2. Steady state fluorescence spectra of only QDs (red), only TCTA (violet), FIrpic:TCTA (cyan), TCTA/QDs (orange) and FIrpic:TCTA /QDs (green). The organic layer thickness is 20 nm. Reprinted (or Adapted) with permission from [190]. Copyright 2014 American Chemical Society.	165
Figure 5.3. (a) PLE at the QD emission peak for the samples of only QDs (red), TCTA/QDs (orange), FIrpic:TCTA/QDs (green) when the organic film thickness is 20 nm. (b) Normalized PLE spectrum of FIrpic emission (cyan) from the FIrpic:TCTA sample and PLE spectrum of TCTA emission from the bare TCTA sample. (c) Cascaded exciton transfer from the organic layer into the QDs (TCTA→FIrpic→QDs). Reprinted (or Adapted) with permission from [190]. Copyright 2014 American Chemical Society.	166
Figure 5.4. (a) Phosphorescence decay curves and their fits for the FIrpic emission from the samples of FIrpic:TCTA (cyan) and FIrpic:TCTA/QDs (red) when the organic film thickness is 20 nm. (b) Fluorescence decay curves and fits for the QD emission from the samples of only QDs (red), TCTA/QDs (orange) and FIrpic:TCTA/QDs (green). The inset exhibits the decay in an early time frame. All of the time resolved measurements were performed using a pulsed laser at 375 nm. Reprinted (or Adapted) with permission from [190]. Copyright 2014 American Chemical Society.	169
Figure 5.5. (a) Fluorescence enhancement factors of the QD emission in the samples of TCTA/QDs (orange) and FIrpic:TCTA/QDs (green) as a function of the organic film thickness and the modelled enhancement factors plotted in dashed curves. (b) Modelled NRET efficiency in the TCTA:FIrpic/QDs sample as a function of organic layer thickness with and without exciton diffusion assistance together with experimentally measured NRET efficiency from time resolved fluorescence measurements. Reprinted (or Adapted) with permission from [190]. Copyright 2014 American Chemical Society.	172
Figure 5.6. Photoluminescence of the QD/FIrpic:TCTA samples when excited at 330 nm. Reprinted (or Adapted) with permission from [190]. Copyright 2014 American Chemical Society.	174

Figure 5.7. (a) 3D schematic of the QLED designed to achieve efficient energy transfer pumping. (b) Energy band alignment of the device in the structure of ITO/PEDOT:PSS/poly-TPD/QD/BPhen/Ir(ppy)₃TCTA/TPBI/LiF/Al. Reprinted (or Adapted) with permission from [21]. Copyright 2014 American Chemical Society.. 178

Figure 5.8. (a) Normalized electroluminescence spectra of the ITO/PEDOT:PSS/poly-TPD/QD/TPBI/LiF/Al, ITO/PEDOT:PSS/poly-TPD/QD/TCTA:Ir(ppy)₃/TPBI/LiF/Al. (b) Normalized electroluminescence spectra of ITO/PEDOT:PSS/poly-TPD/QD/BPhen/TCTA:Ir(ppy)₃/TPBI/LiF/Al with varying the BPhen thickness. Reprinted (or Adapted) with permission from [21]. Copyright 2014 American Chemical Society. 179

Figure 5.9. The current-voltage profile of the devices: ITO/PEDOT:PSS/poly-TPD/QD/ TCTA:Ir(ppy)₃/TPBI/LiF/Al and ITO/PEDOT:PSS/poly-TPD/QD/BPhen/TCTA:Ir(ppy)₃/TPBI/LiF/Al. Reprinted (or Adapted) with permission from [21]. Copyright 2014 American Chemical Society. 180

Figure 5.10. Schematic of the partially phosphorescent co-doped electron transport layer of TCTA. The partial co-doping is positioned in four different zones within the TCTA as indicated by positions 1 to 4 above the scheme, where position 1 is the closest to the QDs. NRET is expected to be the strongest for the co-doping located at the position 1. Reprinted (or Adapted) with permission from [21]. Copyright 2014 American Chemical Society. 182

Figure 5.11. (a) Non-normalized electroluminescence spectra of the ITO/PEDOT:PSS/poly-TPD/QD/BPhen/TCTA:Ir(ppy)₃/TPBI/LiF/Al device with varying the position of the co-doped TCTA:Ir(ppy)₃ layer within the TCTA electron transport layer. (b) External quantum efficiencies of the devices at 5 mA injection current as a function of the position of the co-doping layer into TCTA. (c) EQE vs. current density of the devices: energy transfer pumping and color purity optimized ITO/PEDOT:PSS/poly-TPD/QD/BPhen(1.5 nm)/TCTA:Ir(ppy)₃(2.5nm)/TCTA (7.5nm)/TPBI/LiF/Al and conventional ITO/PEDOT:PSS/poly-TPD/QD/TPBI/LiF/Al. (d) Electroluminescence spectra of the outperforming ITO/PEDOT:PSS/poly-TPD/QD/BPhen/TCTA:Ir(ppy)₃/TPBI/LiF/Al device (Ir(ppy)₃ doping in the first 2.5 nm of the TCTA layer). Reprinted (or Adapted) with permission from [21]. Copyright 2014 American Chemical Society. 183

Figure 5.12. The luminance - current profile of the optimized device of ITO/PEDOT:PSS/poly-TPD/QD/BPhen/TCTA:Ir(ppy) ₃ /TPBI/LiF/Al. (2.5 nm codoped layer is just positioned next to the BPhen layer). Reprinted (or Adapted) with permission from [21]. Copyright 2014 American Chemical Society.	184
Figure 5.13. Time resolved fluorescence spectra of the quantum dot (QD) layer in the bare and in various architecture samples (QD/BPhen, QD/TCTA, QD/Ir(ppy) ₃ :TCTA, QD/ BPhen /Ir(ppy) ₃ :TCTA) along with the bi-exponential fits given with white dots. Reprinted (or Adapted) with permission from [21]. Copyright 2014 American Chemical Society.	186
Figure 6.1 Structure of the core/shell ZnCdS/ZnS quantum dots that simultaneously combine large size, high stability and suppressed Auger recombination thanks to the gradient core/shell interface.	195
Figure 6.2 (a) Absorbance and (b) photoluminescence of the blue-emitting CdZnS/ZnS QDs having different shell growth time. (c) Transmission electron microscopy images of the different shell grown QDs. Reprinted (or Adapted) with permission from [274]. Copyright 2014 American Chemical Society.	196
Figure 6.3 Zn/Cd ratio of the graded QDs with shells grown in 30, 120, and 180 min measured with XPS as a function of etching time. Linear fits are presented to guide the eye. Reprinted (or Adapted) with permission from [274]. Copyright 2014 American Chemical Society.	197
Figure 6.4 Pump intensity dependent PL of (a) 30 min, (b) 120 min and (c) 180 min shell grown CdZnS/ZnS QDs under 1PA pumping. (d) Luminescence vs. pump intensity curve of the 180 min shell grown QDs with 1PA pumping. Reprinted (or Adapted) with permission from [274]. Copyright 2014 American Chemical Society.	199
Figure 6.5 Pump intensity dependent PL of (a) 30 min, (b) 120 min and (c) 180 min shell grown CdZnS/ZnS QDs under 2PA pumping. (d) Luminescence vs. pump intensity curve of the 30 min, 120 min and 180 min shell grown QDs with 2PA pumping. Reprinted (or Adapted) with permission from [274]. Copyright 2014 American Chemical Society.	200

Figure 6.6 (a) PL intensity of the 30 min shell grown QDs under 1PA pumping as a function of pump intensity. At higher pump intensities higher-order multiexcitonic ASE is observed in addition to the regular ASE. (b) Variable stripe length measurement of the gain coefficient of the 180 min shell grown QDs pumped by 1PA. Reprinted (or Adapted) with permission from [274]. Copyright 2014 American Chemical Society. 202

Figure 6.7 (a) Transmission electron microscopy image of the CdSe/CdS QDs having CdSe core of 2.2 nm radius and 6 monolayer CdS shell. Inset shows the high resolution TEM image of a CdSe/CdS QD with diameter of ~8 nm. (b) XRD patterns of CdSe core (bottom) and CdSe/CdS QDs (top). The CdSe core shows zinc-blende structure with matched XRD pattern to its bulk counterpart. After CdS shell growth, diffraction peaks are shifted to higher angles and become narrower, indicating the increased crystalline quality and alloying at the core/shell interface. (c) Photoluminescence (red, solid) and absorbance (blue, dotted) spectrum of the core/shell QD. Emission line width is less than 30 nm (full width at half maximum – FWHM) suggesting the small size distribution. Reprinted by permission from Wiley [18], Copyright 2015 Wiley-VCH Verlag GmbH & Co. KGaA, Weinheim..... 208

Figure 6.8 Transient PL intensity measured at the peak emission wavelength at three different excitation levels for (a) CdSe-core/CdS-shell and (b) core-only CdSe QDs. τ_{XX} is the multi-exciton lifetime, τ_X is the single exciton lifetime of the QDs. The average number of excitons per QD ($\langle N \rangle$) was calculated from the excitation levels. (b) Inset shows the decay of the CdSe QDs at an early time window. Reprinted by permission from Wiley [18], Copyright 2015 Wiley-VCH Verlag GmbH & Co. KGaA, Weinheim..... 210

Figure 6.9 (a) Etch depth profile analysis of the atomic ratio of S to Se. (b) Initial etched part (i.e., top QDs) and deeper etched part (i.e., ensemble region). Reprinted by permission from Wiley [18], Copyright 2015 Wiley-VCH Verlag GmbH & Co. KGaA, Weinheim..... 213

Figure 6.10 Alloyed vs. abrupt core/shell interface in CdSe/CdS QDs along with their atomic composition throughout the QD. Reprinted by permission from Wiley [18], Copyright 2015 Wiley-VCH Verlag GmbH & Co. KGaA, Weinheim. 215

Figure 6.11 (a) The emission spectra of the core/shell QD film under 1PA stripe excitation pumping. The inset shows the integrated emission intensity as a function of 1PA pumping energy intensity. (b) 2PA pumped emission spectra of the QDs at various pump intensities. Inset shows the integrated intensity of the emission as a function of 2PA pump intensity. The narrow ASE peak with a FWHM of 5 nm kicks off at the red-tail of the spontaneous emission spectrum (FWHM of ~29 nm). (c) Laser shot dependent ASE intensity under pump laser shots up to 1.8×10^7 indicating the exceptional stability of the QDs. Reprinted by permission from Wiley [18], Copyright 2015 Wiley-VCH Verlag GmbH & Co. KGaA, Weinheim..... 219

Figure 6.12 Variable stripe length technique based measurement of the net modal gain coefficient and the fit to the experimental data. Reprinted by permission from Wiley [18], Copyright 2015 Wiley-VCH Verlag GmbH & Co. KGaA, Weinheim..... 220

Figure 6.13 Open aperture z-scan measurement reveals the 2PA cross-section of the QDs as 41,885 GM. Although this is not the highest reported 2PA cross-section for the QDs, the threshold for amplified spontaneous emission is the lowest among 2PA pumped QD gain media. This is only possible by the high gain performance of QD materials. Reprinted by permission from Wiley [18], Copyright 2015 Wiley-VCH Verlag GmbH & Co. KGaA, Weinheim. 220

Figure 6.14 Optical constants of SiO₂ and TiO₂ nanoparticle films and absorption of TiO₂ nanoparticles. Reprinted by permission from Wiley [18], Copyright 2016 Wiley-VCH Verlag GmbH & Co. KGaA, Weinheim..... 221

Figure 6.15 (a) Scanning electron microscopy cross-sectional image of the all-colloidal DBR shows alternating stacks as the results of different spin-casted nanoparticles (SiO₂ and TiO₂). Focused ion beam was used to create cross section of the colloidal DBR. Inset shows the close-up of the layered stacks of TiO₂ and SiO₂ nanoparticles at the cleaved edge of a DBR. (b) Surface normal reflectance of the DBR stack with 10-bilayer of TiO₂ and SiO₂ nanoparticles along with the PL of the QDs in the cavity having optical thickness of about 15 μm. (c) Emission intensity as a function of pump intensity for frequency up-converted all-colloidal VCSEL clearly shows the threshold behavior of the AC-VCSEL. Inset shows the emission spectrum of the laser under different excitation pump density. Single mode lasing is achieved with a Q-factor greater than 430. Lasing peak is narrower than 1.5 nm (limited by the spectral

resolution of our measurement system). (d) Photographic image of the lasing spot from the all-colloidal VCSEL. The spectrally and spatially coherent lasing beam is visible as a bright spot on the screen. Reprinted by permission from Wiley [18], Copyright 2015 Wiley-VCH Verlag GmbH & Co. KGaA, Weinheim.	222
Figure 6.16 Single- and multi-mode lasing in AC-VCSELs. Depending on the location of the pump spot on the AC-VCSEL, either single-mode or multi-mode lasing is observed when the pump intensity is above the threshold. Reprinted by permission from Wiley [18], Copyright 2015 Wiley-VCH Verlag GmbH & Co. KGaA, Weinheim.	224
Figure 6.17 High-angle annular dark-field transmission electron microscopy (HAADF-TEM) images of (a) the core-only and core/crown NPLs having a size of (b) 21, (c) 25 and 32 nm. Reprinted (or Adapted) with permission from [17]. Copyright 2014 American Chemical Society.	230
Figure 6.18 Absorbance and photoluminescence of the NPLs: core-only (orange), core/crown NPL having size of 21 nm (blue), 25 nm (green) and 32 nm (red). (b) Photoluminescence excitation spectra of the core-only and core/crown NPLs. Reprinted (or Adapted) with permission from [17]. Copyright 2014 American Chemical Society.	231
Figure 6.19 (a) 2PA pumped ASE of the 21 nm size core/crown NPLs. (b) 2PA pumped luminescence vs. pump intensity of the core-only and core/crown NPLs having a size of 21, 25 and 32 nm. Reprinted (or Adapted) with permission from [17]. Copyright 2014 American Chemical Society.	233
Figure 6.20 2PA pumped ASE of the core-only and core/crown NPLs having size of 25 and 32 nm. Reprinted (or Adapted) with permission from [17]. Copyright 2014 American Chemical Society.	233
Figure 6.21 (a) 1PA pumped ASE of the 21 nm size core/crown NPLs. (b) 1PA pumped luminescence vs. pump intensity of the core-only and core/crown NPLs having a size of 21, 25 and 32 nm. (c) Variable stripe length measurement of the gain coefficient. Reprinted (or Adapted) with permission from [17]. Copyright 2014 American Chemical Society.	235

Figure 6.22 1PA pumped ASE of the core-only and core/crown NPLs having size of 25 and 32 nm. Reprinted (or Adapted) with permission from [17]. Copyright 2014 American Chemical Society.	235
Figure 6.23 (a) Schematic of the VCSEL of the NPLs that employ DBRs having 6-bilayers stack of SiO ₂ and TiO ₂ nanoparticles each. (b) Emission spectrum of the VCSEL is plotted as the pump intensity is progressively increased. (c) Integrated emission intensity vs. pump intensity measurement and the linear fits indicating the 2PA pumped lasing threshold of 2.49 mJ/cm ² . Reprinted (or Adapted) with permission from [17]. Copyright 2014 American Chemical Society.	236
Figure 6.24 Transmission electron microscopy (TEM) images of the 4 ML CdSe NPLs having different lateral sizes: (a) 170.0 ± 22.5 nm ² (NPL-1), (b) 269.6 ± 38.6 nm ² (NPL-2), (c) 377.6 ± 56.4 nm ² (NPL-3) and (d) 391.9 ± 65.7 nm ² (NPL-4), grown using different growth times. Reprinted (or Adapted) with permission from [66]. Copyright 2015 American Chemical Society.	241
Figure 6.25 Absorption and photoluminescence spectra of the 4ML CdSe NPLs grown in lateral direction with different growth times. The peaks labeled as e-lh and e-hh in the absorption spectrum correspond to the electron-light hole and the electron-heavy hole transitions, respectively. Reprinted (or Adapted) with permission from [66]. Copyright 2015 American Chemical Society.	242
Figure 6.26 (a) Time-resolved fluorescence decays of the NPLs having different lateral sizes. The inset shows the zoom-in of the same TRF decay. Evolution of (b) the lifetime components of fluorescence decays, (c) the amplitude-averaged photoluminescence lifetimes, (d) photoluminescence quantum efficiency (PL-QE) (e) the percentage steady state contribution from each decay component of the NPLs and (f) calculated fraction of NPL sub-populations as a function of the lateral size. The dotted lines are a guide for eyes. Reprinted (or Adapted) with permission from [66]. Copyright 2015 American Chemical Society.	245
Figure 6.27 Photoluminescence quantum efficiency (PL-QE) measurements of the 4ML CdSe NPLs grown in lateral direction using different growth times, in comparison to the reference dye of Rhodamine 6G (Rh6G) with 95% PL-QE. Reprinted (or Adapted) with permission from [66]. Copyright 2015 American Chemical Society.	247

Figure 6.28 The schematic representation of the non-defected (yellow) and defected (red) NPLs within the NPL ensembles. The relative change of the fraction of these two different NPL populations as a function of lateral area is shown to match the experimental PL QEs. Reprinted (or Adapted) with permission from [66]. Copyright 2015 American Chemical Society.	250
Figure 6.29 (a) Single-photon absorption (1PA) pumped ASE of the 4ML CdSe NPLs (NPL-1) having a lateral size of 170.0 nm ² . (b) 1PA pumped luminescence vs. pump intensity of the NPLs having different lateral size. (c) Evolution of the 1PA pumped ASE thresholds with lateral size. (d) Two-photon absorption (2PA) pumped ASE of the NPL-4 having a lateral size of 391.9 nm ² . (e) 2PA pumped luminescence vs. pump intensity of the NPLs having different lateral size. (f) Evolution of the 2PA pumped ASE thresholds with lateral size. The dotted lines are a guide for eyes. The 1PA- and 2PA-ASE thresholds exhibit opposite trends over for varying lateral size. Reprinted (or Adapted) with permission from [66]. Copyright 2015 American Chemical Society..	255
Figure 6.30 Comparative open aperture z-scan measurement of the NPL ensembles having lateral area of 269.6 nm ² (NPL-2) and 391.9 nm ² (NPL-4). The fit of the z-scan measurement gives a giant two-photon absorption cross-section of 0.537×10^6 GM and 2.247×10^6 GM for the NPL-2 and NPL-4, respectively. Reprinted (or Adapted) with permission from [66]. Copyright 2015 American Chemical Society.	257
Figure 7.1. (a) Three-level optical gain in conventional nanocrystals. (b) Prospect of four-level optical gain in excitonically engineered next-generation nanocrystals.	265
Figure 7.2. Peak modal gain coefficients as a function of pump intensity in heterostructured nanoplatelets having Type-II electronic structure. (Guzelturk et al., unpublished data.)	266
Figure 7.3. HAADF-STEM images of the self-assembled CdSe nanoplatelets: (a) face-to-face stacked perpendicular-lying nanoplatelets on a substrate, (b) side-by-side oriented flat-lying nanoplatelets on a substrate. (Guzelturk et al., unpublished data.)	268

List of Tables

Table 2.1. Bulk exciton binding energies and exciton Bohr radii of common II-VI and III-V semiconductor compounds.	19
Table 4.1. Fluorescence decay components of the donor 4 ML NPLs.	98
Table 4.2. Fluorescence decay components of the acceptor 5 ML NPLs.	99
Table 4.3. Amplitude averaged fluorescence lifetimes of the donor and acceptor NPLs for the samples having varying A:D ratio. Predicted NRET rates (ns^{-1}) are also presented.	99
Table 4.4. Molecular weights and PDIs of all polymers.	119
Table 4.5. Fluorescence lifetime components of the solid thin film samples measured at the peak emission wavelength (453 nm).	142
Table 4.6. Fluorescence lifetime components of the solid thin film samples measured at the acceptor peak emission wavelength (513 nm).	143
Table 4.7. Donor QDs and acceptor NPLs lifetimes (τ), their NRET rates (k_{NRET}) and efficiencies (η_{NRET}) with varying D/A ratios.	146
Table 4.8. The calculated NRET efficiencies (η_{NRET}) and enhancement in the η_{NRET} for different temperature points. Here, Δ_{Shift} is the shift in the spectral overlap between the PL spectrum of donor and the extracted absorption spectrum of acceptor with decreasing temperature; η_{NRET} is the NRET efficiency using amplitude-average lifetimes; $\eta_{\text{NRET-1}}$ is the NRET efficiency calculated using Δ_{Shift} ; $\eta_{\text{NRET-2}}$ is the NRET efficiency calculated using Δ_{Shift} and quantum yield (QY) of the donor while the	

temperature is decreased; $\Delta-0$, $\Delta-1$ and $\Delta-2$ are the enhancements in η_{NRET} , $\eta_{\text{NRET}-1}$ and $\eta_{\text{NRET}-2}$, respectively, with respect to the NRET efficiency value at 270 K. 152

Table 5.1. Peak external quantum efficiency of the excitonic LEDs and also control devices. 184

Table 5.2. Amplitude-averaged fluorescence lifetimes of the QDs in bare-QD, QD/BPhen, QD/TCTA, QD/Ir(ppy)₃:TCTA and QD/ BPhen /Ir(ppy)₃:TCTA samples. 186

Table 6.1 Fluorescence lifetime components and the corresponding amplitudes for the CdSe/CdS QDs at different pump intensities measured at peak emission wavelength of 626 nm. 210

Table 6.2 Fluorescence lifetime components and the corresponding amplitudes for the zinc-blende CdSe QDs at different pump intensities measured at peak emission wavelength of 567 nm. 211

Table 6.3 Sulfur to Selenium ratio calculated by the volumes of the core and the shell, measured by XPS and calculated by (6.4) assuming abrupt core/shell interface and calculated by (6.5) assuming alloyed core/shell interface with varying alloy width. . 216

Table 6.4 Analysis of UV-Vis and photoluminescence spectra for the 4 ML CdSe NPLs grown using different growth times. 243

Table 6.5 Fluorescence decay components and the fractional emission contributions of the 4 ML CdSe NPLs grown using different growth times (i.e., different lateral areas). 246

Table 6.6 Calculated contribution of the fluorescence lifetime components to the total emission of the NPL samples. 252

Table 6.7 Calculated and experimental fractions emission contributions of the lifetime components are compared, exhibiting a very well match with the calculation and the experiment. 252

Table 6.8 Single- (1PA) and two-photon absorption (2PA) pumped of ASE thresholds of the 4ML CdSe NPLs having different lateral size. 256

Chapter 1

Introduction

Photonics technology is envisioned to enable key technology platforms to combat some of the most difficult societal challenges of the world including sustainable energy generation, energy efficiency, climate change, environmental sustainability, healthy aging of population, and global security. In the past decade, photonics industry has been rapidly growing, which reached a market volume larger than €350 billion in 2013 and is expected to reach €650 billion by 2020 [1]. Photonics technologies encompass a broad range of application areas, including displays, lighting, communication, healthcare and life sciences, defense technologies, photovoltaics, in all of which rapid innovative solutions and disruptive materials are essentially needed. To this end, newly emerging photonic materials are in high demand, being intensively explored and have strategic importance. Among these materials, solution-processed semiconductor nanocrystals, which are synthesized using low-temperature colloidal epitaxy, represent an important alternative to high-temperature gas-phase epitaxy grown semiconductors. Colloidal nanocrystals bring together low-temperature cheap production, ease of material processability on arbitrary substrates and exciting optoelectronic and material properties. Therefore, semiconductor nanocrystals are expected to challenge conventional semiconductors that have been hampered by low throughput and high cost.

Last decade has witnessed the rise of colloidal nanocrystals, which have also recently made their transition from research labs into commercial products. Colloidal nanocrystal-based backlighting, which enlarges the color span of a liquid-crystal display (LCD) TV and enhances the color richness and viewing experience, has attracted an extensive interest from industry (e.g., Sony, 3M, Samsung and Phillips) [2]–[4]. This interest has led to a rapidly growing nanocrystal market, which exceeded \$300 million by 2013. According to a recent market forecast, the nanocrystal market is expected to grow over \$5 billion in 2020 [5]. This remarkable growth is foreseen dominantly in lighting and display technologies, where electrically driven nanocrystal light-emitting diodes (LEDs) are predicted to have a large impact in the display industry to rival current organic-LED (OLED) based displays. The market predictions also show that nanocrystal-based lasers [6], solar cells [7], transistors [8] and sensors [9] will become appealing for the industry in the coming years as a result of the promising basic research and development efforts. Although colloidal semiconductor nanocrystals can potentially enable next-generation low-cost, large-scale and energy-efficient optoelectronics, there exist both practical and fundamental challenges that need to be addressed to make these materials competitive and competent for practical devices. In this thesis, we have addressed numerous challenges that have existed in the conventional colloidal nanocrystals and in their hybrid systems hindering the achievement of energy-efficient optoelectronics and offered new solutions and understanding.

The colloidal nanocrystals could, in principle, empower lasers that can emit in any color in the visible and infrared [10]. However, to date, nanocrystal lasers have been severely obstructed due to their poor performance making them impractical for feasible real-life applications. The limitation in nanocrystal lasers essentially arises from the dominant Auger recombination [11] that leads to the depletion of the available gain by rapid annihilation of the gain-active electronic species. Another challenge is the small optical gain coefficients in the conventional nanocrystals arising from the small stimulated emission cross-sections in them. Thus, nanocrystals that can simultaneously suppress Auger recombination and achieve large stimulated emission cross-sections are highly desired to accomplish the first practical nanocrystal lasers.

Moreover, colloidal nanocrystals and their solid films are exciting for light-harvesting applications such as solar cells [12] and artificial photosynthesis [13] with tunable and broadband light absorption. Yet, ultrashort exciton diffusion lengths (< 20 nm) in the nanocrystal solids make them incompetent for efficient photovoltaics [14]. Nanocrystal solids that can accomplish extended exciton diffusion lengths are crucially required, which can unleash the potential of these materials for efficient light-harvesting.

Additionally, as nanocrystal market forecasts predict, electroluminescent nanocrystal light-emitting diodes will make a niche application for versatile display applications. Although efficient nanocrystal LEDs have been reported based on complex device architectures with multiple charge injection, transport and blocking layers [15], the performance of these electroluminescent devices is deteriorated due to the charge imbalance that detrimentally leads to the charging of nanocrystals and the interfaces in active electroluminescent devices. Furthermore, it is difficult to control the exciton formation zone, thus excitons that are formed outside the nanocrystals result in unfavorable efficiency droops in these devices [16]. Thus, it is needed to understand and control charge and exciton processes in nanocrystal LEDs. Also, exciton recycling is crucially needed to overcome the undesired nonradiative processes, but it has not been systematically studied before.

In this thesis, we have proposed, developed and demonstrated novel energy-efficient optoelectronic devices, based on the engineered excitonic properties of low-dimensional colloidal semiconductors. For this, we have designed and developed new-generation heterostructured semiconductor nanocrystals and their hybrid assemblies, systematically investigated their optical, electronic and material properties and tailored these materials for desired photonic response. As we have explored in this thesis, new-generation designer colloidal nanocrystals can potentially overcome the long standing problems of conventional colloidal nanocrystals. This could therefore potentially lead to efficiency breakthroughs in their optoelectronic devices.

Here, we have achieved remarkable optical gain performance using CdSe/CdS nanoplatelets that accomplish record high optical gain coefficients among all-solution processed semiconductors [17]. Our work has unleashed the great potential colloidal nanoplatelets as lasing media for the first time. We also developed the first all-colloidal nanocrystal lasers that showed record low frequency up-converted lasing threshold. These all-solution processed nanocrystal lasers are highly interesting for under-skin therapy and bio-imaging applications [18]. Moreover, developing the close-packed assemblies of the atomically-flat colloidal CdSe colloidal nanoplatelets, we have uncovered an ultrafast exciton transfer process [19]. This finding suggests the possibility of ultralong exciton diffusion lengths (>100 nm) in self-assembled nanoplatelet solids, which could open up new ways to harvest sunlight efficiently in colloidal nanocrystals solar cells. In addition, we have demonstrated organic-inorganic hybrids of colloidal quantum dots that achieve highly efficient exciton funneling transfer at the nanoscale [20]. These hybrids enabled exciton recycling in the nanocrystal light-emitting diodes, which substantially enhance their power conversion efficiencies and offer an efficient means to tackle the challenge of exciton leakage problem in nanocrystal light-emitting diodes [21]. Overall, the findings of this thesis have contributed to a new understanding of optical and excitonic properties in next-generation colloidal semiconductors, helping to form a bridge between the fields of excitonics and optoelectronics to achieve solution-processed and energy-efficient optoelectronics.

1.1 Organization of the thesis

In Chapter 2, we introduce colloidal semiconductor nanocrystals and discuss their optical properties that are essentially dominated by excitonic processes. We also discuss the basics of optical gain and elucidate the gain mechanism in conventional nanocrystals.

In Chapter 3, we present frequently used experimental methods in this thesis, which include steady state and time-resolved fluorescence spectroscopies. Furthermore, we explain how we characterized colloidal gain media for their gain threshold and modal

gain coefficients through amplified spontaneous emission measurements. We also discuss how to measure nonlinear absorption cross-section of a nanocrystal ensemble via open aperture z-scan measurement.

In Chapter 4, we uncover ultraefficient exciton transfer in the assemblies of the colloidal nanoplatelets. We also discuss their hybrid structures with conjugated polymers and quantum dots for potential applications in photovoltaics, sensitive non-contact temperature probing and enhanced light-generation.

In Chapter 5, we study exciton recycling in quantum dot based light-emitting diodes. We propose the use of phosphorescent small organic molecules as the exciton capturing and transferring agents, using which we enhance the efficiency of the electroluminescence in active quantum dot LEDs without sacrificing the color purity. Use of phosphorescent molecules also allows to harness both single and triplet excitons with high efficiency.

In Chapter 6, we introduce new types of nanocrystals that exhibit optical gain performance beyond the state of the art. In this part, we elucidate the first all-solution processed and all-colloidal nanocrystal lasers that show remarkable lasing performance. Furthermore, we uncover the potential of colloidal nanoplatelets for ultraefficient optical gain, which enables low threshold gain with record high modal gain coefficients.

In Chapter 7, we make the concluding remarks on this thesis. Also, we give a future outlook on the ongoing research while highlighting possible future research directions.

Chapter 2

Scientific Background

2.1 Colloidal semiconductor nanocrystals

The sparking developments that ignited the field of colloidal semiconductor nanocrystals date back to mid 80's. In 1985 Russian scientist Ekimov developed micro and nanocrystals of different II-VI semiconductors (e.g., CdS, ZnS) formed in glassy dielectric matrices, where peculiar size-dependent optical properties were observed [22]. Together with Efros, they corroborated these findings by the quantum confinement effect. Simultaneously, Brus from AT&T Bell Labs uncovered nanoclusters of CdS in the form of free-standing colloids exhibiting quantum confinement effects [23]. In the late 80's, Brus and his co-workers (Alivisatos and Bawendi) led the efforts to understand the photophysical properties of these nanocrystalline colloids, which were called "semiconductor cluster molecules" or "quantum crystallites" at the time [24]–[26]. These efforts helped to unveil the potential of these semiconductor colloids and have attracted an ever increasing interest from the scientific community since then [27].

Although the first generation of nanocrystals in the late 80's exhibited quantum confinement effects, these materials heavily suffered from low crystal quality, abundant surface traps and polydispersity. These also led to poor optical properties in the nanocrystals. A seminal paper in 1993 from Bawendi group paved the way for simple and robust synthesis of monodisperse colloidal nanocrystals of Cd-chalcogenides (e.g., CdSe, CdS and CdTe) using hot-injection method based on organometallic colloidal synthesis [28]. Also, Eychmüller and Weller developed a simple synthetic route to grow quality CdS colloids [29]. These developments in the synthetic colloidal chemistry allowed for the synthesis of high quality nanocrystals of II-VI semiconductors with exceptional optical and electronic properties that could be easily controlled via tuning the size of the particles. Starting from 1993 monodisperse colloidal quantum dots have created a great interest for optoelectronics and electronics as an alternative material system to gas-phase epitaxy grown semiconductors [30], [31]. As compared to the commonly used semiconductor materials such as organic dyes, quantum dots also offered increased environmental stability that makes them exciting for bio-imaging [32] and light-emitting diodes [33].

2.1.1 Shape control and composition tuning

Although free-standing and monodisperse colloidal nanocrystals have been introduced in the early 90's, these nanocrystals did not possess high photoluminescence quantum yields or robustness at ambient environment. Furthermore, they suffered from abundant surface traps that severely quench the photogenerated electron-hole pairs through nonradiative decay processes and cause photobleaching of the nanocrystals due to oxidation of their surfaces.

To improve the material, optical and electronic properties of the colloidal nanocrystals, heterostructured nanocrystal architectures have been explored, inspired by the semiconductors grown by gas-phase epitaxy. The first example of a heterostructured nanocrystal architecture was a core/shell quantum dot in the form of CdSe-core and ZnS-shell. These core/shell quantum dots exhibited substantial

improvement of the emission quantum yield (absolute quantum yield >50%) together with considerably increased environmental stabilities [34], [35]. This has been possible thanks to the localization of the electron and hole away from the surface trap sites by confining the excitons within the core to some extent. Since then capping of the nanocrystals with lattice matched inorganic shells has proven itself a very useful synthetic approach to produce high quality nanocrystals [36]. Later, core/multi-shell structures have been also proposed and demonstrated [37]. Overall, heterostructuring in colloidal nanocrystals has become a very useful strategy to tailor their optical and material properties for targeted applications.

In addition to spherical quantum dots of nanocrystals, different shapes of nanocrystals have become possible in the last decade. Pioneered by Alivisatos group in early 2000, nanocrystals with exotic shapes have become possible. These nanocrystals include one-dimensional nanorods, nanoarrows, nanodumbbells, nanoteardrops, tetrapods, and multipods [38], [39]. These materials have shown unique shape-dependent optical and electronic properties, making them interesting candidates for a broad range of applications, including bio-imaging [40], light-emitting diodes [41], solar cells [12], and lasers [42].

In the past decade, it has become possible to simultaneously control and tune the size and heterostructure of the nanocrystals. These include giant-shell quantum dots, dot-in-rod and rod-in-rod type nanorods, dot-in-bulk quantum dots [43], [44]. Furthermore, advancements in the colloidal synthesis allowed for the development of nanocrystals having fine controlled composition. This also empowered the means for the doping and alloying of the nanocrystals (Nie and Norris groups) [45], [46]. Furthermore, gradient alloying at the core/shell interfaces in the quantum dots have shown promise to realize highly emissive nanocrystals with suppressed Auger recombination [46], [47], making them exciting for light-emitting diodes and lasers [18], [48].

In recent years, understanding and manipulating surface chemistry of the colloidal nanocrystals has become an important field study. To overcome the poor charge

transport in the colloidal nanocrystal films arising from the original bulky organic ligands [33], significant efforts have been given to develop inorganic ligands [49], [50]. These efforts are expected to make colloidal nanocrystals appealing for electronics [51]. Another promising route is the use of cation exchange reactions, which makes it possible to completely and reversibly replace the metal ions in a nanocrystal using simple post-solution processing techniques [52]. Also, colloidal atomic layer deposition technique has enabled the room temperature growth of high-quality heterostructured nanocrystals [53].

Today, state-of-the-art nanocrystals, which are size, shape and composition tailored, can reach near-unity photoluminescence quantum yields (>95%) with exceptional environmental stabilities (>10,000 hours when properly packaged [54]). These quantum dots have already found industrial use as the color conversion materials in white light-emitting diodes. The nanocrystal-based color converter is used to generate high-quality white light, which is used as the backlight in liquid crystal displays (LCDs) [3]. Sony, Samsung, LG, Phillips and others now use the colloidal quantum dot enriched displays in the market [2], [55]. It is expected that 60% of the televisions will be using colloidal nanocrystals by 2025.

2.1.2 Atomically flat colloidal nanocrystals: nanoplatelets

In 2008 Ithurria and Dubertret have reported the synthesis of zinc-blende atomically-flat colloidal nanocrystals of CdSe [56]. Since the shape of these nanocrystals resembles a platelet, they are commonly known as colloidal nanoplatelets, or alternatively colloidal quantum wells. In the last few years, the nanoplatelets have been extensively investigated for their optical and electronic properties, which noticeably differ from those of the common colloidal quantum dots.

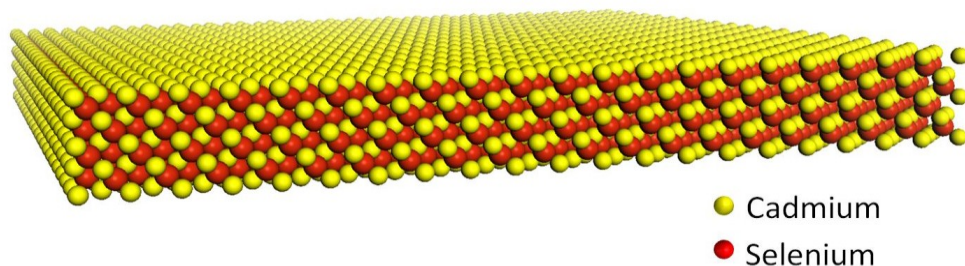


Figure 2.1. A schematic representation of a CdSe nanoplatelet having four CdSe monolayers with an additional Cd layer.

One of the unique aspects of the nanoplatelets is their vertical thickness, which is made up of only a discrete and small number of monolayers (MLs) of the constituting II-VI semiconductor (e.g., CdSe). Therefore, the nanoplatelets are described to have “magic-sized” vertical thicknesses [57]. Figure 2.1 schematically shows an exemplary case of a CdSe nanoplatelet having four monolayer (ML) CdSe repeating units with an additional Cd layer. Although it is still under debate, formation of the nanoplatelets is thought to be through unification of the magic-sized seeds, which leads to the growth of the nanoplatelets along [001] axis. Organic ligands are believed to play an important role by obstructing the growth of the Cd-terminated (100) surface. Because of this, the colloidal nanoplatelets of Cd-chalcogenide compounds are shown to possess Cd-terminated (100) surfaces (see Figure 2.1) [56]. However, nucleation kinetics and the exact mechanism of the nanoplatelet formation have not been fully understood as of yet. Using the colloidal synthesis, one can control the vertical thickness (e.g., 3, 4 and 5 monolayers) of the nanoplatelets and also their lateral size.

Figure 2.2 shows the high-angle annular dark-field scanning transmission electron microscopy (HAADF-STEM) images of two different batches of 4 ML thick CdSe nanoplatelets (vertical thickness ~ 1.2 nm) having different lateral sizes. For CdSe nanoplatelets, each monolayer corresponds to a distance of ca. 0.3 nm. Therefore, the vertical thickness of the nanoplatelets is generally on the order of 1 nm. Figure 2.3 shows the high resolution TEM images of the CdSe core-only and CdSe/CdS core/shell nanoplatelets. The vertical thicknesses were measured to be 1.2 nm for four monolayer

CdSe and 2.7 nm for the core/shell nanoplatelet having four monolayer CdSe core and four monolayer CdS shell.

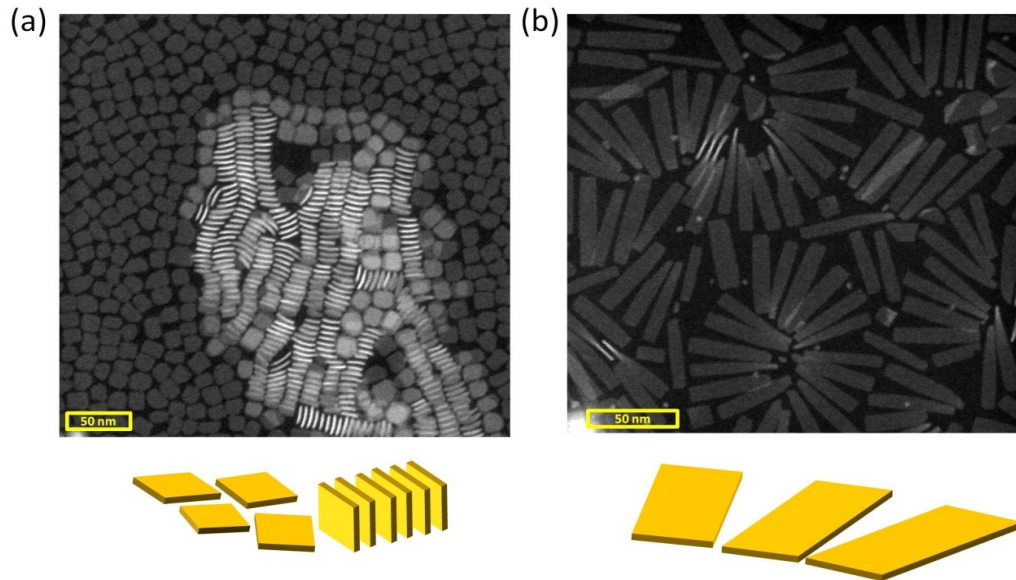


Figure 2.2. High-angle annular dark-field scanning transmission electron microscopy (HAADF-STEM) images of 4 monolayer thick CdSe nanoplatelets (vertical thickness ~ 1.2 nm) with different lateral extents: (a) 15 by 15 nm, (b) 35 by 10 nm.

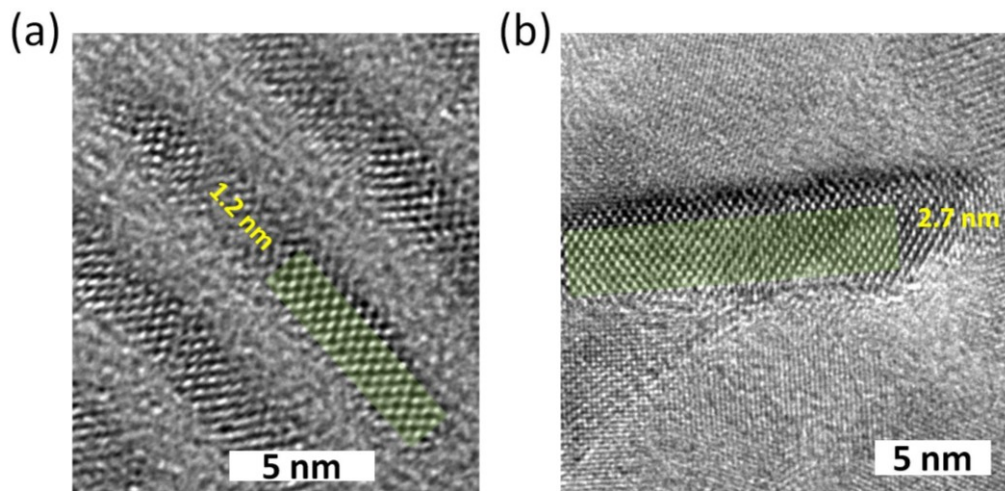


Figure 2.3. High resolution transmission electron microscopy (TEM) images of (a) 4 monolayer thick CdSe nanoplatelet having a fixed vertical thickness of ~ 1.2 nm, (b) CdSe-core/CdSe-shell nanoplatelet having a fixed vertical thickness of ~ 2.7 nm. Green shaded area is drawn as an overlayer to highlight the vertical thickness of the nanoplatelets since they do not perfectly stand upright on the TEM grid.

Lateral size of the nanoplatelets is generally larger than 10 nm (see Figure 2.2). Because of this, colloidal nanoplatelets dominantly exhibit one-dimensional quantum confinement (only along their vertical thicknesses). In the lateral directions, there is either very weak or almost no quantum confinement since the lateral size is much larger than the exciton Bohr radius (5.6 nm for CdSe). Due to strong one-dimensional quantum confinement, the nanoplatelets exhibit unique optical properties that are essentially different than those of the conventional nanocrystals (e.g., colloidal quantum dots). First, nanoplatelet ensembles do not exhibit inhomogeneous broadening in their absorbance and emission spectra [58], [59]. In colloidal quantum dot ensembles, inhomogeneous broadening is inevitable due to their size polydispersity, which leads to broadened emission spectrum since each individual quantum dot has slightly a different bandgap (see Figure 2.4a). Nevertheless, in nanoplatelet ensembles the vertical thickness is fixed; thus, their ensemble emission and absorption spectra are not inhomogeneously broadened since bandgap of each nanoplatelet in the ensemble is the same as dictated by their fixed vertical thickness.

Figure 2.4 schematically exemplifies the absence of inhomogeneous broadening in a colloidal nanoplatelet ensemble. Because of this, ensembles of the nanoplatelets having the same vertical thickness exhibit very narrow emission spectrum (see Figure 2.5 for 3, 4 and 5 ML thick CdSe nanoplatelets). The emission linewidth at room temperature is typically $\sim 35 - 40$ meV, which is comparable to the thermal broadening ($k_B T \sim 26$ meV). Phonon coupling (homogeneous broadening) is expected to broaden the emission spectrum of nanoplatelets at room temperature. The narrow emission spectra of the nanoplatelets at room temperature strongly suggests the absence of vertical thickness variation within the nanoplatelets, which would otherwise cause significant inhomogeneous broadening [57].

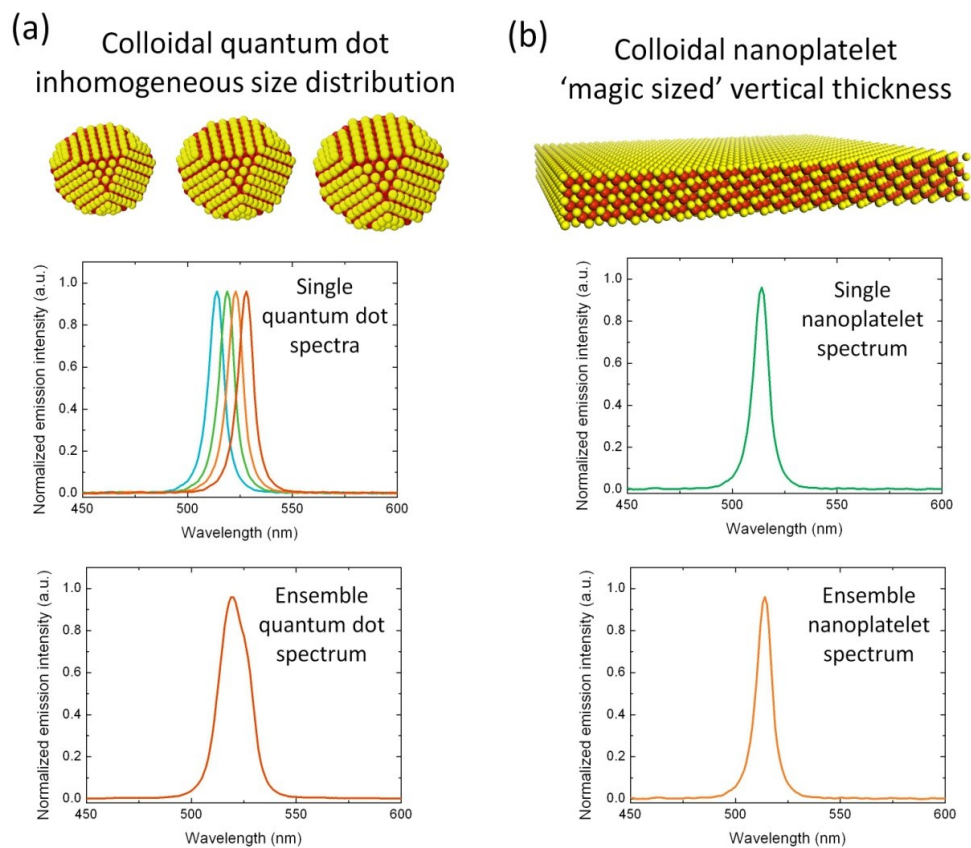


Figure 2.4. (a) Colloidal quantum dots having size polydispersity results in inhomogeneous broadening of their emission spectrum in their ensembles. (b) Colloidal nanoplatelets having magic-sized vertical thickness and large lateral sizes (larger than the exciton Bohr radius) do not exhibit inhomogeneous broadening in their ensembles.

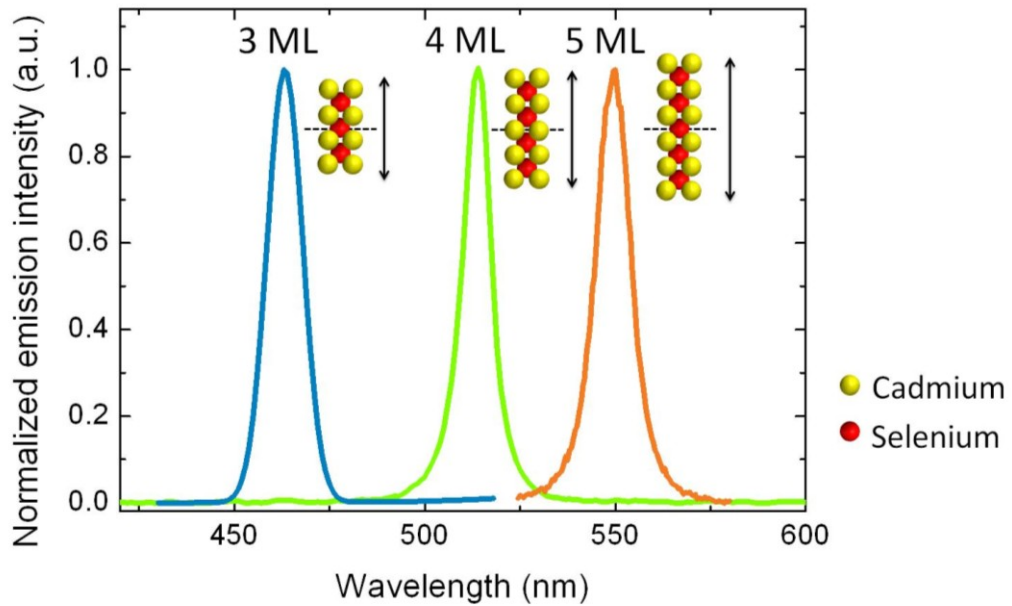


Figure 2.5. Photoluminescence emission spectra of 3, 4 and 5 ML thick CdSe nanoplatelets. 3, 4 and 5 ML CdSe nanoplatelets have their peak emission at 463, 513 and 551 nm, respectively. Full-width at half-maximum of the emission is \sim 8-10 nm (35 - 40 meV) at room temperature.

Strong one-dimensional quantum confinement bestows quantum well-like optical properties upon the colloidal nanoplatelets. Figure 2.6a shows the optical absorption spectrum of 4 ML thick CdSe nanoplatelet ensemble in hexane. The transition at 512 nm is due to excitonic state formed between the electron/heavy-hole (between the conduction band and the heavy-hole band). The absorbance peak at 480 nm is attributed to the electron/light-hole transition. Therefore, splitting of the heavy-hole and light-hole bands are observed in the nanoplatelets as similarly observed in the epitaxial quantum wells before. Generally in cubic semiconductors, heavy-hole (hh) and light-hole (lh) states are degenerate at Γ point ($k=0$). In the case of quantum wells, splitting of hh and lh states are commonly observed due to different degree of one dimensional quantum confinement for different hole bands [60]. Furthermore, strain in quantum wells, which are not lattice-matched, could also induce further energy splitting between the hh and lh states. Yet, strain is not expected to be dominant in our core-only CdSe nanoplatelets. Another contributing factor to the energy splitting of the

hh and lh states would also be the different exciton binding energies of the e/hh and e/lh transitions due to different hole masses. Furthermore, absorbance spectrum of the nanoplatelets exhibit staircase-like profile with the aforementioned excitonic features (see Figure 2.6b) thanks to the quantum well-like density of states in these nanoplatelets. Thus, they are also dubbed as colloidal quantum wells.

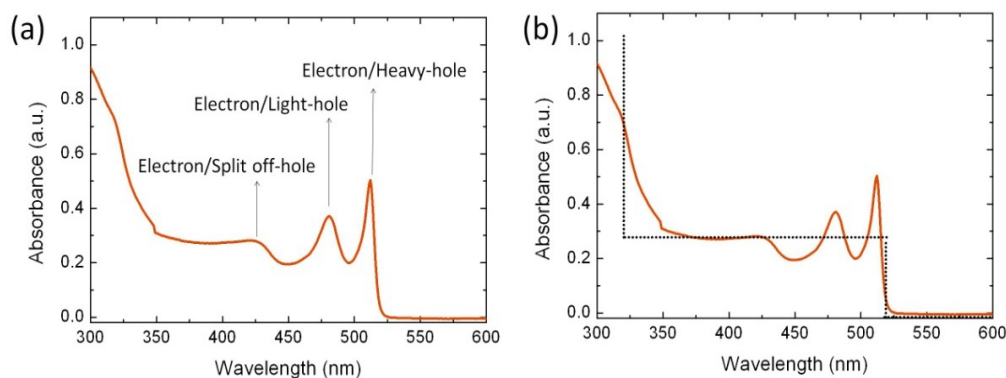


Figure 2.6. (a) Optical absorption spectrum of a 4 ML thick CdSe nanoplatelet in its solution state (dissolved in hexane). (b) Step-like density of states in the nanoplatelets, resembling quantum wells, with additional excitonic features arising from the six-fold degenerate valence band of the CdSe (heavy hole, light hole and split-off states).

In the last few years, optical properties of the nanoplatelets have been investigated by various groups, including Dubertret [61]–[63], Talapin & Pelton [64], [65], Demir [19], [66]–[68], Moreels [69], Lian [70], Woggon [71] and Siebbeles [58]. The findings suggest that the colloidal nanoplatelets can favorably bring together the advantageous properties of both epitaxial quantum wells and colloidal nanocrystals. To this end, the nanoplatelets were shown to exhibit very large exciton binding energies (~ 200 meV) thanks to strong confinement in one dimension and dielectric screening [72]. This exciton binding energy is 5- to 10-folds larger than that of the conventional quantum dots and also conventional epitaxial quantum wells. Similar to the nanoplatelets, excessively large exciton binding energies have also been predicted for recently emerging two-dimensional transition metal dichalcogenide monolayers such as MoS_2 and WSe_2 [73] arising from strong dielectric screening. One direct implication of large exciton binding energy in the nanoplatelets is the resulting large transition dipole moment (or oscillator strength). At room temperature, single exciton radiative

recombination lifetime was found to be 1 - 3 ns [58], whereas it is generally >20 ns for the colloidal quantum dots or rods having the same volume as the nanoplatelets. Moreover, radiative lifetime of the exciton decreases down to ~ 10 ps at cryogenic temperatures [69]. This strongly suggests the existence of giant oscillator strength transition (GOST) in the colloidal nanoplatelets. Increased coherence area of the excitons at lower temperatures leads to increased oscillator strength as the exciton center-of-mass wavefunction extends through many crystal unit cells along the lateral size of the nanoplatelet [74]. GOST effects had previously been observed also for epitaxial quantum wells with tight confinement [74].

As an important consequence of the large exciton binding energies and giant oscillator strengths, we have shown that the linear absorption cross-section of the nanoplatelets can be at least an order of magnitude larger than those of the colloidal quantum dots having the same volume as the nanoplatelets [67]. Similarly, nonlinear absorption cross-section of the nanoplatelets is also at least an order of magnitude larger than those of any other nanocrystal reported so far [66]. Additionally, Auger recombination has been shown to be suppressed in the CdSe nanoplatelets [58], [75], [76]. Although underpinning physics of this suppression is not clear yet, one strong possibility is that the large lateral extent of the nanoplatelets may allow for reduced interactions between quasi two-dimensional excitons.

The intrinsically strong excitonic properties of the nanoplatelets could be fine-controlled and tailored via developing heterostructured nanoplatelets. To date, different hetero-nanoplatelet architectures (see Figure 2.7) in the form of core/crown (having lateral extension), core/shell (having vertical coating) or their combination core/crown/shell have been proposed and demonstrated [53], [77]–[80]. These hetero-nanoplatelets offer enhanced optical and materials properties. For example, CdSe/CdS core/crown nanoplatelets show increased absorption cross-section thanks to the CdS crown acting as a photon absorbing and exciton transferring antenna [78]. These nanoplatelets also enable enhanced optical gain performance with record high gain coefficients [17].

Similarly, CdSe/CdS and CdSe/ZnS core/shell nanoplatelets enhance environmental stability with elongated fluorescence lifetimes due to the spatial separation electron and hole along the vertical thickness. These structures have quasi-Type-II electronic structure. Moreover, pure Type-II electronic structure could be successfully demonstrated using CdSe/CdTe core/crown nanoplatelets that have staggered band alignment at the core/crown interfaces [81], [82]. Further possibilities of forming multiple quantum wells through developing multiple shells or multiple crown type nanoplatelets present exciting opportunities. These complex nanoplatelet structures could facilitate unique excitonic and optical properties in colloidal nanocrystals that have never been attained before.

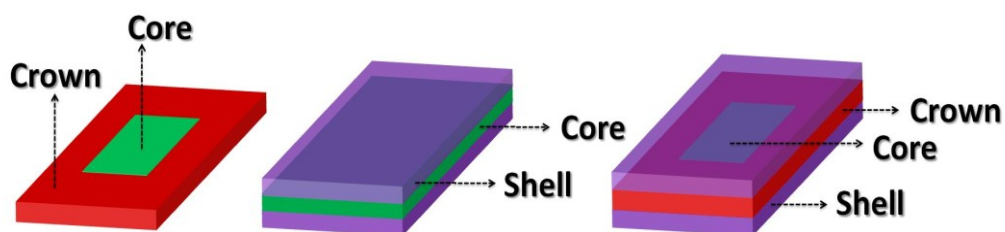


Figure 2.7. Heterostructured nanoplatelets: core/crown (lateral extension), core/shell (vertical coating) and core/crown/shell architectures.

With their unique optical and excitonic properties, colloidal nanoplatelets now make very promising and important class of semiconductor nanocrystals for optoelectronic devices and photonic applications. First of all, narrow emission spectrum makes them an exciting choice of material to use with light-emitting diodes (LEDs). Nanoplatelets could achieve very high color purity thanks to their narrow emission spectrum in their ensembles. This could easily boost color enrichment performance of the already existing and commercialized quantum dot-based color conversion in LED TVs. To date, proof-of-concept electroluminescent devices of the nanoplatelets have also been demonstrated [83], [84], yet these devices have not shown optimized performance yet.

Second, larger absorption cross-section of the nanoplatelets make them highly interesting for solar light-harvesting applications such as solar cells and photodetectors.

Dubertret group have shown sensitive photosensing using the nanoplatelets [85] but their full potential for light-harvesting has not been unleashed yet.

Third, optical gain and lasing have been identified among the most promising areas in optoelectronics for the nanoplatelets. Nanoplatelets enable ultralow threshold optical gain with record high gain coefficients [17], [59], [75], empowered by suppressed Auger recombination [58], large absorption cross-section [67], and close packing densities in their solid films [19] together with the absence of inhomogeneous broadening in their ensembles [58].

Moreover, strong near-field interactions through dipole-dipole coupling also create exciting opportunities for exciton harvesting at the nanoscale for applications ranging from photocatalysis and artificial photosynthesis [19], [68], [86], [87]. Although it has not been explored yet, the nanoplatelets with their giant nonlinear absorption cross-section are expected to appeal two-photon absorption-based bio-imaging applications with abundant multiplexing opportunities.

2.2 Optical properties of colloidal nanocrystals

In this section, we introduce the underlying physics that dictate the optical properties in colloidal semiconductor nanocrystals, specifically in colloidal quantum dots. As we have discussed earlier, optical properties of the quantum dots are size-dependent because of the dominant quantum confinement effect. To understand quantum confinement, one should first consider the natural extent (i.e., Bohr radius) of an exciton (bound electron-hole pair via Coulomb attraction), electron and hole in a semiconductor material [88].

$$a_B = \varepsilon \frac{m_0}{m^*} a_0 \quad (2.1)$$

Here a_B represents the Bohr radius of exciton (a_X), electron (a_e), or hole (a_h); ε is the dielectric constant, m_0 is the rest mass of an electron, m^* is the effective mass of the electronic particle (in terms of electron mass) and a_0 is the Bohr radius of the hydrogen

atom. In Table 2.1, we summarize the exciton Bohr radii (a_X) in common II-VI and III-V semiconductors.

Table 2.1. Bulk exciton binding energies and exciton Bohr radii of common II-VI and III-V semiconductor compounds.

Semiconductor compound	Bulk exciton binding energy (meV)	Exciton Bohr radius (nm)
ZnO	60.0	1.8
ZnS	40.0	2.5
ZnSe	20.4	4.1
ZnTe	13.0	6.7
CdS	29.0	2.9
CdSe	15.0	5.6
CdTe	9.0	7.3
AlN	42.5	1.2
GaN	24.1	2.7
GaAs	5.1	14.5
InN	15.2	8.0
InP	4.8	12.0
InAs	1.5	36.0
PbS	0.019	18.0
PbSe	--	47.0

Depending on the size (r for the radius) of a quantum dot given the material it is made of, different quantum confinement regimes can be observed. When $r \ll a_e, a_h, a_X$, the carriers are tightly confined within the nanoparticle. This case is referred to as the strong confinement regime. When $r > a_e, a_h$ and $r < a_X$, this is the weak confinement regime, where carriers are individually not confined but center of mass motion of the exciton is confined within the nanoparticle. When $a_h < r < a_e, a_X$, only single carrier (electron) is strongly confined, but the other is not. This is called the intermediate confinement regime.

As one can simply solve using particle in a box problem, the energy of the carrier is increased when it is confined to a potential well that is physically smaller than its Bohr radius due to the quantum confinement effect. Assuming three-dimensional confinement (i.e., particle in a sphere problem), the quantized energy levels of the confined electron and hole can be expressed as follows [89]:

$$E_{n,l} = \frac{\hbar^2 k_{n,l}}{2m_0} = \frac{\hbar^2 \alpha_{n,l}^2}{2m_0 r^2} \quad (2.2)$$

Here \hbar is the reduced Planck constant, $k_{n,l}$ is the wave vector that is quantized by the spherical boundary conditions, n ($1, 2, 3, \dots$) and l (s, p, d, \dots) are the quantum numbers, m_0 is the rest mass of the electronic particle, r is the radius of the quantum dot, and $\alpha_{n,l}$ is the n^{th} zero of the l^{th} -order spherical Bessel function. Figure 2.8 schematically depicts the quantized energy levels of the electron (i.e., $E_1(e)$) and the hole (i.e., $E_1(h)$) arising due to quantum confinement. As compared to their bulk bandgap, quantum confined structures of the same materials have a larger effective bandgap ($E_{\text{gap}} = E_1(e) - E_1(h)$), which is the origin of the size dependent absorption and emission properties in the colloidal quantum dots.

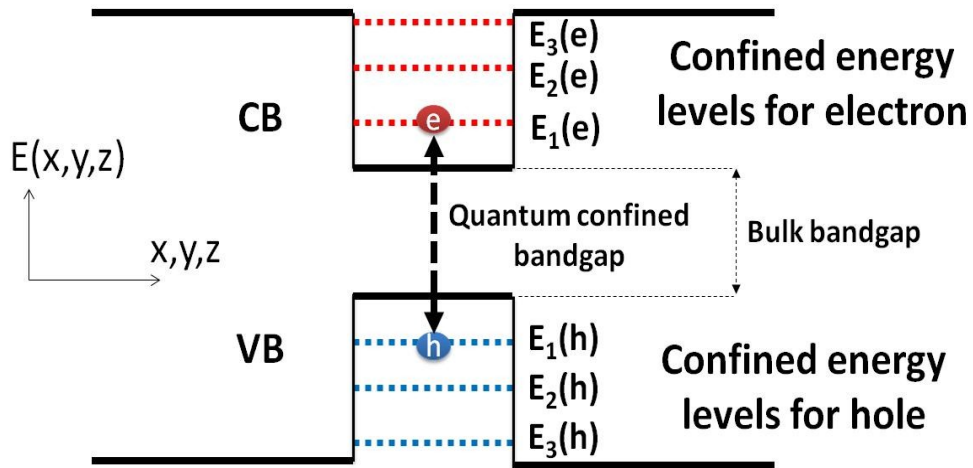


Figure 2.8. Evolution of the quantum confined energy levels for the electron and hole. Quantum confinement leads to a larger effective bandgap than that of the bulk form of the material.

For a quantum dot, the quantized energy levels (where the lowest energy difference gives the effective confined bandgap) can be expressed as in the following without considering the excitonic effects.

$$E_{e-h}(n_e, l_e, n_h, l_h) = E_g(bulk) + \frac{\hbar^2}{2r^2} \left[\frac{\alpha_{n_e, l_e}^2}{m_e^*} + \frac{\alpha_{n_h, l_h}^2}{m_h^*} \right] \quad (2.3)$$

$E_{e-h}(n_e, l_e, n_h, l_h)$ is the effective bandgap energy of the quantum dot given the quantum numbers (n_e, l_e, n_h, l_h) , $E_g(bulk)$ is the bandgap of the bulk form of the material, and m_e^* and m_h^* are the effective masses of the electron and hole in the quantum dot, respectively. Figure 2.9a shows the energy-momentum (E-k) diagram of a common zinc-blende semiconductor. Figure 2.9b depicts the E-k diagram of a quantum dot of the same material having quantized energy states.

Excitonic effects can also strongly prevail in the quantum confined semiconductors. In fact, most of the electron-hole pairs are in the form of bound electron-hole pairs due to strong Coulomb attraction. Attractive Coulomb interaction between electron and hole leads to reduction of their energy by an amount that corresponds to exciton binding energy. Considering the excitonic effect, the bandgap energy of the quantum dot becomes:

$$E_{e-h}(n_e, l_e, n_h, l_h) = E_g(bulk) + \frac{\hbar^2}{2r^2} \left[\frac{\psi_{n_e, l_e}^2}{m_e^*} + \frac{\psi_{n_h, l_h}^2}{m_h^*} \right] - E_X \quad (2.4)$$

E_X is the binding energy of the exciton. Assuming a first-order Coulomb correction, E_X can be calculated as follows:

$$E_X \approx 1.8 \frac{e^2}{4\pi\epsilon r} \quad (2.5)$$

Exciton binding energies in the bulk form of the common semiconductor materials are tabulated in Table 2.1. Figure 2.9c illustrates the changing energy levels (dashed horizontal lines) in the E-k diagram due to exciton effect (i.e., exciton binding energy).

The change of the energy levels due to quantum confinement scales with $\frac{1}{r^2}$, whereas exciton binding energy scales with $\frac{1}{r}$. Therefore, confinement effect becomes the dominant factor in determining the bandgap of a quantum dot that is in the strong confinement regime.

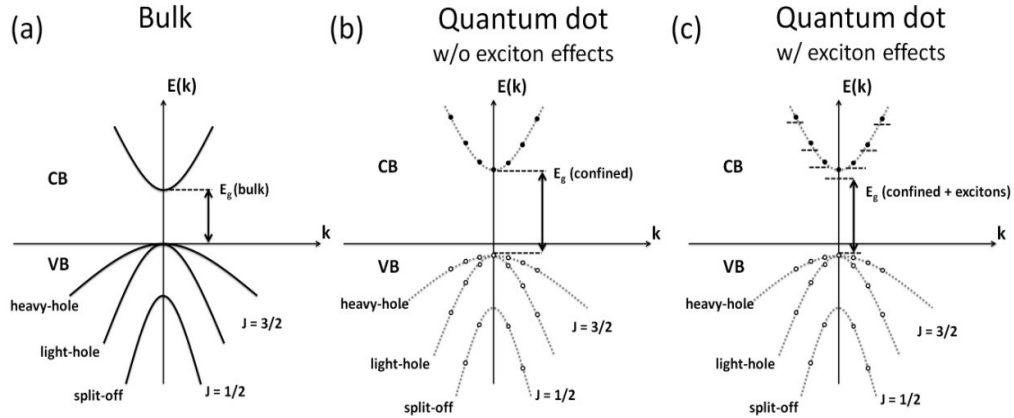


Figure 2.9. E-k diagram for (a) a bulk semiconductor, (b) a quantum dot without considering exciton effect, and (c) a quantum dot considering exciton effect.

In a more realistic band structure picture, complex interactions come into play. For example, in CdSe, the conduction band is formed by Cd 5s atomic orbital, whereas the valence band is formed by the Se 4p. Because of this, the valence band is six-fold degenerate (p_x , p_y and p_z due to p-like orbital nature) at $k = 0$ (Γ point) including the spin. Conduction band, on the other hand, is only two-fold degenerate at $k = 0$ due to the spin. In CdSe quantum dots, it is commonly assumed that the bands are still parabolic at $k = 0$, but six-fold degenerate valence band is split into two subbands due to spin-orbit coupling. Angular momentum quantum number $J = s + l$, where s is the quantum number for spin contribution ($\pm \frac{1}{2}$) and l is the quantum number due to orbital contribution. Hole states are divided into $p_{3/2}$ and $p_{1/2}$ subbands. $p_{3/2}$ subbands form heavy-hole and light-hole bands, whereas $p_{1/2}$ subband forms the split-off band (at a higher energy than the heavy-hole and light-hole bands due to the splitting energy caused by spin-orbit coupling). One consequence of this is that simple particle model in a sphere approximation does not give accurate estimations. Instead of this, effective mass approximation (EMA), k.p method and ab initio calculations using density functional theory are employed to estimate the band structure of the nanocrystals.

Figure 2.10a shows the atomic-like electronic transitions in a spherical quantum dot. Similar to atomic systems, there exist distinct electron and hole states. Dictated by optical selection rules, the available transitions are highlighted with arrows in Figure 2.10a. These transitions are also shown in the exciton manifold in Figure 2.10b. Figure 2.10c depicts steady state optical absorption spectrum of an exemplary case of spherical CdSe quantum dot. Here, the four lowest energy transitions are clearly visible in the absorbance spectrum.

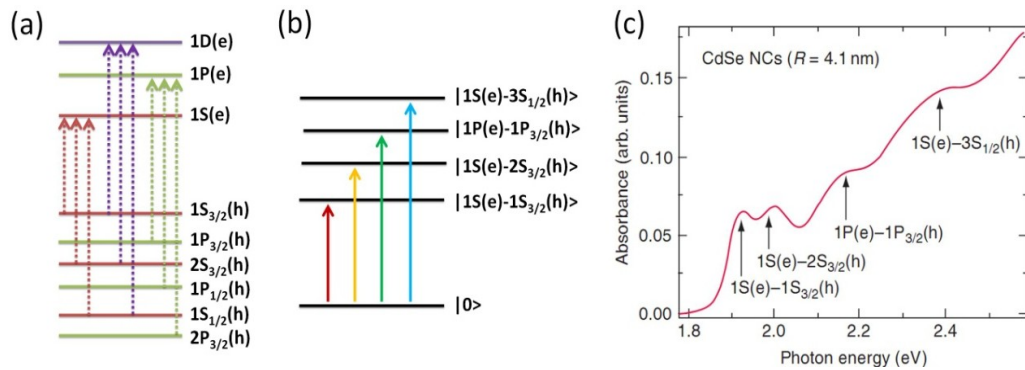


Figure 2.10. (a) Atomic-like electronic states in a spherical CdSe quantum dot, (b) exciton manifold formed by the first four energy states. (c) Steady state optical absorption spectrum demonstrating the first four allowed transitions. The transitions are not sharp since measurement is made at room temperature Homogenous and inhomogeneous broadening overall broadens these atomic-like transitions. From V. I. Klimov, “Spectral and Dynamical Properties of Multiexcitons in Semiconductor Nanocrystals,” *Annual Review of Physical Chemistry* 58, 635-673 (2007).

Up to now, the electronic band structure has been explained in more simplified terms, which is known as the coarse electronic structure. Due to more complex interactions, the so-called second order effects (non-perfect spherical shape, shape anisotropy, crystal field, electron-hole exchange interactions, etc.), exciton fine structure prevails. More interested readers can refer to Norris and Efros’ work on exciton fine-structure in colloidal quantum dots [90]. Although fine structure of the excitons is not observed at room temperature due to thermal broadening, these effects can be clearly observed at low temperatures. For example, anomalously long

fluorescence lifetimes measured in quantum dots (<10 K) have been attributed to the presence of dark excitons, which can be understood from fine exciton structure that is also similar to the triplet states in organic semiconductors [91]. Furthermore, electron-phonon coupling is a very important aspect that essentially affects the optical properties in colloidal nanocrystals. These interactions generally result in emission broadening, observation of satellite emission peaks at low temperatures and Stokes-shift between the emission and the absorption. Spatial separation of the electron and hole pairs in a nanocrystal has been shown to increase the phonon coupling, leading to larger Stokes shift in these nanocrystals (e.g., quasi Type-II). More interested readers can refer to the related book chapter on exciton-phonon interactions in nanocrystals [92] and a recent publication [93].

In the last part of this section, we discuss the transition strength of an exciton. This probability is commonly expressed using Fermi's golden rule:

$$A_{1S(e)-1S(h)} = \frac{1}{\tau_{rad}} = \frac{1}{4\pi\epsilon} \frac{4n\omega^3}{3\hbar c^3} \left(\frac{E_{loc}}{E}\right)^2 \frac{1}{g_b} |\langle 1S(e) - 1S(h) | \mu_c | 0 \rangle|^2 \quad (2.6)$$

Here $A_{1S(e)-1S(h)}$ is the transition rate (1/s), which is inverse of the radiative fluorescence lifetime (τ_{rad}), n is the refractive index, ω is the frequency of the transition, c is the speed of light, ϵ is the dielectric permittivity, $\left(\frac{E_{loc}}{E}\right)^2$ is the local field correction factor, g_b is the degeneracy of the first excited state, $|\langle 1S(e) - 1S(h) | \mu_c | 0 \rangle|^2$ is the dipole matrix element, and μ_c is the transition dipole moment. $\mu_c = \vec{e} \cdot \hat{d}$, where d is generally 1 Å.

For a spherical quantum dot, the radiative recombination rate can be expressed:

$$A_{1S(e)-1S_{3/2}(h)} = \frac{1}{\tau_{rad}} = \frac{2e^2\omega\sqrt{\epsilon}f}{3m_0c^3} \quad (2.7)$$

where f is the oscillator strength, represented by:

$$f = \frac{2|\langle 1S(e) - 1S(h) | \mu_c | 0 \rangle|^2}{m_0 E_{1S_e-1S_h}} \quad (2.8)$$

$E_{1S_e-1S_h}$ is the energy of the transition dipole. Thus, the radiative recombination of an electron-hole pair depends on the transition matrix element dominated by the transition dipole moment. Oscillator strength becomes an important parameter for efficient light-emitting nanocrystals, especially in the presence of competing nonradiative channels such as exciton trapping at the nanocrystals surface. Moreover, by manipulating the local field correction factor $\left(\frac{E_{loc}}{E}\right)^2$ it is possible to tailor the radiative recombination rate of a nanocrystal. This could be possible by placing the quantum dots in photonic crystals having well defined photonic density of states. This also allows for tuning the spectral and dynamics properties of the light emission of the transition dipoles (e.g., inhibition of spontaneous emission and Purcell enhancement of the radiative emission). Similarly, plasmonic coupling to the nanocrystals is intrinsically related to the control and manipulation of the local field factor.

2.3 Excitonics of the nanocrystals

2.3.1 Journey of an exciton: essential excitonic processes

This section is based on the publications: “Excitonics of semiconductor quantum dots and wires for lighting and displays,” **B. Guzelturk**, P. L. H. Martinez, Q. Zhang, Q. Xiong, H. Sun, X. W. Sun, A. O. Govorov and H. V. Demir, *Laser & Photonics Reviews* 8, 73-93 (2014). Adapted (or “Reproduced in part”) with permission from John Wiley and Sons. Copyright 2014 Wiley-VCH Verlag GmbH & Co. KGaA, Weinheim. “Organic–Inorganic Composites of Semiconductor Nanocrystals for Efficient Excitonics,” **B. Guzelturk** and H. V. Demir, *The Journal of Physical Chemistry Letters* 6, 2206-2215 (2015). Adapted (or “Reproduced in part”) with permission from American Chemical Society. Copyright 2015 American Chemical Society.

In the past two decades, the rise of quantum confined materials has been experienced and this is anticipated to continue in the next decades. These quantum confined materials including quantum dots, wires and wells are capable of providing

favorable and unique optical properties, which make them promising for abundant applications in photonics and many others. These properties genuinely include excitonic features owing to the strong confinement effects, which are generally not observed in their bulk counterparts. Therefore, it is essential to understand the nature of such excitonic properties in these quantum confined materials to engineer their potential to full extent. Today the excitonic properties in the nanoscale systems of these confined materials are carefully engineered towards high-performance solid-state lighting, displays and lasers.

An exciton, which is a Coulombically bound electron-hole pair, is the primary form of the excited state energy in the colloidal nanocrystals. An exciton can be created via either optical or electrical excitation (Figure 2.11a). Optical excitation occurs through absorption of a photon, while electrical excitation requires simultaneous injection of an electron and a hole. Within the lifetime of an exciton, it may radiatively or nonradiatively recombine (Figure 2.11b). Radiative recombination results in emission of a photon, whereas nonradiative recombination does not produce light but heat. Exciton diffusion (Figure 2.11c) is another process, which is widely observed in the close-packed solid films of the colloidal nanocrystals as well as organic semiconductors. In the case of organic semiconductors, exciton diffusion/migration can happen either via exciton hopping within the delocalized excited state landscape of a conjugated polymer [94] or via Förster resonance energy transfer (FRET) between different chromophoric units of the conjugated polymer [95], [96]. In the colloidal nanocrystals, exciton diffusion dominantly takes place through long-range nonradiative energy transfer since excitons are confined to the nanocrystals [97], [98]. Exciton diffusion length in the colloidal nanocrystals (and also in organic semiconductors) is typically on the order of 10 nm [98], [99]. For a solar cell, attaining a longer exciton diffusion length is desired for enhanced light-harvesting performance [19], [100]. In the case of a light-emitting diode (LED), exciton diffusion is undesired since it can cause trapping of the excitons at the trap/defect sites (Figure 2.11c) causing nonradiative recombination.

At the interfaces of materials having energetically staggered band alignment, excitons might dissociate through charge transfer. This process involves spatial overlap of the wavefunctions between different materials that are in close proximity (< 2 nm) (Figure 2.11d). Thus, exciton dissociation leads to reactive charged species through formation of free charge carriers, which finds use in photovoltaics for charge separation. On the other hand, in electroluminescent devices, it is essential to control the recombination zone of the excitons within which they are aimed to radiatively recombine. The management of the exciton recombination zone can be achieved through excitation energy transfer (Figure 2.11e) including FRET [101], which is a near-field dipole-dipole coupling between the species that are in close proximity (typically < 10 nm), and Dexter energy transfer [102], which is an electron exchange interaction between two species that are in intimate contact (< 2 nm).

For the nonradiative energy transfer mechanisms to occur, there must be a spectral overlap between the donor emission and the acceptor absorption to satisfy the resonance condition [103]. Additionally, Dexter energy transfer requires the spatial overlap of the wavefunctions between the donor-acceptor pair, whereas FRET does not require this since it is a long-range process. Both nonradiative energy transfer mechanisms preserve the neutrality of the donor and the acceptor materials (does not create free carriers) since excitons are being transferred instead of free carriers. The spatial extent of the colloidal nanocrystals, at least in one dimension, is less than 10 nm making FRET a versatile and efficient tool to control the excitons in the solid thin films of the nanocrystals. In the case of organic semiconductors, only singlet excitons can be transferred through FRET since transition dipole in the donor must have a nonzero oscillator strength. Nevertheless, energy transfer between non-emissive triplet states can happen via Dexter energy transfer [104].

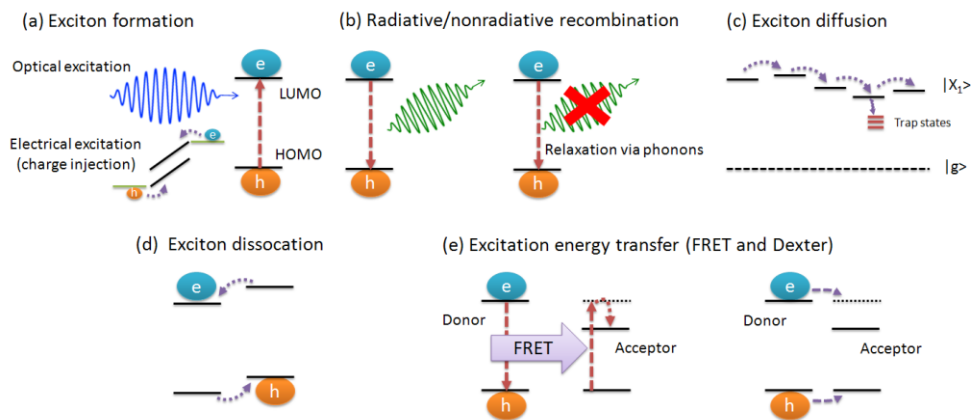


Figure 2.11. Essential excitonic processes are schematically illustrated: (a) Exciton formation via optical excitation or electrical charge injection, (b) radiative and nonradiative recombination, (c) exciton diffusion, (d) exciton dissociation, and (e) excitation energy transfer (FRET and Dexter energy transfer mechanisms). (HOMO: highest occupied molecular orbital level, LUMO: lowest occupied molecular orbital level, $|X_1\rangle$ represents the band edge exciton state, $|g\rangle$ is the ground state.)

In excitons, electrons and holes are bound to each other within a Coulombic interaction energy, which is the exciton binding energy ($E_B \sim E_X$). If the binding energy is considerably greater than thermal energy ($k_B T$), the excitons can remain without dissociation. Although the exciton binding energy is a material specific energy, it can be altered via confining the electrons and holes into small dimensions, as in the case of quantum confinement. Bulk exciton binding energies are approximately 4 – 60 meV for the common II-VI and III-V semiconductors (see Table 2.1). However, through quantum confinement, the exciton binding energies can, in principle, be made considerably larger (more than an order of magnitude) than the bulk-exciton binding energies. This is the reason why quantum confinement is the key to achieving excitonic operation in inorganic semiconductors. For low-binding-energy materials with weak quantum confinements, excitonic behaviour can only be observed at low temperatures.

2.3.1.1 Nonradiative energy transfer – resonance energy transfer

Nonradiative energy transfer (NRET), which was first correctly described by Theodor Förster [101], is also known as Förster resonance energy transfer (FRET) or resonance energy transfer (RET). NRET is the transfer of the excitation energy from an excited state molecule (donor) to a ground state molecule (acceptor) without the process of photon emission/reabsorption. The physical mechanism behind this emissionless energy transfer is explained by the near-field Coulombic interactions between the resonant transition dipoles, which is also known as a dipole-dipole coupling. This nonradiative character of the process ensures a high efficiency of NRET.

The classical formulation of the NRET rate and efficiency has been described in detail in various textbooks [103] and reviews [105]. A single donor-acceptor pair, which is the simplest case to study and formulate, is helpful for understanding the NRET and its involved parameters. The NRET rate k_{NRET} for the case of a single donor-acceptor pair is given by:

$$k_{NRET}(R) = \frac{9\kappa^2 c^4}{8\pi\tau_D n^4 R^6} \int F_D(\omega)\sigma(\omega) \frac{d\omega}{\omega^4} \quad (2.9)$$

where κ is the dipole orientation factor that depends on the donor-acceptor transition dipole arrangement; c is the speed of light; n is the refractive index of the energy transfer medium; τ_D is the radiative lifetime of the donor; R is the actual separation between the donor and the acceptor; $F_D(\omega)$ is the normalised fluorescence spectrum of the donor; $\sigma(\omega)$ is the absorption cross-section of the acceptor; and ω is the optical frequency in radians/s. The integral term is also called the spectral overlap (J) between the donor emission and the acceptor absorption, which corresponds to the strength of the resonance condition. τ_D (radiative lifetime of the donor) can be calculated using the fluorescence lifetime of the donor in the absence of the acceptor ($\tau_{fluorescence}$) and the donor fluorescence quantum yield (QY) is calculated as $\tau_D = \frac{\tau_{fluorescence}}{QY}$.

Furthermore, a hypothetical distance that is called the Förster radius, R_0 , is defined as the separation between the donor-acceptor where the NRET efficiency becomes equal to 0.5. The NRET rate can also be expressed in terms of the Förster radius and the actual separation and the donor radiative lifetime by assuming a dipole-orientation factor, κ^2 , that averages to $\frac{2}{3}$ for random orientation of transition dipoles, which is typical for isotropic emitters.

$$k_{NRET}(R) = \frac{1}{\tau_D} \left(\frac{R_0}{R} \right)^6 \quad (2.10)$$

The efficiency of exciton transfer can be calculated from the measured change in the decay rate of the donor in the presence of the acceptors by comparing to the donor only exciton decay rate (inverse of the exciton lifetime):

$$\eta_{NRET}(R) = \frac{k_{NRET}(R)}{k_{NRET}(R) + \frac{1}{\tau_{fluorescence}}} \quad (2.11)$$

NRET is a highly distance sensitive process owing to the inverse sixth power (R^{-6}) dependence of the separation distance in the case of point-to-point dipole coupling. Therefore, NRET had been first used as a nanoscale ruler [106]. However, the distance dependence could be altered for different acceptor geometries. Typically small molecule acceptors and similarly 3D confined quantum dots are considered to be infinitesimal transition dipoles, which leads to the classical R^{-6} dependence. By contrast, 2D confined quantum wire and 1D confined quantum well acceptors lead to distance dependences that vary with R^{-5} and R^{-4} , respectively [104]. Essentially, quantum confinement of the acceptor changes the distance dependency of the NRET. Furthermore, different assemblies of the acceptors could also alter the distance dependence, as in the case that a 2D-like assembly of the semiconductor quantum dots act as a 1D confined structure, which consequently results in the distance dependence having the form of R^{-4} similar to quantum wells [107].

NRET has historically been exploited in various areas of biology for sensing, labeling, sensitive distance measurement and understanding of the molecular-level interactions. Recently, NRET has been shown to be useful for optoelectronic technologies towards the purpose of creating efficient lighting and solar energy-harvesting systems [108]–[110]. For this purpose, exciton energy transfer in the nanocrystal based systems, which have physical dimensions on the order of the Förster radius, can be employed to control the photonic properties for light-generation and harvesting.

2.3.1.2 Exciton dissociation and charge transfer

Dexter energy transfer [102], which is also known as electron exchange energy transfer, relies on the wavefunction overlap of the electronic states between different molecules in the near field. Dexter energy transfer is a short-range energy transfer unlike FRET, which is known to be a long-range energy transfer owing to the working distances that are on the order of 10 nm. Therefore, Dexter energy transfer is only effective for donor-acceptor separations, which are typically on the order of a nm or even shorter. Furthermore, Dexter energy transfer has exponential distance dependence as compared with the R^{-4} - R^{-6} distance dependencies in the long-range NRET processes. Finally, Dexter energy transfer can also occur between non-emissive electronic states of the materials, such as spin-forbidden triplet states, whereas it is currently widely believed that these excitons cannot be transferred via NRET because they have negligible oscillator strength [111].

Exciton dissociation is the decomposition of the bound electron-hole pairs into free carriers. This dissociation is a crucial step for excitonic solar cells (bulk-heterojunction and dye-sensitised) [112] because the generation of free charge carriers is required to realize the photovoltaic operation. In excitonic solar cells, dissociation of the excitons is facilitated by the interfaces that have type-II band alignments to physically break the excitons into free charges. The resistance against the breaking of the exciton in terms of energy is called the exciton binding energy. Materials with a larger exciton binding

energy have more stable excitons because it is difficult to overcome this large Coulomb energy between the electron-hole pairs.

Another important excitonic process is diffusion of the excitons that also crucially assists exciton dissociation. The excitons can diffuse in a material via NRET in the broadened density of states of the same material, which is further called energy migration. Exciton diffusion has been widely studied for organic semiconductors in search for suitable materials for organic solar cells that have long diffusion lengths to increase the probability of the charge separation at the donor-acceptor hetero-interfaces [113]. In addition to organic materials, exciton diffusion is vital in bulk and quantum confined semiconductor structures. Excitons can be transported in the quantum confined materials or in the assemblies of the quantum dots, which should be well understood and controlled because defects can trap the diffusing excitons such that the emission efficiencies can be significantly reduced as a result of increased nonradiative recombination of the excitons. This picture is also valid for organic semiconductors for organic LEDs (OLED), where the exciton diffusion is not a desired process contrary to organic solar cells (OPV). In quantum dots, excitons can diffuse via inter-particle NRET in the assemblies of the QDs. This exciton diffusion is one of the reasons for the observed red-shifts when QDs are casted into solid-state films in addition to substrate effects [114].

Lately, excitonic processes that involve multi-exciton generation (MEG), Auger recombination and exciton-exciton annihilation have been studied in the quantum-confined semiconductors. Multi-exciton generation, also called carrier multiplication, is the generation of multi-excitons upon the absorption of a high-energy photon $h\nu \geq 2 E_g$. It has been shown that semiconductor QDs can be quite efficient in terms of converting higher-energy photons into multi-excitons [115]. Related to the multi-exciton phenomena, Auger recombination becomes severe because excitons are spatially very close to each other. In Auger recombination, the energy of the recombining exciton is transferred to another already excited charge carrier in the material such that this charge is excited into higher energy states (i.e., hot carrier). This hot carrier quickly thermalises to the respective band edge by losing its energy to

phonon vibrations; therefore, Auger recombination can significantly decrease the efficiency of multi-exciton operation in the quantum-confined structures [6].

2.4 Optical gain in colloidal nanocrystals

2.4.1 Optical gain: basics

In this section, we briefly review the basic interactions between atomic electronic states and electromagnetic waves (e.g., light) and discuss the concept of optical gain and simple laser amplifiers.

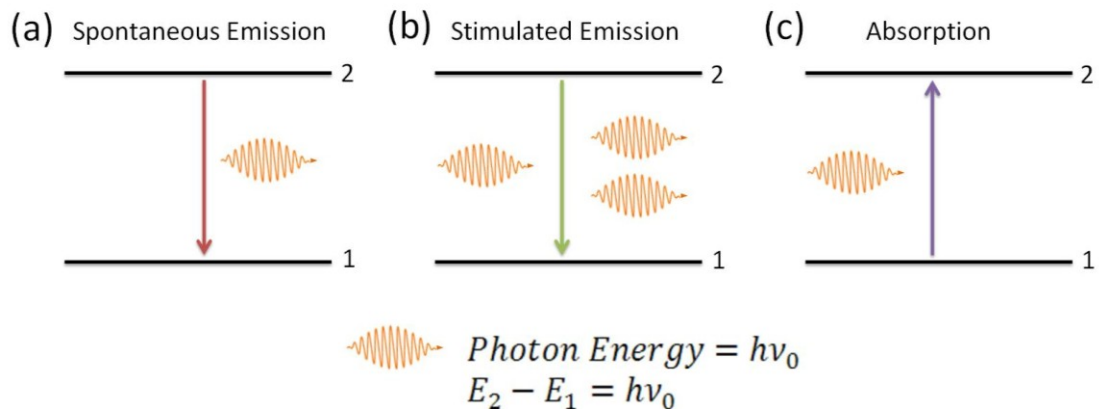


Figure 2.12. Basic optical processes in a two-level atomic system: (a) spontaneous emission, (b) stimulated emission and (c) absorption.

For the simplicity, let's consider a collection of individual quantum emitters (e.g., atoms) with only two states (e.g., 1 and 2). In total, there are $N_{total} = N_1 + N_2$ states. We assume that the energy of state 2 is larger than that of state 1 ($E_2 > E_1$) (see Figure 2.12). Thus, atoms in level 2 will decay into the ground state (i.e., level 1). Spontaneous emission happens when an atom in level 2 undergoes radiative emission process and then the atom is converted into level 1. The energy difference between two states is ($E_2 - E_1 = h\nu_0$), where ν_0 is the frequency of the radiation and h is the Planck constant, is released as the energy of the emitted photon (see Figure 2.12a). In

spontaneous emission, although emitted photons have the same energy ($h\nu_0$), spontaneously emitted photons from the same atom do not have the same direction neither the same phase. On the other hand, stimulated emission happens when a photon (with an energy of $h\nu_0$) triggers the emission of another photon from an atom that is in level 2. In result, the atom turns back to level 1 and two identical photons (i.e., the same energy, phase and direction) are emanated from the matter (see Figure 2.12b). Thus, stimulated emission forms the working principle of a laser. The last process is absorption, which is also a stimulated process since a photon (with energy $h\nu_0$) is absorbed by an atom in level 1 to be excited into level 2 (see Figure 2.12c).

Now, let's look into the rates of these basic optical processes. For spontaneous emission, the change of the population of the atoms in level 2 is expressed as:

$$\left(\frac{dN_2}{dt}\right)_{sp} = -P_{sp}N_2 \quad (2.12)$$

N_2 is the population of the atoms in level 2 and P_{sp} is the spontaneous emission rate, which is related to:

$$P_{sp} = \frac{c}{V} \sigma_{21}(\nu) \quad (2.13)$$

Here c is the speed of light, V is the cavity volume, and $\sigma_{21}(\nu)$ is the transition cross-section between the atomic states 2 and 1. Thus, the change of the excited state atom population can be described by an exponential decay function:

$$N_2(t) = N_2(0)e^{-\frac{t}{\tau_{sp}}} \quad (2.14)$$

τ_{sp} is the spontaneous emission lifetime, which is related to the spontaneous emission rate (P_{sp}) using the following simple relation:

$$P_{sp} = \frac{1}{\tau_{sp}} \quad (2.15)$$

Stimulated emission rate (W_{21}) can be expressed in terms of:

$$W_{21} = P_{st} = n \frac{c}{V} \sigma_{21}(\nu) \quad (2.16)$$

where n is the number of photons available in the mode at frequency ν , c is the speed of light and V is the cavity volume, and $\sigma_{21}(\nu)$ is the stimulated emission cross-section between the states 2 and 1. The photon flux density (photons/cm²-s) is:

$$\phi = n \frac{c}{V} \quad (2.17)$$

Using the photon flux density in (2.17), the stimulated emission rate is expressed as:

$$W_{21} = \phi \sigma_{21}(\nu) \quad (2.18)$$

Similar to the stimulated emission rate, the absorption rate is:

$$W_{12} = P_{abs} = n \frac{c}{V} \sigma_{12}(\nu) = \phi \sigma_{12}(\nu) \quad (2.19)$$

Here $\sigma_{12}(\nu)$ is the absorption cross-section between the states 1 and 2. $\sigma_{12}(\nu)$ and $\sigma_{21}(\nu)$ are related to each other by the degeneracy of the corresponding atomic levels:

$$g_2 \sigma_{21}(\nu) = g_1 \sigma_{12}(\nu) \quad (2.20)$$

$$g_2 W_{21} = g_1 W_{12} \quad (2.21)$$

where g_1 is the degeneracy of the level 1 and g_2 is the degeneracy of the level 2. For the simplicity, we will assume that $g_1 = g_2$. In the case of conventional semiconductors, this assumption may not be valid due to complex nature of the conduction and valence bands. Stimulated emission and absorption cross-sections ($\sigma_{21}(\nu)$ or $\sigma_{12}(\nu)$) are expressed as:

$$\sigma_{21 \text{ (or } 12)}(\nu) = S_{21 \text{ (or } 12)} g_{21 \text{ (or } 12)}(\nu) \quad (2.22)$$

S is the transition strength and $g(\nu)$ is the normalized lineshape function (e.g., Lorentzian). Considering three dimensional density of photonic modes in a cavity, we can relate S (transition strength) to the spontaneous emission rate:

$$P_{sp} = \frac{1}{\tau_{sp}} = \frac{\lambda^2}{8\pi} S \quad (2.23)$$

In 1917, Einstein calculated the transition strengths and probabilities in atomic levels. Therefore, Einstein was the first to predict the existence of stimulated emission process. The factors that he calculated for the transition strengths are called Einstein's A and B coefficients. Coefficient A directly relates to the spontaneous emission rate:

$$A = P_{sp} \quad (2.24)$$

B_{21} coefficient relates to the stimulated emission and B_{12} to absorption processes by:

$$W_{21 (or 12)} = B_{21 (or 12)} \rho(\nu) \quad (2.25)$$

$\rho(\nu)$ is the spectral energy density. Assuming the same degeneracy for the two atomic levels ($g_1 = g_2$):

$$B_{21} = B_{12} \quad (2.26)$$

$$B_{21} = B_{12} = \frac{\lambda^3}{8\pi h} P_{sp} = \frac{\lambda^3}{8\pi h} A \quad (2.27)$$

Thus, Einstein B coefficients are equal for the stimulated emission and the absorption processes. Furthermore, B coefficients are related to the spontaneous emission rate by (2.27).

Next, we consider laser amplifiers and the amplification of electromagnetic field via stimulated emission. Let's assume that photon flux ϕ enters a medium of atoms having length Δz (see Figure 2.13). Some of the atoms are in excited state, thus could make stimulated emission. Depending on the population of the excited state atoms, it could be possible to achieve net gain or induce transparency. Figure 2.13 exemplifies the three possible cases under the assumption that the medium is homogeneous. The incident flux can be increased if the population of the excited state atoms is larger than that of the atoms in ground state. This is the net gain case. In the transparency condition, the flux will not change since stimulated emission and absorption cancel out

each other. In the case of dominant population being the ground state atoms, the absorption leads to decreased flux as the light propagates through the medium.

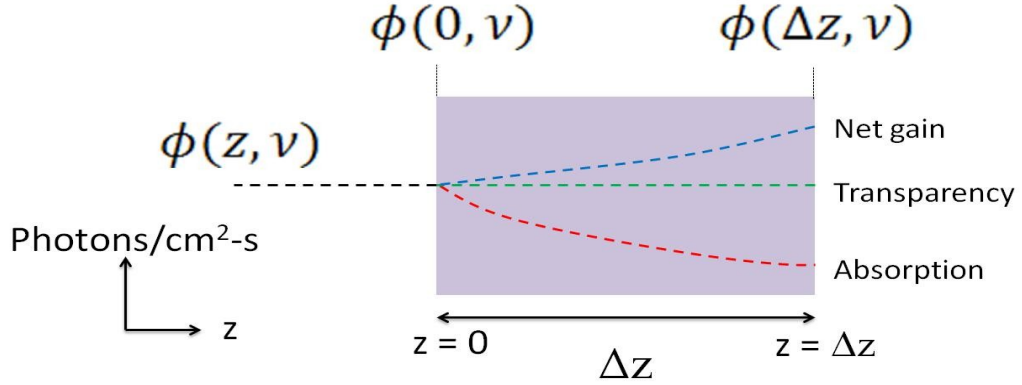


Figure 2.13. Photon flux entering a medium at $z = 0$ and the medium length is Δz . The increase of the flux indicates the dominant net optical gain in the system. If flux does not change at all, the medium is in transparency condition (equal amount of absorption and stimulated emission), whereas if flux decreases as light propagates, this indicates the presence of dominant absorption process.

To quantitatively consider gain in a medium, we should consider the competition between the absorption and the stimulated emission processes. Using $W_i = W_{abs} = W_{st} = \phi \sigma(\nu)$, we can write the change of the photon flux as a function of propagation length (z) in the medium:

$$\frac{d\phi}{dz} = (N_2 - N_1) W_i = N \phi \sigma(\nu) = N \sigma(\nu) \phi \quad (2.28)$$

N_2 is population of the atoms in level 2 and N_1 is the population of atoms in level 1. Thus, population difference ($N = N_2 - N_1$) gives the population inversion factor. If $N < 0$, the absorption process will dominate and the flux will be decreased as the light propagates. If $N = 0$, this is called the induced transparency condition, where stimulated emission will balance out absorption and the flux will not change within the medium. If $N > 0$, population inversion will prevail. In this case, the flux will increase due to net gain provided by the medium. Thus, the photon flux through the medium can be expressed using the population difference term (N) and the stimulated emission/absorption cross-section as a function of z :

$$\phi(z) = \phi(0) e^{N\sigma(\nu)z} \quad (2.29)$$

Here the following term in the exponent is called as the material gain coefficient:

$$g_{material}(\nu) = N \sigma(\nu) \quad (2.30)$$

Material gain is the absorption with a reverse sign, thus the intensity of light increases as it propagates through a medium that have net optical gain at the frequency of the electromagnetic wave. However, typically the propagating beam of light will not see the gain across its entire cross-sectional spatial profile, but a fraction of it, which is quantified by a confinement factor. It is thus more common to consider a modal gain coefficient since it can be directly measured. The modal gain is related to the material gain as follows:

$$g_{modal}(\nu) = \Gamma N \sigma(\nu) = \Gamma g_{material}(\nu) \quad (2.31)$$

where Γ is the optical confinement factor related to the field square over the active medium. Γ is calculated by integrating the field over the active area and by dividing by the total field in the cavity:

$$\Gamma = \frac{\int_{-V_a}^{V_a} \vec{E} \cdot \vec{E}^* dV}{\int_{-\infty}^{\infty} \vec{E} \cdot \vec{E}^* dV} \quad (2.32)$$

The modal gain is a fraction the material gain since $0 \leq \Gamma \leq 1$.

Let's now consider a simple cavity formed by a slab waveguide with surface reflectivities of R_1 and R_2 (see Figure 2.14). The waveguide length is L and the waveguide loss coefficient is α_{loss} . To realize lasing in this cavity, the modal gain should overcome the total losses in the cavity. This is also called the condition for lasing (threshold point).

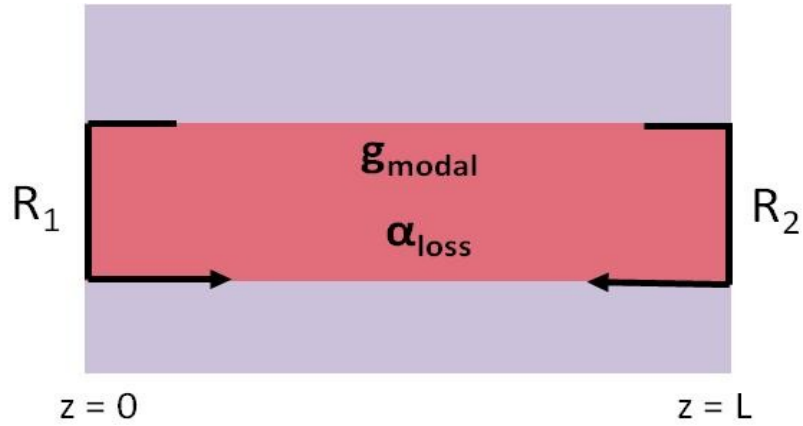


Figure 2.14. Schematic of a waveguide having a gain material within. The end mirror reflectivities of the waveguide are R_1 and R_2 . There is also intrinsic waveguide loss (α_{loss}) due to the scattering or intrinsic absorption losses.

The lasing condition for a round trip is:

$$R_1 R_2 e^{(g_{\text{modal}} - \alpha_{\text{loss}})2L} = 1 \quad (2.33)$$

The modal gain should thus compensate the total loss (mirror loss α_{mirror} and waveguide loss α_{loss}) in the system:

$$g_{\text{modal}} = \frac{1}{2L} \log\left(\frac{1}{\sqrt{R_1 R_2}}\right) + \alpha_{\text{loss}} = \alpha_{\text{mirror}} + \alpha_{\text{loss}} \quad (2.34)$$

Therefore, lasing can be achieved for a generated modal gain that is larger than the threshold modal gain expressed in (2.34).

For low threshold and efficient lasing, quality factor (Q-factor) of the cavity becomes important. Before Q-factor, let us consider the cavity photon lifetime (τ_c), which is directly related to the losses in the cavity as follows:

$$\frac{1}{\tau_c} = c_n (\alpha_{\text{mirror}} + \alpha_{\text{loss}}) \quad (2.35)$$

c_n is the velocity of light in the cavity. The cavity photon lifetime denotes the average time that photons are lost from the cavity. Thus, longer cavity photon lifetime is

desired for achieving lower threshold lasing. Q-factor of the optical cavity is directly related to the cavity photon lifetime:

$$Q = \tau_c 2\pi\nu_0 \quad (2.36)$$

Q-factor (of a cold cavity) can also be measured by the transmission of the cavity:

$$Q = \frac{\nu_0}{\Delta\nu} \quad (2.37)$$

Here, $\Delta\nu$ is the linewidth (full-width at half-maximum) of the resonant mode at ν_0 .

Now, we introduce common optical gain systems and discuss the rate equations to calculate their gain kinetics.

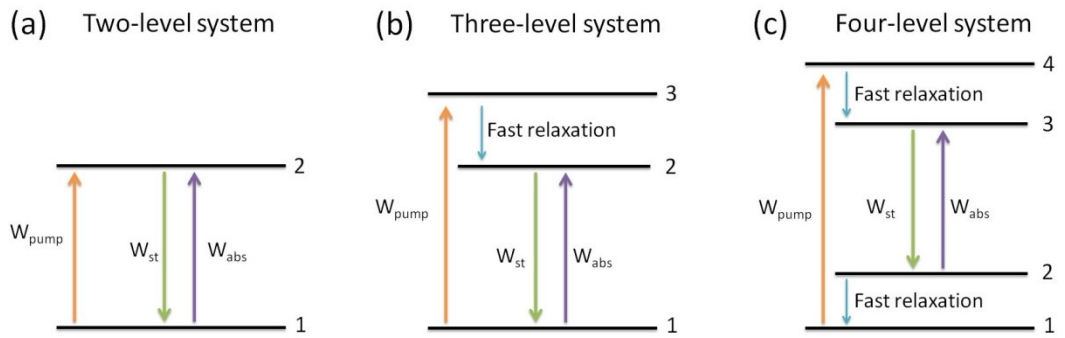


Figure 2.15. Commonly considered gain systems: (a) two-level system, where net gain is not possible, (b) three-level system and (c) four-level system.

First, we consider a true two-level system, where level 1 is the ground state and level 2 is the excited state. We can write the rate equations for both levels under optical pumping:

$$\frac{dN_2}{dt} = W_{pump}N_1 - W_{pump}N_2 - W_{st}N_2 + W_{st}N_1 - \frac{N_2}{\tau_{21}} \quad (2.38)$$

$$\frac{dN_1}{dt} = W_{pump}N_2 - W_{pump}N_1 - W_{st}N_1 + W_{st}N_2 + \frac{N_2}{\tau_{21}} \quad (2.39)$$

where τ_{21} is the lifetime of the level 2. Assuming steady state condition ($\frac{dN_1}{dt} = 0$ and $\frac{dN_2}{dt} = 0$), we can relate N_1 and N_2 to each other:

$$N_1(W_{pump} + W_{st}) = N_2(W_{pump} + W_{st} + \frac{N_2}{\tau_{21}}) \quad (2.40)$$

According to this, $N = N_1 \geq N_2$, therefore population inversion can never be achieved ($N_2 - N_1 \leq 0$). This suggests that a pure two-level system can only achieve transparency, but not net gain.

In a three-level system, where the lasing action takes place between level 2 and the ground state (level 1). Transition from level 3 to level 2 is assumed to be very fast (τ_{32} is very small). The rate equations are as follows:

$$\begin{aligned} \frac{dN_3}{dt} &= W_{pump} N_1 - \frac{N_3}{\tau_{32}} \\ \frac{dN_2}{dt} &= \frac{N_3}{\tau_{32}} - W_{st} N_2 + W_{st} N_1 - \frac{N_2}{\tau_{21}} \\ \frac{dN_1}{dt} &= -W_{pump} N_1 + W_{st} N_2 - W_{st} N_1 + \frac{N_2}{\tau_{21}} \end{aligned} \quad (2.41)$$

We assume $N_3 \sim 0$ due to its very fast relaxation into the level 2. Furthermore, we assume small signal gain condition ($W_{st} \sim 0$). $N_1 + N_2 = N_{total}$ and the population inversion term $N = N_2 - N_1$ is expressed:

$$N = N_{total} \left(\frac{W_{pump} - \frac{1}{\tau_{21}}}{W_{pump} + \frac{1}{\tau_{21}}} \right) \quad (2.42)$$

In a three-level system, we also express the modal gain coefficient:

$$g_{modal}(\nu) = \Gamma N \sigma_{21}(\nu) = \Gamma \sigma_{21}(\nu) N_{total} \left(\frac{\tau_{21} W_{pump} - 1}{\tau_{21} W_{pump} + 1} \right) \quad (2.43)$$

In a three-level system, a threshold point for gain exists since $\tau_{21} W_{pump} - 1 \geq 0$, where the pump rate should make it over a threshold value to achieve net gain. In

Figure 2.16, we plot the gain coefficient in a three-level system as a function of w_{pump} . Threshold behavior can be clearly observed.

In the case of a four-level gain system, we assume that levels 4 and 2 are quasi empty (N_4 and $N_2 \sim 0$) due to their ultrafast nonradiative relaxation times (τ_{43} and τ_{21}). We calculate the population inversion in a four-level system by assuming small signal gain ($W_{st} \sim 0$) condition as follows:

$$N = N_{total} \left(\frac{w_{pump}}{w_{pump} + \frac{1}{\tau_{32}}} \right) \quad (2.44)$$

Different from three-level gain, there is no threshold condition for the pump rate. This makes four-level gain systems more efficient and favorable. This is also referred to as “thresholdless” lasing (see Figure 2.16). The modal gain in a four-level system has the following relation:

$$g_{modal}(v) = \Gamma N \sigma_{32}(v) = \Gamma \sigma_{32}(v) N_{total} \left(\frac{\tau_{32} w_{pump}}{\tau_{32} w_{pump} + 1} \right) \quad (2.45)$$

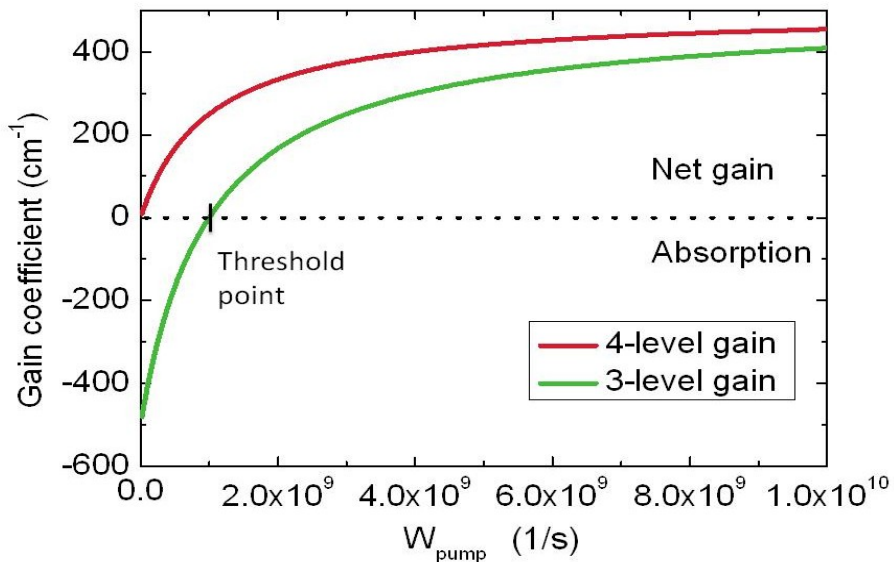


Figure 2.16. Gain coefficients in a four-level and three-level gain systems having the same stimulated emission cross-section, optical confinement factor and spontaneous

emission lifetime. Four-level gain system acts as a “thresholdless” laser, whereas three-level gain medium requires a threshold pump rate to achieve net gain.

2.4.2 Optical gain systems in colloidal nanocrystals

Colloidal quantum dots offer exciting opportunities for optical gain and lasers since their emission color can be easily tuned in the whole visible range using a single material system (i.e., CdSe) [28], which is not possible using any other semiconductor material system, especially the ones that are grown by high temperature gas-phase epitaxy. In colloidal nanocrystals, it is also possible to extend the emission color into ultraviolet or infrared by changing the material system to PbSe (for infrared) and ZnSe (for ultraviolet) [31]. These materials, in principle, could empower lasers that can emit any color in a broad spectral range. Moreover, quantum dots with three dimensional quantum confinement possess atomic-like electronic states. This is expected to lead to temperature insensitive gain in the quantum dots, whereas in bulk semiconductors gain performance is highly temperature sensitive due to the continuous density of states at the band-edge [116], [117]. Asada et al. studied GaAlAs/InP material system for the peak gain coefficients, which increases as the quantum confinement dimensionality is increased (from bulk to quantum dots) (see Figure 2.17a) [118]. Concomitant with the increasing peak levels of gain coefficients in quantum dots, these materials are expected to accomplish reduced lasing thresholds as compared to the other quantum confined systems (see Figure 2.17b). This makes quantum dots an exciting candidate for optical gain.

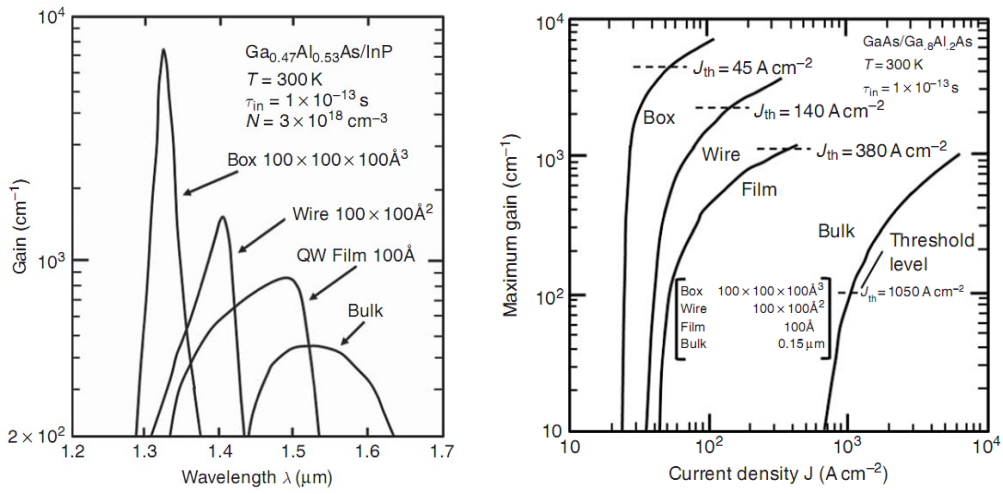


Figure 2.17. (a) Calculated gain spectra for GaInAs/InP quantum dot (10 nm × 10 nm × 10 nm), quantum wire (10 nm × 10 nm), quantum well (10 nm) and bulk at room temperature. (b) Calculated maximum gain as a function of the injection current density for the same material system with varying quantum confinement dimensionality. [1986] IEEE reprinted, with permission, from [M. Asada, Y. Miyamoto, Y. Suematsu, Gain and the threshold of three-dimensional quantum-box lasers, IEEE Journal of Quantum Electronics, and Sep/1986.]

Although colloidal quantum dots are highly promising for optical gain, the optical gain performance has remained severely limited since its first demonstration [6]. This limitation has been believed to arise from the dominant Auger recombination in these materials as first revealed by Klimov and Bawendi groups [119]. To date, colloidal quantum dots could not make it into practical lasers because gain thresholds (excitation intensity required to achieve net optical gain) have been unfavorably high (~ 1 mJ/cm²) together with low gain coefficients (< 100 cm⁻¹). Furthermore, optical gain lasts only for undesirably short time duration ($\ll 100$ ps) due to the competing ultrafast Auger process. These limitations made it almost impossible to realize lasing using conventional pump sources such as continuous-wave lasers, laser diodes, light-emitting diodes, and electrical injection.

The underlying reason behind these limitations is the degeneracy of the first excited state in common II-VI semiconductors (e.g., CdSe, CdS and ZnSe). Because of this,

single exciton state ($|X\rangle$) in a CdSe quantum dot typically cannot provide net optical gain since stimulated emission and absorption cancels out each other (see Figure 2.18). Thus, quantum dot with a single exciton is in a transparency condition. Thus, it is required to create biexcitons ($|XX\rangle$) to achieve net optical gain. However, biexcitons in these quantum dots are rapidly (few to 100 ps [11]) annihilated due to nonradiative Auger recombination (see Figure 2.19). Especially in the strongly confined quantum dots having very small volume, Auger recombination effects are immensely escalated [120]. Overall, Auger recombination poses a great challenge against achieving efficient gain since it competes and also suppresses the buildup of the optical gain by depleting the gain-active biexcitons.

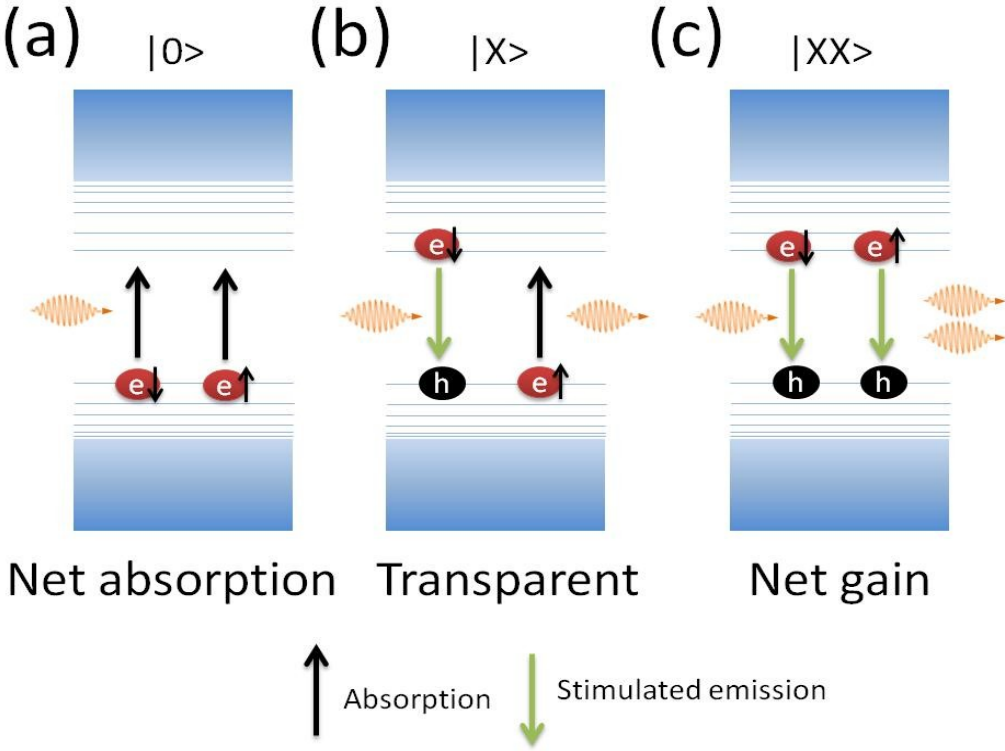


Figure 2.18. Quantum dots in three different states: (a) Ground state ($|0\rangle$), (b) single exciton state ($|X\rangle$) and (c) biexciton state ($|XX\rangle$). (a) ground-state quantum dot has net absorption, while (b) quantum dot in $|X\rangle$ state leads to transparency. (c) $|XX\rangle$ state can provide net gain.

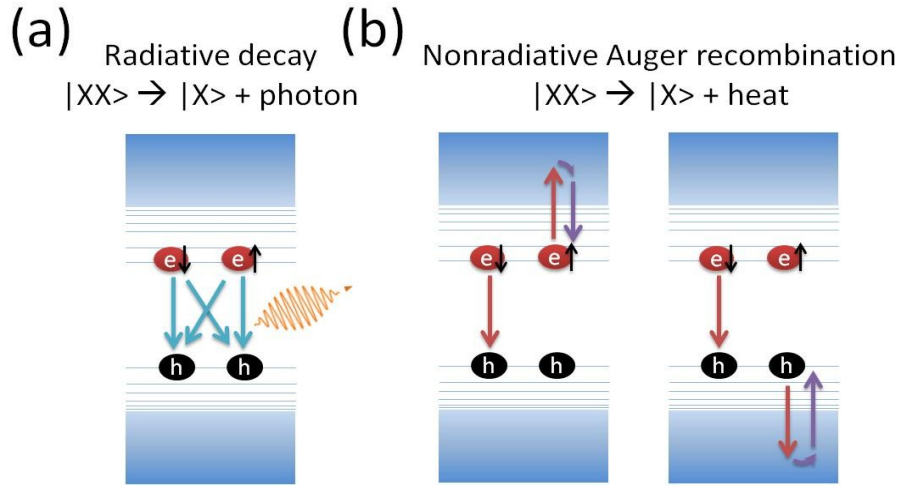


Figure 2.19. (a) Radiative emission of a biexciton state. (b) Nonradiative Auger recombination of a biexciton state. The recombination energy of the exciton is given to a third particle, i.e., electron or hole, to produce a hot carrier, which then relaxes to band-edge via interacting with phonons (lattice vibrations). Thus, energy is lost into heat.

Another limitation in colloidal gain systems is the small absorption cross-section of the nanocrystals. As we have discussed above, to achieve net gain, biexcitons should be created per quantum dot. Therefore, quantum dots with larger absorption cross-sections are desired. This arises from the fact that the average number of generated excitons per quantum dot ($\langle N \rangle$) under optical pumping is directly proportional to the absorption cross-section of the nanocrystal:

$$\langle N \rangle = f(\lambda) \times \sigma(\lambda) \quad (2.46)$$

Here, $f(\lambda)$ is the optical pump intensity (photons/cm²) and $\sigma(\lambda)$ is the absorption cross-section of the material (cm²) at the corresponding wavelength (λ). $\langle N \rangle$ is commonly considered to have Poisson distribution [11]. Therefore, one could easily estimate the population of the quantum dots that are in their ground state ($|0\rangle$), single exciton state ($|X\rangle$) or biexciton state ($|XX\rangle$).

In conventional nanocrystals, biexciton binding energy is relatively small (few meV). Thus, the photons emitted by the biexciton state can be absorbed by the ground-

state quantum dots (see Figure 2.20). This leads to the condition that biexciton population (N_{XX}) must overcome the ground state population (N_0) to achieve population inversion (N):

$$N = N_{XX} - N_0 \quad (2.47)$$

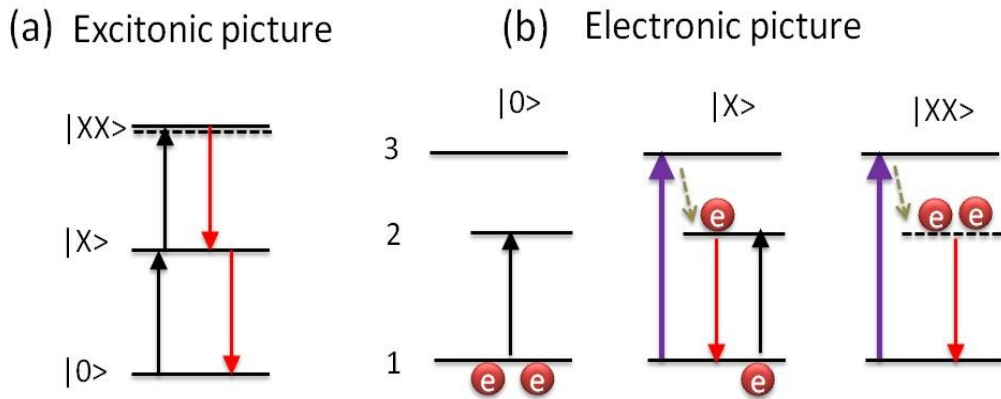


Figure 2.20. Optical gain model in conventional colloidal nanocrystals. (a) Exciton manifold for the $|0\rangle$, $|X\rangle$ and $|XX\rangle$ states and their transitions (black: upward for absorption, red: downward for radiative emission). (b) Electronic picture of the optical gain. $|X\rangle$ is optically transparent. $|XX\rangle$ state can achieve net gain, while $|0\rangle$ has net absorption. N_{XX} should overcome N_0 to realize population inversion.

Using Poisson distribution, we can calculate the critical exciton density ($\langle N_{th} \rangle$), which produces $N = 0$ (transparency point). This is found to be $\langle N_{th} \rangle \approx 1.15$ (see Figure 2.21). Thus, the gain model in conventional quantum dots resembles a quasi two-level gain system, or three-level gain. Excited state ($|XX\rangle$) population should beat the ground state population ($|0\rangle$).

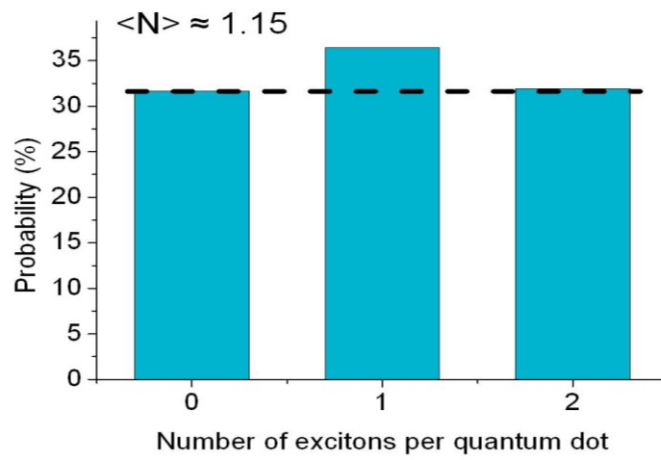


Figure 2.21 Occurrence probabilities of the number of excitons (e.g., 0, 1 and 2) per quantum dot when the average number of excitons is $\langle N \rangle \approx 1.15$. This excitation level induces the transparency since the population difference $N = N_{XX} - N_0 \approx 0$.

Chapter 3

Experimental Methods

3.1 Steady state and time-resolved fluorescence spectroscopy

Steady state optical characterizations are very useful to understand the optical properties of semiconductor materials. Here, we will summarize common steady state optical techniques including steady state linear absorption spectroscopy (also known as UV/Vis absorption spectroscopy), photoluminescence emission spectroscopy and photoluminescence excitation spectroscopy, which were frequently employed for the characterization of colloidal semiconductor nanocrystals in this thesis.

Figure 3.1a shows the schematic diagram describing the experimental setup that is used to measure the linear absorption spectrum of solution-processed semiconductors (e.g., colloidal nanocrystals and organic semiconductors) and metal nanoparticles. Using the same technique, it is also possible to measure the absorption spectrum of a solid thin film. To measure absorption spectrum, a broadband light source such as Xe

lamp is used together with a monochromator to excite the sample with a monochromatic light (λ_{abs}). As the monochromator scans across excitation wavelength, transmission of the light through the sample, which is a cuvette filled with the solution of nanoparticles dispersed in a solvent (e.g., toluene, hexane, chloroform, and water), is measured using a photodetector. To find the absorbed light intensity as a function of λ_{abs} , transmission of the light through the cuvette under test is compared with respect to that through a reference sample, which is a cuvette with the solvent but without the nanoparticles in it. The change in optical transmission is attributed to the absorption of the material. Thus, it is important to ensure that there is no strong scattering from the sample, which would be otherwise mistakenly attributed to absorption. The measured quantity in this technique is called absorbance (A), which relates the incident and transmitted light intensities as follows:

$$\phi_T(\lambda) = \phi_I(\lambda)10^{-A(\lambda)} \quad (3.1)$$

where $\phi_I(\lambda)$ and $\phi_T(\lambda)$ are the incident and transmitted light intensities, respectively. $A(\lambda)$ is the measured absorbance (unitless). If $A = 1$, then the transmitted light intensity will be 10% of the incident light. According to the Lambert-Beer's law, A is expressed by:

$$A = \varepsilon \times L \times c \quad (3.2)$$

Here ε is the molar extinction coefficient (L/mol-cm), L is the optical pathlength (cuvette width, cm) and c is the concentration of the solution (mol/L). In optics, A is also known as the optical density (O.D.). Figure 3.1b shows an exemplary absorbance spectrum of a four monolayer thick CdSe nanoplatelet in the spectral range of 300 – 600 nm. This material exhibits sharp excitonic absorption features at 513 and 480 nm due to electron/heavy-hole and electron/light-hole excitonic transitions. Absorption spectrum of the nanocrystals is useful to understand the spectral position (photon energy) of the excitonic features, the inhomogeneous broadening and the presence of undesired nanocrystal sub-populations.

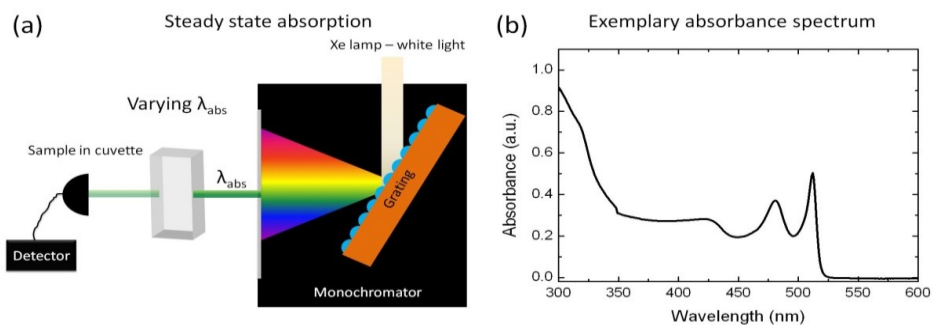


Figure 3.1. (a) Schematic diagram of an experimental setup that can be used to perform steady state linear absorption spectroscopy. (a) An exemplary absorbance data of a four monolayer thick CdSe nanoplatelet in hexane.

Figure 3.2a schematically shows the experimental setup that can be used for steady state photoluminescence spectroscopy. Similar to the absorption spectroscopy, a broadband light source is used together with a monochromator (i.e., excitation monochromator) to excite the sample with a monochromatic light (λ_{exc}). For a fixed λ_{exc} , the photoluminescence from the sample is collected through a second monochromator (i.e., emission monochromator), which scans a broad spectral range to capture the emitted light spectrum. For single-photon absorption based experiments, the wavelength of the emitted light (λ_{em}) is always larger than λ_{exc} due to the Stokes-shift. Figure 3.2b plots the photoluminescence spectrum of a four monolayer CdSe nanoplatelet in hexane. The photoluminescence peak is at 513 nm and it has a full-width at half-maximum of 8 nm (38 meV) at room temperature.

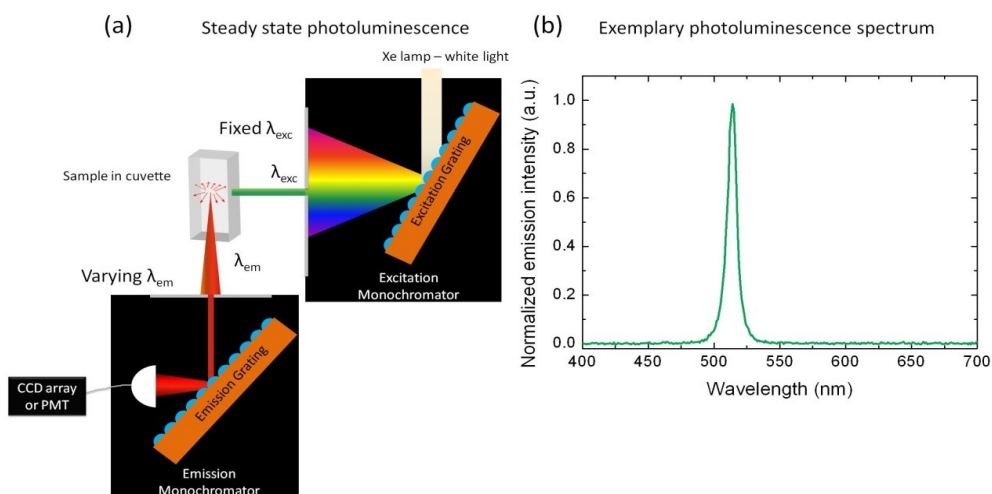


Figure 3.2. (a) Schematic diagram of the experimental setup to measure steady state photoluminescence spectrum. (a) An exemplary photoluminescence spectrum of a four monolayer thick CdSe nanoplatelet in hexane.

The other important steady state spectroscopy technique is the photoluminescence excitation (PLE) spectroscopy. In PLE, the emission monochromator is set to a fixed value (fixed λ_{em}), which is generally the peak emission wavelength of the photoluminescence and the excitation wavelength (λ_{exc}) is swept across a large spectral range (see Figure 3.3a for the schematic view). For different λ_{exc} , the emission intensity at λ_{em} is recorded. Therefore, PLE measurements reveal the excitation spectrum of the material and it shows at which wavelengths the material can be excited well. Generally, excitation spectrum resembles the absorbance spectrum of the corresponding material since materials emit more when they can absorb more. Therefore, it is possible to measure the dependency of photoluminescence emission quantum yield on the excitation wavelength by normalizing the excitation spectrum of a material to its absorption spectrum. In Figure 3.3b, we show an exemplary excitation spectrum of a four monolayer thick CdSe nanoplatelet. In the measured spectral range of 300 – 500 nm, the excitation spectrum well resembles its absorption spectrum (see Figure 3.1b). Thus, one would not expect a strong dependence of the emission quantum yield on the excitation wavelength. However, in quantum dots and others, excitation wavelength dependency of the photoluminescence quantum yield has been previously

observed [121], which was attributed to the presence of surface traps above the bandgap that can capture hot electrons and/or holes before they could thermalize to the band edge.

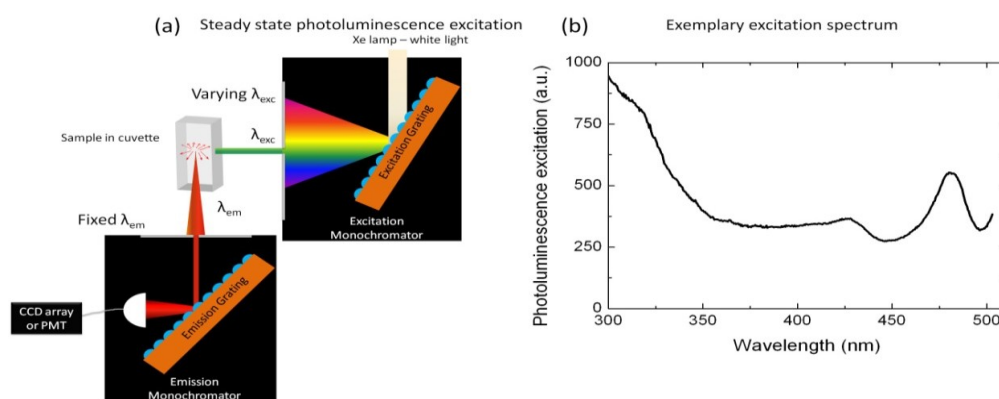


Figure 3.3. (a) Schematic diagram of the experimental setup for steady state photoluminescence excitation spectroscopy. (a) An exemplary excitation spectrum of a four monolayer thick CdSe nanoplatelets in hexane.

In addition to the steady state measurements, time-resolved spectroscopy offers a powerful means to understand the excited state kinetics in colloidal nanocrystals. It is possible to understand the optical quality of the nanocrystals through understanding the competition between the radiative and nonradiative recombination channels using time-resolved fluorescence measurements. Furthermore, near-field interactions such as nonradiative energy transfer and plasmonic coupling, which alters the recombination rate of an exciton, can be probed via transient photoluminescence measurements. To this end, in this thesis we have frequently used time-correlated single photon counting (TCSPC) technique to perform time-resolved fluorescence spectroscopy.

The working principle of a TCSPC is schematically explained in Figure 3.4a. Generally, a pulsed laser having 60 – 100 ps pulse width is used as the excitation source. The repetition rate of the pulsed laser can be adjusted from 100 kHz to 80 MHz. After each excitation pulse, photon collection is resumed for time duration, the so-called detection time window, which is determined by the repetition rate of the laser

(the period of laser pulses). For example, the longest detection time window for a pulsed laser with a 10 MHz repetition rate would be ~ 100 ns. In this time window, photon arrival times are recorded under each detector time bin, which is generally a few ps in conventional TCSPC systems. As shown in Figure 3.4a, photons are registered for their arrival times for each excitation cycle and the number of arrived photons in the corresponding time bin is updated after each pulse (see Figure 3.4a). The data acquisition generally takes a few minutes to achieve statistically meaningful decay curves with a high signal-to-noise ratio. Thus, it is important to acquire as many photons as possible. Figure 3.4b shows the fluorescence decay of a four monolayer thick CdSe nanoplatelet (black curve) measured at its peak emission wavelength (513 nm) when the sample is excited with a picosecond pulsed laser at 375 nm.

The instrument response function (IRF) is also presented (see Figure 3.4b – inset). The IRF has a non-zero temporal width arising from the pulse width of the laser and also the limited detection speed of the detector (e.g., photomultiplier tube). In our case, temporal width of the IRF is ~ 200 ps. Fluorescence decays that have lifetime components comparable to or shorter than the IRF temporal width is hard to resolve. However, it is mathematically possible to deconvolve the IRF from the measured decay curve, allowing to resolve decay lifetimes that can be faster than the IRF width [122]. Yet, this requires possessing very high quality decay data with a very high signal-to-noise ratio.

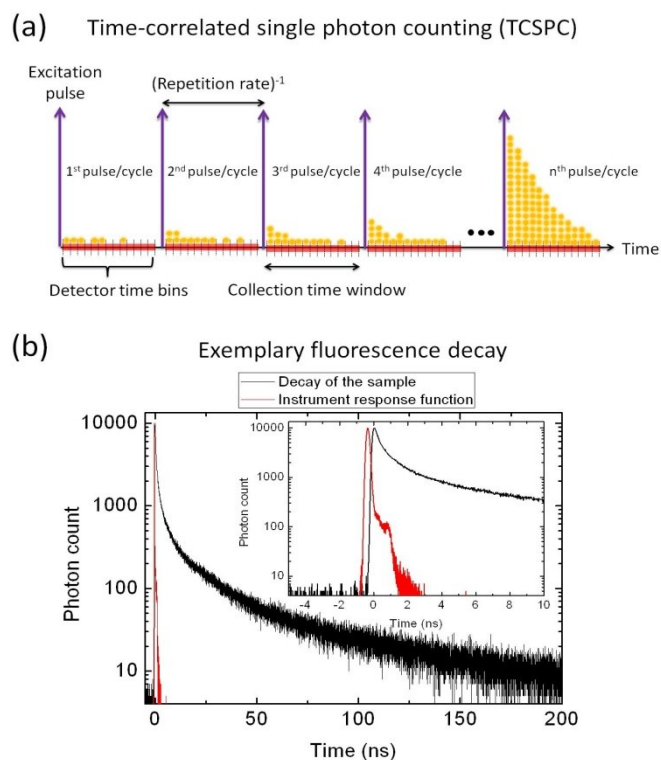


Figure 3.4. (a) Schematic diagram explaining the working principle of time-correlated single photon counting technique for time-resolved fluorescence spectroscopy. (b) Exemplary fluorescence decay curve measured at the peak emission wavelength of a four monolayer CdSe nanoplatelet (black curve) together with the instrument response function (IRF) (red curve). The inset shows the decay curve and the IRF in an early time window.

TCSPC is not limited to picosecond lasers and one could use femtosecond lasers to improve the time resolution for capturing ultrafast decay processes (e.g., Auger recombination). However, even the fastest single photon counting detectors (e.g., multi-channel plate photomultiplier tubes) are limited with time resolution on the order of 10 ps. To improve time resolution, streak cameras can be employed that can realize time resolution on the order of few picoseconds. Also, time-resolved fluorescence using Kerr-gating could improve the time resolution below a ps [123]. In addition to time-resolved fluorescence, time-resolved absorption spectroscopy techniques have proven to be quite powerful to understand exciton and charge kinetics. For example,

pump-probe transient absorption spectroscopy becomes very handy to probe the ultrafast electronic transitions in colloidal semiconductors and their complex media with other semiconductors or metal nanoparticles. Since absorption bleach is monitored in transient absorption spectroscopy by controlling the time delay between the pump and the probe, one can easily achieve time resolution on the order of ~ 100 fs. In this thesis, streak camera measurements as well as transient absorption characterizations were also used through collaborative work.

3.2 Measuring optical gain properties

Optical gain measurements are essential to characterize gain materials. The important parameters include net modal gain coefficients and net gain thresholds, which also depend on the optical losses in the system. There exist various techniques, which can be both steady state and time-resolved techniques. Here, we will introduce amplified spontaneous emission measurements, modal gain coefficient measurements via variable stripe length method and discuss how to characterize the nonlinear absorption cross-section of a material using open aperture z-scan measurements.

Amplified spontaneous emission (ASE) is commonly observed in the solid films of luminescent semiconductors (e.g., colloidal quantum dots, conjugated polymers, epitaxial quantum wells, etc.) when these materials are pumped with pulsed lasers with high enough pump intensities that net optical gain could prevail in the system. ASE can be considered as a cavity-less lasing and it is the precursor of lasing. The performance of ASE in a material gives a direct indication of its possible laser performance. In the ASE experiments, nanocrystal samples are typically spin-coated or drop-casted on quartz substrates. Thus, the cavity is formed by the lateral waveguiding effect of the thin film. Generally stripe excitation is used for the ASE measurements. The emission is collected from the edge of the sample co-aligned with respect to the excitation stripe.

Figure 3.5a shows a schematic configuration that illustrates the experimental setup for the ASE measurements. As the pump source, femtosecond lasers are typically used since Auger recombination in the nanocrystals is very fast and rapidly annihilates the

gain-active biexcitons. Thus, it is needed to form the biexcitons before Auger recombination can nonradiatively annihilate them. To this end, in our experiments we employed Spectra Physics – Spitfire Pro XP regenerative amplifier system having 120 fs pulse width at 800 nm with a 1 kHz repetition rate as the pump source. For the single-photon absorption pumping, we double the pump wavelength using a nonlinear Beta Barium Borate (BBO) crystal. To eliminate the residual 800 nm beam, we use a bandpass filter. We also use a rotatable round neutral density filter that allows to continuously vary optical density to adjust the pump intensity incident on the sample. When spin-coated or drop-casted, the resulting thin film sample has >100 nm thickness. Using a cylindrical lens, we excite the samples in a stripe geometry (see Figure 3.5a). Pump-intensity dependent emission is collected from the edge of the sample along the stripe using a fiber coupled to a spectrometer (Maya2000 Pro).

Figure 3.5b shows exemplary emission spectra of a 4 monolayer thick CdSe nanoplatelet film measured at different excitation intensities. The transition from spontaneous emission into ASE, which is the newly emerging red-shifted emission peak, is achieved at a threshold pump intensity of $70 \mu\text{J}/\text{cm}^2$. As shown in Figure 3.6a, it is also possible to excite the samples at 800 nm, which results in two-photon absorption pumping. Since it is a nonlinear optical process, it requires higher excitation intensities ($\sim\text{mJ}/\text{cm}^2$) to realize ASE, which is 100- to 1000-folds larger than the threshold required for single-photon absorption pumping.

Figure 3.6b exemplifies an input-output curve measured from a four monolayer thick CdSe nanoplatelet film, which shows the emission intensity as a function of the excitation intensity. At lower pump intensities, the emission is dominated with the spontaneous emission. Above the ASE threshold, the emission from the sample is dominated by the ASE and the slope of the emission significantly increases.

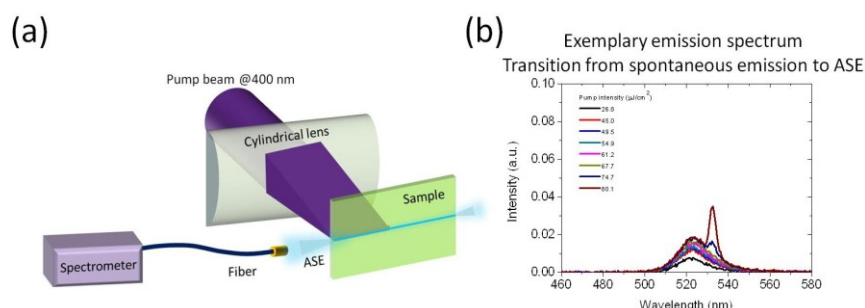


Figure 3.5. (a) Schematic diagram of the experimental setup to measure amplified spontaneous emission under single-photon absorption pumping (pump laser 400 nm, 120 fs, 1 kHz repetition rate). (b) Exemplary emission spectra from a four monolayer thick CdSe nanoplatelet film showing the transition from spontaneous emission into amplified spontaneous emission as the pump intensity is gradually increased.

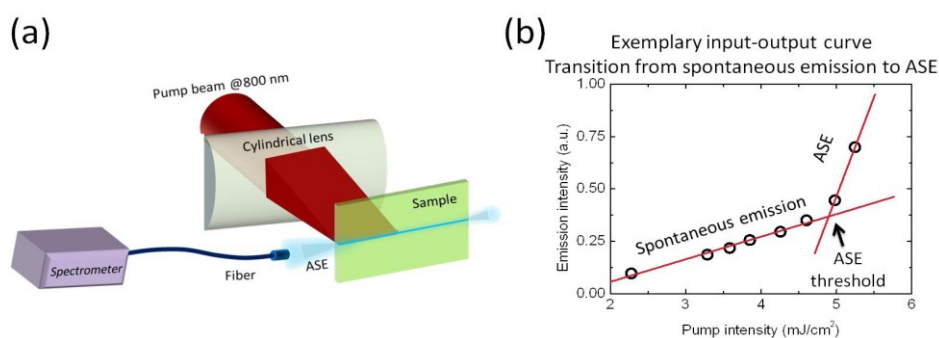


Figure 3.6. (a) Schematic diagram of the experimental setup to measure amplified spontaneous emission under two-photon absorption pumping (pump laser 800 nm, 120 fs, 1 kHz repetition rate). (b) Exemplary input-output plot from a four monolayer thick CdSe nanoplatelet film showing the transition from spontaneous emission into amplified spontaneous emission as a function of the pump intensity. The threshold for optical gain can be also characterized from this plot.

We show the photographs of a nanoplatelet (core/crown CdSe/CdTe) film when the pump intensity is below (Figure 3.7a) and above (Figure 3.7b) the amplified spontaneous emission threshold. The sample becomes much brighter since amplified spontaneous emission kicks in. As shown in Figure 3.6b, the emission intensity

increases steeply for excitation levels above the ASE threshold due to the net optical gain in the system. Figure 3.8 also shows the photograph of CdSe/CdS core/shell quantum dot film when the excitation intensity is above the ASE threshold.

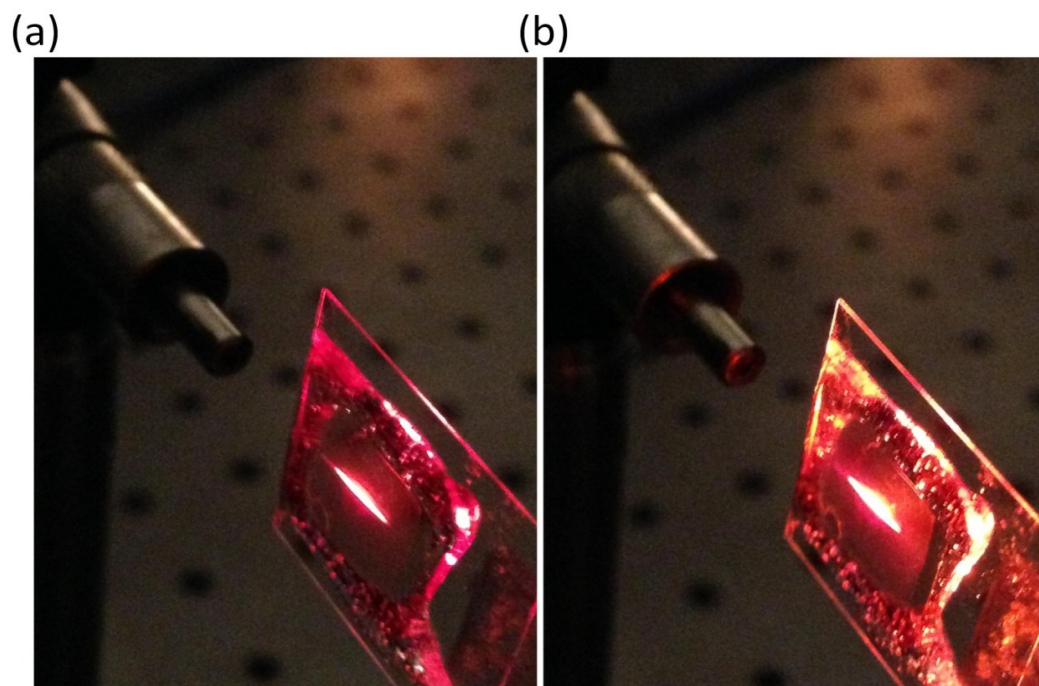


Figure 3.7. Solid film of a colloidal nanoplatelet (heterostructured CdSe/CdTe core/crown architecture) film encapsulated with a cover glass and epoxy. The sample is excited in stripe geometry with a femtosecond laser. Emission from the sample (a) below and (b) above the amplified spontaneous emission threshold.

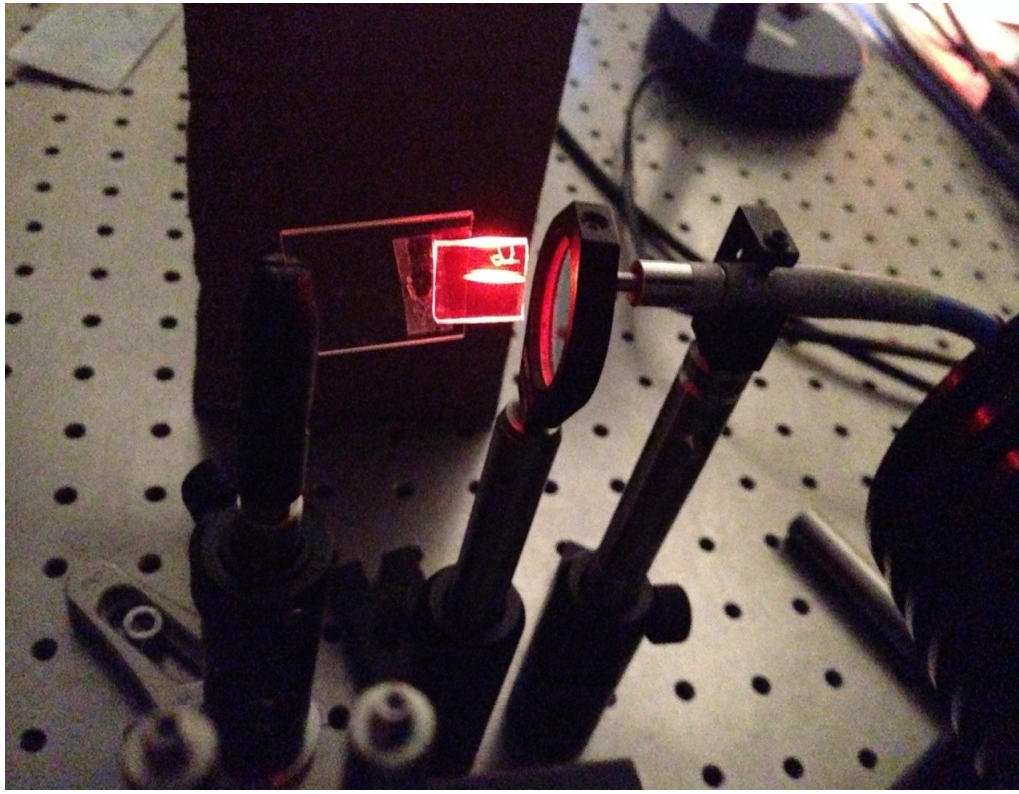


Figure 3.8. CdSe/CdS core/shell quantum dots spin-coated on quartz substrate excited with a pump intensity above the amplified spontaneous emission threshold.

We characterized net modal gain coefficients in colloidal nanocrystals (in their spin-coated and encapsulated films) via variable stripe length (VSL) method [124]. We used stripe geometry for the excitation of the samples (see Figure 3.9a). Similar to the ASE measurements, frequency-doubled output (400 nm, using a BBO crystal) of a femtosecond Ti:sapphire regenerative amplifier (Spitfire Pro, Spectra Physics) having a 120 fs pulse duration with a 1 kHz repetition rate was used as the pump source. The width of the excitation beam was chosen to be $\sim 120 \mu\text{m}$ to ensure the one-dimensional amplifier assumption and to maximize the emission of the ASE from the edge of the sample. Also, we only used the mid-portion of the excitation spot to ensure the homogeneity of the excitation stripe. The sample was prepared by spin-coating technique (film thickness $\sim 150 \text{ nm}$) to provide a waveguiding structure. Adjustable slit was used to vary the stripe length. The slit was placed as close as possible (few 5-6 mm) to the sample to prevent diffraction effects. We show an exemplary VSL data

from a CdSe/CdS core/crown nanoplatelet film in Figure 3.9b. To fit the VSL data, we employ the following that assumes a one-dimensional amplifier model [124]:

$$I(\lambda, l) = I_S \frac{(e^{(g(\lambda) - \alpha(\lambda))l} - 1)}{g(\lambda) - \alpha(\lambda)} \quad (3.3)$$

where $g(\lambda)$ is the modal gain coefficient, $\alpha(\lambda)$ is the waveguide loss factor, I_S is a constant related to the emission intensity of the sample. $g(\lambda) - \alpha(\lambda)$ is the net modal gain coefficient. Similar to the VSL measurements, one can measure the optical waveguide loss coefficient in the solid films of the semiconductors. A narrow excitation stripe is used and the stripe is translated across the sample from the edge using a translation stage. Thus, the distance between the stripe and the edge of the sample is varied while leaving an unexcited region of the material. As a function of the width of the unexcited region, we can relate the collected emission intensity as follows: $I(\lambda) = I_0 e^{-\alpha(\lambda)l}$, where $\alpha(\lambda)$ is the waveguide optical loss coefficient, l is the distance from the edge of the sample to the end of the stripe and I_0 is the intensity when $l = 0$.

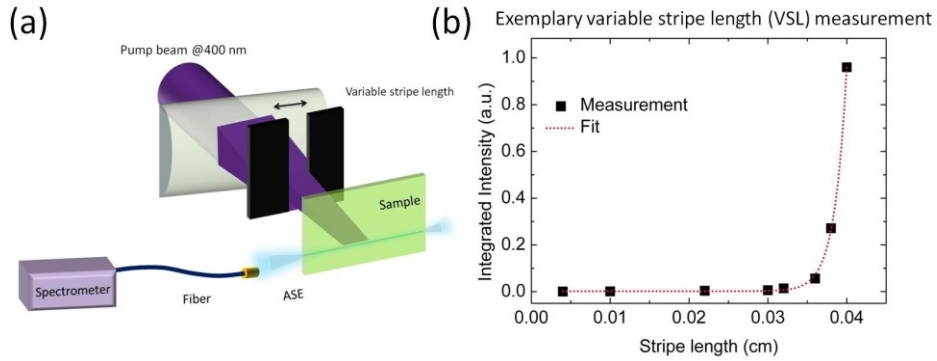


Figure 3.9. (a) Schematic diagram of the experimental setup to perform variable stripe length (VSL) method for the measurement of net modal gain coefficients. (b) Exemplary data for the variable stripe length measurement.

Open aperture z-scan technique is frequently used to measure the two-photon absorption cross-section in materials. For this, the excitation source is a Ti:Sapphire laser system (Spitfire Pro XP, Spectra Physics) having 120 fs pulse width at 800 nm with 1 kHz repetition rate. A 1 mm quartz cuvette was used as the container of the

nanocrystal solution. Figure 3.10a shows the schematic diagram of the open aperture z-scan measurements. Also, Figure 3.11 shows a photograph of the actual z-scan setup. The femtosecond laser beam, a Gaussian beam, is focused by a lens (with a long focal length ~50 cm). A stage translates the cuvette containing the nanocrystal dispersion sample through the focus of the femtosecond laser beam (see Figure 3.10a). The transmitted intensity of the beam is monitored through a photodetector at the end of the translation stage. Figure 3.10b shows an exemplary z-scan data that shows the change of the transmittance as the sample is translated through the focus (at $z = 0$).

The following equation has been employed to fit the measured open aperture z-scan transmission data:

$$T(z) = \frac{1}{1 + \frac{I_0 \times \beta \times l}{1 + \left(\frac{z}{z_0}\right)^2}} \quad (3.4)$$

Here $T(z)$ is the normalized transmittance given as a function of the sample position on z . I_0 is the peak on-axis irradiance at the focus. β is the two-photon absorption coefficient, which is to be fitted. l is the cuvette length. z_0 is the Rayleigh range. Excitation per pulse energy is attenuated to a level where the solvent does not exhibit nonlinear response. Using the fitted two-photon absorption coefficient (β), we can calculate the two-photon absorption cross-section (σ_{2PA}):

$$\sigma_{2PA} = \frac{h \times \nu \times \beta}{N_A \times d_0 \times 10^{-3}} \quad (3.5)$$

Here $h\nu$ is the energy of excitation photons, N_A is the Avagadro's number and d_0 is the molar concentration of the nanocrystals. Concentration of the nanocrystal solutions (d_0) is determined using an elemental analysis such as inductively coupled plasma optical emission spectroscopy (ICP-OES).

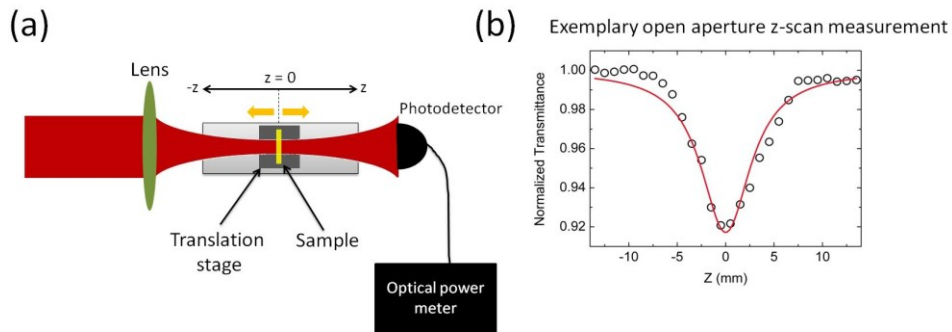


Figure 3.10. (a) Schematic diagram of the experimental setup for open aperture z-scan technique. (b) Exemplary transmittance data for a four monolayer CdSe nanoplatelet in toluene as the sample is translated through the focus of 800 nm femtosecond Gaussian laser beam.

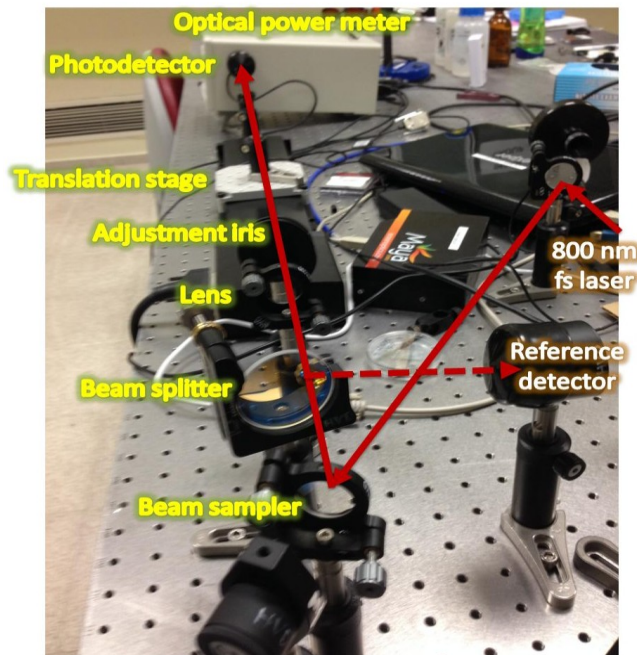


Figure 3.11. Open aperture z-scan setup to measure the nonlinear absorption cross-section constructed and used for this thesis work.

In this thesis, we have used numerous material, optical and electrical characterization techniques. For the material characterization, we have employed

transmission electron microscopy (TEM), scanning electron microscopy (SEM), x-ray photoelectron spectroscopy (XPS), X-ray diffraction (XRD), atomic force microscopy (AFM), thermal gravimetric analysis (TGA), Dektak profilometer and dynamic light scattering (DLS). For optical characterization, we also made use of scanning near-field optical microscopy (SNOM), Raman spectroscopy, micro-photoluminescence, confocal microscopy, Fourier transform infrared spectroscopy (FTIR), ellipsometry and reflectometry. For the sample preparation and fabrication, we employed the following processing steps: photolithography, thermal evaporation, sputtering, e-beam evaporation, plasma enhanced chemical vapor deposition (PECVD), spin-coating, layer-by-layer deposition, and air/liquid self-assembly.

Chapter 4

Harnessing Exciton Transfer at the Nanoscale in Designer Nanocrystal Assemblies

4.1 Introduction to harnessing exciton transfer

Excitons make the primary excited state species in strongly quantum confined semiconductors including colloidal nanocrystals (e.g., colloidal quantum dots), organic semiconductors (e.g., conjugated polymers) and newly emerging two-dimensional transition metal dichalcogenide monolayers (e.g., MoS₂). In all of these material systems, it is crucial to transport excitons at the nanoscale for relatively long distances to accomplish ultraefficient light harvesting. In nature, such exciton transport occurs at an ultimate efficiency level, for example, in a cell of a green leaf, which converts light into chemical energy [125]. During photosynthesis, sunlight is absorbed to form an exciton in a chlorophyll molecule (a pigment protein that absorbs visible light). Then, generated excitons are funneled through these proteins to the reaction center, where

CO₂ and H₂O are reacted together with radical free electrons that are formed through dissociation of the photogenerated excitons. Similarly, exciton transport in artificial materials (quantum dots, conjugated polymers, etc.) is also possible, yet it has proven hard to realize such ultraefficient exciton transport that a leaf could achieve.

To make an analogy, small molecules or nanocrystals can act as an antenna that creates an exciton upon absorption of a photon. The receiver molecule (the so-called acceptor) that is nearby the antenna molecule (the so-called donor) can be excited via near-field dipole-dipole coupling (Donor* + Acceptor → Donor + Acceptor*). This near-field energy transfer phenomenon has been first correctly explained by T. Förster in late 1940's [101]. Thus, this type of energy transfer is also commonly known as Förster resonance energy transfer (FRET). In the community, alternatively, nonradiative energy transfer (NRET) has been coined to describe this phenomenon as well.

In the colloidal nanocrystals, FRET has been first observed by Kagan *et al.* in the solid films of the nanocrystal quantum dots [97]. Later, Crooker *et al.* have uncovered the extent of this process in more detail [98]. Colloidal quantum dots and nanorods could act as exciton donors and acceptors in combination with various material systems; e.g., epitaxial quantum wells, bulk silicon, organic dyes, and conjugated polymers have been considered with various material systems (see our review paper on exciton transfer in colloidal nanocrystals [126], also that by Prof. Rogach [127] and our invited perspective on the excitonic organic-inorganic hybrids [20]).

We can elucidate the need for tailoring exciton transport at the nanoscale for efficient optoelectronic devices by giving a few examples, where exciton transfer and funneling could be used to boost the performance of a solar cell or a photodetector. Silicon is the most commonly used material for solar cells. However, silicon is an indirect bandgap material; thus, it has poor light absorption. It is possible to increase the absorption of silicon by sensitizing with other strongly absorbing materials (e.g., colloidal quantum dots). Excitons formed in the quantum dots could be transferred to silicon via NRET [128]. This has the potential of enhancing the photocurrent of a

silicon solar cell, hence, its power conversion efficiency [129], [130]. Also, two-dimensional materials, such as graphene, exhibit unique electrical and optical properties. However, total optical absorption is limited in these materials due to their ultimate thinness (only a monolayer of atoms), although the absorption per unit length is very strong. Therefore, exciton transfer-based sensitization offers exciting possibilities towards high-performance graphene-based photodetectors by synergistically combining the strong absorption of the nanocrystal films and high conductivity of the graphene [131], [132]. Also, exciton harvesting is quite interesting for light generation. Using a wider bandgap nanocrystal as the exciton antenna to transfer the excitation energy to the acceptor molecule to enhance fluorescence of the latter is a favorable route for enhancing the color conversion-based light-emitting diodes [108], [133] and lasers [134].

One severe limitation in the colloidal nanocrystals (also in organic semiconductors) is that the exciton transport distances are very short, generally on the order of 10 nm. This mainly arises from the fact that these materials exhibit inhomogeneous broadening in their ensembles. During the lifetime of an exciton, it can be easily trapped in a quantum dot with slightly narrower effective bandgap energy than that of its surrounding quantum dots. This has been shown to lead sub-diffusive exciton transport in the conventional nanocrystal solid films [14], [135]. Another limitation in the colloidal quantum dots and other organic semiconductors is that the molar extinction coefficient (the strength of absorption per single molecule/quantum dot) is small. Therefore, Förster radius (critical energy transfer radius), which is the distance between the donor and the acceptor when the exciton transfer efficiency is 50%, is generally 3-6 nm.

Recently, atomically flat colloidal nanocrystals, which are commonly referred to as colloidal nanoplatelets (and also known as colloidal quantum wells), have been introduced as a new addition to the class of colloidal nanocrystals [56]. These nanoplatelets have unique optical properties, distinguishing them from the conventional nanocrystals. First, the nanoplatelets have a fixed (the so-called “magic sized”) vertical thickness, which is formed by few monolayers. Second, they are

atomically flat and their lateral dimensions are much larger than the exciton Bohr radius. Thus, there is dominantly only one-dimensional quantum confinement in the nanoplatelets. That is why their optical properties resemble those of the epitaxial quantum wells. Moreover, reduced dielectric screening and strong one-dimensional confinement result in remarkably large exciton binding energies (>100 meV) [57]. This also leads to large absorption and emission cross-sections in these materials, considerably increasing their molar extinction coefficients as well.

Previously, NRET (or FRET) has not been elucidated in the colloidal nanoplatelets and their thin films. Also, the geometric advantages of the nanoplatelets due to their anisotropic shapes have not been explored nor considered to maximize exciton transfer at the nanoscale. In this thesis, we have explored the exceptional potential of the nanoplatelets as efficient exciton antennas and exciton sinks that could be favorably used for their photodetection and light-generation applications. In this chapter, we will introduce different nanocrystal assemblies, commonly comprising nanoplatelets. We have uncovered the efficient exciton transfer in these nanocrystal assemblies that offer the potential to make energy-efficient devices and help to find numerous use in optoelectronic and sensing applications.

4.2 Ultraefficient exciton transfer in nanoplatelet assemblies for long-range exciton diffusion

This section is based on the publication “Stacking in Colloidal Nanoplatelets: Tuning Excitonic Properties,” **B. Guzelturk**, O. Erdem, M. Olutas, Y. Kelestemur and H. V. Demir, *ACS Nano* 8, 12524-12533 (2014). Adapted (or “Reproduced in part”) with permission from American Chemical Society. Copyright 2014 American Chemical Society.

4.2.1 Motivation

Controlling the nanoscale assembly of colloidal semiconductor quantum wells, also alternatively known as NPLs and understanding their emerging properties are crucial in the light-generation based applications. Previously, stacking of the colloidal NPLs has been reported both in solution and solid films [63], [136]. Stacked NPL assemblies exhibit different optical properties as compared to the non-stacked ones. For instance, low-temperature photoluminescence spectrum of the stacked NPLs was shown to differ from that of the non-stacked NPLs by the phonon-line emission in the stacked NPLs [63]. Additionally, polarized light-emission was demonstrated in the stacked NPL assemblies [136]. However, steady state and transient excitonic properties of the stacked NPLs have not been understood nor elucidated to date. Moreover, strong near-field dipole-dipole coupling between the NPLs of the same population in their close-packed stacked assemblies has not been considered before.

Here we first hypothesized and then demonstrated that excitons should efficiently hop back and forth between the NPLs within the stacked assemblies via FRET [101]. In the case of colloidal quantum dot-based close-packed assemblies, FRET was observed within the same population of the QDs resulting in a red-shift of the photoluminescence spectrum due to the intrinsic inhomogeneous size broadening favoring downhill exciton funneling towards QDs having a smaller band gap [97], [98]. In the case of NPLs, the density of states is not inhomogeneously broadened since the magic sized vertical thickness (e.g., fixed 3, 4 and 5 monolayers) of the NPLs dictates their bandgap energy [59], [126], [137]. Quantum confinement due to the lateral direction in the NPLs is very weak because lateral sizes are typically larger than the exciton Bohr radius [137]. Therefore, one should expect to observe different signatures for the exciton transfer via FRET in the stacked NPL assemblies as compared to ones in the close-packed QD assemblies.

4.2.2 Experimental

For the synthesis of 4 ML CdSe NPLs; 170 mg of cadmium myristate, 12 mg of selenium and 15 mL of octadecene (ODE) were loaded into a three-neck flask. After evacuation of solution at room temperature, the solution was heated to 240⁰C under argon atmosphere. When the temperature reaches 195⁰C, the color of solution becomes yellowish. Then, 45 mg of cadmium acetate dihydrate was introduced. After 4 minutes growth of CdSe NPLs at 240 ⁰C, the reaction is stopped and cooled down to room temperature with the injection of 1 mL of oleic acid (OA). 4 ML CdSe NPLs were separated by other reaction products with the successive purification steps.

For time-resolved photoluminescence spectroscopy: Pico Quant FluoTime 200 equipped with TimeHarp time-correlated single-photon counting (TCSPC) unit was utilized to record the fluorescence decays with 375 nm picosecond pulse laser. Full-width at half-maxima of the instrument response function (IRF) is 200 ps. Per-pulse energy of the pump laser was measured to be 15.6 pJ at 3.31 eV (spot radius is ~100 μ m). FluoFit program was employed to make deconvolution fitting with the IRF. 4th order exponential decay models were employed to fit the photoluminescence decay curves of the NPLs resulting in reduced χ^2 of ~1 and uniform residuals.

4.2.3 Results and discussion

In this section, we systematically investigated the steady state and transient excitonic properties of the controlled stacked NPL assemblies and revealed ultra-long exciton migration in the stacked NPL assemblies. Controlled stacking of the CdSe NPLs having 4 monolayer vertical thickness was achieved in solution phase via step-by-step addition of ethanol to the solution. Transmission electron microscopy imaging supports the controlled formation of the NPL stacks. Ultra-long Förster radius of ~13.5 nm and extremely long exciton migration length of 133 nm were found for the stacked NPLs thanks to close-packed stacking, strong self-spectral overlap arising due to large extinction coefficient of the NPLs along with the parallel and collinear orientation of the transition dipoles in column-like ordered NPL stacks. However, in the NPL stacks,

we did not observe the common signatures of homo-FRET: red-shifting photoluminescence emission as observed in the close-packed assemblies of the colloidal nanocrystals. This is because of the fact that there is no inhomogeneous broadening in the NPLs. We observed that as the NPLs form into large stacks, photoluminescence quantum yield (QY) of the NPLs decreases by a factor as high as 10-folds and transient fluorescence decay of the NPLs was also concomitantly accelerated. These observations were accounted for trapping of the excitons by non-emissive NPLs in the stacked NPL assemblies assisted by homo-FRET (i.e., FRET in between the same populations of emitters) within the stacks. Trapped excitons then undergo rapid nonradiative recombination accelerating the overall photoluminescence decay kinetics. We developed a rate equation based model that considers the possible excitonic interactions (i.e., the exciton transfer, the radiative and nonradiative recombination) and the actual distribution of the stack size using TEM imaging. The results of the model are in excellent agreement with the experimental time-resolved fluorescence results. Consequently, we revealed the critical significance of stacking control in NPL solids for their potential use in optoelectronics.

Figure 4.1a shows the absorbance (dashed line) and photoluminescence (solid line) spectrum of the 4 ML CdSe NPLs (having a vertical thickness of 1.2 nm) in solution. After size selective precipitation via ultracentrifugation, there were no side-products such as colloidal quantum dots or different vertical thickness NPLs, as can be seen by the pure 4 ML NPL emission and absorbance spectra in Figure 4.1a. Characteristic to the colloidal NPLs, we observed absorbance spectrum featuring two peaks at 480 and 512 nm corresponding to the electron/light-hole and electron/heavy-hole transitions, respectively. The photoluminescence emission peak is located at 513 nm with a full-width at half-maximum (FWHM) of ~ 8 nm. Transmission electron microscopy (TEM) images of the 4 ML NPLs are shown in Figure 4.1b exhibiting rectangular shape with an average lateral size of 20.08 nm (± 2.36 nm) by 11.50 nm (± 1.39 nm). Therefore, quantum confinement along lateral dimensions is expected to be very weak in these NPLs since the lateral size is much larger than the size (~ 5 -7 nm) of the first exciton [137], [138].

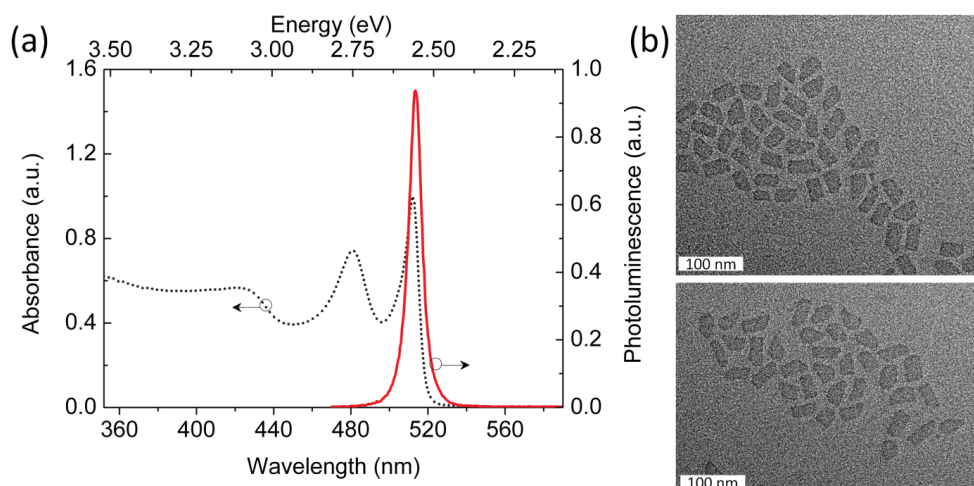


Figure 4.1. (a) Absorbance (dashed line) and photoluminescence (solid line) spectrum, (b) transmission electron microscopy images of the 4 ML CdSe NPLs. Reprinted (or Adapted) with permission from [19]. Copyright 2014 American Chemical Society.

Previously, Dubertret *et al.* have demonstrated that addition of a polar solvent such as ethanol into the solution of the NPLs, which is dissolved in apolar solvents (e.g., hexane and toluene), leads to the stacking of the NPLs on top of each other resulting in column-like assemblies [136]. When ethanol is introduced, NPLs tend to minimize their surface energy by drawing away ethanol since ethanol is an antisolvent for the ligands (oleic acid) of the NPLs. Removal of the oleic acid ligands due to ethanol was shown previously [58], [63]. Therefore, addition of ethanol tends to bring NPLs together, where strong van der Waals forces between the surfaces of the NPLs induce the formation of column-like 1D stacks of the NPLs (see Figure 4.2). We observed that, once stacked, NPLs cannot be separated anymore due to strong attractive forces. Previously, small-angle X-ray scattering (SAXS) measurements confirmed the formation of the ordered structures with a spatial period of ~ 5 nm [63]. Here, we found the average center-to-center distance between the stacked NPLs to be 4.29 nm (± 0.36 nm) using high resolution TEM imaging (see Figure 4.2).

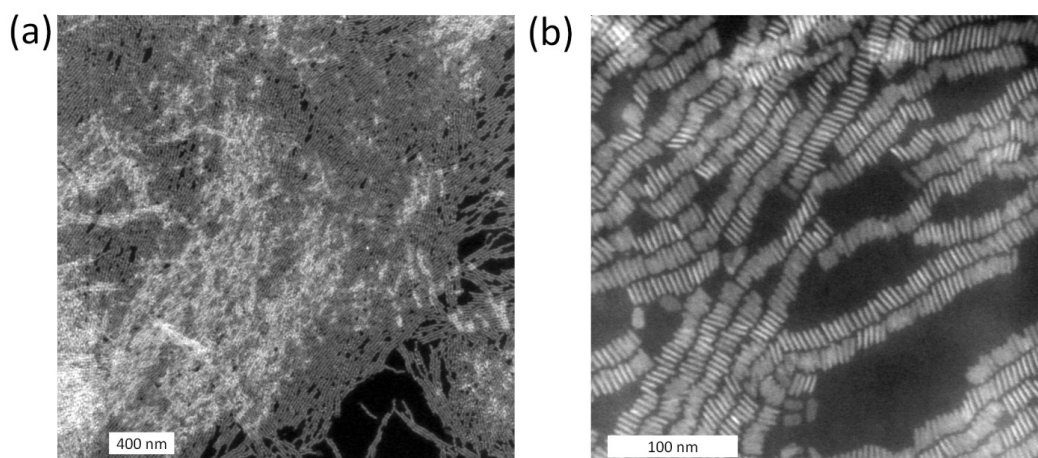


Figure 4.2. TEM images of the highly stacked NPLs. The scale bar is (a) 400 nm and (b) 100 nm. Column-like ordered stacking of the NPLs is clearly visible. Reprinted (or Adapted) with permission from [19]. Copyright 2014 American Chemical Society.

To initiate and control the stacking, we added ethanol carefully step by step to the solution of the 4 ML NPLs (in a total of 3.1 mL volume having 16.79 nM of the NPLs). We could sensitively control the degree of stacking via tuning the amount of added ethanol to the solution of the NPLs. Figure 4.3 exhibits the high-angle annular dark-field scanning transmission electron microscopy (HAADF-STEM) images of NPLs for different amounts of ethanol addition (0, 55, 135 and 455 μL of ethanol added in total in the corresponding samples of Figure 4.3a to Figure 4.3d, respectively). When there is no ethanol added to the solution of the NPLs, we could not detect any discernible stacking. Figure 4.3a exhibits completely flat-lying NPLs without any stacking. Figure 4.3b shows the NPLs when 55 μL ethanol has been added to the solution. In this case, we can clearly observe that stacking has been initiated. Contrast difference between the NPLs in the TEM image reveals the presence of two NPLs sitting on top of each other (i.e., brighter) or non-stacked NPLs (i.e., darker). However, most of the NPLs are still non-stacked. As we further continued adding ethanol, as shown in Figure 4.3c for a total of 135 μL added ethanol, we started to observe the formation of the flat-lying stacks of 2-3 layers of NPLs on top of each other. Also we observed longer stacks (more than 4 nanoplatelets stacked together) lying perpendicular to the TEM grid. Finally, the NPLs mostly form column-like

ordered stacks when a total of 455 μL ethanol was added to the solution as shown in Figure 4.3d.

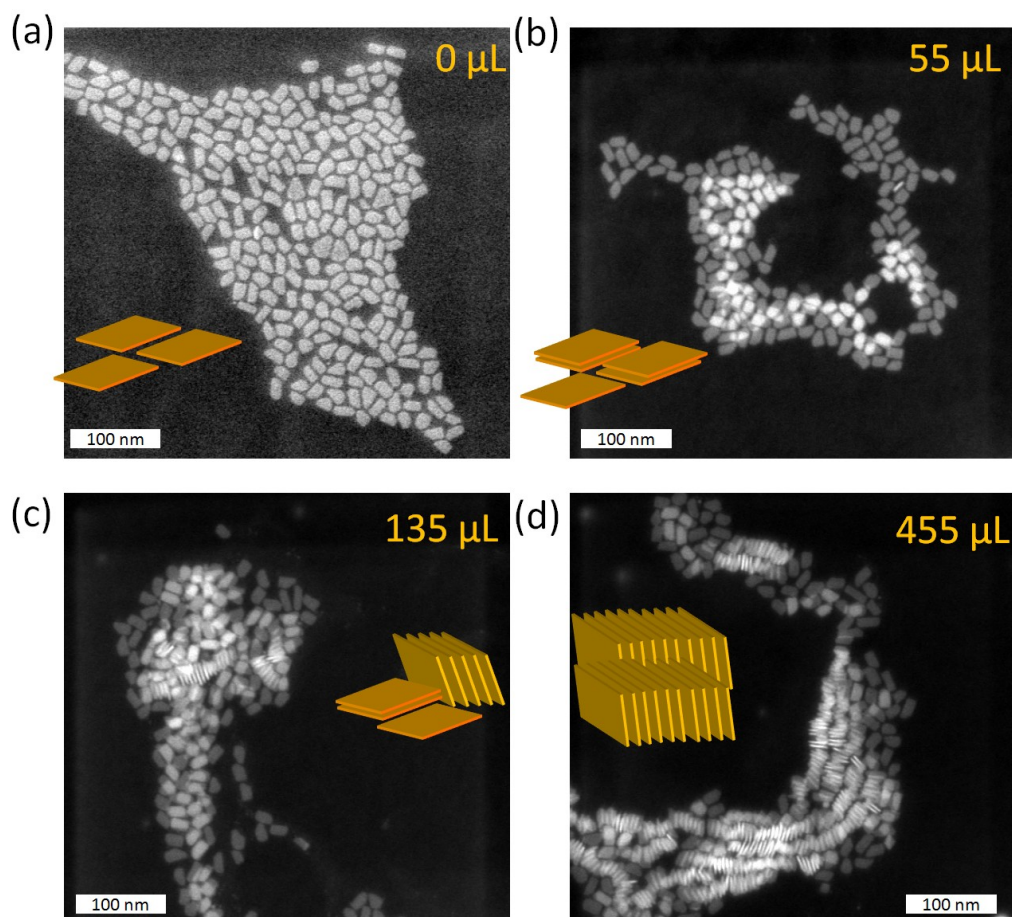


Figure 4.3. High-angle annular dark-field (HAADF) TEM images of the NPLs with (a) no ethanol, a total of (b) 55 μL , (c) 135 μL , and (d) 455 μL ethanol added. The scale bars are 100 nm. As the total added ethanol amount is increased gradually, longer column-like stacks of the NPLs are formed. On each image, cartoon like depiction of the evolution of the stacking in NPLs is presented by yellow-colored NPLs. Reprinted (or Adapted) with permission from [19]. Copyright 2014 American Chemical Society.

Next we investigated the optical properties of the stacked NPL assemblies via steady state and transient photoluminescence spectroscopy. Figure 4.4a exhibits the measured photoluminescence decay curves and their fits. As the total added amount of ethanol is increased (0 to 455 μL), photoluminescence decays become considerably

faster. Inset of Figure 4.4a depicts the shorter time window of the decay curves clearly exhibiting the acceleration of the fast decay components. Figure 4.4b presents the steady state photoluminescence spectra of the same samples having different amounts of ethanol added to the solution. Photoluminescence intensity quickly drops as stacking is initiated. Quenching of the photoluminescence intensity was found to be as high as 10-folds when a total of 455 μL of ethanol was used for a high degree of stacking.

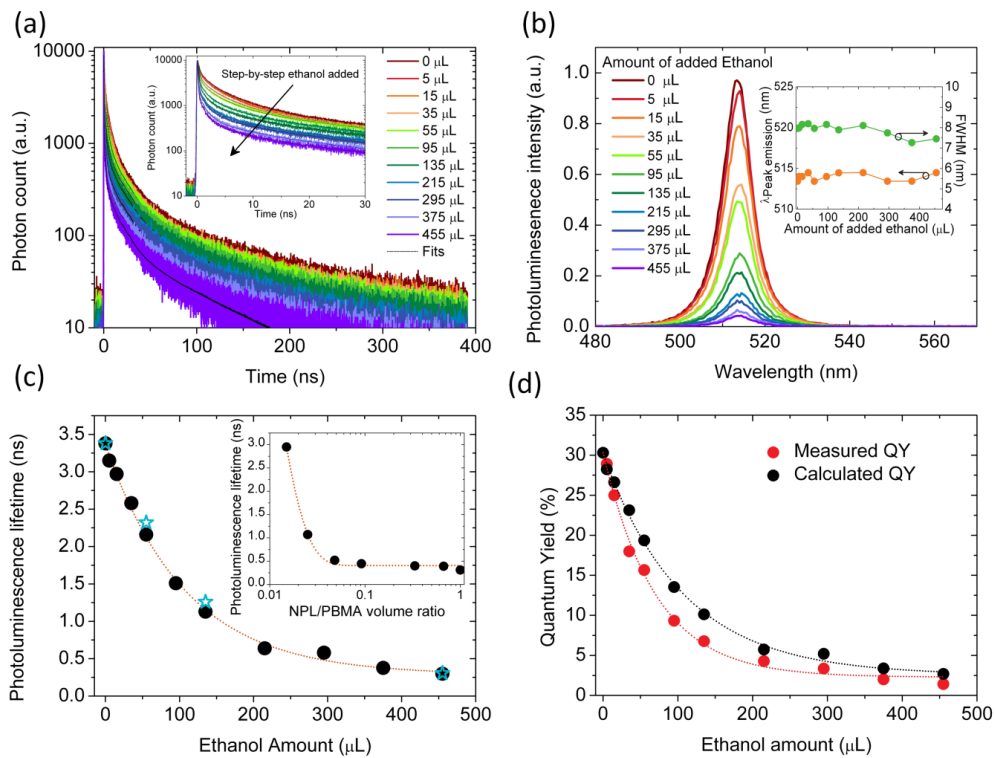


Figure 4.4. (a) Time resolved photoluminescence decays together with their multi-exponential fits. Inset shows the same photoluminescence decay curves in a shorter time window. (b) Steady state photoluminescence intensity of the NPLs while ethanol is added gradually to the solution of the NPLs. Inset shows the peak emission wavelength and photoluminescence FWHM of the NPLs as a function of the total added amount of ethanol. (c) Amplitude averaged photoluminescence lifetimes of the NPLs shown by black dots as a function of the total added ethanol amount. Blue stars show the modeled photoluminescence lifetimes of the NPLs for 0, 55, 135 and 455 μL ethanol added cases. The inset shows the average photoluminescence lifetimes of the

NPLs in PBMA host matrix given for different NPL/PBMA volume ratios. Transition from non-stacking to stacking in the photoluminescence decay kinetics of the NPLs is observed without using any ethanol. As the NPL/PBMA volume ratio is gradually increased, phase segregation occurs that result in stacking. This increases the total decay rate of the NPLs. (d) Photoluminescence QY of the NPLs as a function of total added ethanol amount measured directly from steady state photoluminescence measurements and calculated semi-empirically from the photoluminescence lifetimes assuming the radiative recombination does not change. Reprinted (or Adapted) with permission from [19]. Copyright 2014 American Chemical Society.

These observed features may indicate the presence of exciton migration in these NPL stacks via homo-FRET. Previously, in close-packed QD solids, homo-FRET has been shown to possess characteristic signatures including strong red-shift of the emission spectrum due to downhill funneling of the excitons within the inhomogeneously broadened density of states in the QDs. Furthermore, exciton transfer within solids of the same QD population was shown to decrease photoluminescence quantum yield due to trapping by small band gap and non-emissive QDs [16], [139]. Finally, homo-FRET in the energetically disordered QD populations leads to strong modification (shortening) of the photoluminescence lifetimes at the blue-tail emission of the QDs [14], [126], [128], [140], [141]. However, in the stacked NPL assemblies contrary to the QDs, we observed neither a shift in the peak emission wavelength (see Figure 4.4b and its inset) nor a significant modification in the fluorescence lifetimes at different spectral positions of the emission (see Figure 4.5). In the NPLs, downhill migration of the excitons (i.e., red-shift) would not be expected since all of the NPLs have the same magic sized (4 ML in this case) vertical thickness; thus, there is no inhomogeneous broadening due to vertical size. Furthermore, FWHM of the NPL emission was observed not to change in a significant way with the stacking (see the inset of Figure 4.4b). This indicates that the ambient dielectric environment around the transition dipole in an NPL also does not change significantly as they form into stacks. This may be probably due to the fact that inorganic crystal part of the NPLs, which has a larger dielectric constant, is thinner as compared to the bulky organic ligands surrounding the NPLs, which have lower dielectric constant. Therefore, the dielectric

constant of the ligands would largely set the average dielectric constant within the NPL stacks. These observations imply that NPLs having no inhomogeneous broadening, strongly contrasting with common colloidal semiconductor nanomaterials, do not exhibit the widely known signatures of the exciton transport/migration in their steady state and transient photoluminescence properties.

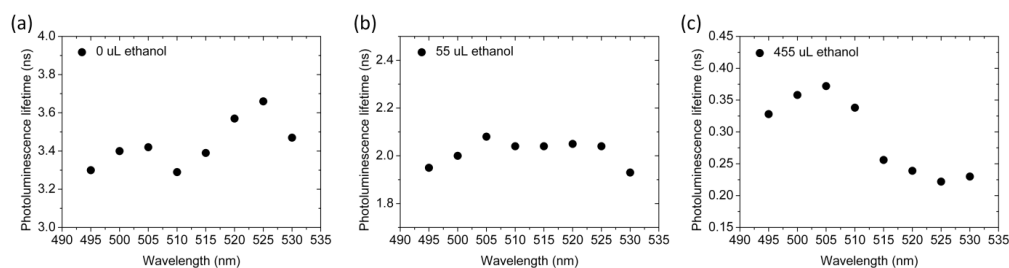


Figure 4.5. Amplitude averaged photoluminescence lifetime of the NPLs as a function of wavelength measured for (a) 0 μL , (b) 50 μL and (c) 455 μL ethanol addition. Reprinted (or Adapted) with permission from [19]. Copyright 2014 American Chemical Society.

In Figure 4.4a photoluminescence decay curves were fitted using four exponential decay functions after deconvolving with the instrument response function of the time resolved fluorescence system. Multi-exponential decay (three or four exponential decay functions) in the NPLs was also previously observed [57], [58], [137]. Figure 4.4c depicts the amplitude averaged photoluminescence lifetimes of the NPLs as a function of total added ethanol amount (See Figure 4.6 for the individual lifetime components). The NPLs have ~ 3.38 ns average photoluminescence lifetime before stacking is induced, which is in accordance with the photoluminescence lifetime of the 4 ML CdSe NPLs [57]. As ethanol was added gradually to the solution of the NPLs, we observed that photoluminescence lifetime of the NPLs can decrease as high as by an order of magnitude. We observed the fastest amplitude averaged photoluminescence lifetime (300 ps) in the case of total 455 μL ethanol added to the NPL solution, where the longest stacks are present. Before inducing any stacking, the photoluminescence QY was measured to be 30.3% by comparing the emission of the NPLs to a reference dye of Rhodamine 6G having a quantum yield of 95%. Figure 4.4d (red-dots) demonstrates the change of the measured photoluminescence QYs as a function of the

total added ethanol amount, where the QY decreases in a similar trend as observed for the photoluminescence lifetimes. In the case of 455 μL ethanol added to the NPL solution, the QY was measured to be as low as 1.42%.

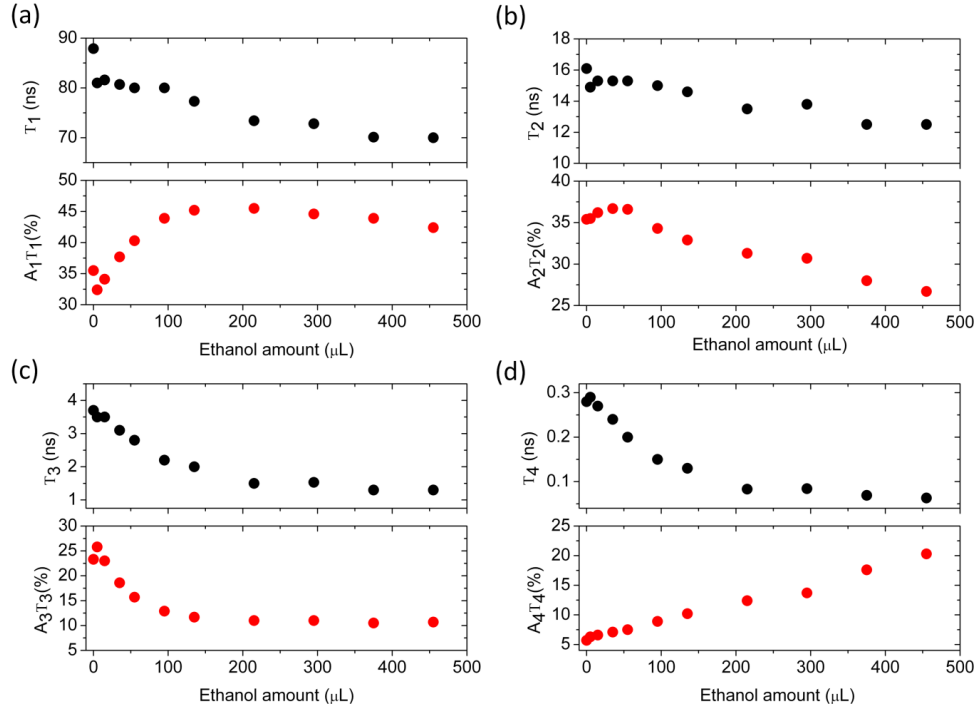


Figure 4.6. Photoluminescence lifetime components (a) τ_1 , (b) τ_2 , (c) τ_3 and (d) τ_4 , along with their contribution to the overall emission (a) $A_1\tau_1$, (b) $A_2\tau_2$, (c) $A_3\tau_3$ and (d) $A_4\tau_4$, respectively. Reprinted (or Adapted) with permission from [19]. Copyright 2014 American Chemical Society.

To understand the underpinning physics of decreased photoluminescence QYs in the stacked NPLs, we correlated the measured photoluminescence QYs to the amplitude averaged photoluminescence lifetimes as shown in Figure 4.4c. From $QY = \frac{\gamma_{radiative}}{\gamma_{total}}$, we calculated $\gamma_{radiative} \sim 0.09 \text{ ns}^{-1}$ when no ethanol was added. Then, we obtained the photoluminescence QYs as a function of the added ethanol amount utilizing the measured amplitude averaged photoluminescence lifetimes ($\gamma_{total} = \frac{1}{\tau_{total}}$) and assuming that the radiative rate ($\gamma_{radiative}$) does not change upon stacking. Except for the change of the effective dielectric medium, radiative recombination rate

is not expected to change upon stacking as observed for the other nanoemitters [114]. The calculated photoluminescence QYs are given in Figure 4.4d (black-dots). These two QYs (i.e., measured and calculated) are in a good agreement with each other. This supports that the radiative rate ($\gamma_{radiative}$) does not change upon stacking of the NPLs, whereas the nonradiative recombination rate of the excitons significantly increases. Our hypothesis is that stacking of the NPLs should lead to efficient exciton migration among the NPLs via homo-FRET, similar to the close-packed QD solids. The exciton transport via homo-FRET in the NPL stacks should strongly assist trapping of the excitons by non-emissive NPLs (i.e., defected NPLs) existing within the same population. Therefore, the nonradiative recombination channels are effectively boosted in the stacked NPL assemblies.

Addition of ethanol to the solution of the NPLs may also cause removal of the surface ligands of the NPLs, which might create a larger number of non-emissive NPLs in the population [58], [61], [142], [143]. To eliminate the possibility that addition of ethanol to the NPL solution may cause any significant effect on the decay kinetics of the NPLs, we test stacking of the NPLs without using ethanol. To this end, we incorporated the same NPLs (with a concentration of 517.61 nM) into PBMA (poly(butyl methacrylate), 1w%) insulating host polymer matrix at varying NPL/PBMA volume ratios and investigated the transient photoluminescence kinetics in the drop casted solid film samples. It has been also known that solid film formation can trigger the stacking of the NPLs due to solvent evaporation [136]. In addition, phase-segregation between the colloidal nanocrystals and the polymers is known to increase the aggregation of the colloidal nanocrystals, which would possibly cause the stacking of the NPLs [109], [144], [145]. We present the amplitude averaged photoluminescence lifetimes of the NPLs in these different solid film samples as shown in the inset of Figure 4.4c (also see the decay curves in Figure 4.7). First, by using very low density of NPLs in the polymer matrix, we intentionally prevented stacking of the NPLs via suppressing phase segregation. Therefore, the photoluminescence lifetime in the sample that has the smallest NPL/PBMA volume ratio (~ 0.015) is ~ 3 ns, which is in very good agreement with that (~ 3.38 ns) of the non-stacked NPLs in solution phase before adding any ethanol (see Figure 4.4c). This

strongly suggests that the NPLs are well-separated in the host matrix at small NPL/PBMA volume ratios. As the NPL/PBMA volume ratio was increased from 0.025 to 1, the average photoluminescence lifetime of the NPLs decreased from ~ 1 to ~ 0.3 ns, respectively (see Figure 4.4c-inset). Therefore, the lifetime span (3 ns – 0.3 ns) is successfully realized using the NPL:PBMA samples exhibiting an excellent quantitative agreement with the photoluminescence lifetimes (3.38 – 0.3 ns) of the stacking NPLs in solution phase with the addition of ethanol. Consequently, we can observe the transition from non-stacking to stacking in the photoluminescence decay kinetics of the NPLs in the NPL:PBMA samples without using any ethanol. This observation also strongly suggests that stacking is the main cause of the stark changes observed in the photoluminescence decay kinetics of the NPLs.

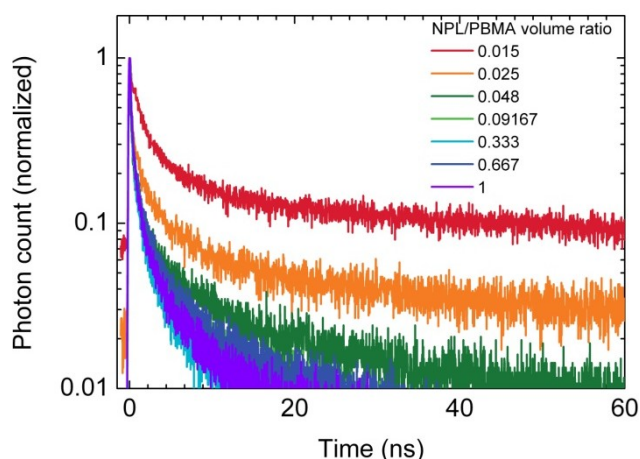


Figure 4.7. Photoluminescence decays of the NPLs in PBMA polymer host matrix in drop-casted solid thin film samples having different NPL/PBMA volume ratio. In the case of the smallest NPL/PBMA volume ratio, NPLs are well-separated in the polymer matrix as observed by their slower photoluminescence decay kinetics. As the NPL/PBMA volume ratio is increased, the photoluminescence decays become faster due to stacking of the NPLs via phase segregation in the polymer matrix. Reprinted (or Adapted) with permission from [19]. Copyright 2014 American Chemical Society.

Previously, increased exciton decay rates and quenched photoluminescence intensity were observed in dense fluorescent dye solutions [146], [147]. This was attributed to the exciton hopping among dye chromophores and quenching via non-

emissive dye dimers. Theoretically, Loring, Anderson and Fayer developed a model on homo-FRET systems and showed that these systems are prone to strong quenching due to exciton diffusion-assisted trapping [148]. Also in the stacked NPL assemblies, excitons are expected to hop back and forth between the NPLs along the column-like ordered stacked assembly due to strong near-field dipole-dipole coupling between the NPLs. There is no significant Stokes-shift (~1 nm) in the NPLs enabling a large self overlap between the emission and absorption spectra. Here, for the NPLs in the same stack, we found the Förster radius (R_0) [101], [103], the separation distance at which the exciton transfer efficiency is 50%, to be 13.48 nm. In the calculation of the Förster radius the dipole orientation term (κ^2) is generally assumed to be 2/3 due to dynamic averaging of the dipoles that are randomized by the rotational diffusion in solution. In the case of column-like oriented stacks of the NPLs, transition dipoles are expected to be both parallel and collinear. Therefore, here, κ^2 term can take its maximum value of 4 [103]. Other parameters used to predict the Förster radius are the photoluminescence QY of the NPLs of 30%, the refractive index (n) of 1.8 and the absorption cross-section of $3.1 \cdot 10^{-14} \text{ cm}^2$ at 400 nm for the 4 ML CdSe NPLs [59]. When stacked, the center-to-center distance between the NPLs was measured to be 4.29 nm using high-resolution TEM imaging (considering 1.2 nm thickness of the NPLs, oleic acid ligands has to be interpenetrating) [63], [128]. Overall, FRET efficiency was calculated to be as high as 99.9% for the exciton transfer between neighboring NPLs within the stacked assemblies. NPL-to-NPL hopping time can be as fast as ~3 ps. Therefore, excitons can hop many times among the NPLs within the stacks before either radiative or nonradiative recombination occurs. In thin film organic semiconductors, Menke *et al.* [149] described the exciton migration length (L_D) assuming isotropic transport using;

$$L_D = \sqrt{A} \frac{R_0^3}{d^2} \quad (4.1)$$

where R_0 is the Förster radius, d is the center-to-center distance between the donor-acceptor species and A is a term related to distribution of the molecular separation in the amorphous film, which is generally close to 1 [149]. Using (4.1), the calculated exciton migration length was found to be as high as 133.1 nm (± 12.0 nm) with the assumption of isotropic transport giving us a lower limit for the exciton migration

length in the stacks of the NPLs. This exciton migration length is the longest among all other colloidal semiconductor nanocrystals reported to date [14]. Therefore, this suggests that stacked NPL assemblies will be very promising for light harvesting applications owing to their ultra-long range exciton migration capability.

In the presence of ultra-long range exciton migration in the NPL stacks, quenching of the photoluminescence emission can be explained by exciton migration assisted exciton sinking in the stacked NPLs. Figure 4.8 schematically highlights the proposed exciton quenching mechanism. In the case of non-stacked NPLs, exciton recombination has its own intrinsic radiative and nonradiative channels. In the case of stacked NPLs, ultra-efficient homo-FRET in the absence of inhomogeneous broadening should not have increased the intrinsic decay rates in the NPLs unless there are exciton trapping non-emissive NPLs. In CdSe-based nanocrystals it is well known that surface defects, poorly-passivated surface sites and crystal defects could cause various exciton and charge trapping mechanisms, resulting in non-emissive nanocrystals [150]–[153]. Hole trapping in CdSe nanocrystals was found to be related to poor surface passivation and Cd vacancies and was shown to cause fast nonradiative recombination of the excitons with time constants on the order of 10 ps [154], [155]. In the CdSe NPLs, it is expected that there might arise both the surface traps and the Cd vacancies leading to inter-band hole traps states, which may rapidly quench the excitons nonradiatively [137]. Previously, blinking was also reported in the NPLs suggesting that non-emissive or dark states exist in the NPL ensembles [58], [138]. Here in Figure 4.8, a non-emissive NPL (red color) is considered to act as an exciton sink and to quench the emission of the other NPLs (yellow color) in the stack due to long range exciton transfer boosting the trapping. As the stacked assemblies grow larger, more of the NPLs are affected from the trapping since ultra-long exciton transfer range of 130 nm spans the entire/or majority of the stack. Therefore, presence of even a few non-emissive NPLs can strongly quench the photoluminescence intensity from a long NPL stack. Synthesis of NPLs for light-generation applications in the future would require minimizing the density of the non-emissive NPLs for achieving high quantum yield.

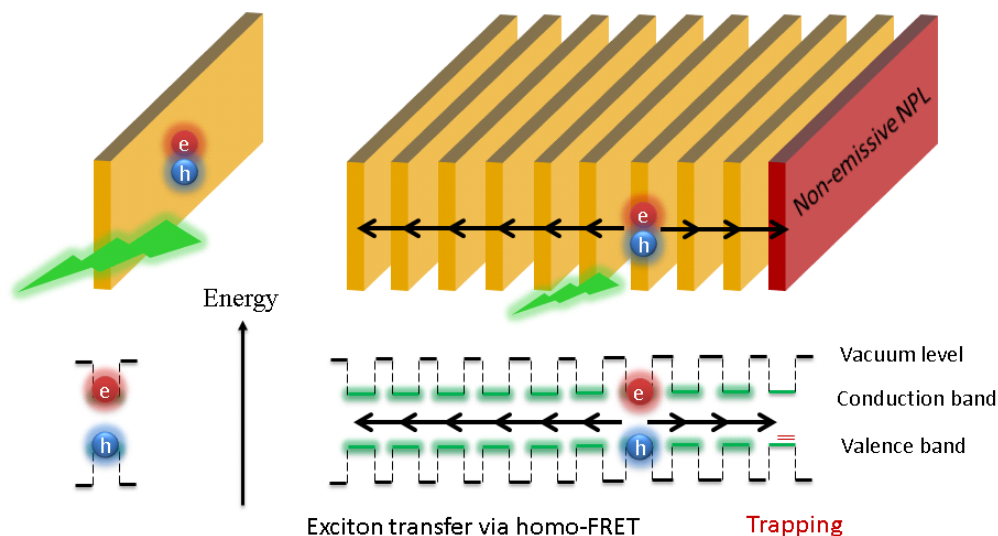


Figure 4.8. Schematic depicting the ultra-long range exciton transfer in the stacked NPL assemblies via exciton hopping through homo-FRET. The non-emissive NPL in the stack causes trapping with the assistance of long-range exciton migration causing nonradiative recombination of the excitons that quenches the photoluminescence emission of the NPLs in the stack. Reprinted (or Adapted) with permission from [19]. Copyright 2014 American Chemical Society.

To develop a deeper understanding and explain the evolution of the photoluminescence decay kinetics of the NPLs as they form into stacks, we also developed a rate equation model that accounts for the excitonic interactions in the stacked NPLs: the exciton transfer among the NPLs, the radiative recombination in the NPLs and the fast nonradiative recombination (i.e., hole trapping) at the defected NPLs. The possible excitonic pathways including the exciton transfer, the nonradiative and radiative recombination in the NPLs are schematically illustrated in Figure 4.9b for a representative stack containing four defected NPLs as shown Figure 4.9a.

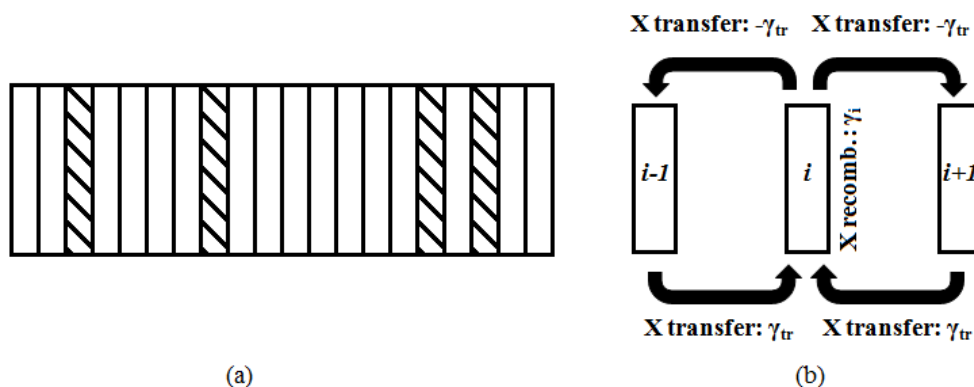


Figure 4.9. a) A sample NPL stack with 20 NPLs. The shaded spots schematically represent the defected NPLs. b) Exciton dynamics acting on the NPL located in the i^{th} index of a stack array. The recombination and other energy transfer processes related to $(i-1)^{\text{th}}$ and $(i+1)^{\text{th}}$ NPLs are not shown. Reprinted (or Adapted) with permission from [19]. Copyright 2014 American Chemical Society.

In the model, we considered the size distribution of the stacks (see Figure 4.10) as investigated via TEM imaging for three different ethanol added cases (i.e., 55, 135 and 455 μL).

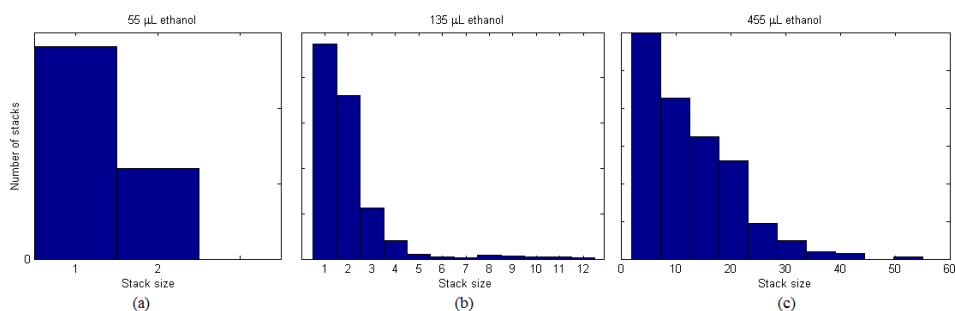


Figure 4.10. Distribution of stack size for the nanoplatelet solution mixed with a) 55 μL , b) 135 μL and c) 455 μL ethanol. Reprinted (or Adapted) with permission from [19]. Copyright 2014 American Chemical Society.

To construct the rate equations, we considered a stack with a fixed size (i.e., fixed number of NPLs), say k . In this stack, m of these NPLs were taken to be defected ($m \leq k$) depending on the fraction of the defected NPL population. Here, let n_i denote

the number of the i^{th} NPL ($i=1:k$) that is excited. The rate equations were then constructed for each NPL within the stack of a size k as:

$$\begin{aligned}
\frac{dn_1}{dt} &= -(\gamma_1 + \gamma_{tr})n_1 + \gamma_{tr}n_2 \\
\frac{dn_2}{dt} &= -(\gamma_2 + 2\gamma_{tr})n_2 + \gamma_{tr}(n_1 + n_3) \\
&\vdots \\
\frac{dn_{k-1}}{dt} &= -(\gamma_{k-1} + 2\gamma_{tr})n_{k-1} + \gamma_{tr}(n_{k-2} + n_k) \\
\frac{dn_k}{dt} &= -(\gamma_k + \gamma_{tr})n_k + \gamma_{tr}n_{k-1}
\end{aligned}
\tag{4.2}$$

Here, γ_i is the recombination rate associated with an NPL located in the i^{th} position of the stack and is defined as

$$\gamma_i = \begin{cases} \gamma + \gamma', & i = d_1, d_2 \dots \text{or } d_m \\ \gamma, & \text{otherwise} \end{cases}
\tag{4.3}$$

where γ is the effective recombination rate of the non-defected NPLs (including the radiative and the intrinsic nonradiative recombination in the non-defected NPLs). γ' is the nonradiative recombination rate in a defected NPL due to fast hole trapping. The defected NPLs can be at the positions d_1, d_2, \dots, d_m , where d_i 's refer to the locations of NPLs in the stack depending on the fraction of the defected NPL population. γ_{tr} is the exciton transfer rate between two consecutive NPLs within the same stack. The exciton transfer rate (γ_{tr}) was $(3 \text{ ps})^{-1}$ as calculated using the Förster radius and the inter-NPL separation within the stacks, the nonradiative recombination rate (γ') at the trap sites in defected NPLs is $(35 \text{ ps})^{-1}$ due to fast hole trapping [137] and the effective recombination rate (γ) is $(3.38 \text{ ns})^{-1}$.

The rate equations in (4.2) are k -first order linear homogeneous differential equations. When they are put in the matrix form, they can be expressed as follows:

$$\frac{d\bar{n}}{dt} = C\bar{n}
\tag{4.4}$$

where $\bar{n} = \begin{bmatrix} n_1 \\ n_2 \\ \vdots \\ n_k \end{bmatrix}$ and

$$C = \begin{bmatrix} -(\gamma_1 + \gamma_{tr}) & \gamma_{tr} & 0 & \dots & 0 \\ \gamma_{tr} & -(\gamma_2 + 2\gamma_{tr}) & \gamma_{tr} & \dots & 0 \\ \vdots & \ddots & \ddots & \ddots & \vdots \\ 0 & \dots & \gamma_{tr} & -(\gamma_{k-1} + 2\gamma_{tr}) & \gamma_{tr} \\ 0 & \dots & 0 & \gamma_{tr} & -(\gamma_k + \gamma_{tr}) \end{bmatrix} \text{ is the k-by-k}$$

coefficient matrix. The analytical solution can be obtained by taking the Laplace transform of both sides:

$$s\bar{N}(s) - \bar{n}(0) = C\bar{N}(s) \quad (4.5)$$

leading to $\bar{N}(s) = (s - IC)^{-1}\bar{n}(0)$.

Calculating the analytical solution was difficult since there were stacks having size >40 NPLs, as can be seen in TEM images (Figure 4.2). Therefore, we solved this set of equations numerically to find $n_1(t)$, $n_2(t)$, ..., $n_k(t)$. After this, we calculated the total emission decay as $\sum_{i=1}^k n_i(t) = n_1(t) + n_2(t) \dots + n_k(t)$. Since each NPL in a stack has the same probability of absorbing a photon as each other, the initial condition $\bar{n}(0)$ has been set by assigning random integers uniformly distributed in the same interval to $n_i(0)$'s. The solution $\sum_{i=1}^k n_i(t)$ becomes a multiexponential decay. Consequently, we calculated the average lifetime for the total emission decays.

The recombination rate of a NPL was determined by whether a NPL has a trap site (i.e., it is defected) or not. Hence, the ‘‘properties’’ of a stack were determined by the number of NPLs it has, say k , and which of these NPLs are defected. Let $D = \{d_1, d_2, \dots, d_m\}$ denote the set containing the locations of all the defected NPLs in the stack, where m is the number of defects. d_1, d_2, \dots, d_m are simply integers denoting at which index the defects are located in the NPL array. Therefore, a separate set of rate equations were constructed for each collection of stacks having different k and/or D . The decay for the whole ensemble was determined by solving the rate equations for every possible subset of stacks having common properties (i.e. k and D), and adding up each solution. However, we should also determine the distribution of different NPL sizes in an

ensemble as well as how the defects are distributed in stacks. To determine the stack size distribution in an ensemble, TEM images were carefully analyzed to find the distribution of the stack size (see Figure 4.10). Weight constants have been assigned for different stack sizes to account for the analyzed distribution. We assumed that defected NPLs should be randomly distributed in a stack. We used MATLAB's 'ode23' function, which is a numerical differential equation solver, to solve the rate equations for the time interval $0 \leq t \leq 40$ ns with a fixed time step of 4 ps. The solution is in the form $s(t) = \sum A_i e^{-t/\tau_i}$, where $s(t)$ is the total emission decay coming from a subset of stacks. The average lifetime for the emission of the stack is

$$\tau_{stack} = \frac{\sum A_i \tau_i}{\sum A_i} \quad (4.6)$$

The quantities in the numerator and denominator can be calculated without having to calculate individual lifetimes and amplitudes because $\sum A_i \tau_i$ is simply the area under the solution curve, i.e.,

$$\sum A_i \tau_i = \int_0^{\infty} s(t) dt \quad (4.7)$$

Similarly, the sum of amplitudes of all exponential components is simply the value of the solution at the first time instant, i.e.,

$$\sum A_i = s(0) \quad (4.8)$$

so that

$$\tau_{stack} = \frac{\int_0^{\infty} s(t) dt}{s(0)} \quad (4.9)$$

Note that the average lifetime calculation involved only a particular subset of stacks. We proceed to involve all other stacks, obtain $\sum A_i \tau_i$ and $\sum A_i$ summations from them as well, collecting all $\sum A_i \tau_i$ terms on the numerator and all $\sum A_i$ terms on the denominator to find the average photoluminescence lifetime that can be associated for

the whole ensemble. We solved the set of differential equations for varying size and distribution of stacks for 10,000 times to achieve the averaged results.

The last parameter to determine was the fraction of the defected NPL population (r) within the whole NPL population. Depending on the synthesis route, the NPL populations may include NPLs having hole-trap sites. A recent report has also revealed that a varying fraction of the CdSe NPLs may contain hole traps as observed by time-resolved fluorescence and pump-probe transient absorption measurements [62]. To find the percentage of the defected NPL population (r), we swept this parameter to match the modeled lifetime with the experimental lifetime of the 55 μL ethanol added case. We chose 55 μL ethanol added case due to its simple stack size distribution consisting of stacks either only one or two nanoplatelets (see Figure 4.10). The resulting fraction of the defected NPL population was found to be $r = 0.22$. We used the same defected NPL population fraction for all of the three cases (i.e., 55, 135 and 455 μL).

Using the model we calculated the photoluminescence lifetimes of the stacked NPL ensembles in 55, 135 and 455 μL ethanol added cases as 2.32, 1.26 and 0.306 ns, respectively. These calculated lifetimes are shown in Figure 4.4c with blue stars together with the no ethanol added case as a trivial solution. The lifetimes calculated by the model exhibited an excellent agreement with the experimental lifetimes for the three ethanol added cases of 55, 135 and 455 μL , which were measured to be 2.16, 1.13 and 0.30 ns, respectively. The error between the modeled lifetimes and the experimental lifetimes is less than 12%. This excellent agreement between the model and the experiment in three different stacked NPL ensembles exhibits a vigorous support for the hypothesis that homo-FRET assisted exciton trapping and nonradiative recombination are the dominant excitonic effects in the stacking NPLs. Furthermore, the fraction of the defected NPL population ($r = 0.22$) works very well for all of three cases, and this elucidates that adding ethanol does not cause additional nonradiative trap sites.

As an alternative mechanism to exciton hopping via FRET, radiative energy transfer (RET) between the NPLs in the stacks is possible. RET is difficult to

distinguish from the FRET in steady state measurements [156]. The small difference between the calculated and experimental quantum yields (see Figure 4.4d) could be probably explained due to the presence of RET. However, investigation of the transient photoluminescence kinetics and modeling as a function of controlled stacking strongly suggests that the dominant exciton transport mechanism is based on nonradiative exciton transfer (i.e., homo-FRET). RET, alternatively, can support the transport of the excitons among the different stacks of the NPLs since FRET would not be efficient among the NPLs within different NPL stacks due to large lateral sizes (i.e., 10 nm or larger) limiting the exciton hopping between different stacks.

4.2.4 Summary

As a summary, we demonstrated controlled stacking of the NPLs that exhibit different steady state and transient excitonic properties as compared to the non-stacked NPLs. First, photoluminescence quantum yield and lifetime were decreased by an order of magnitude when long column-like stacks of the NPLs are formed. These observations were well explained by the ultra-long exciton transfer among the NPLs within the stacked assembly owing to ultra-efficient homo-FRET. However, exciton transport increases trapping of the excitons by non-emissive NPLs, acting as exciton sinks. This causes the strong quenching of the photoluminescence and acceleration of the decay rates. The exciton transfer in the NPLs exhibited different signatures as compared to the colloidal quantum dots due to the absence of inhomogeneous broadening in the NPLs. These observations include no red-shift and fixed emission line-width despite ultra-efficient exciton transfer. Moreover, we developed a rate equation based model that strongly agrees with the observed changes in the photoluminescence decay kinetics explained by ultra-efficient exciton transfer assisted exciton trapping in the NPL stacks due to the presence of defected NPLs. Overall, the results show the critical significance of stacking control in NPL solids for efficient light generation and harvesting.

4.3 Nonradiative energy transfer in nanoplatelet films

This section is based on the publication “Nonradiative energy transfer in colloidal CdSe nanoplatelet films,” **B. Guzelturk**, M. Olutas, S. Delikanli, Y. Kelestemur, O. Erdem, and H. V. Demir, *Nanoscale* 7, 2545-2551 (2015). Adapted (or “Reproduced in part”) with permission from The Royal Society of Chemistry. Copyright 2015 The Royal Society of Chemistry.

4.3.1 Motivation

To date, CdSe NPLs having zinc blende crystal structure have been the most extensively studied type among other types of NPLs thanks to their optimized synthesis route resulting in high quality NPLs having a magic sized vertical thickness with reasonably uniform lateral size distribution [57], [157]. The vertical thickness of the NPLs is denoted by the number of monolayers of the repeating lattice units. Commonly synthesized vertical thickness of the CdSe NPLs ranges from 3 to 6 MLs. The peak emission wavelength of 3, 4 and 5 ML CdSe NPLs corresponds to 463, 513 and 551 nm, respectively, with emission full-width at half-maxima (FWHM) as narrow as 8 nm at room temperature.

Previously optical properties of the NPLs have been studied both in solution and solid phases. In the case of solid thin films, either ensemble or single NPL based studies have been reported [58], [61], [63], [65], [137], [158], [159]. However, in all of these previous reports only a single population of NPL emitter having a fixed vertical thickness was considered and investigated. On the other hand, it is widely known that nonradiative energy transfer, also commonly referred to as FRET [101], can take place within the close-packed assemblies of semiconductor nanostructures (e.g., colloidal nanocrystals and nanorods) with different sizes through near field dipole-dipole coupling [126], [128], [160], [161]. Therefore, it is expected to realize NRET in close-packed solid films incorporating NPL populations, each of a different vertical

thickness. However, NRET has not been systematically studied nor demonstrated in the solid assemblies of the NPLs having different vertical thicknesses to date.

4.3.2 Experimental

For the synthesis of the 4 ML thick NPLs; 170 mg of cadmium myristate, 12 mg of selenium and 15 mL of octadecene (ODE) were loaded into a three-neck flask. After evacuation of the mixed solution at room temperature, it was heated to 240⁰C under inert atmosphere. When the temperature reaches 195⁰C, the color of solution becomes yellowish. Then, 80 mg of cadmium acetate dihydrate was introduced. After 10 mins growth of CdSe NPLs at 240⁰C, the reaction was stopped and cooled down to room temperature with the injection of 0.5 mL of oleic acid (OA). The resulting 4 ML CdSe NPLs were separated by other reaction products with successive purification steps.

For the synthesis of the 5 ML thick NPLs; 170 mg of cadmium myristate and 15 mL of ODE were loaded into a three-neck flask. After evacuation of solution at room temperature, the solution was heated to 250⁰C under inert atmosphere. 12 mg of Se dispersed in 1 ml ODE was swiftly injected. 80 mg of cadmium acetate dihydrate was introduced one minute later. After 10 minutes growth of CdSe NPLs at 250⁰C, the reaction was stopped and cooled down to room temperature with the injection of 0.5 mL of OA. 5 ML CdSe NPLs were separated by other reaction products with the successive purification steps.

For the purification and size-selective precipitation of the nanoplatelets; as-synthesized NPLs were centrifuged at 4500 rpm for 5 min. The supernatant solution was removed from the centrifuge tube. The precipitate was dried under nitrogen and dissolved in hexane and centrifuged again at 4500 rpm for 10 min. The supernatant was used for the further process. Ethanol was added into the supernatant solution until it became turbid. Then, the turbid solution was centrifuged at 4500 rpm for 10 min. The precipitate was dissolved in hexane and filtered with 0.20 micrometer filter.

For the preparation of the solid NPL thin films; the concentration of the 4 and 5 ML NPL solutions was calculated as 7.976×10^{-7} and 4.493×10^{-8} M, respectively. Samples of 4-5 ML NPL solutions having different acceptor-to-donor (A:D) molar ratios, mixed using ultrasonication for 5 min, were prepared. The quartz substrates of 1.5 by 1.5 cm in size were cleaned using piranha solution for 30 min and rinsed with DI-water and dried in an oven at 80°C for 30 min. The mixed NPL solid thin films were prepared using spin-coating the mixed solutions at 2000 rpm for 1 min.

For the steady state and time-resolved optical characterizations; steady state photoluminescence spectra and photoluminescence excitation spectra were collected using Cary Eclipse Fluorescence Spectrometer. Photoluminescence quantum yield measurements were performed in solution phase using Rhodamine 6G reference dye. Confocal microscopy images were collected using Zeiss LSM 510. Ar laser line at 458 nm was employed as the excitation source for the confocal imaging. Time-resolved fluorescence decay kinetics were measured using PicoQuant FluoTime 200 that employ PicoHarp 300 time-correlated single photon counting (TCSPC) unit and a picosecond pump laser at 375 nm. Fluorescence decay curves were fitted by using FluoFit program using multi-exponential decay functions.

4.3.3 Results and discussion

In this part of the thesis, we presented the first spectroscopic evidence of NRET within the solid films of CdSe NPLs of different vertical thicknesses (i.e., 4 and 5 ML). We systematically investigated NRET as a function of the donor-to-acceptor ratio via time resolved and steady state fluorescence spectroscopy, which conclusively revealed the existence of NRET from 4 to 5 ML NPLs. Furthermore, the NRET efficiency was analyzed and it was found to be limited to ~60%. This limitation is understood by investigation of the morphology of the mixed solid thin films, where stacking of the donor and acceptor NPLs within their own population results in to a nanoscale phase segregation between the donor-acceptor pairs. This type of phase segregation has not

been observed in the mixed donor-acceptor pairs of the colloidal quantum dots and rods.

CdSe NPLs with 4 and 5 ML vertical thicknesses exhibiting 30-50% photoluminescence quantum yield were synthesized using a modified recipe and dissolved in hexane (see Experimental) [56]. The absorption (dashed) and photoluminescence (solid) spectra of the synthesized 4 and 5 ML NPLs are shown in Figure 4.11. Absorbance of the NPLs exhibits pronounced sharp features corresponding to the electron/light-hole (480 nm for 4 ML and 518 nm for 5 ML) and the electron/heavy-hole (512 nm for 4 ML and 549 nm for 5 ML) transitions characteristic to the NPLs [57]. During the synthesis of 4 and 5 ML NPLs, quantum dots and/or NPLs with different vertical thickness could be also possibly synthesized as a side product. However, using size selective precipitation via ultracentrifugation it is possible to totally eliminate these side products. As shown by the absorbance of the NPL solutions after size selective precipitation in Figure 4.11, there was no contribution from the side products. Therefore, we were able to achieve NPL solutions containing only single NPL population. In these NPLs, radiative recombination takes place at the electron/heavy-hole transition resulting in the peak emission wavelength at 513 nm from 4 ML NPLs and 551 nm from 5 ML NPLs, both with FWHM of ~8 nm as shown by Figure 4.11.

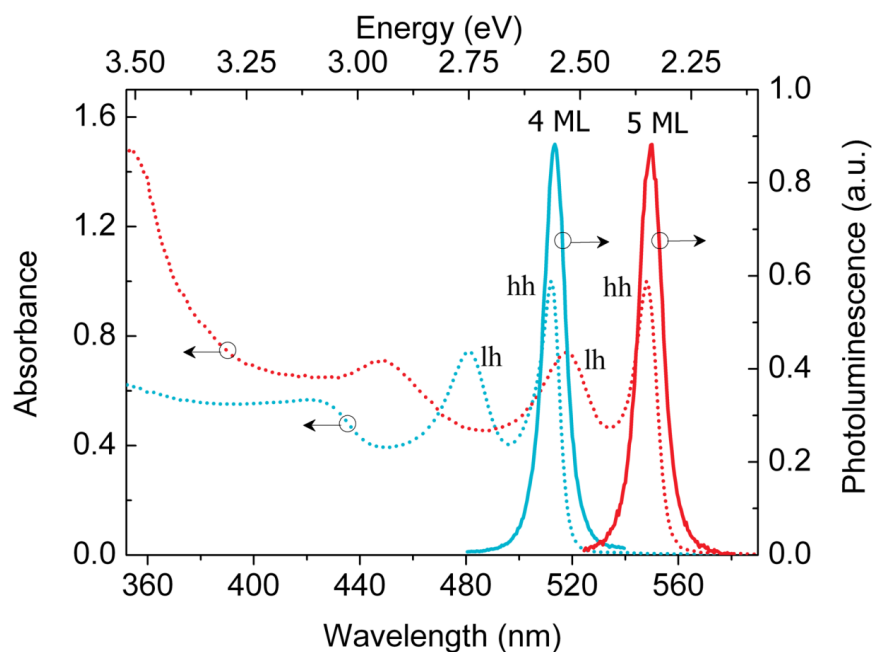


Figure 4.11. Absorption (dashed lines) and photoluminescence (solid lines) of the 4 ML (cyan) and 5 ML (red) NPLs. Reprinted with permission from The Royal Society of Chemistry [68]. Copyright 2015 The Royal Society of Chemistry.

High-angle annular dark field transmission electron microscopy (HAADF-TEM) was utilized to image the 4 and 5 ML NPLs on carbon coated ultrathin copper grids as shown in Figure 4.12a and Figure 4.12b, respectively. The average size of the 4 ML NPLs was 23.57 nm (\pm 2.90 nm) by 12.17 nm (\pm 1.94 nm), and that of 5 ML NPLs was 26.32 nm (\pm 2.55 nm) by 9.04 nm (\pm 1.41 nm). Both NPLs were observed to form stacks on TEM grids, as can be observed in Figure 4.12, which has been previously observed in the literature [63], [136]. Stacking of the NPLs can be triggered during the solid film formation.

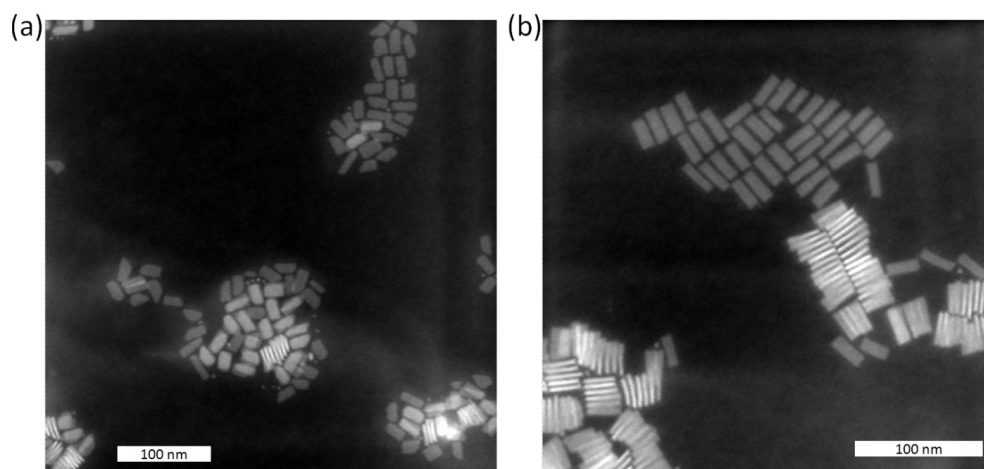


Figure 4.12. HAADF-TEM images of the NPLs of (a) 4 ML having the average size of 23.57 nm (\pm 2.90 nm) by 12.17 nm (\pm 1.94 nm) and (b) 5 ML having the average size of 26.32 nm (\pm 2.55 nm) by 9.04 nm (\pm 1.41 nm). Stacking of the NPLs is clearly visible in both NPL populations. The scale bars are 100 nm. Reprinted with permission from The Royal Society of Chemistry [68]. Copyright 2015 The Royal Society of Chemistry.

NPLs were transferred to solid thin films via spin-coating them on pre-cleaned quartz substrates. The surface coverage and homogeneity of the mixed NPL thin film samples were inspected via confocal microscopy using pump laser as Ar-ion laser line at 458 nm, which can pump both of the NPL populations simultaneously. Figure 4.13 presents exemplary case of mixed thin film sample having acceptor-to-donor molar ratio of 0.28. Figure 4.13a shows the confocal image of the sample when the collection channel was located in the spectral range of 505-530 nm matching only the emission of 4 ML NPLs. Figure 4.13b shows the confocal image of the same location of the same sample when the collection channel was located in the spectral range of 560-615 nm matching only the emission of 5 ML NPLs. Both confocal images indicate very high surface coverage and film uniformity owing to the observation of homogenous emission all around the sample surface except a few brighter spots indicating aggregation. Therefore, the spin-coated samples were highly homogenous at the micron scale. However, as we will discuss later, we observed stacking of the NPLs via TEM imaging leading to a nanoscale phase separation between the 4 and 5 ML NPLs.

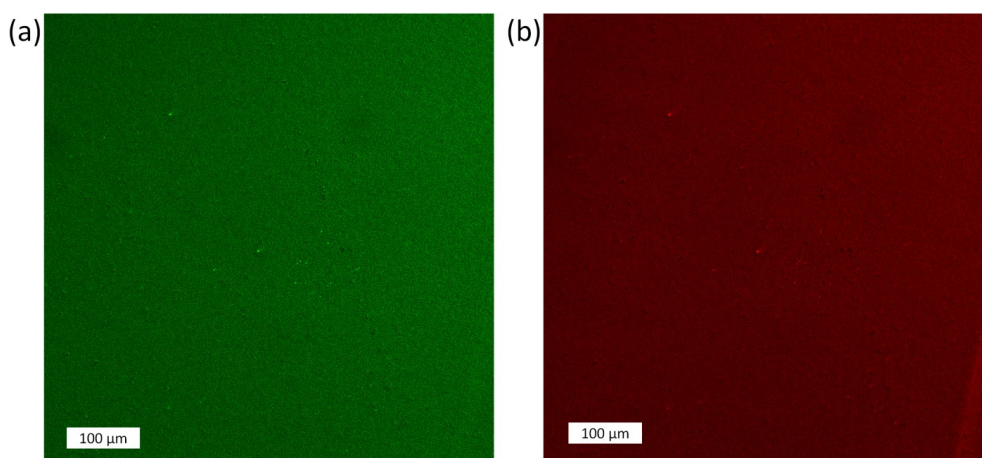


Figure 4.13. Confocal images of the mixed solid films of the 4 and 5 ML NPLs. The collection window is (a) 505-530 nm matching only the emission of 4 ML NPLs, (b) 560-615 nm matching only with the emission of 5 ML NPLs. In both images, artificial coloring is used to represent the emission intensity. The scale bar is 100 μm . Reprinted with permission from The Royal Society of Chemistry [68]. Copyright 2015 The Royal Society of Chemistry.

For the NRET study, we prepared eight solid thin film samples. Two of these were the only donor and only acceptor reference samples and rest of them were the mixed samples having different acceptor-to-donor (A:D) molar ratios. We then performed time resolved fluorescence spectroscopy on these samples as shown by the fluorescence decay curves in Figure 4.14. Figure 4.14a and Figure 4.14b depict the fluorescence decay curves of the 4 and 5 ML NPLs, respectively, for different samples with varying A:D ratio, which was calculated by using Beer-Lambert law. The concentration of the donor and acceptor NPLs was calculated to be 7.976×10^{-7} and 4.493×10^{-8} M using the absorption cross sections (at 3.1 eV) of 3.1×10^{-14} and 2.5×10^{-13} cm^2 , respectively [58], [59]. In Figure 4.14a, as the A:D ratio is increased, the donor NPLs are observed to decay faster. This indicates a new decay channel, of energy transfer, being opened up for the donor NPLs as the density of the acceptor NPLs is increased. In the case of decay kinetics of the acceptor 5 ML NPLs, we observed that the fluorescence decay was slowed down compared to the decay of the only acceptor solid film. As frequently observed for the colloidal quantum dot based

acceptors, elongation of the fluorescence decay indicates the presence of exciton feeding via NRET into acceptor material [97].

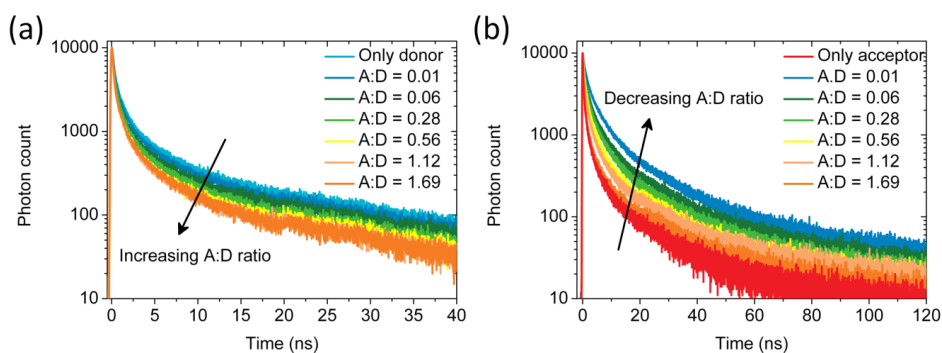


Figure 4.14. Time resolved fluorescence spectroscopy of the (a) 4 ML and (b) 5 ML NPLs in their solid thin films. Reprinted with permission from The Royal Society of Chemistry [68]. Copyright 2015 The Royal Society of Chemistry.

The fluorescence decay of the NPLs exhibited multi-exponential decay behavior as attributed to the complex decay kinetics of these materials [58]. Generally, three or four exponential decay functions were employed in the literature to fit the fluorescence decay of the NPLs. In this work, we employed four exponential decay functions and fit the fluorescence decay curves in Figure 4.14 with near unity reduced χ^2 and uniform residuals (see Table 4.1 and

Table 4.2 for the fluorescence lifetime components and their fractional contributions). A possible approach to handle multi-exponential decay kinetics is to use amplitude averaged fluorescence lifetimes, although this does not fully capture the individual decay kinetics. Previously, amplitude averaged fluorescence lifetimes were also employed to investigate the NRET kinetics in the case of donors having intrinsic multi-exponential decay channels [103]. Therefore, for the further analysis of the NRET rates

and efficiencies, we employed the amplitude averaged fluorescence lifetimes as presented in Table 4.3.

As shown in Table 4.1 and

Table 4.2, all of the fluorescence decay components are altered due to NRET. This suggests that all of the complex fluorescence decay channels were affected due to the presence of nonradiative energy transfer. As the A:D ratio was increased from 0.01 to 1.69 (see Figure 4.14), we observed that the donor fluorescence decay curves became progressively faster (i.e., the fluorescence lifetime of the donor NPLs shortens). This can be explained with the increase in number of the acceptor NPLs per donor NPL. It is also important to note that for the A:D ratios above 0.56, we observed that the donor decay curves did not change noticeably. This indicates a saturation of NRET process between these donor-acceptor pairs. In the case of acceptor decays in Figure 4.14b, the acceptor lifetime is elongated as high as by 6-folds (see

Table 4.3.) in the case of small A:D ratios, where there are a large number of donor NPLs per acceptor NPL.

As the A:D ratio is increased, the acceptor decays converge to the decay of the only acceptor thin film since the number of donors per acceptor is considerably decreased. Therefore, most of the acceptors are excited directly via pump laser instead of NRET pumping, although all of the available donor NPLs, which are less in number, are transferring at a maximum rate. This shows that, from the acceptor point of view, exciton feeding becomes insignificant at high A:D ratios. As shown in

Table 4.3., NRET rates were also calculated for different A:D ratios, where the predicted NRET rate can be as high as 1.193 ns^{-1} .

Table 4.1. Fluorescence decay components of the donor 4 ML NPLs.

TRF Decay Components								
Acceptor – Donor Ratio (A:D)	τ_1 (ns)	τ_2 (ns)	τ_3 (ns)	τ_4 (ns)	$A_1\tau_1$ (%)	$A_2\tau_2$ (%)	$A_3\tau_3$ (%)	$A_4\tau_4$ (%)
Only donor	64.0	11.8	1.8	0.25	27.6	31.8	23.6	17.0
0.01	63.0	10.9	1.7	0.22	27.9	30.9	23.2	18.0
0.06	60.0	10.4	1.5	0.20	27.1	29.8	22.8	20.2
0.28	59.1	10.5	1.6	0.22	22.5	28.2	25.3	24.0
0.56	55.0	9.4	1.4	0.16	23.3	27.4	23.6	25.6
1.12	53.0	8.8	1.2	0.14	21.5	27.3	25.5	25.7
1.69	49.0	8.2	1.3	0.16	20.8	28.2	25.4	25.5

Table 4.2. Fluorescence decay components of the acceptor 5 ML NPLs.

TRF Decay Components								
Acceptor – Donor Ratio (A:D)	τ_1 (ns)	τ_2 (ns)	τ_3 (ns)	τ_4 (ns)	$A_1\tau_1$ (%)	$A_2\tau_2$ (%)	$A_3\tau_3$ (%)	$A_4\tau_4$ (%)
Only acceptor	52.1	8.2	1.3	0.19	19.1	30.0	26.7	24.2
0.01	87.0	16.6	4.5	0.75	19.7	34.6	35.1	10.6
0.06	76.5	13.3	3.0	0.43	20.4	37.3	31.4	10.9
0.28	67.4	11.5	2.6	0.42	19.0	36.2	32.0	12.8
0.56	75.5	12.9	2.6	0.45	17.3	31.1	33.6	18.0
1.12	77.9	12.5	2.3	0.36	20.6	29.8	30.5	19.0
1.69	64.0	11.0	1.7	0.23	20.7	29.1	27.2	23.0

Table 4.3. Amplitude averaged fluorescence lifetimes of the donor and acceptor NPLs for the samples having varying A:D ratio. Predicted NRET rates (ns^{-1}) are also presented.

Acceptor – Donor Ratio (A:D)							
	Only donor (or acceptor)	0.01	0.06	0.28	0.56	1.12	1.69
τ_{donor} (ns)	1.18	1.02	0.84	0.78	0.57	0.49	0.54
τ_{acceptor} (ns)	0.66	4.13	2.59	2.15	1.79	1.47	0.83

NRET Rate (ns ⁻¹)	-	0.133	0.343	0.435	0.907	1.193	1.00
----------------------------------	---	-------	-------	-------	-------	-------	------

Additionally, we employed photoluminescence excitation (PLE) spectroscopy to investigate the steady state evidence of NRET in these mixed NPL solid thin films. We measured the PLE spectra of the only donor and only acceptor thin film samples while monitoring the peak emission wavelength of the 4 and 5 ML NPLs, respectively, as shown in Figure 4.15a. These PLE spectra highly resemble absorption spectra of these NPLs (see Figure 4.11). Spectral features observed at 480 and 518 nm correspond to the electron/light-hole transitions in 4 and 5 ML NPLs, respectively. Figure 4.15b shows the evolution of the PLE curves measured at the peak emission wavelength of the acceptor (5 ML NPLs), as the A:D ratio in the mixed samples was changed from 0.01 to 1.69, together with the PLE of the only acceptor sample. Here, we normalized the PLE curves at 530 nm, since there is no contribution from the donor NPLs at this wavelength (i.e., neither absorption nor neither emission). In Figure 4.15b, at small A:D ratios, where there are a large number of donors per acceptor, we observed emerging spectral features in the PLE spectrum of the acceptor emission, which can be attributed to the NRET from the donor NPLs.

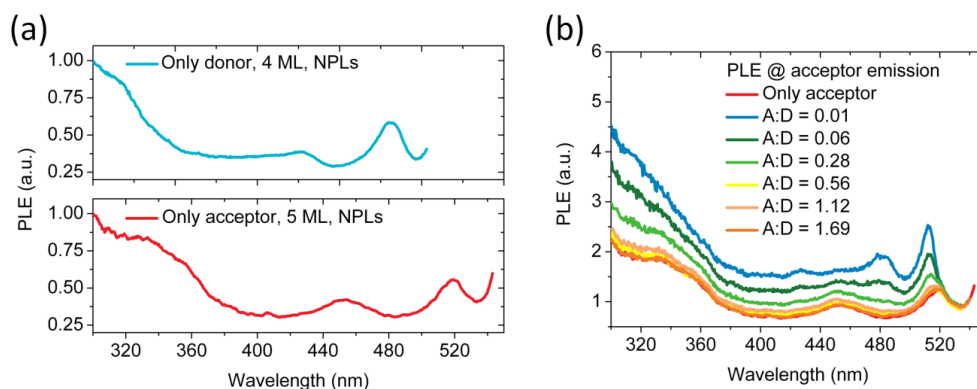


Figure 4.15. (a) Photoluminescence excitation spectra of the 4 and 5 ML NPLs featuring the electron/light-hole and continuum bands. (b) Enhancement of the 5 ML NPL PLE owing to the NRET from the 4 ML NPLs. Reprinted with permission from The Royal Society of Chemistry [68]. Copyright 2015 The Royal Society of Chemistry.

To understand the origin of the newly emerged spectral features in Figure 4.15b, we calculated the spectral enhancement of the PLE curves in the mixed samples normalizing with respect to the only acceptor sample. The resulting curves are presented in Figure 4.16. We observed that the spectral enhancement resembles the PLE spectrum of the donor NPL. The features observed around 510 and 480 nm correspond to the electron/heavy-hole and electron/light-hole transitions in the donor 4 ML NPLs. This indicates that across spectral ranges where the donor NPLs are better excited, the energy transfer into the acceptor NPLs becomes stronger and more efficient. In addition, at the higher photon energy tail of 480 nm peak, there is enhancement of the PLE due to the continuum absorption states in the donor NPLs. The largest enhancement of the PLE of the acceptor NPLs was achieved when the donors are 100× of the acceptors (corresponding to the A:D ratio of 0.01) due to presence of abundant donor NPLs increasing the probability of the funneling excitons into the acceptor NPLs. At small A:D ratios, the dominant excitation mechanism of the acceptor NPLs is through NRET since PLE enhancement factor as high as 2.8-folds could be achieved. As the A:D ratio is increased, we observed that enhancement of the PLE gradually diminishes since the number of donors per acceptor is concomitantly decreased. At these large A:D ratios, the acceptor NPLs are dominantly excited via the pump light instead of being excitonically pumped by NRET from the donor NPLs since the PLE enhancement factor is close to 1 in this range.

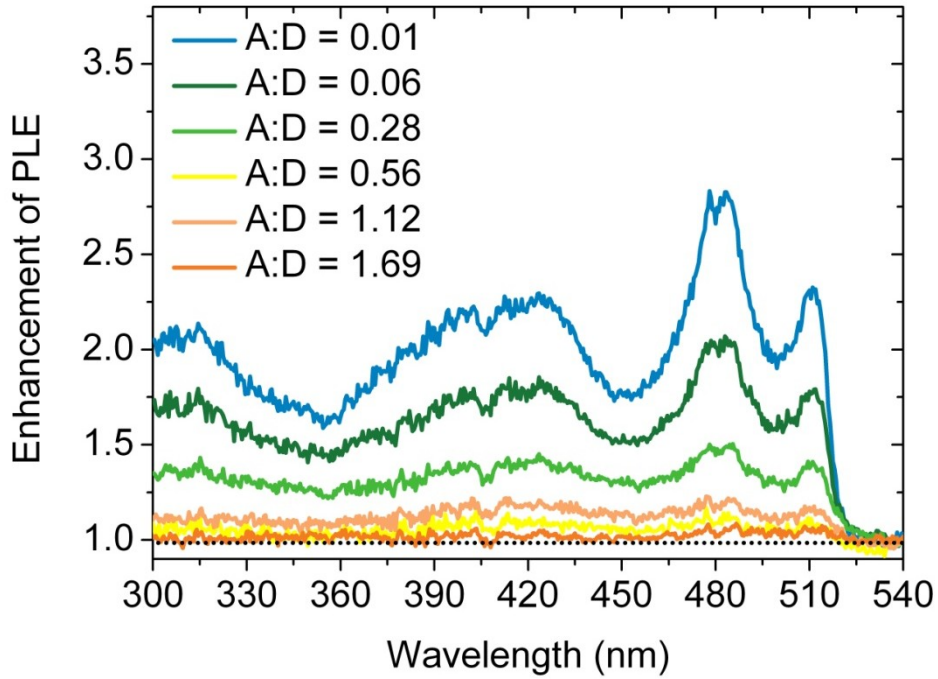


Figure 4.16. Enhancement of the acceptor NPL emission excitation exhibiting spectral features resembling the spectral PLE features of the donor NPLs. At small A:D ratios, the dominant excitation mechanism of the acceptor NPLs is through NRET, whereas at large A:D ratios the acceptor NPLs are dominantly excited through direct absorption of the pump photons. Reprinted with permission from The Royal Society of Chemistry [68]. Copyright 2015 The Royal Society of Chemistry.

Figure 4.17 shows the NRET efficiency as a function of the A:D ratio as computed as follows:

$$\gamma_{donor} = \gamma_{radiative} + \gamma_{nonradiative}$$

$$\gamma_{donor_with_acceptor} = \gamma_{radiative} + \gamma_{nonradiative} + \gamma_{NRET}$$

$$\eta_{NRET} = 1 - \frac{\tau_{donor_with_acceptor}}{\tau_{donor}} \quad (4.10)$$

Here, γ_{donor} ($= \frac{1}{\tau_{donor}}$) is the fluorescence decay rate of the donor NPLs in the absence of acceptors. $\gamma_{radiative}$ and $\gamma_{nonradiative}$ are the intrinsic radiative and nonradiative decay rates of the donor NPLs, respectively. $\gamma_{donor_with_acceptor}$

($= \frac{1}{\tau_{donor_with_acceptor}}$) is the fluorescence decay rate of the donor NPLs in the presence of acceptors. γ_{NRET} is the rate of the NRET process and η_{NRET} is the efficiency of the NRET. Because of the architecture and dimensionality of the NPLs, the NRET efficiency is expected to be large since the close-packing in NPL assemblies would be achieved owing to the small magic sized vertical thickness (3 ML \sim 0.9 nm, 4 ML \sim 1.2 nm, 5 ML \sim 1.5 nm) of the NPLs. In our case, however, NRET efficiencies were observed to be limited to 60% as given in Figure 4.17. Based on Coulombic dipole-dipole coupling, we computed the Förster radius [103] to be 10.83 nm between the donor-acceptor pairs using the following parameters. The extinction coefficient of 5 ML NPLs at 500 nm is calculated as $4.86 \times 10^7 \text{ M}^{-1} \text{ cm}^{-1}$, the quantum yield of the donor NPLs as 10%, the dipole orientation factor (κ^2) as 2/3 assuming random transition dipole orientations and the refractive index of the medium as 1.8. If the 4 and 5 ML NPLs were to perfectly assemble in the form of inter-mixed stacks (similar to two bunches of poker cards well mixed together), then the donor-to-acceptor separation distance would be expected to be comparable to 4 nm on the average due to interpenetrating ligands as previously demonstrated by small-angle x-ray scattering measurements (SAXS) [63], [136]. Therefore, NRET greater than 95% would have been possible in these solid films in the case of perfect inter-stacking. On the other hand, we experimentally observed the saturation of the NRET efficiencies below such high efficiency level.

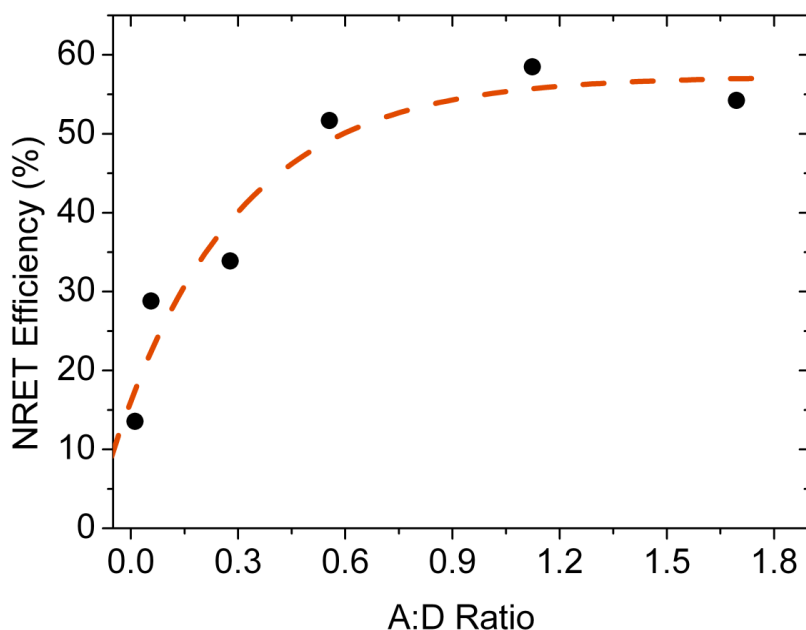


Figure 4.17. NRET efficiency as a function of A:D ratio. Reprinted with permission from The Royal Society of Chemistry [68]. Copyright 2015 The Royal Society of Chemistry.

To understand the possible reason of this limited NRET, we synthesized 5 ML NPLs that intentionally contain ~5% of 4 ML NPLs as a side product of the synthesis (i.e., a mixed NPL solution containing 5 ML NPLs with a population of ~95%). This time we did not perform size selective precipitation such that these mixed NPL populations stayed together. Then, we casted the mixed solution on TEM grids to investigate their solid film assemblies via TEM imaging. Here, the 4 ML NPLs had the square-like shape with an average size of 10.81 nm (± 0.53 nm) and the 5 ML NPLs had a rectangle-like shape with an average size of 43.67 nm (± 3.31 nm) and 12.94 nm (± 1.51 nm) (see Figure 4.18). We observed stacking of the NPLs within their own population. Figure 4.19 demonstrates the HAADF-TEM image of the mixed solid film together with the representative cartoon to illustrate the limitation of the NRET resulting from the nanoscale phase segregation between the donor and acceptor NPL populations due to their self-stacking. Here NRET is found limited with the longer lateral size of the NPLs, which is on the order of 10 nm, since it is not possible to achieve inter-mixed stacked assemblies of the different populations of NPLs, but

instead the mixture of the self-stacked assemblies. Due to this nanoscale phase segregation, NRET efficiencies were limited to ~60% corresponding to almost average separation about the Förster radius (i.e., 10.83 nm), which matches well with the center-to-center separation of 10.61 nm ($0.5 \times 12.17 \text{ nm} + 0.5 \times 9.04 \text{ nm}$) between two adjacent donor and acceptor NPLs. A similar type of phase segregation has been also observed in the conjugated polymer – colloidal quantum dot based hybrids limiting the NRET in those organic–inorganic assemblies [109], [144]. Due to this larger separation between the donor and acceptor species, higher order multi-polar interactions are not expected to be significant [105].

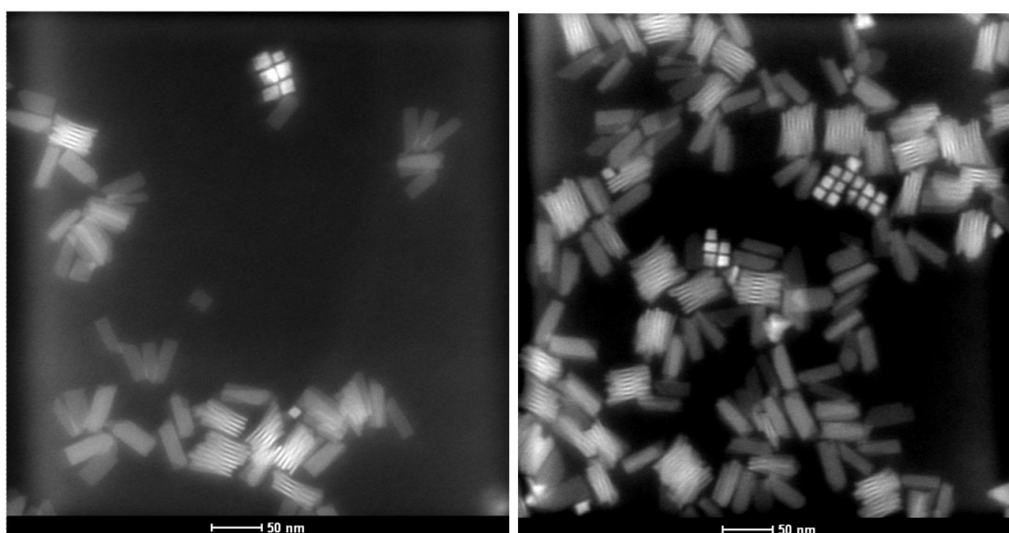


Figure 4.18. HAADF-TEM images of mixed NPL populations incorporating 2-3% 4 ML NPLs while the rest of the NPLs are 5 ML. 4 ML NPLs have the square-like shape with an average size of 10.81 nm ($\pm 0.53 \text{ nm}$) and 5 ML NPLs have the rectangle-like shape with an average size of 43.67 nm ($\pm 3.31 \text{ nm}$) and 12.94 nm ($\pm 1.51 \text{ nm}$). Reprinted with permission from The Royal Society of Chemistry [68]. Copyright 2015 The Royal Society of Chemistry.

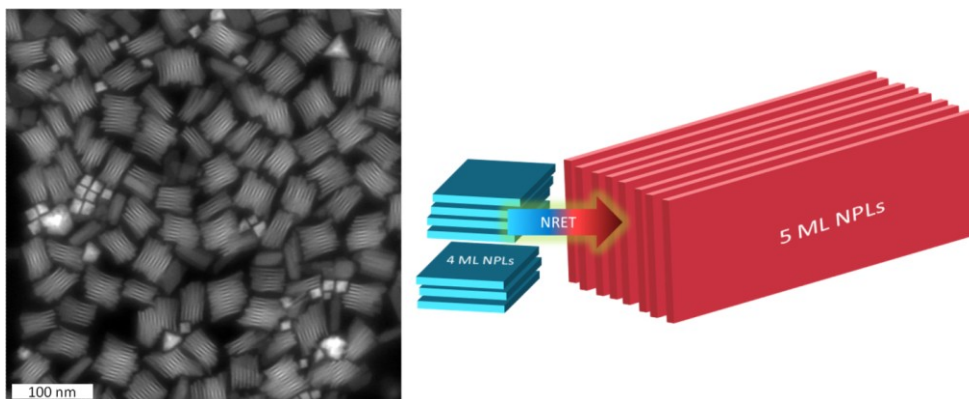


Figure 4.19. HAADF-TEM image of the mixed NPL assembly (without size selective precipitation) of square-like 4 ML NPLs and rectangle-like 5 ML NPLs. Schematic of the NRET as limited by the nanoscale phase segregation between the NPLs of different populations. Reprinted with permission from The Royal Society of Chemistry [68]. Copyright 2015 The Royal Society of Chemistry.

4.3.4 Summary

In summary, we have demonstrated the first account of the spectral evidence of the nonradiative energy transfer in the solid thin film assemblies incorporating colloidal CdSe nanoplatelets of different vertical thicknesses. Both steady state and time resolved fluorescence spectroscopy proved that excitons generated in the donor, 4 ML thick NPLs can be funneled into the acceptor, 5 ML thick NPLs via near field dipole-dipole coupling. The efficiency of NRET can reach 60%, however, further increase in the efficiency was limited by the nanoscale phase segregation between the donor and acceptor NPL populations due to the self-stacking of the NPLs within their own populations leading to increased distance between the donor-acceptor pairs. This type of nanoscale phase separation has not been observed in the mixed solid films of the quantum dots and nanorods to date. As a future work, developing inter-stacked NPL assemblies of mixed populations will boost the NRET efficiencies in the assemblies of the NPLs.

4.4 Conjugated polymer - nanoplatelet hybrids for efficient exciton dissociation

This section is based on the publication “Colloidal Nanoplatelet/Conducting Polymer Hybrids: Excitonic and Material Properties,” **B. Guzelturk**, F. Menk, K. Philipps, Y. Kelestemur, M. Olutas, R. Zentel, and H. V. Demir, *The Journal of Physical Chemistry C* 120, 3573-3582 (2016). Adapted (or “Reproduced in part”) with permission from American Chemical Society. Copyright 2016 American Chemical Society.

4.4.1 Motivation

Organic-inorganic hybrids comprising organic semiconductors and colloidal nanocrystals make an attractive combination of soft material systems for optoelectronic devices including solar cells [12], [20], [162]–[164] and light-emitting diodes [20], [21], [109], [165]–[168]. Strong interest in hybrid materials stems, in particular, from their solution processability, which allows for fabrication of possibly large-area devices via low-cost printing and patterning techniques essentially on arbitrary substrates at large scale. There has been an ever growing interest for this type of hybrid systems since the breakthrough achievement of Alivisatos’ group reporting a hybrid solar cell composed of CdSe nanorods and poly(3-hexylthiophene) (P3HT) conjugated polymers [12]. Recent reports show that the power conversion efficiencies in the hybrid solar cells can attain over 5% [169], [170]. Also, based on theoretical calculations, hybrid solar cells are predicted to achieve efficiencies that could possibly exceed 10% by employing optimized hybrid structures offering enhanced free carrier generation and charge transport [171], [172].

In a hybrid solar cell, exciton dissociation, charge transport and charge extraction are the essential processes. Efficient free carrier generation via exciton dissociation requires assistance of exciton diffusion since excitons should reach the exciton dissociating interfaces before they would recombine [145]. Unfortunately, exciton diffusion in the colloidal nanocrystals and organic semiconductors is generally limited

to short distances (< 20 nm) [20]. As a result of this limitation, it is commonly desired to realize nanoscale morphologies having very small domains on the order of exciton diffusion length so that free carrier generation could be maximized. In addition to nanoscale morphology, extrinsic and intrinsic properties of the inorganic nanocrystals, including their ligands, size and geometry also play a significant role in the free carrier generation efficiency and, thus, the overall solar cell efficiency in hybrid systems [20], [173].

Long alkyl chain-based insulating ligands of the nanocrystals restrict charge separation and transport in their solid films. In an early report, Geenham *et al.* described ligand modification of CdSe quantum dots (QDs) that were primarily coated with insulating tri-*n*-octylphosphine oxide (TOPO) ligands by the treatment with an excess of pyridine [145]. Since then, various ligand modification procedures have been developed either using short organic or inorganic ligands [168], [172], [174], [175]. However, ligand exchange does not simply change the QD/QD and QD/polymer distances, it also affects the conductivity, energy levels, stability and the morphology of casted films [176]–[178]. Furthermore, some functional groups such as thiols are known to create charge traps in the nanocrystals and quench their photoluminescence [179], [180]. Therefore, predicting the influence of a specific ligand on the optical properties of the hybrids is difficult and complex. Consequently, studies that separately investigate the influence on the individual aspects depending on both the size and the functional group of the ligands are required.

Morphology of the nanocrystals (i.e., size, shape and dimensionality) is another important feature determining the performance of the organic-inorganic hybrids. To date, CdSe and CdS nanorods have shown favorable performance as compared to that of the colloidal QDs thanks to their large surface area and high aspect ratio, which considerably increases the overall free carrier generation efficiency at the organic-inorganic interfaces [99], [164], [173]. High aspect-ratio organic materials such as conjugated polymer nanowires have been also previously shown to enhance the power conversion efficiencies through creating a nanoscale morphology favorable for charge separation and transport [181].

Recently, a new type of colloidal semiconductors commonly known as colloidal nanoplatelets, or alternatively colloidal quantum wells, has been introduced [182]. Thanks to their favorable optical and material properties, recent reports have shown that the NPLs are highly promising for the applications of light-emitting diodes [83], lasers [17], [75], photodetectors [85], [183] and photocatalysis [70]. Moreover, ultra-efficient exciton transfer has been shown to prevail in the close-packed solid films of the NPLs [68], [87], which is expected to facilitate long exciton diffusion lengths (> 100 nm) in their solid films [19]. These long exciton diffusion lengths would clearly manifest the high potential of NPLs in light-harvesting applications. In addition, their high aspect-ratio, large surface area and anisotropic shape also make the NPLs interesting candidates for organic-inorganic hybrid systems. However, to date, there has been no demonstration or of any systematic study of organic-inorganic nanocomposites containing the NPLs and the conjugated polymers.

4.4.2 Experimental

All commercially available chemicals were purchased from Alfa Aesar, Acros Organics, Fluka, Sigma-Aldrich, or Tokyo Chemical Industry and used without further purification unless otherwise noted. Anhydrous THF was freshly distilled from sodium at dry argon atmosphere. All reactions were carried out under dry argon using standard Schlenk line techniques unless otherwise noted. 2',5'-di(2''-ethylhexyloxy)-4'-methyl-*N*-benzylideneaniline (**1**) and the reactive ester block copolymer **P1** were synthesized according to a modified literature procedure.¹ $^1\text{H-NMR}$ and $^{19}\text{F-NMR}$ spectra were acquired on a Bruker ARX 400 at a Larmor frequency of 400 MHz. FTIR spectra were performed on a Vector 22 ATR-FTIR-spectrometer made by Bruker. Molecular weights of all synthesized polymers were determined by gel permeation chromatography (GPC) with a concentration of $1.2 \text{ mg} \cdot \text{mL}^{-1}$ in THF with polystyrene as the external standard and toluene as the internal standard.

Cyclic voltammetry measurements were carried out on a drop-cast film at room temperature in a nitrogen-filled glove box. Platinum electrodes were used as working

and counter electrodes. The reference electrode was an Ag/Ag⁺ electrode and the measurements were conducted in a 0.1 M solution of tetrabutylammonium hexafluorophosphate (TBAPF₆) as the supporting electrolyte in anhydrous acetonitrile. Ferrocene was used as an internal standard and the energy levels were calculated from the onsets of the oxidation and reduction potential, respectively, with an assumed level of the Fc/Fc⁺ redox couple of -5.1 eV versus the vacuum.

For the general procedure for post-polymerization modifications; The precursor polymer **P1** (0.032 mmol, 1 eq.) was dissolved in 2.5 mL of dry THF under an argon atmosphere. The respective primary amine (0.476 mmol, 15 eq.) and triethylamine (0.476 mmol, 15 eq.) were added and the reaction mixture was stirred at 30 °C for 48 h. Purification was achieved by precipitation in methanol and redissolving in DCM for three times.

P2a: ¹H-NMR (400 MHz, CDCl₃, δ): 7.38 – 7.60 (m, 36H, Ar), 7.02 – 7.26 (m, 36H, CH=CH), 3.68 – 4.06 (m, 80H, O-CH₂), 2.60 (br, 8H, S-CH₂), 2.13 (br, 12H, S-CH₃), 1.17 – 1.86 (m, 336H, CH + CH₂), 0.82 – 1.05 (m, 222H, CH₃); ¹⁹F-NMR (400 MHz, CDCl₃, δ): no signals; FTIR: ν = 1676 cm⁻¹.

P2b: ¹H-NMR (400 MHz, CDCl₃, δ): 7.38 – 7.56 (m, 36H, Ar), 7.02 – 7.24 (m, 36H, CH=CH), 3.65 – 4.02 (m, 80H, O-CH₂), 2.87 (br, 8H, N-CH₂), 2.23 (br, 24H, N-CH₃), 1.17 – 1.86 (m, 336H, CH + CH₂), 0.83 – 1.04 (m, 222H, CH₃); ¹⁹F-NMR (400 MHz, CDCl₃, δ): no signals; FTIR: ν = 1672 cm⁻¹.

P2c: ¹H-NMR (400 MHz, CDCl₃, δ): 7.38 – 7.56 (m, 36H, Ar), 7.02 – 7.24 (m, 36H, CH=CH), 3.65 – 4.01 (m, 80H, O-CH₂), 2.84 (br, 8H, N-CH₂), 2.25 (br, 24H, N-CH₃), 1.17 – 1.86 (m, 352H, CH + CH₂), 0.83 – 1.03 (m, 222H, CH₃); ¹⁹F-NMR (400 MHz, CDCl₃, δ): no signals; FTIR: ν = 1668 cm⁻¹.

4.4.3 Results and discussion

In this part, we proposed and demonstrated hybrid composites combining for the first time colloidal nanoplatelets and conjugated polymers. In this hybrid system, we studied different anchor groups of the conductive polymer to hybridize with CdSe NPLs. To this end, we developed DEH-PPV based block copolymers having two ligands of varying size and anchor groups. Through investigation of steady-state optical properties of the hybrids in the solution phase, we revealed strong photoluminescence quenching in both the co-integrated polymers and the nanoplatelets. The emission quenching is well explained with exciton dissociation at the polymer/nanoplatelet interfaces having a staggered band alignment. Among different anchors, sulfides led to the strongest quenching as attributed to their higher tendency to attach to the NPL surfaces. Also, a shorter ligand size of the same anchor group was shown to yield a larger photoluminescence quenching as compared to the ligands with a larger size. Furthermore, we observed that the hybridization helps to form well-dispersed NPL films as revealed by transmission electron microscopy, whereas the NPLs alone tend to form aggregated assemblies in the absence of functional polymers. The proposed hybrid composites with exciton dissociating interfaces and homogenous NPL distribution are highly promising for making hybrid solar cells.

Surfactants have a strong influence on the properties of organic-inorganic nanocomposites with regard to their optoelectronic performance and applications. As both, the size and the functional group of a surfactant affect the properties, here we studied the influence of the two aspects separately. The required interaction of the inorganic nanocrystals and the conjugated polymer was accomplished by the incorporation of anchor groups into the polymer. These anchor groups were composed of a functional group targeted to enable an effective binding to the inorganic nanocrystals and a spacer that determined the distance between polymers and nanocrystals. Due to its favorable optoelectronic properties, the poly(*p*-phenylene vinylene) derivative DEH-PPV was selected as the conjugated block. DEH-PPV can be synthesized via Siegrist polycondensation, which offers a defined functional end group.

This end group was further exploited for the incorporation of a second block, which is non-conjugated, composed of a reactive ester repeating unit via RAFT polymerization [184], allowing for the incorporation of different anchor groups (see Figure 4.20). To guarantee that the observed differences in the properties originate from the varying anchor groups, all polymers employed in the study were synthesized from a single precursor polymer as illustrated in Figure 4.20. By exploiting only the same block copolymer architecture, influence of the anchor groups on the torsion and, thereby, photophysical properties of the conjugated backbone was also avoided. The precursor polymer that does not have any anchor group is hereafter named as the reference polymer **P1**. The functional polymers with anchors based on sulfide is called **P2a** and the ones based on amino are called **P2b** and **P2c**. The ligand size is the same in **P2a** and **P2b** polymers, while the spacer is longer in **P2c** (see Figure 4.20).

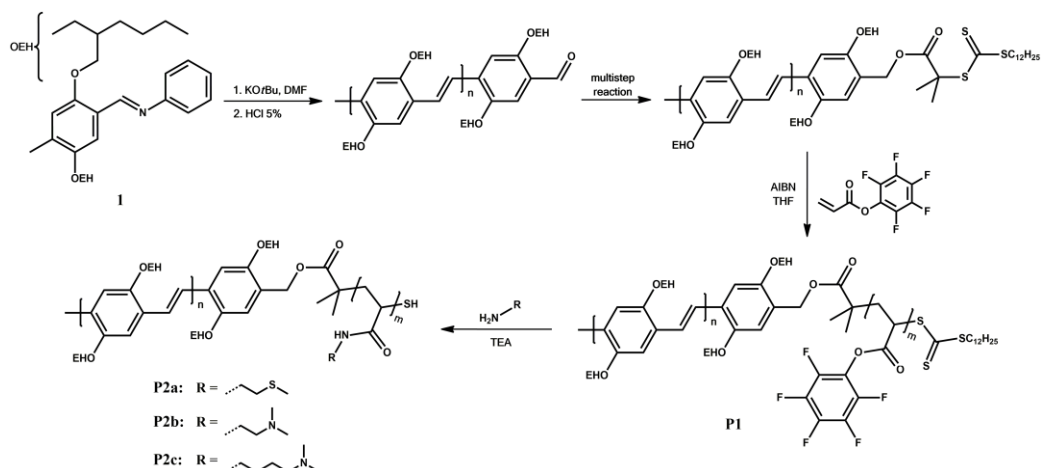


Figure 4.20. General reaction scheme for the incorporation of anchor groups into the block copolymer containing a conjugated DEH-PPV block and assignment of the polymers **P1** and **P2a-c**. Reprinted (or Adapted) with permission from [185]. Copyright 2014 American Chemical Society.

When incorporating anchor groups into a conjugated polymer, several aspects have to be taken into account. The incorporation of anchor groups as the side chains into the conjugated polymer backbone or as the end groups is usually relatively simple. Unfortunately, both approaches come along with disadvantages. The incorporation of anchor groups as the side chains disturbs the polymer's regioregularity, causes torsion

in the backbone and decreases the planarity of the conjugated backbone [163], [186]. Also, with an increasing chain length of the polymer the possibility of a single functional end group to be in a suitable position for interacting with the nanocrystal surface is significantly decreased. In the latter case, only very strong anchor groups such as enediols in the case of TiO₂ nanoparticles could form stable coatings [187], [188]. Therefore, the use of block copolymers, which we employed here, is highly desired since they both allow for multiple anchor groups and, thereby, enable the formation of a stable coating without sacrificing the original optoelectronic properties of the conjugated polymer owing to the separation of the conjugated block from the anchor groups. Since the combination of a conjugated PPV block and a non-conjugated block via one-pot block copolymerization can be solely achieved by applying ring-opening metathesis polymerization (ROMP), which involves complicated monomer synthesis, a synthetic route exploiting the defined end group installed via Siegrist polycondensation was applied [184], [189].

Successful incorporation of the anchor groups via post-polymerization modification was evidenced via FTIR spectroscopy. Upon incorporation of the anchor groups, the band originating from the pentafluorophenyl ring at 1519 cm⁻¹ disappears. Moreover, the C=O band shifts from 1783 cm⁻¹ in the reactive ester to approximately 1670 cm⁻¹ in the amides (see Figure 4.21a, Figure 4.22a and Figure 4.23a for all of the polymers). Full conversion of the post-polymerization modification was confirmed by the absence of any signals in the ¹⁹F-NMR spectra of the amides. In addition, the successful incorporation of the anchor groups was verified via ¹H-NMR spectroscopy. After post-polymerization modification, the NMR spectra of the polymers exhibit signals that can be assigned to the respective anchor group (see Figure 4.24, Figure 4.25 and Figure 4.26 for all of the polymers).

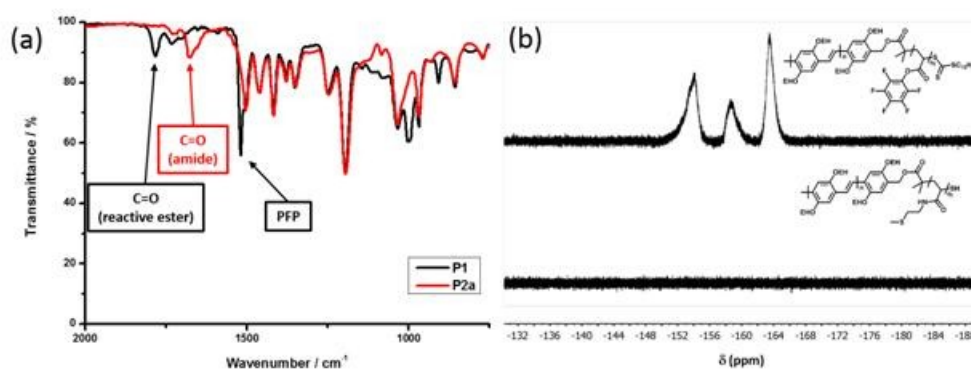


Figure 4.21. (a) FTIR spectra verifying the success of the post-polymerization modification and (b) ^{19}F -NMR spectra of polymers **P1** and **P2a**. While the signals of the reactive ester occur in the ^{19}F -NMR spectrum of precursor polymer **P1**, full conversion of the post-polymerization modification is evidenced by the absence of any signals in the spectrum of polymer **P2a**. Reprinted (or Adapted) with permission from [185]. Copyright 2014 American Chemical Society.

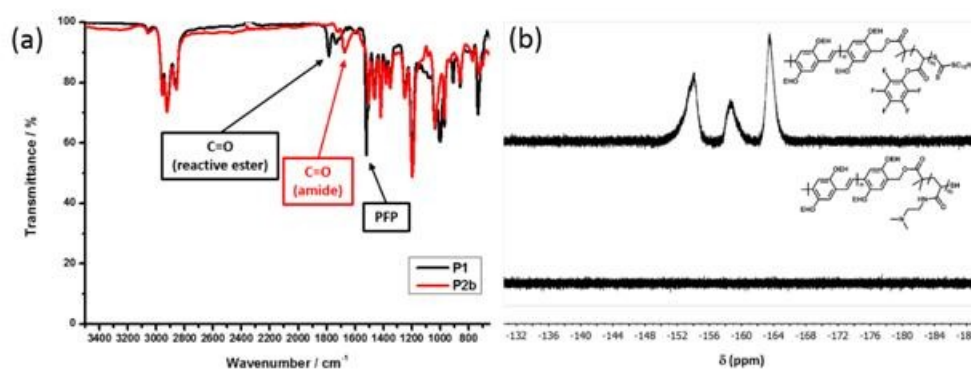


Figure 4.22. (a) FTIR spectra verifying the success of the post-polymerization modification and (b) ^{19}F -NMR spectra of polymers **P1** and **P2b**. While signals of the reactive ester occur in the ^{19}F -NMR spectrum of precursor polymer **P1**, full conversion of the post-polymerization modification is evidenced by the absence of any signals in the spectrum of polymer **P2b**. Reprinted (or Adapted) with permission from [185]. Copyright 2014 American Chemical Society.

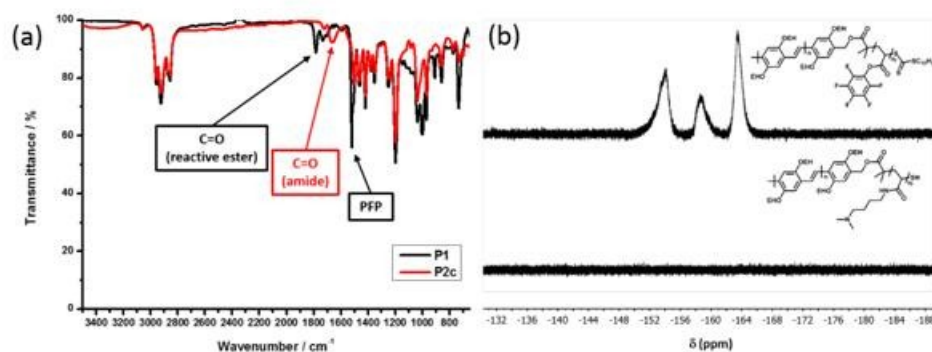


Figure 4.23. (a) FTIR spectra verifying the successful post-polymerization modification (transferring P1 to P2c) and (b) ^{19}F -NMR spectra of polymers **P1** and **P2c**. While signals of the reactive ester occur in the ^{19}F -NMR spectrum of precursor polymer P1, no signals occur in the spectrum of P2c which verify full conversion of the post-polymerization modification. Reprinted (or Adapted) with permission from [185]. Copyright 2014 American Chemical Society.

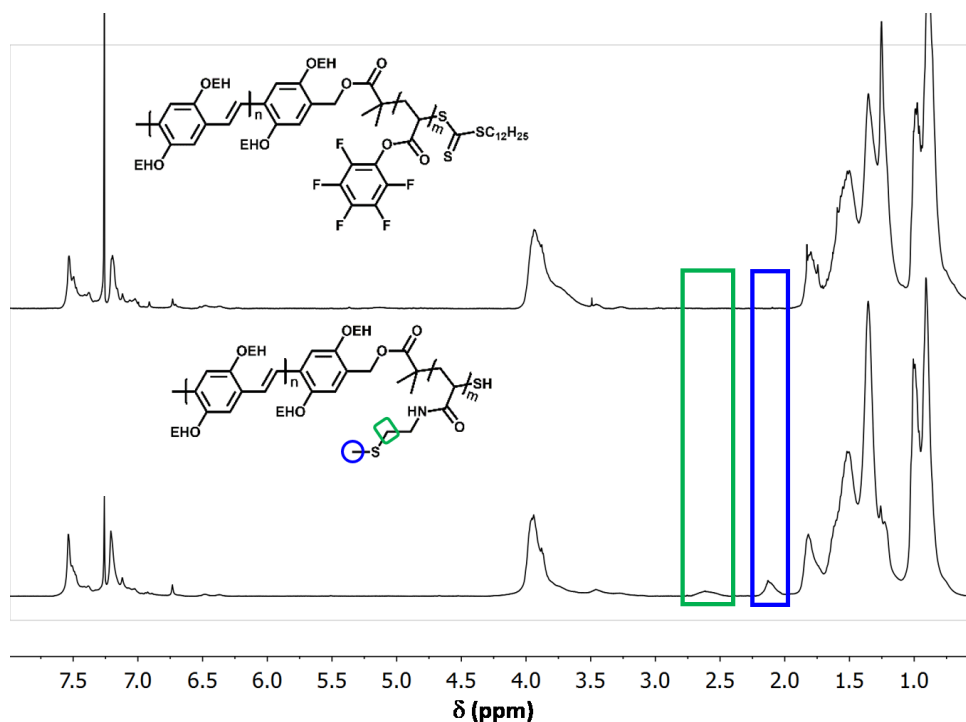


Figure 4.24. 400 MHz ^1H -NMR spectra of the precursor polymer **P1** and polymer **P2a** carrying a sulfide anchor group (in CDCl_3). After post-polymerization modification

signals of the anchor group are detected in the spectrum. Reprinted (or Adapted) with permission from [185]. Copyright 2014 American Chemical Society.

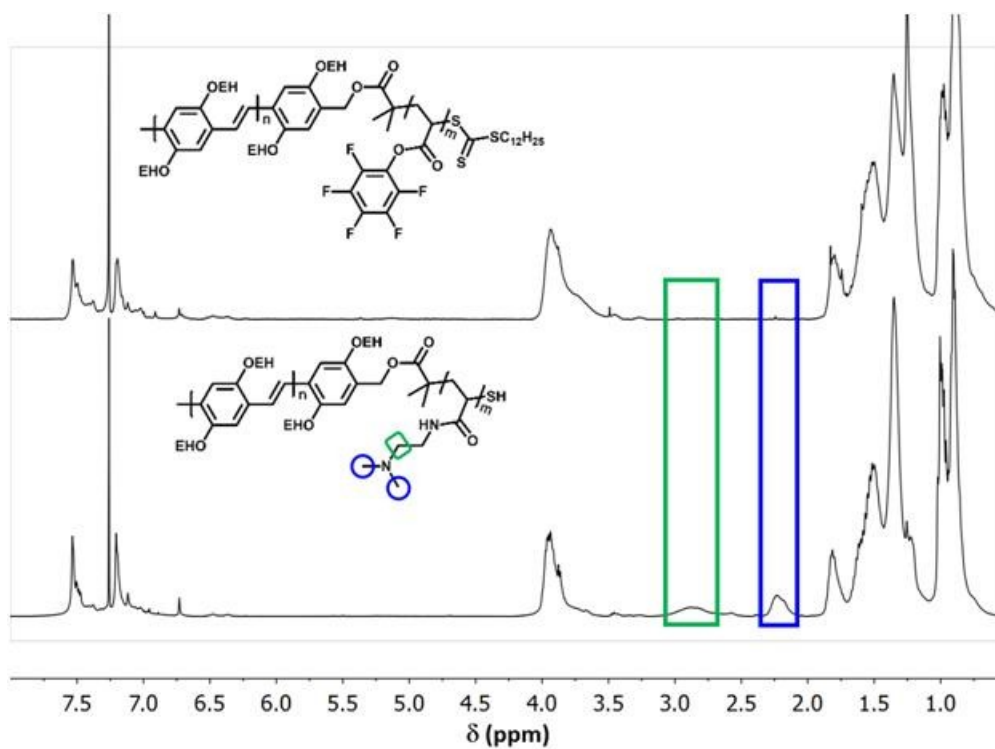


Figure 4.25. 400 MHz ¹H-NMR spectra of the precursor polymer **P1** and polymer **P2b** carrying an amino anchor group (in CDCl₃). After post-polymerization modification signals of the anchor group are detected in the spectrum. Reprinted (or Adapted) with permission from [185]. Copyright 2014 American Chemical Society.

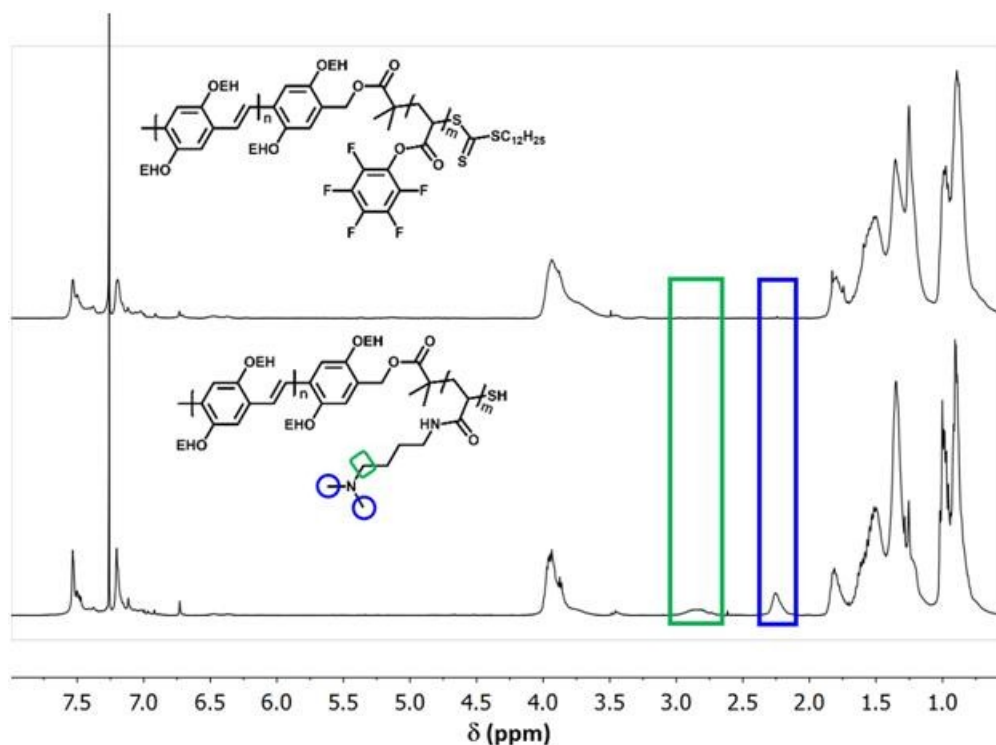


Figure 4.26. 400 MHz ^1H -NMR spectra of the precursor polymer **P1** and polymer **P2c** carrying an amino anchor group (in CDCl_3). After post-polymerization modification signals of the anchor group are detected in the spectrum. Reprinted (or Adapted) with permission from [185]. Copyright 2014 American Chemical Society.

As the inorganic nanocrystals, we employed atomically flat CdSe NPLs having four monolayer (ML) vertical thickness (~ 1.2 nm). We chose 4 ML CdSe NPLs because of their well-established synthesis and increased stability. In Figure 4.27a, absorbance and photoluminescence (PL) spectra of the NPLs are shown (in solution phase). The absorbance of the NPLs exhibit two peaks that are at 480 and 512 nm arising from electron/light-hole and electron/heavy-hole transitions, respectively. The PL peak arises from the recombination of the excitons at the electron/heavy-hole transition (~ 513 nm). The emission linewidth in the NPLs was as narrow as ~ 8 nm due to absence of inhomogeneous broadening [59]. The inset in Figure 4.27a shows a high-angle annular dark-field scanning transmission electron microscopy (HAADF-STEM) image of the NPLs. In the STEM image, most of the NPLs can be seen lying flat on the TEM grid, while some of them can be observed to form stack-like assemblies, which

lie perpendicular to the TEM grid. The stacking of the NPLs has been commonly observed in their solid films since the NPLs tend to assemble together in long chains due to strong van der Waals forces between their large and flat surfaces [136]. The absorbance and PL spectra of the conjugated polymers are also presented in Figure 4.27b. The PL peak of the polymers are at ~ 550 nm and their absorption peaks are at approximately at 460 nm. We observed very slight spectral shifts between the absorbance and emission spectra of different polymers used here, which may arise from the use of different ligands.

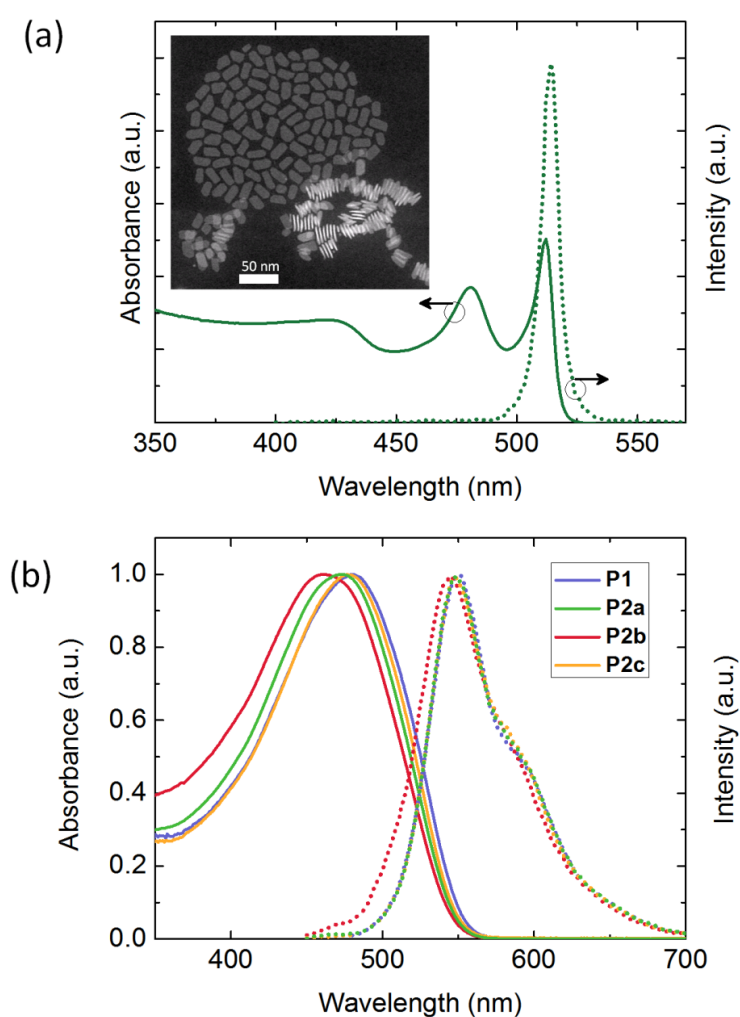


Figure 4.27. Absorbance (solid) and photoluminescence (dotted) of (a) 4 monolayer thick CdSe nanoplatelets, and (b) conjugated polymers P1 and P2a-c. Inset in (a) shows the HAADF-STEM image of the CdSe nanoplatelets, the scale bar is 50 nm. Reprinted (or Adapted) with permission from [185]. Copyright 2014 American Chemical Society.

We investigated the steady-state PL of the NPLs and the polymers when they were mixed together in the solution phase. For this, first, we prepared a dilute nanoplatelet solution in toluene. The absorbance of the initial NPL solution was very low (~ 0.1 at the first exciton peak 512 nm) to prevent reabsorption and concentration based energy transfer effects. The concentration of the NPLs was calculated to be 12.3 nM (in 3 mL toluene) by using their reported absorption cross-section [59]. Polymer solutions were prepared separately using toluene as the solvent with a concentration of 2 mg/mL. Then, step-by-step we added small amounts of a polymer into the NPL solution. Each step added 5 μ L polymer solution into the NPL solution, which corresponds to addition of ~ 1.4 nmol for **P2a** and **P2b** polymers and ~ 1.3 nmol for **P1** in each step as calculated by their molecular weight (see Table 4.4).

Table 4.4. Molecular weights and PDIs of all polymers.

Polymer	Block Ratio ^{a)} (PPV:Acrylate)	M_n ^{b)} (g · mol ⁻¹)	M_n ^{c)} (g · mol ⁻¹)	PDI ^{b)}
P1	($\approx 18:4$) ^{d)}	9538	≈ 7700	1.31
P2a	$\approx 18:4$	10319	≈ 7200	1.33
P2b	$\approx 18:4$	8566	≈ 7200	1.28
P2c	$\approx 18:4$	8731	≈ 7300	1.30

^{a)} calculated from the ¹H-NMR spectra, ^{b)} determined by GPC which was calibrated with polystyrene standards, ^{c)} calculated from block ratio (including end groups), ^{d)} estimated value from polymers **P2a-c**.

As the polymer **P2a** (polymer with sulfide anchor) was added to the NPL solution, we observed that the NPL emission started to immediately decrease (see Figure 4.28a) when excited at 375 nm. In the case of polymer **P2b**, which carries an amine anchor with the same ligand size as in **P2a**, the decrease in the NPL emission was also evident (see Figure 4.28b). As more polymer was added step by step, the NPL emission was observed to further decrease (see Figure 4.28a-b). The insets in Figure 4.28a-b also

show the evolution of the NPL emission after spectral profile of the polymer emission has been mathematically subtracted for each case. The precursor polymer (**P1**), which does not carry any specific anchor group but the same conjugated block, was also investigated as the negative control group (see Figure 4.28c). Addition of **P1** was observed to cause a decrease in the NPL emission, which was, however, weaker than that observed with **P2a** and **P2b**. Figure 4.28d summarizes the change in the NPL emission as a function of the increasing polymer amounts. In the case of reference polymer **P1**, the quenching of the NPL was found to be up to 2-folds. This decrease in the NPL emission can be partially explained by the optical absorption of the NPL emission by the polymer since there is a non-zero absorbance of polymers at the emission peak of the NPLs (see Figure 4.27b for the absorbance of the polymers). We measured the absorbance of the polymer **P1** as ~ 0.30 at 512 nm, when 5.2 nmol **P1** was added to the solution. The absorbance of **P2a** and **P2b** was also measured ~ 0.32 when 5.6 nmol of these polymers were added to the solution. According to the relation $\phi_{transmitted} = \phi_{incident} \times 10^{-A}$, where ϕ is the light intensity and A is the measured absorbance (in log scale). For the measured $A = 0.30$, one could simply calculate a 2-fold decrease (i.e., 50% change) in the NPL emission due to the absorption by the polymer. Therefore, this completely accounts for the decrease in the NPL emission when mixed with the polymer **P1**.

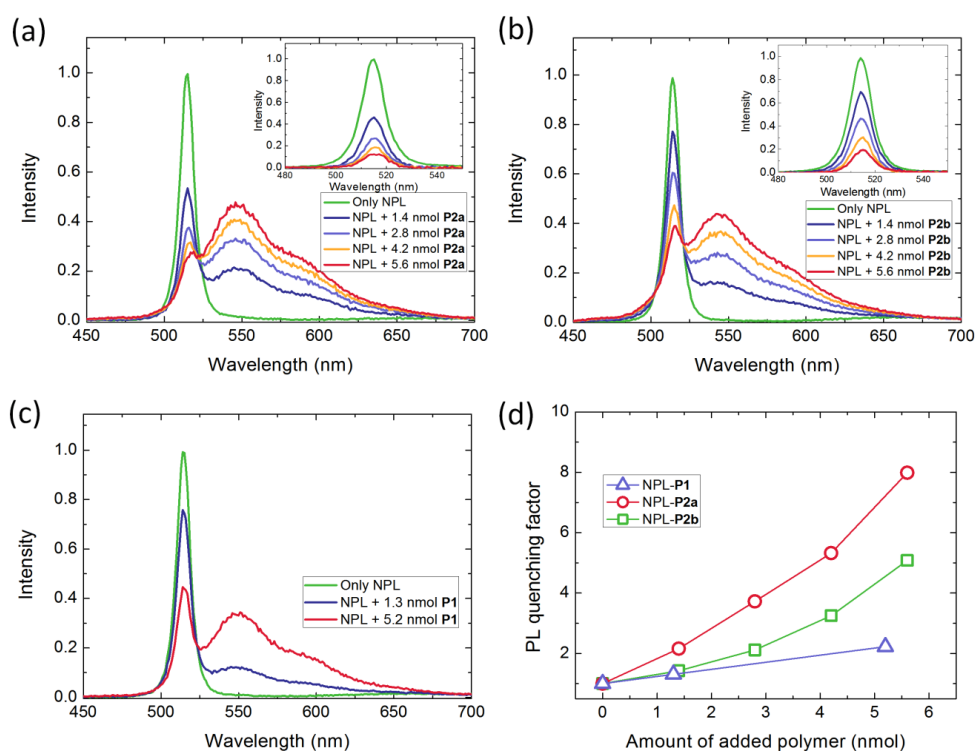


Figure 4.28. Steady-state photoluminescence spectra of the hybrids as the polymer were added step by step in the case of (a) NPL-P2a, (b) NPL-P2b and (c) NPL-P1 samples. The excitation wavelength for all cases was 375 nm. The insets in (a) and (b) show the NPL emission after spectral shape of the polymer emission has been subtracted. (d) Evolution of the NPL emission as a function of the added polymer amount for three different cases. Reprinted (or Adapted) with permission from [185]. Copyright 2014 American Chemical Society.

In the case of polymers with anchor groups, the PL quenching was found to be much stronger than that caused by **P1**. With polymer **P2b** (having amine anchor), we observe that the quenching of the NPL emission was up to 5-folds (80% decrease in the NPL emission). Moreover, polymer **P2a** carrying the sulfide anchor showed the largest quenching in the NPL emission, a factor larger than 8 (~90% decrease in the NPL emission). Therefore, strong quenching of the NPL emission in the presence of functional polymers (**P2a** and **P2b**) suggests that an additional process exists in addition to merely optical absorption of the polymers.

There exists a spectral overlap between the NPL emission and the polymer absorption. Thus, FRET may be possible in these hybrids and FRET might be the underlying process that can explain the emission quenching in the NPLs. To check out this hypothesis, we investigated and analyzed steady-state PL emission of the polymers. In FRET process, the emission of the donor is decreased while the emission of the acceptor is concomitantly increased due to the exciton transfer from the donor to the acceptor [103], [126], [190]. Therefore, we looked for a sign of an increased polymer emission as a result of possible FRET. Figure 4.29a shows the emission spectra of polymer **P2a** emission in the absence (dotted line) and presence (solid line) of the NPLs when excited at 375 nm. The emission of the polymer in its pristine form (only **P2a**) was larger than the polymer emission in NPL-**P2a** samples. This simply rules out the possibility that FRET cannot be the dominant process behind the PL quenching in the NPLs. Figure 4.29b illustrates the overall change of the emission intensity in the functional polymers **P2a** and **P2b** as a function of the added polymer amount (calculated from the emission spectra measured under excitation of 375 nm). Both polymers exhibit a decreased emission when mixed with the NPLs. The decrease in the polymer emission was larger for **P2a** than that of **P2b** (see Figure 4.29b).

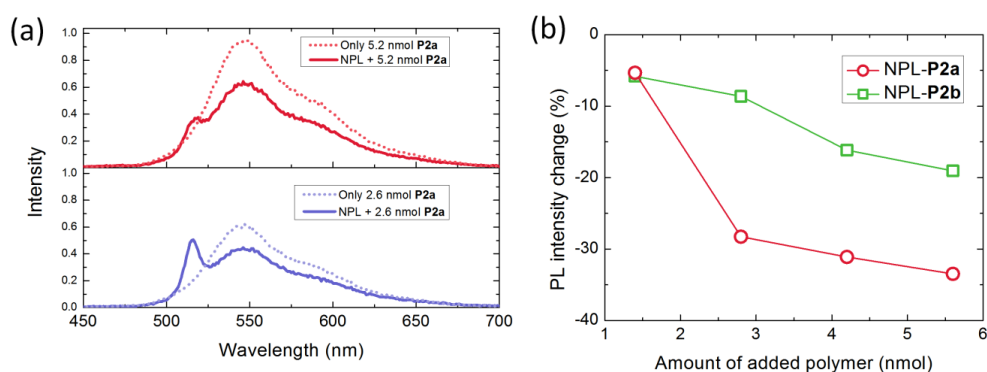


Figure 4.29. (a) Emission of the only polymer P2a and NPL + P2a for 5.2 nmol (top) and 2.6 nmol (bottom) polymer amounts. The excitation wavelength for all cases is 375 nm. (b) Emission intensity change in the polymers P2a and P2b in the presence of the NPLs as compared to bare polymer emission. Reprinted (or Adapted) with permission from [185]. Copyright 2014 American Chemical Society.

To explain the emission quenching in both the NPLs and the polymers when mixed together, we considered another hypothesis, which is the exciton dissociation at the NPL-polymer interface. Exciton dissociation is expected to decrease radiative emission since free carriers are generated instead of exciton recombination. Previously, DEH-PPV based polymers have been shown to be effective electron donors through exciton dissociation at the organic-organic interfaces with C60 molecules [191]. To check out the possibility of exciton dissociation in polymer/NPL hybrids, we looked into the excitation spectra of the NPLs and the polymers. Figure 4.30a shows the excitation spectra of the NPL peak emission (at 513 nm) for three different cases: Only NPL, NPL + 1.4 nmol **P2a** and NPL + 2.8 nmol **P2a**. To analyze the decrease in the excitation spectra of the NPL emission, first we consider the absorption of the excitation light by the **P2a**. Using the measured absorbance spectrum of the **P2a**, we calculated the decreased excitation light intensity by the following relation: $\phi_{transmitted} = \phi_{incident} \times 10^{-A}$. Then, we estimated the decrease in the NPL's excitation spectra due to the polymer absorption as plotted by the dotted curves in Figure 4.30a for the NPL + 1.4 nmol **P2a** and NPL + 2.8 nmol **P2a** samples. We observed that experimentally measured excitation spectrum of the NPL emission in the presence of **P2a** is lower than the estimated excitation spectra, which suggests the presence of photo-induced hole transfer from the NPL into the polymer. The excitation spectra of the NPLs showed a broadband quenching as the polymer amount was increased in the hybrid. This indicates that excitons formed in the NPLs are quenched independent of the excitation wavelength. This strongly suggests the possibility of a photoinduced charge transfer from the NPL into the polymer through exciton dissociation at the interface.

In Figure 4.30b, we also present the excitation spectra of the polymer **P2a** emission measured at its peak emission wavelength (at 545 nm) in two different cases: only 5.6 nmol **P2a** and NPL + 5.6 nmol **P2a**. Here we also observed a broadband decrease in the excitation spectrum of the polymer when the polymer was mixed with the NPLs. To analyze the decrease in the excitation spectra of the **P2a** emission, we also consider the absorption of the excitation light by the NPLs using the same methodology as used in Figure 4.30a. We estimated the decrease in the polymer's excitation spectra due to

the NPL absorption, which is plotted by the black solid curve in Figure 4.30b. We observed that experimentally measured excitation spectra of the **P2a** emission in the presence of the NPLs (red solid curve) are still much lower than the estimated excitation spectra (black solid curve). Moreover, for excitation wavelengths longer than 520 nm, where there is no NPL absorbance, the excitation spectrum of the **P2a** also shows decreased intensity in the hybrid sample as compared to the estimated excitation. These observations strongly suggest that the excitons in the polymer **P2a** are also dissociated at the polymer/NPL interface, possibly via photoinduced electron transfer from the polymer.

As a control sample, we also tested the excitation spectra of the polymer **P1** before and after being mixed with the NPLs. Figure 4.30c shows the excitation spectra (measured at the peak emission wavelength of the polymer) of only 5.2 nmol **P1** and NPL + 5.2 nmol **P1** samples. Here, we observed that the black curve (calculated excitation spectrum by considering absorption of the excitation light by the NPLs) and the orange curve (experimental excitation spectrum of the polymer in the presence of the NPLs) shows a very good agreement as depicted in Figure 4.30c. Therefore, this strongly supports our view that the change in the excitation of the **P1** polymer just arises from the NPL absorption since there is no considerable near-field interactions between the species (**P1** and the NPLs) in their solution phase. However, in the case of **P2a**, there have to be near-field interactions (i.e., exciton dissociation) between the species to explain the observed changes. Also, Figure 4.31 shows the spectral quenching of excitation spectrum of the NPL and **P2a**, which shows a flat spectral response arising from the reciprocal exciton dissociation (hole transfer from the NPL and electron transfer from the polymer) at the organic-inorganic interface, which is independent of the excitation wavelength as long as it is above the bandgap of the material.

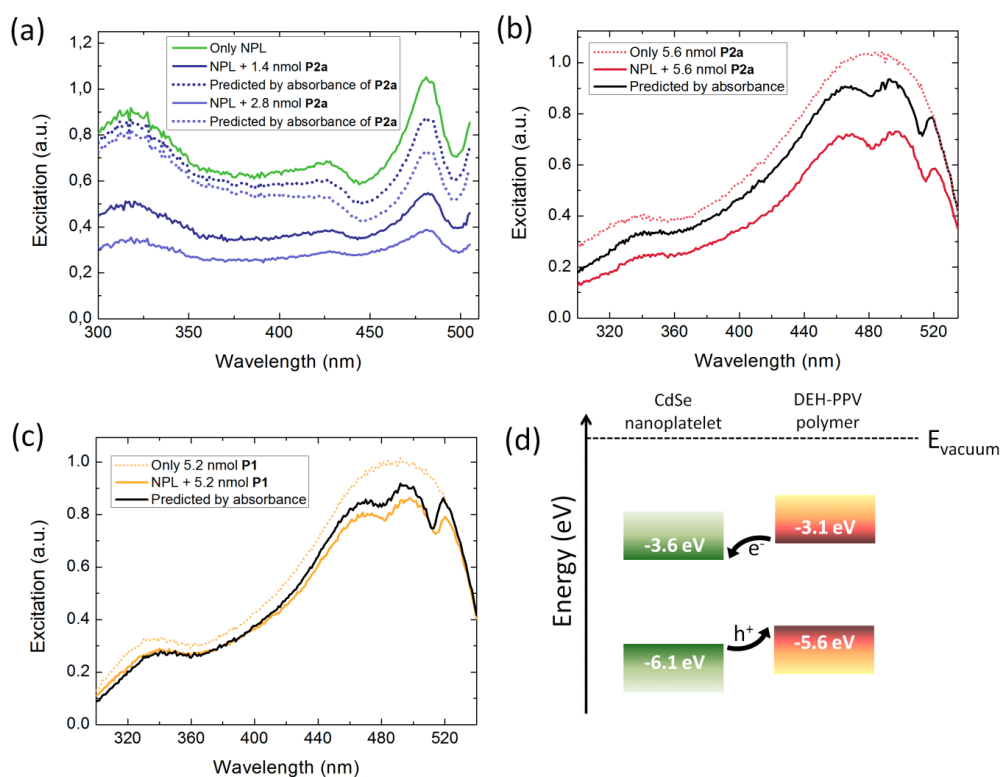


Figure 4.30. (a) Excitation spectra of the NPL emission for three different samples: only NPL (green), NPL + 1.4 nmol **P2a** (dark blue) and NPL + 2.8 nmol **P2a** (light blue). Excitation of the NPL emission is estimated by considering absorption of the excitation light by the **P2a** for two different cases (dotted curves). (b) Excitation spectra of the **P2a** for only 5.6 nmol **P2a** (red dotted curve) and NPL + 5.6 nmol **P2a** (red solid curve) samples. Also, excitation of the **P2a** emission is estimated by considering absorption of the excitation light by the NPLs (black solid curve). (c) Excitation spectra of the **P1** for only 5.2 nmol **P1** (orange dotted curve) and NPL + 5.2 nmol **P1** (orange solid curve) samples. Also, excitation of the **P1** emission is estimated by considering absorption of the excitation light by the NPLs (black solid curve). (d) Energy bands of the NPLs and polymers exhibiting a staggered (Type II) band alignment favoring exciton dissociation. Reprinted (or Adapted) with permission from [185]. Copyright 2014 American Chemical Society.

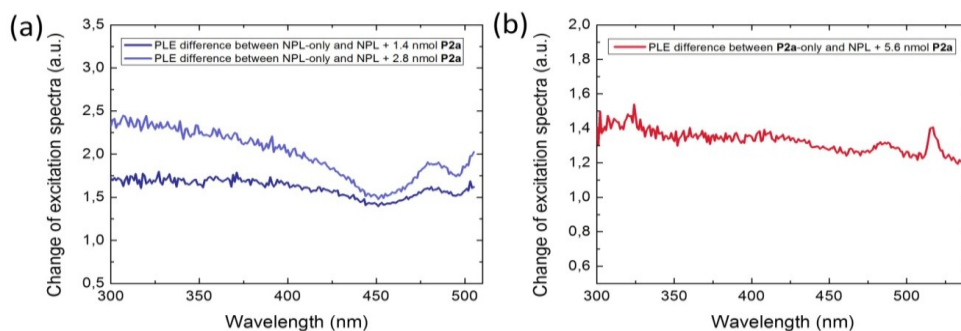


Figure 4.31. (a) Quenching of the NPL's excitation spectra in the NPL+1.4 nmol **P2a** and NPL+2.8 nmol **P2a** samples with respect to NPL-only sample. (b) Quenching of the **P2a**'s excitation spectra in the NPL+5.6 nmol **P2a** sample with respect to **P2a**-only sample. Reprinted (or Adapted) with permission from [185]. Copyright 2014 American Chemical Society.

To further elaborate on the exciton dissociation at the NPL-polymer interfaces, we investigated the energy band alignment between the NPLs and polymers. For this, we applied cyclic voltammetry (CV) to determine the energy levels of the polymers. From the CV data, the onset potentials for oxidation and reduction were found to be $E^{\text{Ox}} = 0.5 \text{ V}$ and $E^{\text{Red}} = -2.0 \text{ V}$ vs Fc/Fc^+ . Thus, with an assumed level of the Fc/Fc^+ redox couple of -5.1 eV versus the vacuum, the HOMO and LUMO energy levels were calculated to be -5.6 eV and -3.1 eV , respectively (see Figure 4.32) [192]. Previously, the conduction and valence band levels have been measured via ultraviolet photoelectron spectroscopy (UPS) in 4 ML thick CdSe NPLs as -3.6 eV and -6.1 eV , respectively [84]. The resulting band alignment at the polymer-NPL hybrids is illustrated in Figure 4.30d, which exhibits a staggered (i.e., Type-II-like) band alignment. Therefore, exciton dissociation is expected to be favored via hole transfer to the polymer and electron transfer to the NPLs (see Figure 4.30d). Based on these observations, we can propose that exciton dissociation in the NPL-polymer hybrids is the dominant process.

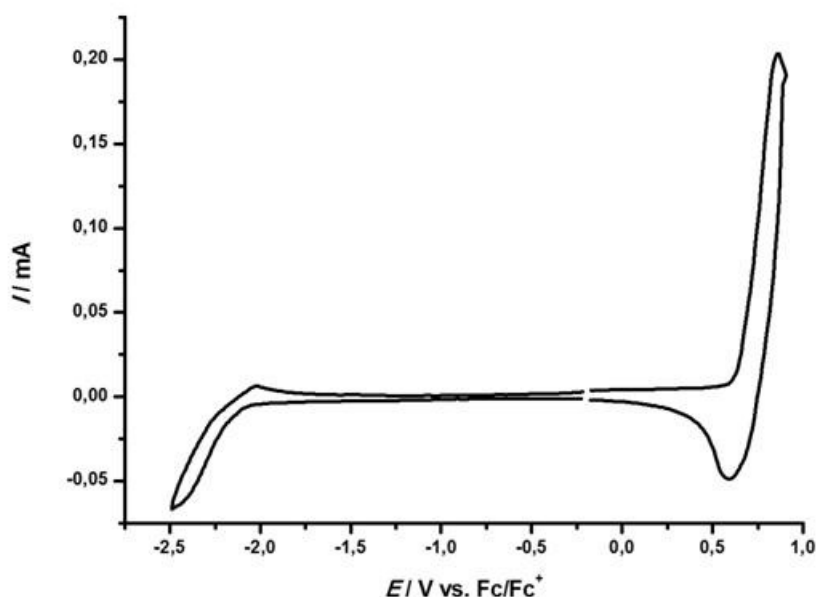


Figure 4.32. Cyclic voltammetry measurement of precursor polymer **P1** measured in a 0.1 M solution of TBAPF6 in anhydrous acetonitrile versus Fc/Fc⁺. Reprinted (or Adapted) with permission from [185]. Copyright 2014 American Chemical Society.

Considering Figure 4.28a, which summarizes the emission quenching in the NPLs as a function of the added polymer amount for different polymers, **P2a** (functional polymer with the sulfide anchor) is observed to lead to a stronger quenching in the NPL emission than **P2b** (functional polymer with the amine anchor) while the ligand lengths are the same. This may suggest that **P2a** has a higher tendency to bind to the NPL surfaces than **P2b**. Thus, the emission of more NPLs could be quenched in the solution phase since more **P2a** molecules were attached to the NPLs. Another possibility for the stronger quenching might be that sulfide anchors in **P2a** could create surface traps in the NPLs leading to nonradiative decay of the excitons. Such emission quenching arising from ligands of the nanocrystals have been shown previously [172], [180]. Generally, thiol-based ligands were shown to create mid-gap trap states in the quantum dots causing charge trapping and emission quenching [172]. However, we observed a larger emission quenching of the polymer **P2a** emission as compared to **P2b** as shown in Figure 4.29b. Thus, this opposes the possibility that the sulfide anchor might act as quencher, but most likely it acts as a stronger agent for hybridization with

the NPLs than amine-based anchors. Moreover, enhanced interaction of **P2a** with the CdSe NPLs would explain the stronger PL quenching on both side of the hybrid via exciton dissociating Type-II interfaces.

Previously, exciton dissociation via ultrafast electron transfer (<1 ps) from the conjugated polymer into the colloidal quantum dots have been shown feasible [193], [194]. Thus, this could make it possible for nanocrystals to replace commonly used electron acceptors such as C60. However, hole transfer from the spherical quantum dots into conjugated polymers has been generally found to be limited arising from its slow rate [194]. Based on our observations, which suggest efficient exciton dissociation in the NPLs through hole transfer into the conjugated polymers, we believe that atomically flat nanoplatelets might stand out as a more promising candidate for conjugated polymer – nanocrystal hybrids. The favorable geometry of the nanoplatelets arising from their large and flat surfaces may enable more efficient and faster hole transfer rates into organic semiconductors as predicted here.

In addition to different anchor types, we also investigated the effect of the ligand size on the optical properties of the resulting hybrids. For this, we developed **P2b** and **P2c** polymers both having amine-based anchors but with different sizes. **P2c** has an amino anchor that has a larger size than that of **P2b** polymer as shown in Figure 4.20. Figure 4.33 shows the emission spectra of the NPL + 9 nmol **P2b** and NPL + 9 nmol **P2c** samples. As presented in the inset of Figure 4.33, after the spectral profile of the polymer emission is subtracted mathematically, we observe that quenching of the NPL emission was found larger in **P2b**. The quenching factor of the NPL emission was calculated to be 11.3 and 6.8 for **P2b** and **P2c**, respectively. This also suggests that shorter ligands are more efficient for exciton dissociation. The charge transfer process, which generally occurs for distances shorter than 1 nm, is highly distance sensitive. Therefore, slight increase in the ligand size (as in the case of **P2c** polymer) can decrease the exciton dissociation efficiencies considerably.

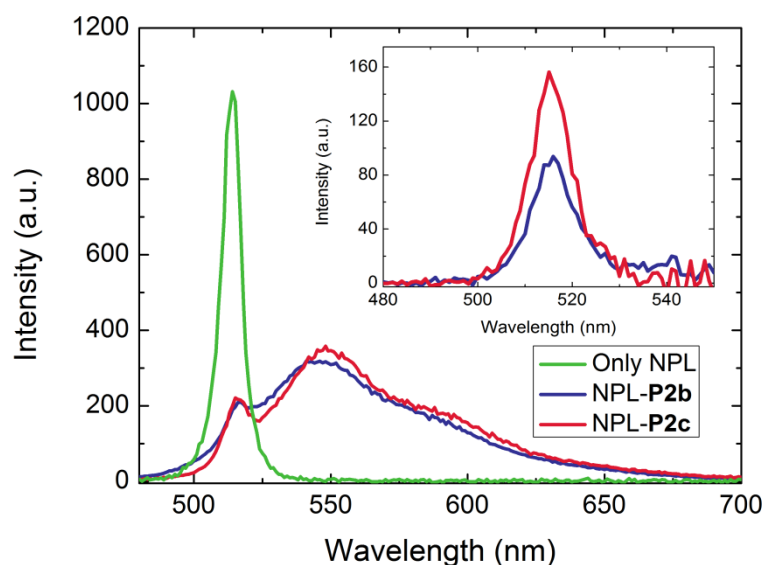


Figure 4.33. Emission spectra of the only NPL, NPL + 9 nmol P2b and NPL + 9 nmol P2c samples. The inset shows the NPL emission after spectral profile of the polymer emission is subtracted. The emission quenching is larger for P2b than P2c since P2b has a shorter anchor ligand. Reprinted (or Adapted) with permission from [185]. Copyright 2014 American Chemical Society.

Finally, we studied the solid-film morphology of the hybrids and found that hybrids exhibit homogeneously distributed NPLs in their solid films. For this, we prepared solutions with only NPL and NPL/**P2a** samples. Figure 4.34a shows HAADF-STEM images of the NPLs before they were mixed with the functional polymers. The NPLs on their own tend to exhibit aggregation while drying their solvent, which also leads to stacking of the NPLs via strong van der Waals forces. In the case of NPL/**P2a** hybrid sample, Figure 4.34b shows highly uniform distribution of the NPLs without any considerable aggregation although the same amount of NPLs have been employed. This suggests that the functional polymers bind to the NPL surfaces and help creating an increased separation between the NPLs so that NPL-to-NPL interactions could significantly be reduced. Such hybrids could be utilized for hybrid optoelectronic applications. The homogenous distribution of the NPLs would be useful for efficient exciton dissociation in solar cells or exciton injection in light-emitting diodes.

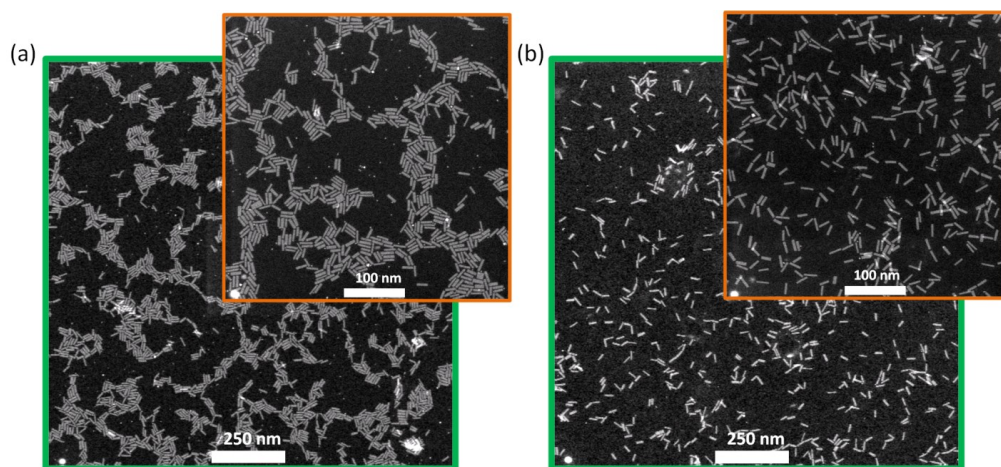


Figure 4.34. HAADF-STEM images of (a) only NPLs and (b) NPL-P2a hybrids. The insets show zoomed-in images with scale bar of 100 nm. Reprinted (or Adapted) with permission from [185]. Copyright 2014 American Chemical Society.

4.4.4 Summary

Here, we introduced a hybrid conjugated polymer/nanoplatelet system for the first time, which exhibits strong photoluminescence quenching in their dilute solutions. The quenching has been explained with exciton dissociation at Type-II-like band alignment at the organic-inorganic interfaces. Uniquely enabled by atomically flat and large surface area nanoplatelets, the proposed composite system offers the opportunity to substantially enhance hole transfer into the polymers, as suggested by the steady state spectroscopy. Thus, this work is expected to initiate future investigations based on ultrafast transient optical probes to capture the details of charge transfer kinetics in the hybrid organic-inorganic systems of colloidal nanoplatelets. As an important architectural feature of the proposed organic-inorganic composite, we found out that anchor type is effective for the hybridization efficiency. To this end, sulfide-based anchors showed a stronger binding affinity to the NPL surfaces as compared to amine-based anchors. Also, shorter ligands with the same anchor led to more efficient exciton dissociation thanks to closer integration of the polymers to the NPL surfaces. These findings indicate that the proposed organic-inorganic hybrids, which also allow for

uniform NPL distribution in their solid thin-films, are very promising for hybrid optoelectronics, particularly in solar cells.

4.5 Efficient exciton transfer in quantum dot – nanoplatelet solids for sensitive temperature probing

This section is based on the publication “Highly Efficient Nonradiative Energy Transfer from Colloidal Semiconductor Quantum Dots to Wells for Sensitive Noncontact Temperature Probing,” M. Olutas, **B. Guzelturk**, Y. Kelestemur, K. Gungor, and H. V. Demir, *Advanced Functional Materials* (2016). DOI: 10.1002/adfm.201505108. Adapted (or “Reproduced in part”) with permission from John Wiley and Sons. Copyright 2016 Wiley-VCH Verlag GmbH & Co. KGaA, Weinheim.

4.5.1 Motivation

FRET is a nonradiative energy transfer process mediated by near-field dipole-dipole coupling between two species (donor and acceptor) that are in close proximity. Exciton transfer rate in NRET depends on the distance between the donor and acceptor species, the spectral overlap between the donor emission and the acceptor absorption, the fluorescence quantum yield of the donor, the dipole orientation and the refractive index of the medium [101], [103]. Although the early applications of NRET were mostly in biology [195]–[198], recent studies have shown that NRET can be effectively used for energy-efficient optoelectronics [21], [108], [109], [133], [134], [199]–[208] for enhanced light-generation and -harvesting.

Among semiconductor materials, colloidal semiconductor nanocrystals are interesting candidates for NRET-enabled systems, where NRET is strongly dependent on the dimensionality of the quantum confinement [126], [209]–[213]. To date, there have been several theoretical and experimental reports on NRET in semiconductor nanocrystals (*i.e.*, colloidal quantum dots (QDs) and nanorods (NRs)) and their hybrids (quantum dot – conjugated polymer, dye, epitaxial quantum well, *etc.*) regarding the effects of size, composition, dimensionality and architecture on NRET [126], [127],

[208]–[210], [214]–[216]. Such NRET-enabled colloidal systems were also shown to be suitable for use in devices including light-emitting diodes (LEDs) [133] and solar cells [130].

Owing to the 2D geometry and extremely large absorption cross-section, the colloidal NPLs stand out as highly efficient exciton acceptors suitable for light-harvesting applications [68], [87]. One key advantage of the NPLs that makes them exceptional exciton harvesters is their large absorption cross-section ($> 10^{-14} \text{ cm}^2$). This makes long range dipole-dipole coupling possible with a Förster radius $\geq \sim 10 \text{ nm}$. Recently, 2D monolayers such as graphene and transition metal dichalcogenides (*e.g.*, MoS₂) have also been shown to exhibit strong exciton sink property through NRET. However, colloidal NPLs with their solution-processability represent a versatile alternative as efficient exciton acceptors for light-harvesting. To date, NRET studies for NPLs have been limited with only NPL based donor-acceptor ensemble systems [68], [87]. Even though there are numerous reports on NRET from 3D-confined colloidal semiconductor QDs (as donors) to indirect band-gap semiconductors [128], 2D-materials [131], [217], epitaxial QWs [218], colloidal NCs [219], organic dye molecules [210] (as acceptors) and vice versa [20], [133], [209], [220], NRET has not been studied for an ensemble including colloidal QDs and NPLs. Also, the efficiency limits of such a mixed-dimensionality system have not been elucidated to date.

4.5.2 Experimental

For the synthesis of CdZnS/ZnS core-shell QDs; 1 mmol of cadmium oxide (CdO), 10 mmol zinc acetate (Cd(OAc)₂), 7 mL of oleic acid (OA) and 15 mL of octadecene (ODE) were loaded to a 100 mL three-neck flask. The solution was degassed around 100-110 °C for an hour. After degassing step, the solution was heated to 310 °C for dissolution of cadmium and zinc precursors. When the precursors were completely dissolved, 2.4 mL of sulfur stock solution (0.67 M S-ODE solution), which initiated the nucleation of alloyed CdZnS core QDs, was injected into the hot mixture. After the growth of alloyed CdZnS core QDs for 12 min, 5 mL sulfur stock solution (0.8 M S-

OA solution) was injected at the rate of 0.5 mL/min for the successive ZnS shell coating. After an hour growth at 310 °C, we performed additional injection of 2 mL of sulfur stock solution (0.8 M S-OA solution) with the same rate. Then, the solution was further kept for 2 h at 310 °C. Finally, the reaction was cooled down to room temperature and CdZnS/ZnS core/shell QDs were precipitated with the addition of ethanol. Then, the precipitated QDs were dissolved in hexane and stored for further steps.

For the synthesis of 4 ML CdSe NPLs; 340 mg of cadmium myristate ($\text{Cd}(\text{myr})_2$), 24 mg of selenium (Se) and 30 mL of octadecene (ODE) were introduced into a 100 mL three-neck flask. The mixture was degassed under vacuum at 90 °C with 1000 rpm magnetic stirring until it was completely dissolved and became colorless. After setting the temperature at 240 °C and the flask was filled with argon gas at 100 °C. When the temperature reached 190 °C, the color of solution became yellowish, 120 mg of cadmium acetate dihydrate ($\text{Cd}(\text{OAc})_2(\text{H}_2\text{O})_2$) was introduced swiftly into the hot mixture and the reaction was allowed to proceed 10 min at 240 °C. At the end of the 10 min growth process, 1 mL of oleic acid was added and then the mixture was quickly cooled down to room temperature. After adding 5 mL of hexane into the solution, it was centrifuged for 10 min at 4500 rpm. The supernatant was removed into another centrifuge tube and ethanol was added into supernatant solution until it became turbid. The turbid solution was centrifuged at 10000 rpm for 10 min, and then the precipitate was dissolved in hexane and filtered with 0.20 micrometer filter.

For the photoluminescence quantum yield (PL QY) measurements; photoluminescence quantum yield (PL QY) measurements of the donor-only film were determined utilizing a Spectral Products monochromator integrated xenon lamp as the excitation source (at an excitation wavelength of 375 nm), a Hamamatsu integrating sphere, and an Ocean Optics Maya 2000 spectrometer, and we followed the de Mello's method [221] step by step. Briefly, this method is basically comprised of three steps. First, excitation spectrum is recorded without sample in the integrating sphere. In the second step, the sample is placed into the integrating sphere and the spectrum is again

taken as the sample is directly illuminated by the excitation source. Finally, the sample is rotated and the spectrum is recorded when the sample is excited only under scattered excitation light. Previously, to test the accuracy of our integrating sphere system, we also measured the PL QY of the dye of Rhodamine 6G at 460 nm excitation wavelength to be 94.7 %, which is in good agreement with the standard value of 95%. In this study, the PL QY of the donor-only film was measured three times in different time periods as 36.5, 38.9 and 37.6 %.

4.5.3 Results and discussion

In this part of the thesis, we studied NRET from colloidal CdZnS/ZnS core/shell QDs to CdSe NPLs. We systematically investigated the energy transfer processes as a function of the donor-to-acceptor (D/A) molar ratio by using steady-state and time-resolved fluorescence spectroscopy in the hybrid films incorporating both the donor QDs and the acceptor NPLs. The significant shortening in PL decay lifetime of the donor QDs and the elongation in the PL decay lifetime of the acceptor NPLs were simultaneously observed, which suggests the exciton transfer from QDs into NPLs. In addition, the existence of NRET was further supported by the steady state photoluminescence excitation (PLE) spectra of the acceptor NPLs in the hybrid thin films. We also found that the resulting NRET efficiency can reach unprecedented levels of ~90% at room temperature. Furthermore, the NRET efficiency was shown to further increase up to ~94% at cryogenic temperatures. The observed enhancement with decreasing temperature is well explained by increasing PL quantum yields and changes in the spectral overlap. We observed that NRET efficiency shows a highly linear monotonic correlation with temperature in the range from 50 to 300 K, which makes the QD-NPL hybrid system a highly sensitive non-contact optical thermal probe.

As the exciton donor, we have employed a blue-emitting alloyed-core/gradient-shell CdZnS/ZnS QDs since they are highly luminescent with relatively long PL decay lifetimes. CdSe NPLs (green-emitting at ~513 nm, 4 monolayer vertical thickness) were used as an exciton acceptor. Both the donor QDs and the acceptor NPLs were

synthesized using modified recipes from the literature (see Experimental) [77], [222]. Figure 4.35a and Figure 4.35b show the absorption and steady-state PL spectra of the donor and the acceptor materials suspended in hexane at room temperature, respectively. Absorption spectrum of the donor QDs exhibits an absorption onset at 475 nm. The absence of a strong first exciton peak in the absorption is due to alloyed ZnCdS core, but not due to size distribution. The full-width at half-maximum (fwhm) of the QD emission at the peak emission wavelength (453 nm) is ~ 30 nm, which is comparable to the best reports for blue-emitting QDs. On the other hand, the acceptor NPLs, thanks to quasi-1D quantum confinement, exhibit epitaxial QW-like absorbance features. The two distinct peaks observed in the NPLs arise from the electron/light-hole (480 nm) and electron/heavy-hole (512 nm) transitions. In addition, the PL spectrum for the acceptor NPLs shows a single emission peak at 513 nm with a fwhm of ~ 8 nm. All these spectral features that are consistent with the existing literature suggest that the materials are of high quality. Figure 4.35c and Figure 4.35d show the transmission electron microscopy (TEM) images of both donor and acceptor ensembles on ultrathin carbon coated copper grids. The mean size of the donor QDs is 9.3 ± 1.2 nm, whereas that of the acceptor NPLs is 12.8 ± 1.9 nm by 10.5 ± 1.5 nm.

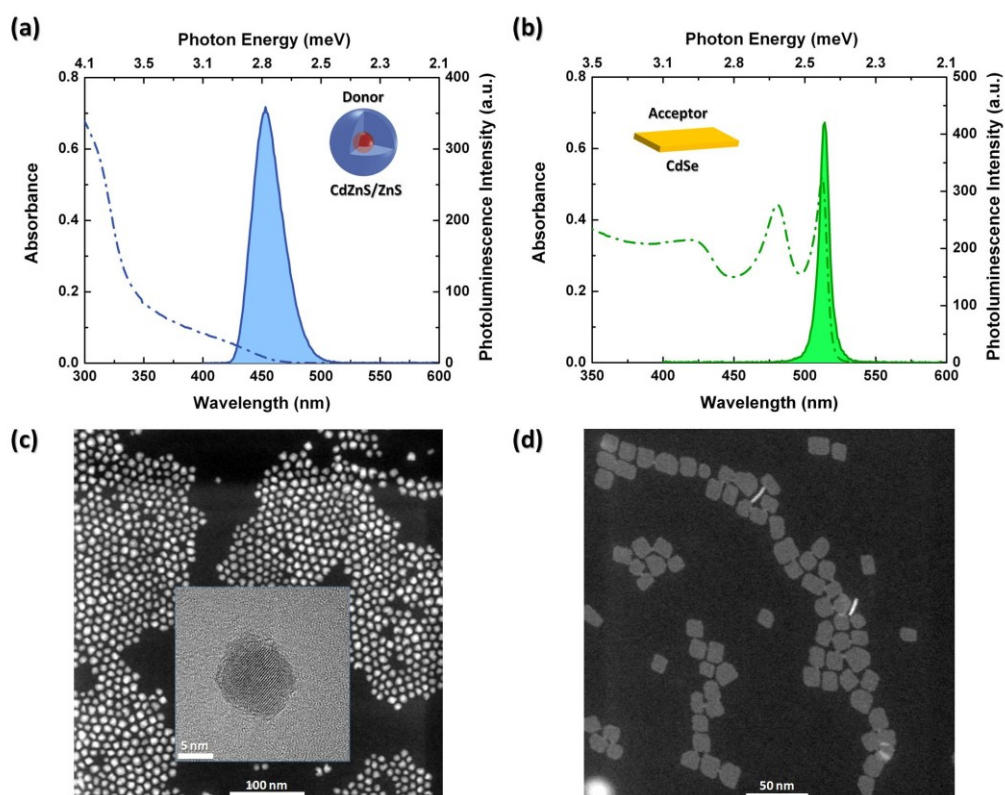


Figure 4.35. Absorption and photoluminescence spectra of (a) the blue-emitting CdZnS/ZnS core/shell QDs and (b) the green-emitting 4ML CdSe NPLs, which are dissolved in hexane at room temperature. High-angle annular dark-field scanning transmission electron microscopy (HAADF-STEM) images of (c) the donor-QDs having 9.3 ± 1.2 nm and (d) the acceptor-NPLs having 12.8 ± 1.9 nm by 10.5 ± 1.5 nm mean sizes. The inset in (c) shows the transmission electron microscopy (TEM) image of a CdZnS/ZnS core/shell QDs. Reprinted by permission from Wiley [110], Copyright 2015 Wiley-VCH Verlag GmbH & Co. KGaA, Weinheim.

We prepared seven hybrid thin film samples having different donor to acceptor molar ratios, which is called D/A ratio hereafter, in addition to the reference samples of only donor and only acceptor. The samples were deposited on pre-cleaned quartz substrates using the pre-mixed solutions of the QDs and the NPLs by spin-coating. The molar concentrations of donor (QDs) and acceptor (NPLs) solutions, which were used for the hybrid film preparation process, were calculated as 3.28×10^{-7} M and 2.16×10^{-6} M, respectively. To calculate the molar concentrations, we employed inductively

coupled plasma-mass spectrometry (ICP-MS) technique. In addition, the surface coverage of the prepared solid thin film samples was analyzed via scanning electron microscopy (SEM). For an exemplary case, Figure 4.36 shows the surface coverage of the thin film sample having D/A molar ratio = 0.01. In Figure 4.36a the QDs are seen as white spots due to their size (with radius ~ 4 nm) creating a larger contrast as compared to the very thin NPLs (vertical thickness ~ 1.2 nm). Although the surface coverage is less than 100%, the QDs and the NPLs are observed to be intermixed well. The donor QDs are well distributed among the acceptor NPLs, which can be found either lying flat or stacked and lying perpendicular to the substrate as shown in Figure 4.36b and cartoon in Figure 4.36a.

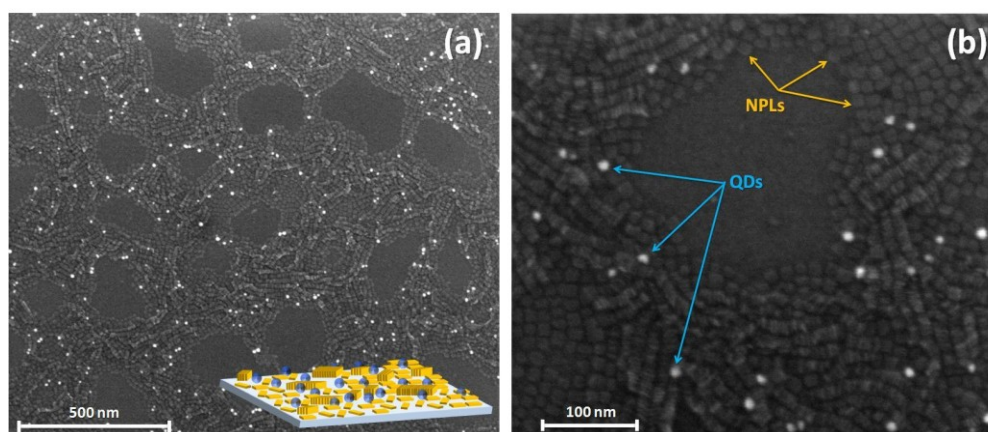


Figure 4.36. Scanning electron microscopy (SEM) images of the hybrid solid thin films of the donor QDs (bright ones) and the acceptor NPLs having 0.01 D/A molar ratio for (a) 500 nm and (b) 100 nm scale bars. The yellow and blue arrows given in (b) point at the QDs and the NPLs, respectively. Reprinted by permission from Wiley [110], Copyright 2015 Wiley-VCH Verlag GmbH & Co. KGaA, Weinheim.

Steady-state photoluminescence measurements revealed a clear evidence of NRET in the hybrid film incorporating both the donor QDs and the acceptor NPLs. Figure 4.37 shows the steady state PL spectra of the thin films of only-donor, only-acceptor and a hybrid case of with a molar D/A ratio of 0.10, where all samples are excited at 350 nm by a continuous-wave light source. Hybrid film exhibits strong quenching of donor emission (at 453 nm), while the acceptor emission (at 513 nm) is simultaneously

enhanced. The quenching ratio of the donor emission suggests energy transfer efficiency to be ~90%.

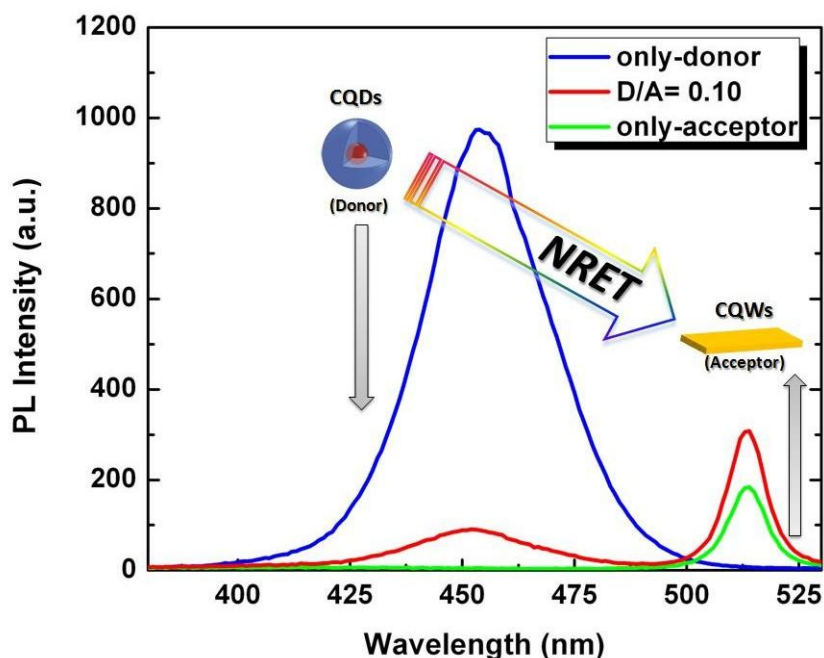


Figure 4.37. Steady-state PL spectra of the solid films of only-donor (blue line), only-acceptor (green line) and donor-acceptor having $D/A = 0.10$ (red line) cases. Reprinted by permission from Wiley [110], Copyright 2015 Wiley-VCH Verlag GmbH & Co. KGaA, Weinheim.

However, steady-state PL measurements are not only governed by the NRET, but also affected by the radiative energy transfer due to the absorption of the emitted photons by the acceptor NPLs. Therefore, we systematically studied the time-resolved PL kinetics in the hybrid samples with varying D/A ratio, which would directly reveal the NRET efficiencies and its kinetics. For this, we excited the samples using a picosecond pulsed pump laser at 375 nm. The decay curves (time-correlated single photon counting instrument, PicoQuant PicoHarp 300) were measured at the band edge emission peak of both donor (453 nm) and acceptor (513 nm) to study NRET at room temperature. There is no cross-talk between the emissions of the donor and acceptor due to narrow emission linewidths of the donor and acceptors. Figure 4.38 depicts the

fluorescence decay curves of the prepared samples with different D/A molar ratios. As seen in Figure 4.38a, the PL decay of the donor QDs becomes faster as the acceptor content of the hybrid film increases. This strongly indicates that an additional relaxation process (*e.g.*, NRET) for the excited state in the donor QDs opens up and it becomes dominant with increasing the NPL acceptor concentration in the hybrid films. On the other hand, in the case of the PL decay curves of the acceptor, the decay is observed to slow down with increasing concentration of the QD donors. This elongation in the acceptor decay has been previously observed for the QD, nanorods and NPL acceptors, which is the characteristic signature of the delayed luminescence arising from the recombination of the excitons that have been transferred from the donors. Therefore, the changes in the PL decay kinetics of both donor and acceptor indicate the presence of strong exciton transfer/funneling by NRET [97].

To analyze the PL decay curves, all collected fluorescence decay data were fitted with multi-exponential decay functions. We used four exponential decay functions for both donor and acceptor, which has been previously found to be intrinsic for NPLs and this type of QDs [58], [223]. The pump laser intensity (at 375 nm, PicoQuant picosecond pulsed laser) was also kept low (~ 1 nJ/cm²) so that number of photogenerated excitons per QD and NPL was much less than 1 to avoid multiexciton effects. The fitting parameters and the amplitude-averaged photoluminescence lifetimes (τ_{av}) of the donor QDs and the acceptor NPLs are summarized in Table 4.5 and

Table 4.6. τ_{av} of the donor QDs decreases from 8.78 (donor-only sample) to 0.92 ns (sample with D/A=0.01, where there is the largest number of acceptors per donor). Furthermore, τ_{av} of the donor saturates at ~ 0.90 ns. These major modifications in the PL lifetime of the donor as a function of the increasing number of acceptor per donor can be explained by the strong energy transfer from the donor QDs to the acceptor NPLs. In the case of acceptors, τ_{av} is increased from 0.48 (acceptor-only sample) to 2.19 ns (sample with D/A=1.37, where there is the largest number of donors per acceptor).

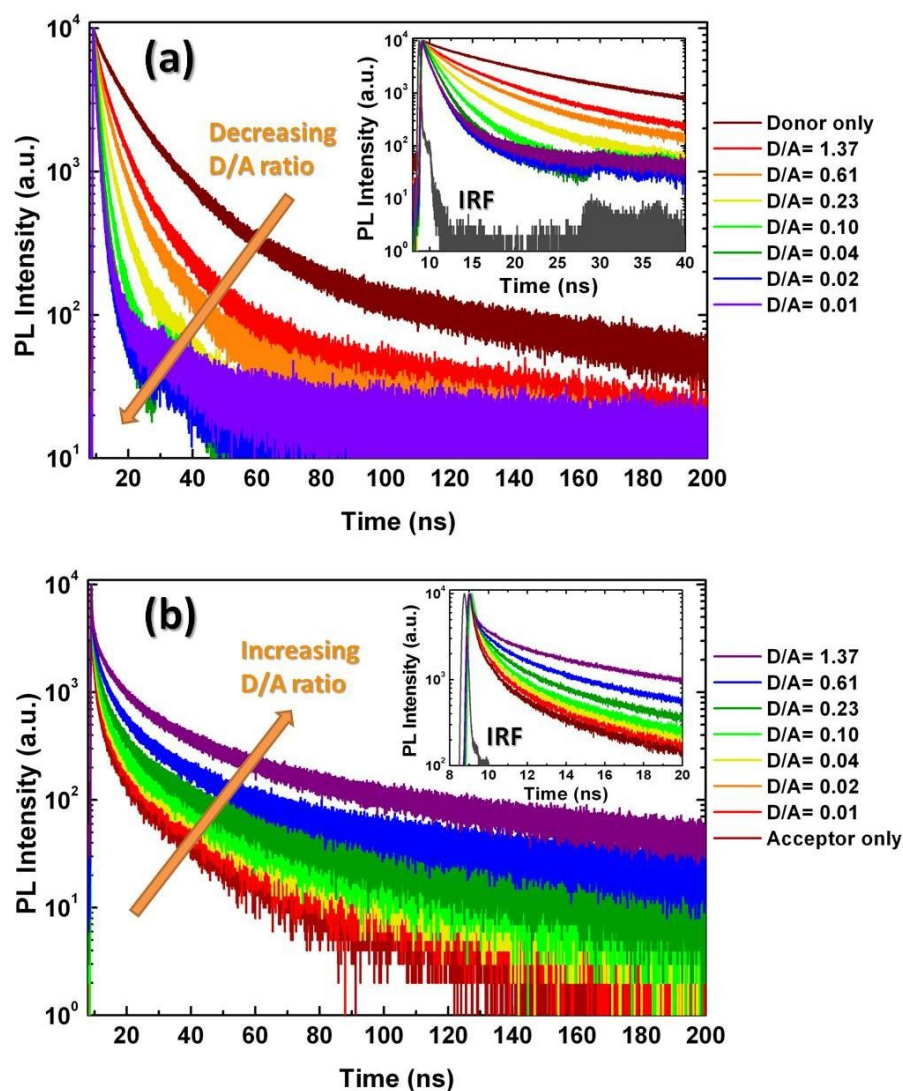


Figure 4.38. Time-resolved fluorescence decay curves of the solid thin film samples including donor-only, acceptor-only and hybrid cases with varying D/A molar ratios measured (a) at the donor band-edge emission wavelength (453 nm) and (b) at the acceptor band-edge emission wavelength (513 nm). The insets show the zoom-in of the same decay curves and the impulse response function (IRF). Reprinted by permission from Wiley [110], Copyright 2015 Wiley-VCH Verlag GmbH & Co. KGaA, Weinheim.

Table 4.5. Fluorescence lifetime components of the solid thin film samples measured at the peak emission wavelength (453 nm).

Sample	TRF decay components								Amplitude- average lifetimes ($\frac{\sum A_i \times \tau_i}{\sum A_i}$)
	τ_1 (ns)	τ_2 (ns)	τ_3 (ns)	τ_4 (ns)	A_1	A_2	A_3	A_4	τ_{av} (ns)
s-1	41.25	5.74	1.18	0.35	40.70	359.3	7076	9095	0.92
s-2	42.70	5.54	1.18	0.41	28.84	298.5	6853	8576	0.92
s-3	34.11	4.19	1.32	0.55	33.14	674.2	10930	13248	1.08
s-4	32.00	4.80	1.59	0.55	44.47	1083.1	10457	7742	1.42
S-5	33.85	5.74	1.90	0.53	62.60	2358.4	7184	4308	2.26
s-6	31.35	6.68	2.19	0.51	189.6	4176.0	7673	5900	2.99
s-7	33.78	7.70	2.62	0.55	313.4	5544.7	6179	5690	4.09
Only-D	81.99	21.31	8.61	1.52	212.8	1917.2	8553	5260	8.78

Sample	Standard deviation in TRF decay components								τ_{av} (ns)
	τ_1 (ns)	τ_2 (ns)	τ_3 (ns)	τ_4 (ns)	A_1	A_2	A_3	A_4	
s-1	±3.79	±0.35	±0.03	±0.02	±3.74	±30.7	±220	±823	±0.03
s-2	±4.44	±0.35	±0.03	±0.03	±3.15	±28.8	±215	±646	±0.04
s-3	±3.29	±0.19	±0.02	±0.03	±3.98	±54.8	±299	±1110	±0.04
s-4	±2.22	±0.20	±0.03	±0.03	±4.69	±57.6	±251	±992	±0.05
S-5	±1.95	±0.09	±0.04	±0.06	±5.36	±60.9	±201	±717	±0.06
s-6	±1.08	±0.08	±0.05	±0.07	±9.40	±72.9	±240	±1700	±0.07
s-7	±0.85	±0.08	±0.08	±0.08	±12.1	±79.3	±230	±1540	±0.09
Only-D	±3.78	±0.30	±0.08	±0.13	±7.46	±37.3	±101	±856	±0.14

Sample	Fractional emission contributions ($\frac{A_i \times \tau_i}{\sum A_i \times \tau_i}$)			
	$A_1 \times \tau_1$ (%)	$A_2 \times \tau_2$ (%)	$A_3 \times \tau_3$ (%)	$A_4 \times \tau_4$ (%)
s-1	11.01	13.53	58.80	20.65
s-2	8.51	11.44	55.77	24.28
s-3	4.62	11.55	59.13	24.71
s-4	5.17	18.90	60.37	15.56
S-5	6.55	41.85	44.49	7.11
s-6	11.08	52.01	31.33	5.58
s-7	14.59	58.87	22.26	4.28
Only-D	12.47	29.20	52.61	5.72

Table 4.6. Fluorescence lifetime components of the solid thin film samples measured at the acceptor peak emission wavelength (513 nm).

Sample	TRF decay components								Amplitude- average lifetimes ($\frac{\sum A_i \times \tau_i}{\sum A_i}$)
	τ_1 (ns)	τ_2 (ns)	τ_3 (ns)	τ_4 (ns)	A_1	A_2	A_3	A_4	τ_{av} (ns)
Only-A	36.53	6.66	1.28	0.20	74.87	534.0	2133	27840	0.48
s-1	37.17	6.93	1.37	0.20	109.97	673.0	2306	35350	0.49
s-2	37.58	7.09	1.43	0.21	88.28	603.3	2218	34610	0.48
s-3	34.87	6.67	1.46	0.22	125.76	700.6	2467	38200	0.51
s-4	34.94	6.83	1.53	0.23	144.52	789.1	2794	35230	0.59
s-5	38.54	7.47	1.55	0.22	176.09	1059.0	3223	19530	1.00
s-6	41.75	8.44	1.84	0.21	259.49	1377.5	2880	22200	1.21
s-7	47.91	9.99	2.03	0.21	478.70	1826.9	2600	17980	2.19
Standard deviation in TRF decay components									
Sample	τ_1 (ns)	τ_2 (ns)	τ_3 (ns)	τ_4 (ns)	A_1	A_2	A_3	A_4	τ_{av} (ns)
Only-A	±1.47	±0.28	±0.07	±0.01	±4.39	±27.8	±154	±1690	±0.02
s-1	±1.62	±0.26	±0.08	±0.01	±5.29	±31.2	±163	±2280	±0.02
s-2	±1.87	±0.27	±0.08	±0.01	±4.86	±29.3	±155	±2150	±0.02
s-3	±1.16	±0.26	±0.07	±0.01	±5.79	±33.5	±165	±2300	±0.02
s-4	±1.11	±0.26	±0.07	±0.01	±6.24	±35.7	±168	±2210	±0.02
s-5	±0.95	±0.23	±0.07	±0.01	±6.60	±37.9	±168	±1450	±0.03
s-6	±1.06	±0.21	±0.09	±0.01	±7.93	±40.6	±158	±1880	±0.03
s-7	±0.78	±0.21	±0.12	±0.01	±10.4	±45.0	±164	±1680	±0.05
Fractional emission contributions ($\frac{A_i \times \tau_i}{\sum A_i \times \tau_i}$)									
Sample	$A_1 \times \tau_1$ (%)		$A_2 \times \tau_2$ (%)		$A_3 \times \tau_3$ (%)		$A_4 \times \tau_4$ (%)		
Only-A	18.68		24.30		18.72		38.30		
s-1	21.61		24.66		16.67		37.06		
s-2	18.37		23.70		17.56		40.34		
s-3	20.74		22.10		16.98		40.18		
s-4	22.07		23.55		18.67		35.71		
s-5	28.14		32.66		20.86		18.34		
s-6	33.49		35.94		16.37		14.20		
s-7	45.65		36.34		10.49		7.52		

Subsequently, we analyzed the energy transfer rates (k_{NRET}) and efficiencies (η_{NRET}) for all hybrid samples using the fitted PL decay parameters. Table 4.7 shows the rate of energy transfer as a function of the D/A ratio. As the number of acceptor per donor is

increased, the NRET rate also increases. The maximum average k_{NRET} was computed to be 0.97 ns^{-1} . In our analysis,

$$\frac{1}{\tau_{DA}} = \frac{1}{\tau_D} + \frac{1}{k_{NRET}} \quad (4.11)$$

was used, where τ_{DA} and τ_D are the amplitude-averaged PL lifetimes of the donor QDs in the presence and absence of acceptor NPLs, respectively. The efficiency of the energy transfer was obtained by the following relation:

$$\eta_{NRET} = 1 - \frac{\tau_{DA}}{\tau_D} \quad (4.12)$$

Figure 4.39 depicts η_{NRET} as a function of the varying donor-to-acceptor molar concentration ratio. NRET efficiencies progressively increase with the decreasing D/A ratio. Also, η_{NRET} saturates at $\sim 90\%$ for the D/A ratios below 0.04. To the best of our knowledge, this NRET efficiency is the highest reported efficiency at room temperature between colloidal nanocrystal ensembles. Previously, the NRET efficiency was reported up to 80% in the case of QD-based donor-acceptor pairs [200], [224]. Using all NPL based donor-acceptor pairs, the NRET efficiency was limited ($\sim 60\%$) in the hybrid solid thin films of 4 ML and 5 ML NPLs donor-acceptor pairs due to inter-NPL stacking [68]. Recently, Talapin group [87] has shown that NRET between 4 ML and 5 ML NPLs can be as efficient as $\sim 90\%$. However, this NRET was only limited to donor-acceptor pairs that are face-to-face stacked and only separated by the ligands. As discussed in the latter work, these face-to-face stacked donor-acceptor NPLs are very few in number in the ensemble. Therefore, the ensemble NRET efficiencies were much lower.

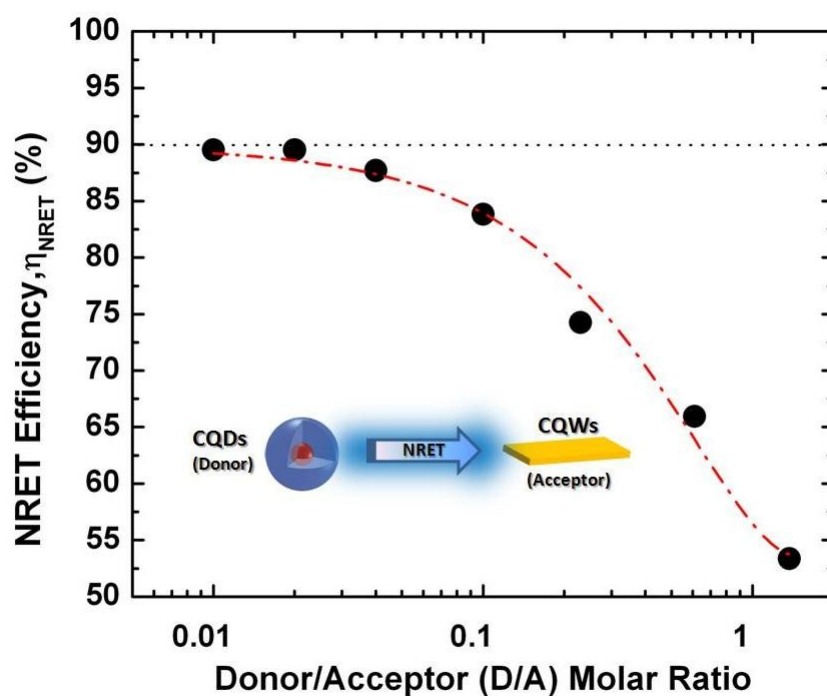


Figure 4.39. Evolution of the nonradiative energy transfer (NRET) efficiency as a function of the donor QDs to acceptor NPLs (D/A) molar ratios. The dash-dot lines are a guide for the eyes. Reprinted by permission from Wiley [110], Copyright 2015 Wiley-VCH Verlag GmbH & Co. KGaA, Weinheim.

Förster radius in the QD-NPL donor-acceptor system was also calculated. To this end, the molar extinction coefficient of the NPL acceptors at 512 nm was calculated to be $1.46 \times 10^7 \text{ M}^{-1} \text{ cm}^{-1}$, while the quantum yield (QY) of the QD donors in film was determined to be 38% using an integrating sphere. In addition, the refractive index of the medium was taken to be 1.8, whereas for the dipole orientation factor (κ^2) we used $2/3$ corresponding to random dipole orientations. Using these parameters given above, the Förster radius was computed to be 9.51 nm. In addition, to estimate the distance between the adjacent QDs and NPLs, we also used the calculated Förster radius and found the closest distance between the QDs and the NPLs to be 5.48 nm by taking into account the distance scaling of the exciton transfer in our hybrid system is r^{-4} , where the r is average distance between donor and acceptor [213].

Table 4.7. Donor QDs and acceptor NPLs lifetimes (τ), their NRET rates (k_{NRET}) and efficiencies (η_{NRET}) with varying D/A ratios.

D/A Ratio	τ_{acceptor} (ns)	τ_{donor} (ns)	k_{NRET} (ns^{-1})	η_{NRET}
Acceptor only	0.48	---	---	---
0.01	0.49	0.92	0.973	0.90
0.02	0.48	0.92	0.973	0.90
0.04	0.51	1.24	0.686	0.86
0.10	0.59	1.65	0.492	0.81
0.23	1.00	2.26	0.329	0.74
0.61	1.21	2.99	0.221	0.66
1.37	2.20	4.09	0.130	0.53
Donor only	---	8.78	---	---

To further investigate the steady-state evidence of NRET, the photoluminescence excitation (PLE) spectroscopy was carried out for the donor-acceptor hybrid thin film samples. Figure 4.40a depicts the PLE spectra of the thin films including the bare donor and the bare acceptor, which were measured for their peak emission wavelengths. Excitation spectra given in Figure 4.40a exhibit similar spectral features as the absorption spectra of the QDs and NPLs (see Figure 4.35). For example, the peak at 480 nm in the excitation spectrum of the NPLs arises from the electron-light hole (e-lh) transition in the absorption spectrum of acceptor NPLs. We also measured the excitation spectra of the hybrid donor-acceptor samples with varying D/A molar ratios. Figure 4.40b exhibits the excitation spectra of the NPLs (measured at the emission wavelength of 513 nm) in four different hybrid samples with the D/A molar ratios of 0.02, 0.10, 0.23 and 0.61. These excitation spectra are normalized at the e-lh transition peak (~ 480 nm) of the NPLs since donor QDs do not have any absorption at this wavelength (see Figure 4.35a). Therefore, Figure 4.40b depicts the normalized excitation spectra of the NPLs in their hybrids. The excitation spectra of the NPLs show increased intensity at shorter wavelengths as the number of donor QDs per NPL is increased (*i.e.*, increasing D/A ratio).

Furthermore, the spectral enhancements in the excitation spectra of the hybrid samples were computed by dividing the normalized excitation spectra of the hybrid cases to that of the acceptor-only case. The inset of Figure 4.40b represents the relative

spectral enhancement of the acceptor NPL emission due to the NRET from the donor QDs for different D/A molar ratios. The enhancement of the excitation curve resembles the absorption of the donor QDs as expected. Furthermore, the spectral enhancement is found to reach to 2-folds for the sample with a large number of donors per acceptor (D/A = 0.61).

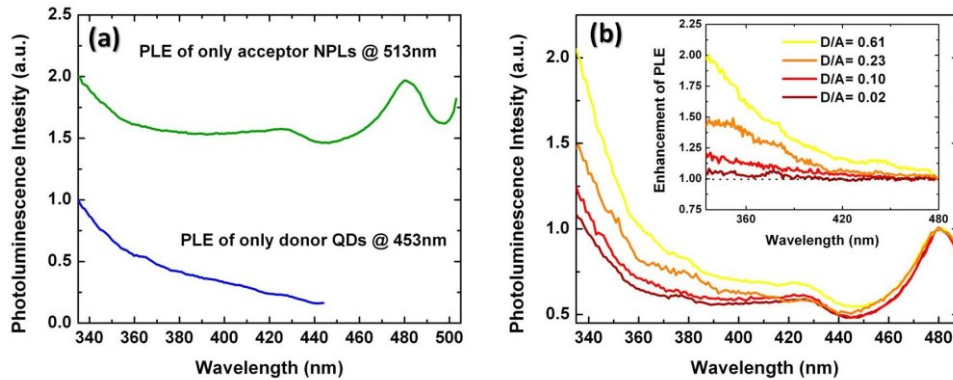


Figure 4.40. (a) Photoluminescence excitation (PLE) spectra of the only-donor QDs (blue-line) and the only-acceptor NPLs (green-line) measured at their emission peak wavelengths (453 and 513 nm, respectively). (b) Excitation spectra of the samples having different D/A ratio normalized at the e-lh transition peak wavelength (480 nm). The inset shows the enhancement in the excitation spectra of the hybrid donor-acceptor samples due to the NRET from donor QDs. Reprinted by permission from Wiley [110], Copyright 2015 Wiley-VCH Verlag GmbH & Co. KGaA, Weinheim.

To investigate the effect of temperature on the NRET in the hybrid solid thin films of the donor QDs-acceptor NPLs, we performed time-resolved fluorescence measurements as a function of the temperature under vacuum using a closed-cycle He cryostat. We investigated the thin film sample exhibiting the highest NRET efficiency (~90 %) at room temperature, which has the lowest D/A molar ratio (*i.e.*, 0.01), together with the donor-only and the acceptor-only samples as the reference samples. The measured PL decay curves as a function of the temperature were again fitted by multi-exponential decay functions. In the case of the donor-only in Figure 4.41a and the acceptor-only in Figure 4.41b, the PL decay curves are accelerated with decreasing temperature from 270 to 50 K. Such a temperature dependent PL lifetime behavior was previously reported for the NPLs [57] and epitaxial QWs [74], revealing the giant

oscillator strength transition (GOST) in these materials. The PL lifetime measurements were also carried out for the hybrid sample. Figure 4.41c and Figure 4.41d show the PL decay curves taken at the maximum PL emission peak of the donor and acceptor as a function of the temperature, respectively. Temperature-dependent NRET efficiencies were computed and presented in Figure 4.42a. At 270 K, the NRET efficiency is found to be about 87%. Here, the slight decrease in the NRET efficiency, which was measured as 90% at RT under ambient conditions, can be due the measurement of the decay curves under vacuum conditions. A recent report indicated that the PL lifetime of the NPLs is affected by the oxygen physisorbed at surface of the NPLs [225]. Oxygen passivation of the surface traps elongates the PL lifetime in the NPLs under ambient conditions as compared to the vacuum. Therefore, the change of the PL kinetics of the acceptor is expected to slightly change the overall NRET efficiency under vacuum. As it is seen from Figure 4.42a, with decreasing temperature, the NRET efficiency increases almost linearly. More importantly, NRET efficiency remarkably reaches 94% at 50 K.

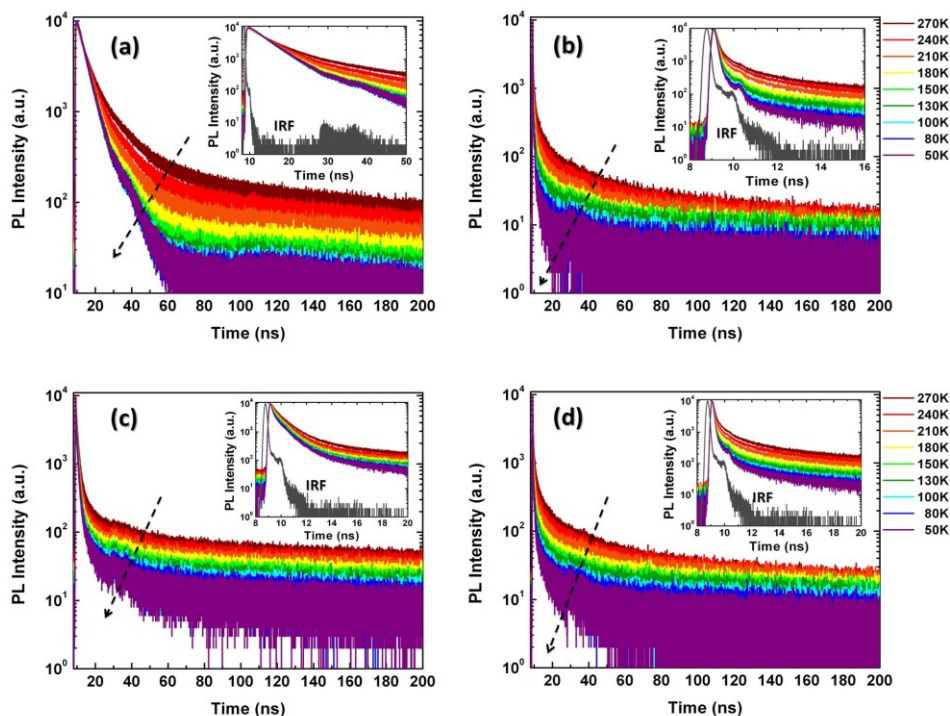


Figure 4.41. Time-resolved fluorescence decay curves of the solid thin film samples including (a) the donor-only, (b) the acceptor-only, and the blended case of donor and

acceptor for D/A=0.01 molar ratio measured (c) at the donor band-edge emission wavelength (453 nm) and (d) at the acceptor band-edge emission wavelength (513 nm). The dashed arrows show the direction of decreasing temperature. The insets show the zoom-in for the early phase, along with the impulse response function (IRF). Reprinted by permission from Wiley [110], Copyright 2015 Wiley-VCH Verlag GmbH & Co. KGaA, Weinheim.

To explain the increase in NRET efficiency with decreasing temperature, one possible hypothesis is the enhancement in the spectral overlap between the emission spectrum of the donor and the absorption spectrum of acceptor. To investigate this hypothesis, we first performed the temperature-dependent transmission (T) measurements to obtain the absorption behavior of the acceptor with temperature. 1-T (*i.e.*, absorption and reflection) curves are presented in Figure 4.43a. In addition, the temperature-dependent PL spectra of the donor were taken (see Figure 4.43b). We observed that the absorption spectra of the acceptor and the PL spectra of the donor are blue-shifted with decreasing temperature. The calculated spectral shifts (Δ_{Shift}) for given a five set of temperatures (*i.e.*, 270, 240, 210, 180 and 150 K) are given in

Table 4.8. Also, we calculated the spectral overlap (J) integral using the spectral shift differences between the emission of the donor and absorption of acceptor as a function of temperature (see

Table 4.8). For this, we used the spectral information in Figure 4.43a. We computed relative enhancement of the NRET efficiencies in the 250-150 K range and compared them with the experimentally measured NRET efficiencies. Here, we first calculated the relative enhancement of the NRET efficiency by assuming the same parameters (*e.g.*, κ^2 , n, QY and r) while only considering the changing spectral overlap as a function of the temperature. The Figure 4.43b shows the computed efficiencies (black diamond) along with the experimental data (blue solid circle). The change due to the spectral overlap does not successfully predict the change in the NRET efficiency as a function of the temperature.

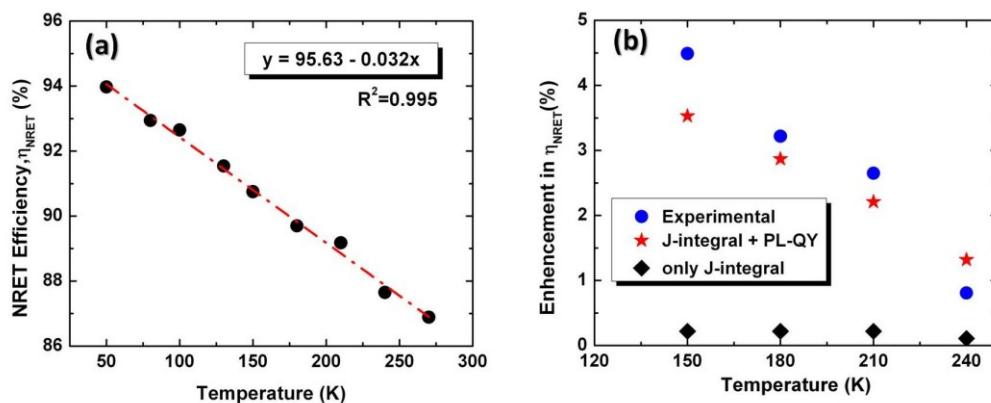


Figure 4.42. (a) Evolution of the NRET efficiency (η_{NRET}) for D/A=0.01 ratio as a function of the temperature. The dash-dot lines show the linear fitting curve with 0.032 of slope. (b) Enhancement in η_{NRET} corresponding based on the experimental data (blue-circle) and the calculated results using the shift in spectral overlap between the PL spectrum of donor and the absorption spectrum of acceptor (black-diamond) and those using both the shift in spectral overlap and the change in PL QY with decreasing temperature. Reprinted by permission from Wiley [110], Copyright 2015 Wiley-VCH Verlag GmbH & Co. KGaA, Weinheim.

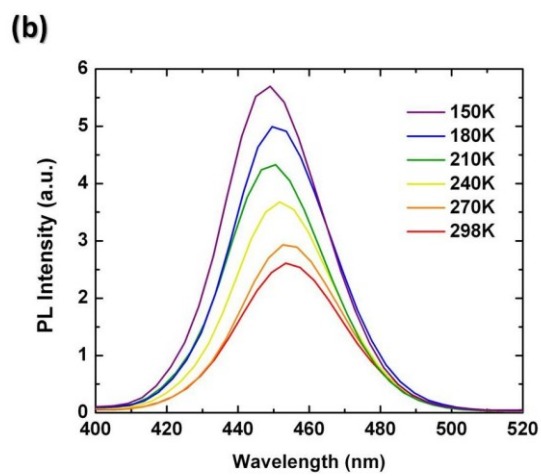
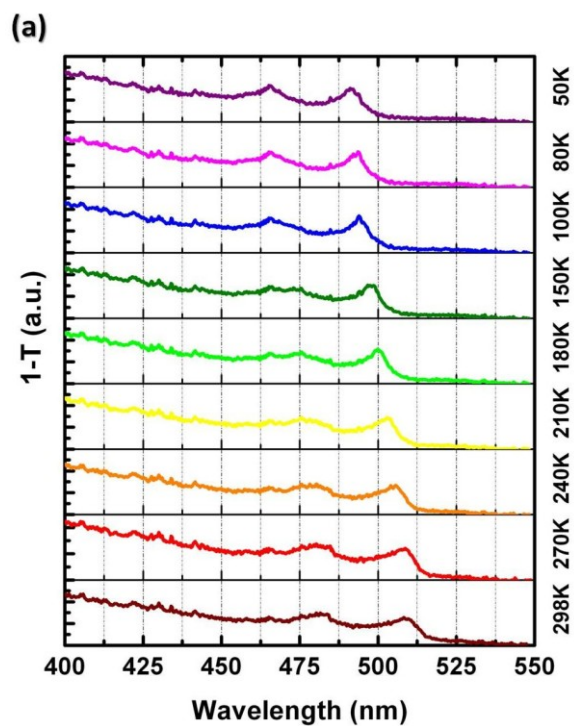


Figure 4.43. (a) Temperature dependent 1-T (transmission) spectra for the acceptor-only case. (b) Photoluminescence (PL) spectra of the donor-only case at different temperatures.

Table 4.8. The calculated NRET efficiencies (η_{NRET}) and enhancement in the η_{NRET} for different temperature points. Here, Δ_{Shift} is the shift in the spectral overlap between the PL spectrum of donor and the extracted absorption spectrum of acceptor with decreasing temperature; η_{NRET} is the NRET efficiency using amplitude-average lifetimes; $\eta_{\text{NRET-1}}$ is the NRET efficiency calculated using Δ_{Shift} ; $\eta_{\text{NRET-2}}$ is the NRET efficiency calculated using Δ_{Shift} and quantum yield (QY) of the donor while the temperature is decreased; $\Delta-0$, $\Delta-1$ and $\Delta-2$ are the enhancements in η_{NRET} , $\eta_{\text{NRET-1}}$ and $\eta_{\text{NRET-2}}$, respectively, with respect to the NRET efficiency value at 270 K.

T (K)	η_{NRET} (%)	$\Delta-0$ (%)	Δ_{Shift} (nm)	J-integral ($\text{cm}^{-1}\text{M}^{-1}\text{nm}^4$)	$\eta_{\text{NRET-1}}$ (%)	$\Delta-1$ (%)	PL-QY (%)	$\eta_{\text{NRET-2}}$ (%)	$\Delta-2$ (%)
270	86.9	---	0.45	3.50×10^7	90.0	---	41.6	90.6	---
240	87.6	0.81	1.66	3.53×10^7	90.1	0.11	51.4	91.8	1.32
210	89.2	2.65	3.39	3.59×10^7	90.2	0.22	60.2	92.6	2.21
180	89.7	3.22	3.43	3.59×10^7	90.2	0.22	69.8	93.2	2.87
150	90.8	4.49	4.19	3.62×10^7	90.2	0.22	79.0	93.8	3.53

Next, we considered PL QY of the donor QDs as a function of the temperature. To this end, we measured the PL QY of the donor for the temperature range under consideration. We found that PL QY of the donor QDs increases from 38 to 79% when the temperature is decreased from RT to 150 K (see Figure 4.43b and

Table 4.8). We calculated the relative enhancement of the NRET efficiency (red star) by assuming the same parameters (*e.g.*, κ^2 , n and r) while taking into account the changing quantum yield and spectral overlap as a function of the temperature. The inclusion of the temperature dependent PL QYs resulted in very close agreement with the experimentally observed enhancement of the NRET efficiency over temperature as shown in Figure 4.43b. The computed NRET efficiencies ($\eta_{\text{NRET-2}}$) for different temperatures are given in

Table 4.8 and the percentage increments in calculated efficiency exhibit very close match with the experimental ones. For example, the percentage enhancements in

NRET efficiency (Δ -2) were calculated to be 1.32, 2.21, 2.87 and 3.53% (see the red stars in the Figure 4.43b) corresponding to the NRET efficiency value at 270 K, whereas they were computed to be 0.81, 2.65, 3.22 and 4.49% (see the blue solid circles in the Figure 4.43b) for 240, 210, 180 and 150 K, respectively.

Very interestingly, a perfect linear correlation between energy transfer efficiency and temperature was observed as shown in Figure 4.43a. This highlights the potential of the QD-NPL hybrid system for optical thermal probe applications. Previously, temperature sensing nanocomposites that rely on energy transfer have been studied and proposed. However, all of these previous works have used the change of absolute steady state emission intensities to relate to the temperature change [208], [226]–[229]. Since absolute intensity of the steady state emission is very sensitive to measurement conditions such as sample position, detector itself and photobleaching, reliability of the previous temperature probing using nanocomposites based on ratiometric sensing was quite limited. Different from previously common ratiometric sensing, the presented NRET efficiency represents a new metric for non-contact temperature sensing, which can possibly overcome the reliability limitation of previous nanoscale temperature probes. As shown in Figure 4.43a, we remarkably achieve a sensitivity level as high as 3.2% per K in the broad range of 50-300 K, which is enabled by efficient exciton transfer unique to the QD-NPL hybrids. To the best of our knowledge, our sensitivity level is comparable to the best reported sensitivities (3.5% per K) in non-contact nanoscale temperature probes [228], [229]. In addition to temperature sensing, these nanocomposites with such exceptional exciton transfer efficiencies can further be used in light-harvesting applications in solar cells and artificial photosynthesis.

4.5.4 Summary

In summary, we have investigated the nonradiative energy transfer of excitons in solid thin films of the hybrid ensembles of colloidal CdZnS/ZnS core/shell QDs and CdSe NPLs as a function of the temperature. We found remarkably high NRET efficiencies reaching 90%, which is enabled by large absorption cross-section of the NPLs. To the best of our knowledge, this NRET efficiency level is the highest between colloidal

semiconductor nanocrystals reported ever to date. In addition, NRET efficiencies were observed to exhibit highly linear monotonic response and increase with decreasing temperatures, reaching maximum levels as high as 94%, which is well explained by the increasing PL QY of the donor QDs at low temperatures. Owing to the highly linear monotonic behavior of the NRET efficiency with decreasing temperature in the range of 50 – 300 K, this QD-NPL hybrid system is suitable for the temperature sensing applications with significantly high sensitivity. This presents a new metric based on change of NRET efficiency for contact-free temperature sensing, which could possess improved reliability as compared to previously reported nanoscale temperature probes that rely on ratiometric sensing principle. We also believe that such highly efficient NRET between these two colloidal systems having different quantum confinement dimensionality (QDs and NPLs) will enable high-performance optoelectronic devices utilizing NRET at high efficiency.

4.6 Summary of the chapter

In this part of the thesis, we have explored the potential of colloidal nanoplatelets as efficient exciton transferring species in their assemblies at the nanoscale.

- 1) We studied exciton transfer among the nanoplatelets having the same vertical thickness for the first time and uncovered ultraefficient exciton transfer rates and ultrahigh exciton transfer efficiencies.
 - a. We showed that extremely large Förster radii (>10 nm) are possible when using the nanoplatelets as the exciton acceptors thanks to their large absorption cross-section.
 - b. We unveiled ultrafast (~ 3 ps) and ultraefficient ($\sim 99.9\%$) exciton transfer in controllably face-to-face assembled nanoplatelet stacks.
 - c. We estimated exciton transport lengths on the order of 100 nm, which is an order of magnitude larger than that of the conventional nanocrystals. This could heavily impact solar cells and artificial photosynthesis applications that require large exciton diffusion lengths for high efficiencies.

- d. We revealed the important consequence of the efficient exciton transport in the nanoplatelet ensembles, which is the exciton transfer assisted exciton trapping due to the presence of the defected nanoplatelets in their ensembles. This phenomenon causes strongly quenched photoluminescence in the close-packed and stacked nanoplatelet assemblies.
- 2) We investigated the exciton transfer in the nanoplatelet films incorporating different populations having different vertical thicknesses.
 - a. We realized photoluminescence enhancement up to 3-folds in the acceptor nanoplatelets (having larger vertical thickness) owing to the exciton transfer from the nanoplatelets with smaller vertical thickness, which act as the exciton transferring antenna.
 - b. Exciton transfer efficiencies were limited by 60% in the NPL ensembles in contrast to theoretical expectations, where ~99% exciton transfer efficiency was estimated. This limitation was observed to arise from the fact that the nanoplatelets with different vertical thicknesses tend to form their own face-to-face stacked assemblies, leading to a nanoscale phase segregation that physically separates the donor-acceptor species.
 - c. We suggest that the nanoplatelets could be effectively used as both exciton transferring antennas and exciton sinks that can find applications both in light-harvesting and light-generation applications.
 - d. After our works, Talapin group [87] demonstrated the evidence of ultrafast (10 ps) exciton transfer among the nanoplatelets having different vertical thickness, fully supporting our predictions and observations. Due to the similar lateral extent of nanoplatelets with different vertical thickness, inter-stacking of these different nanoplatelets was possible without suffering from the nanoscale phase segregation.
 - 3) We proposed and demonstrated for the first time a nanoplatelet – conjugated polymer hybrid system, which showed dominantly exciton dissociation instead of exciton transfer due to the favorable staggered band alignment.

- a. Nanoplatelet – conjugated polymer hybrids can be used for solar-cells and photodetectors since excitons can be efficiently dissociated.
 - b. Utilization of nanoplatelets and their large planar surfaces may allow for fast hole transfer from the inorganic part into the organic semiconductor, which has remained as a challenge in quantum dot – conjugated polymer hybrids to date.
- 4) We developed colloidal quantum dot – nanoplatelet hybrids for the first time. These blended systems reached exceptionally high exciton transfer efficiencies as high as 94%.
- a. We achieved highly linear response of exciton transfer efficiency as a function of temperature (40 – 300 K) that allowed using these blended hybrid assemblies as highly sensitive non-contact temperature probes.

Chapter 5

Excitonic Light-Generation Using Colloidal Nanocrystals

5.1 Introduction to excitonic light-generation

The nanocrystals can be used as light-emitters in light-emitting diodes (LEDs) in two different strategies. The first method relies on using nanocrystals as color conversion materials, where a blue LED is used to excite them optically, and then the nanocrystals fluoresce. The second method is based on the electrical charge injection, which leads to exciton formation in the nanocrystals, and then they electroluminesce. In both cases, it is desired to have many of the generated excitons end up in the nanocrystals that are targeted to generate the photons with the desired spectral properties (e.g., emission wavelength and linewidth). Therefore, it is crucial to understand and control the exciton flow at the nanoscale to achieve efficient light-generation. To realize ultrahigh efficiency nanocrystal-based light-engines, it is essential to form the excitons either in the nanocrystals directly or funnel the excitons into the nanocrystals before these

excitons have been trapped, nonradiatively recombined, annihilated or dissociated somewhere else.

The first electrically driven LED of colloidal quantum dots was developed by Alivisatos group in 1994, which had shown the potential of these materials for electroluminescent devices [33]. In the early days of the quantum dot LEDs, the fundamental challenge was the poor device performance arising from the poor charge injection and transport across the thin-films of the colloidal nanocrystals due to their organic ligands. The organic ligands (also the so-called surfactants) bestow stability and solubility to the nanocrystals as well as preserving their intrinsic optical properties via passivating the dangling bonds at their surfaces. Yet, due to their insulating nature, these organic ligands have been believed to create large electronic barrier against efficient charge injection and transport across the nanocrystal films.

In the last decade, different methods have been developed to overcome this limitation in the nanocrystal films. The most efficient technique has been identified to use very thin quantum dot layers (a monolayer or few layers) to alleviate the burdens of the poor charge transport. This method was first proposed by Bulovic and Bawendi groups in 2002 [230]. These LEDs possessing very thin emissive quantum dot layer (generally a monolayer) have created an ever increasing interest [16]. These LEDs are commonly based on multiple layers, including charge injection and blocking layers, that help to control the charge balance in these devices. However, complexity arising from the presence of multiple interfaces (e.g., interface between the electron transport layer and the quantum dots) that generally comprise organic and inorganic semiconductors (e.g., small organic molecules, conjugated polymers, ZnO nanoparticles) results in the difficulty of spatially controlling the exciton recombination zone in these devices. Since quantum tunneling can be efficient at these interfaces, excitons can be easily transferred to the adjacent transport layers. Thus, these excitons instead of ending up in the quantum dot emissive layer, they could leak into the adjacent layers, and can either radiatively and nonradiatively recombine in the adjacent layer. Furthermore, these excitons can be also trapped at the interface, causing significant losses to overall electroluminescence efficiency.

It is possible to harvest excitons that have leaked into the adjacent transport layers by transferring them back into the emissive quantum dot layer via nonradiative energy transfer (through near-field dipole-dipole coupling - FRET). Although exciton harvesting has been considered in quantum dot LEDs [139], electroluminescent devices that actively use exciton recycling concept have remained elusive. To date, there has not been any quantum dot LED that had been developed to efficiently harvest the leaked excitons via nonradiative energy transfer.

Another important factor to consider is that the most common charge transport layers are commonly made of organic semiconductors (e.g., TCTA, TAZ, CBP as electron transport layers or poly-TPB as a hole transport layer). Due to spin-statistics, under electrical charge injection $\frac{3}{4}$ of the generated excitons in an organic semiconductor is in its triplet state, while the rest is in the single state [231]. Triplet state is a spin-forbidden state, thus, it has zero oscillator strength. Because of this, excitons that are in the triplet state cannot be used for light-generation neither can be transferred via FRET. To overcome this limitation, phosphorescent small organic molecules make advantageous class of organic semiconductors that could potentially harvest triplet state excitons. These molecules can efficiently make use of triplet states for light-generation thanks to enhanced spin-orbit coupling, which causes the mixing of the singlet and triplet states thanks to a strong inter-system crossing.

Previously, spectroscopic evidence of nonradiative energy transfer from a phosphorescent small organic molecule into a quantum dot has been observed, yet it was not clear whether this exciton transfer was mediated through NRET or Dexter-type energy transfer [232]. Few reports have also suggested to couple phosphorescent molecules with the quantum dots in electroluminescent devices [233], but it was not possible to achieve spectrally pure color emission in these LEDs due to poorly controlled exciton formation region and incomplete exciton transfer from the phosphorescent molecules into the QDs. Therefore, exciton harvesting schemes have not been fully understood nor implemented in quantum dot LEDs.

In this thesis, we have proposed and developed exciton harvesting organic layers that are adjacent to quantum dots, where organic layer comprises phosphorescent small organic molecules to utilize both singlet and triplet state excitons for harvesting back in to the QDs. We have investigated the exciton transfer both ex-situ (outside an active LED) and in-situ (in an active LED). These exciton harvesting systems are expected to boost the performance of the quantum dot LEDs and also other optoelectronic applications such as lasers.

5.2 Singlet- and triplet-state harvesting via energy transfer from phosphorescent molecules

This section is based on the publication “Singlet and Triplet Exciton Harvesting in the Thin Films of Colloidal Quantum Dots Interfacing Phosphorescent Small Organic Molecules,” **B. Guzelturk**, P. L. Hernandez-Martinez, D. Zhao, X. W. Sun and H. V. Demir, *The Journal of Physical Chemistry C* 118, 25964-25696 (2014). Adapted (or “Reproduced in part”) with permission from American Chemical Society. Copyright 2014 American Chemical Society.

5.2.1 Motivation

Phosphorescent small organic molecules have been promising materials for organic light-emitting diodes, owing to their luminescent triplet states, which enabled internal quantum efficiencies up to unity [234], [235]. On the other hand, optical properties of the phosphorescent molecules are not versatile; for example, it is difficult to tailor emission colour and the fwhm of the phosphorescent emission and it is generally wide [236], [237]. Alternatively, colloidal QDs are appealing fluorescent material systems, which are versatile light-engines owing to their high photoluminescence quantum yield and ease of colour tunability through quantum confinement effect and their narrow emission fwhm [238], [239]. Combining the favourable properties of these material systems holds great promise for achieving superior light-emitting materials towards efficient hybrid optoelectronic devices.

Previously, several works reported blended systems of the QDs and the phosphorescent molecules in the form of hybrid thin films [233], [240], [241]. In Refs. [233] and [241], a phosphorescent emitter was shown to enhance the electroluminescence performance of the QDs, which was attributed to the presence of energy transfer from the phosphorescent molecules into the QDs. However, this nonradiative energy transfer in these hybrid thin films were not understood well, nor engineered for the singlet and triplet exciton harvesting by the QDs [126].

To date, only Anikeeva *et al.* have experimentally shown the possibility of nonradiative energy transfer (NRET) in a bilayer thin film of a QD monolayer and green emitting phosphorescent small organic molecule Irppy₃ co-doped into the CBP (a fluorescent host). In this architecture, proof-of-concept demonstration of the fluorescence emission enhancement of the QDs was shown by a factor of 1.55 [232]. This enhancement was attributed to NRET, which is either due to FRET or Dexter-type energy transfer. Therefore, the underpinning mechanism of this energy transfer from phosphorescent Irppy₃ molecules, which are doped into CBP fluorescent host, into the QDs was not clear, nor understood in this aforementioned work [232]. More importantly, the potential of this type of nonradiative energy transfer in terms of enhancement of the emission of the QDs was not systematically studied before. Also, the effect of fluorescent host (i.e., CBP, TCTA, etc.) to the energy transfer into the QDs in these phosphorescent co-doped exciton donor media was not considered. However, these wide bandgap fluorescent host material could substantially affect the NRET because excitons are primarily formed in these fluorescent host and funnelled into the phosphorescent molecules and then transferred into the QDs via NRET.

5.2.2 Results and discussion

In this part of the thesis, we studied NRET in a bilayer organic-inorganic thin film consisting of phosphorescent emitter FIrpic that is doped into wide bandgap fluorescent host TCTA, where the organic layer is interfaced to the core/shell CdSe/ZnS QDs. Figure 5.1a exhibits the representative schematic of the hybrid bilayer thin films. FIrpic is a cyan-emitting phosphorescent molecule and was chosen specifically to enhance the spectral overlap between the donor emission and the acceptor QDs' absorption to maximize the critical energy transfer radius (i.e., Förster radius) [101]. The acceptor QDs, core/shell CdSe/ZnS, were chosen because of their increased environmental stability and ease of colour tunability through one-pot synthesis route [242]. Additionally, the inorganic ZnS shell thicker than 2 nm helps to block any charge injection into the QDs. We investigated the energy transfer when TCTA or FIrpic:TCTA layer was introduced to the QD layer via steady state and time

resolved fluorescence spectroscopies. Also, we showed direct evidence of NRET, which actually takes place into the QDs after a cascaded exciton transfer in the organic layer, through photoluminescence excitation (PLE) measurements. This type of cascaded energy flow has been observed for the thin films of all organic molecules before, but not in organic-inorganic hybrids [207], [243]. When the QDs were interfaced to the phosphorescent co-doped organic film, the excitons that were initially funnelled to FIrpic are now transferred to the QDs. Additionally, bare fluorescence host TCTA film is also an efficient energy transfer donor for the acceptor QDs even there is no phosphorescent co-doping owing to the efficient singlet exciton harvesting. In the case of FIrpic co-doped organic layers, NRET was found to be further enhanced as compared to the TCTA-only case owing to the increased dipole-dipole coupling and harvesting of the singlet and triplet excitons and also increased exciton diffusion in the phosphorescent co-doped organic layers. To reveal the potential of the NRET in these inorganic-organic system, we systematically varied the thickness of the organic film from 5 to 20 nm. The maximum enhancement factor of the fluorescence of the QDs was found to be as high as 2.5-folds when the organic film thickness is 20 nm. The theoretical energy transfer model that considers the exciton diffusion assistance to NRET, which was shown to be due to Förster-type dipole-dipole coupling, was proposed. This energy transfer model excellently predicted the experimental fluorescence enhancement factors in the QD emission.

In Figure 5.1b, absorbance and PL spectra of the QDs are shown together with the emission spectra of TCTA and FIrpic. The QDs have broad absorption spectra that match well with the emission of TCTA and FIrpic. Therefore, near-field coupling between FIrpic co-doped TCTA film and the QDs is expected to be strong.

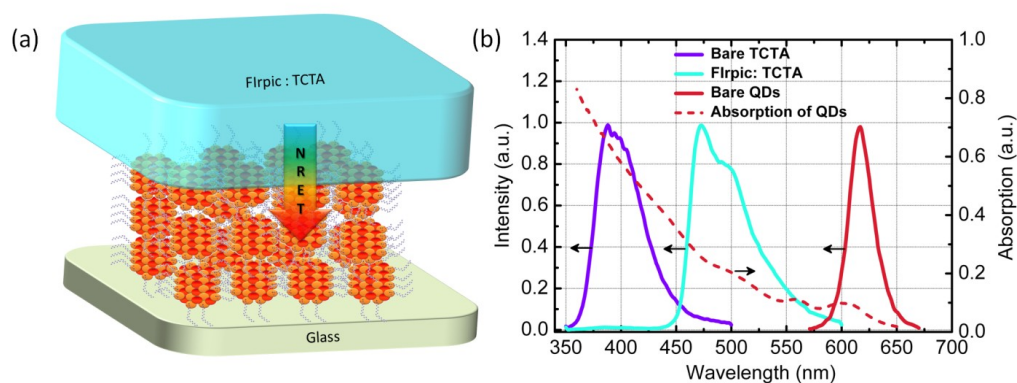


Figure 5.1. (a) Representative schematic of the organic-inorganic exciton transferring thin film. (b) Fluorescence of TCTA (violet), Flrpic (cyan) and QDs (red) along with the absorbance of QDs (red-dashed). Reprinted (or Adapted) with permission from [190]. Copyright 2014 American Chemical Society.

The energy transferring thin films were prepared first via spin coating of the QD layer on pre-cleaned glass substrates followed by the thermal evaporation (i.e., sublimation) of the organic films under high vacuum conditions (base pressure $< 4 \times 10^{-6}$ Torr). The thickness of the QD layer was measured as 20 nm (± 0.1 nm) by optical ellipsometry corresponding to an approximately three-monolayer-equivalent QD layer, as also verified by the small root mean square surface roughness (< 2 nm) via atomic force microscopy. The ellipsometry measurements were performed in the near infrared region to eliminate the absorption of the red-emitting QDs in the visible. For the organic film, the co-doping concentration of Flrpic in TCTA was set as 10% to prevent quenching of the triplet states. The thickness of the organic layer was varied between 5 and 20 nm while keeping the co-doping concentration as the same. We performed both steady state and time resolved fluorescence spectroscopy on the film samples including bare QDs, bare TCTA, Flrpic:TCTA, TCTA/QDs, and Flrpic:TCTA/QDs. Figure 5.2 exhibits the fluorescence of these samples (for the organic layer thickness of 20 nm), when excited by pump wavelength at 330 nm.

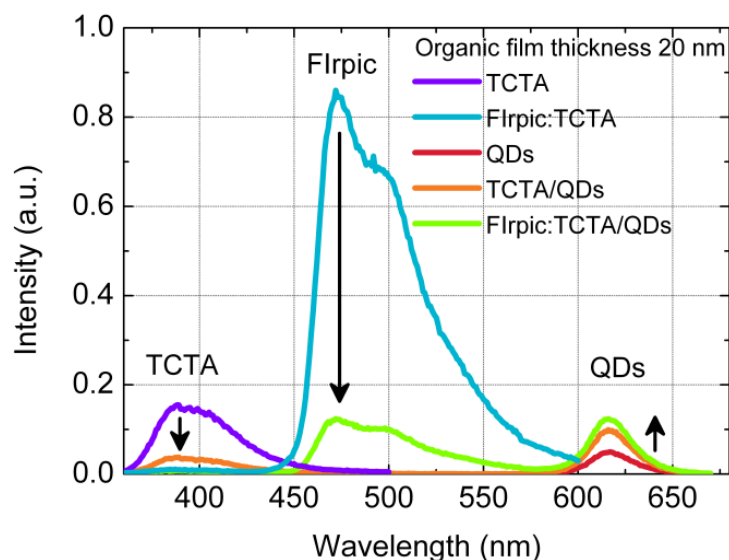


Figure 5.2. Steady state fluorescence spectra of only QDs (red), only TCTA (violet), FIrpic:TCTA (cyan), TCTA/QDs (orange) and FIrpic:TCTA /QDs (green). The organic layer thickness is 20 nm. Reprinted (or Adapted) with permission from [190]. Copyright 2014 American Chemical Society.

As shown by Figure 5.2, the emission of the TCTA peaks at 388 nm. FIrpic has a peak emission at 470 nm. For the FIrpic:TCTA sample, the emission of TCTA was completely suppressed due to the almost complete exciton funnelling into FIrpic from TCTA [243]. When the organic layer was interfaced with the QDs, the QDs acted as an efficient exciton sink for the co-doped organic layer. Due to NRET, the emission of TCTA and/or FIrpic is quenched, while the emission of the QDs is simultaneously enhanced. Figure 5.3a shows the PLE spectra measured for the peak emission wavelength of the QDs. For the bare QD sample, the PLE curve (red-solid curve) follows a similar trend as the absorption of the QDs. When TCTA or FIrpic:TCTA energy transferring organic layer is introduced to the QDs, two additional peaks arise in the PLE spectra of the QD emission around 300 and 330 nm as shown by orange and green curves in Figure 5.3a. These peaks correspond to the spectral regions where TCTA and FIrpic are optically excited as shown by the PLE curves for the TCTA and FIrpic emission peaks in Figure 5.3b. This enhancement of the PLE of the QDs in these specific spectral regions clearly indicates the transfer of the excitons into the QDs from the organic layer.

The PLE enhancement of the QD emission was greater (by a factor of 1.25) in the case of Firpic:TCTA as compared to the case of the TCTA-only donor. Since the PLE spectrum of the Firpic emission almost exactly resembles the PLE spectrum at the TCTA emission peak (see Figure 5.3b), this asserts that Firpic molecules are dominantly excited via strong internal excitation energy transfer of the excitons in the host materials due to its abundance (90% in our case). This has been observed in the literature for a similar phosphorescent emitter Irppy₃ [244]. Thus, the excitons that are primarily generated in the host (TCTA) are funnelled to the phosphorescent small organic molecule (Firpic). However, as we cannot differentiate the characteristic PLE signal of the Firpic, therefore, it is not possible to quantitatively discuss the degree of the exciton transfer efficiency from Firpic into the QDs by using only the PLE measurements.

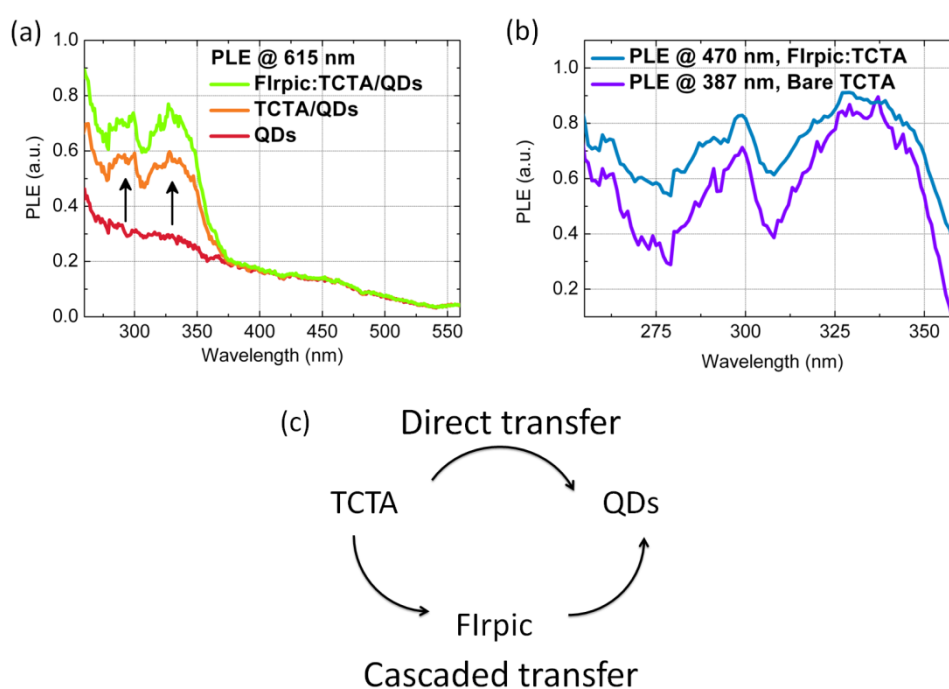


Figure 5.3. (a) PLE at the QD emission peak for the samples of only QDs (red), TCTA/QDs (orange), Firpic:TCTA/QDs (green) when the organic film thickness is 20 nm. (b) Normalized PLE spectrum of Firpic emission (cyan) from the Firpic:TCTA sample and PLE spectrum of TCTA emission from the bare TCTA sample. (c) Cascaded exciton transfer from the organic layer into the QDs (TCTA→Firpic→QDs).

Reprinted (or Adapted) with permission from [190]. Copyright 2014 American Chemical Society.

To quantitatively verify the contribution of FIrpic to the NRET, we performed time resolved fluorescence measurements on these samples using a picosecond pulsed pump laser at 375 nm. Figure 5.4a depicts the phosphorescent decay curves of FIrpic molecules for the FIrpic:TCTA and FIrpic:TCTA/QDs samples (when the organic film thickness is 20 nm). In Figure 5.4a, the phosphorescence decay curves of the FIrpic are shown when these molecules are interfacing the QD layer (red decay curve) or not (cyan decay curve). FIrpic phosphorescence decay is significantly accelerated when the QDs are interfaced with the organic layer, which undoubtedly verifies the presence of the exciton transfer from the FIrpic molecules. Thus, FIrpic molecules can clearly contribute to the exciton transfer into the QDs. In the absence of the QDs, FIrpic phosphorescence decay lifetime is 994 ns. When the QDs are introduced, the lifetime drops to 366 ns (here a double exponential fit is used with 47.8% of 645 ns and 52.2% of 112 ns). The shortening of the phosphorescence lifetime of FIrpic indicates that a new channel has been opened up for the relaxation of the FIrpic molecules in addition to the intrinsic radiative and nonradiative decay channels. The NRET rate and NRET efficiency is calculated as $1.72 \times 10^{-3} \text{ ns}^{-1}$ and 63%, respectively. When we investigated thinner co-doped organic layers, the lifetime of FIrpic is observed to be much shorter as compared to the thicker co-doped layers. This shows that the NRET efficiency grows stronger as the thickness of the organic layer is kept thinner from the donor point of view. In the case of 5 and 10 nm thick co-doped organic films interfacing the QDs (QD/FIrpic:TCTA), the FIrpic lifetime was measured to be 40 and 60 ns, respectively. Thus, a surpassing NRET efficiency as high as 95% is achievable in these hybrid QD-phosphorescent energy transferring thin films. Alternatively, excitons in the hybrid thin films can be transferred directly from TCTA into the QDs as illustrated in Figure 5.3c in contrast to the cascaded energy transfer route.

In the case of the fluorescence decay of the acceptor QDs, the NRET is independently verified by the observation of slowing down QD fluorescence decay curves when the energy donating TCTA or FIrpic:TCTA is introduced to the QDs. This

slow down of the QD fluorescence decay is due to the exciton feeding via NRET. The lifetime of the acceptor QDs is increased from 5.07 ns (bare QDs) to 7.87 ns (TCTA/QDs) and 7.80 ns (FIRpic:TCTA/QDs) (see Figure 5.4b). There is no drastic change in the emission kinetics of the QDs since the time-resolved fluorescence spectra are recorded using a picosecond pump laser at 375 nm, where only little number of excitons can be generated in the organic layer (see PLE of the TCTA and FIRpic in Figure 5.3b, where 375 nm excitation is not very suitable since it can hardly excite TCTA host molecules). Therefore, the QDs are dominantly excited by directly absorbing the pump photons and only little number of excitons could be nonradiatively transferred from the organic layer. This is also understood by the very little enhancement of the PLE of the QDs at 375 nm as shown in Figure 5.3a. In the inset of Figure 5.4b, the decay of the QDs are shown at an early time window, where the decay is slowed down for the samples of TCTA/QDs and FIRpic:TCTA/QDs. This initial exciton feeding is actually attributed to the fast NRET rate, which should be mainly caused by TCTA due to fast singlet-based NRET. Thus, the NRET rate due to TCTA will have a faster rate on the order of ns^{-1} as compared to the phosphorescent FIRpic donor, which has a slower NRET rate ($1.72 \times 10^{-3} \text{ ns}^{-1}$) due to the intrinsic slow radiative decay of the phosphorescence process [245]. Therefore, the exciton feeding effects in the acceptor decay kinetics arising from energy transfer from the phosphorescent molecules should be observed at later times as shown in Figure 5.4b, where tail of the QD fluorescence decay becomes elongated for the FIRpic:TCTA/QDs sample as compared to the TCTA/QDs and bare QDs samples. This indicates that FIRpic has slow NRET rate due to the intrinsic slow radiative depopulation rate of the phosphorescent molecules.

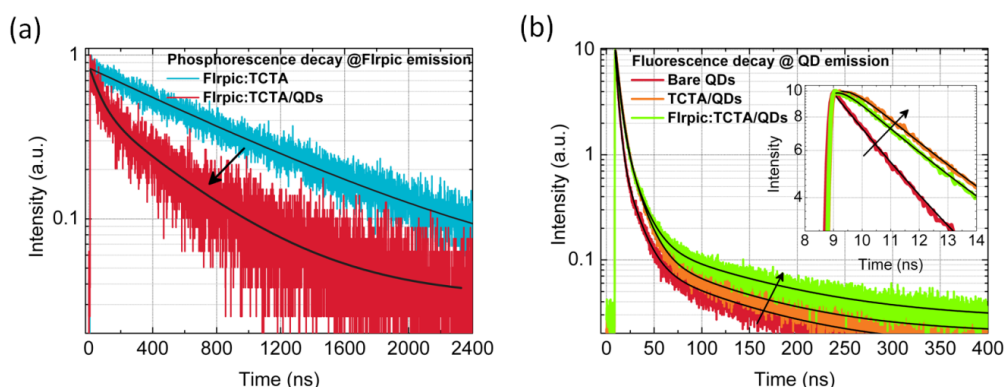


Figure 5.4. (a) Phosphorescence decay curves and their fits for the FIrpic emission from the samples of FIrpic:TCTA (cyan) and FIrpic:TCTA/QDs (red) when the organic film thickness is 20 nm. (b) Fluorescence decay curves and fits for the QD emission from the samples of only QDs (red), TCTA/QDs (orange) and FIrpic:TCTA/QDs (green). The inset exhibits the decay in an early time frame. All of the time resolved measurements were performed using a pulsed laser at 375 nm. Reprinted (or Adapted) with permission from [190]. Copyright 2014 American Chemical Society.

In Figure 5.5a experimentally measured fluorescence enhancement of the steady state PL of the QDs is plotted as a function of organic film thickness (from 5 to 20 nm in a 5 nm step size) when the excitation pump wavelength is 330 nm. The maximum enhancement of the QD emission is 2.5-folds and 2-folds for the FIrpic:TCTA and TCTA donors, respectively. Although NRET efficiency was found the highest (~95%) for the thinnest organic layer case (i.e., 5 nm), the fluorescence emission enhancement in the QDs was found the highest for the thickest organic layer case (i.e., 20 nm). This is attributed to the fact that enhancement of the QD emission depends on the multiplication of the number of excitons created in the organic layer and the NRET efficiency. Thus, as the thickness of the organic layer increases, the total number of excitons transferred to the QD layer increases since number of excitons in the organic film increases although the NRET efficiency slightly decreases. This suggests that exciton diffusion should greatly assist the exciton funnelling into the QDs.

To understand this possible exciton diffusion assistance to the NRET in these bilayer film samples, we devised an NRET model, which considers exciton diffusion in the organic layer in the form of random walk and Förster-type nonradiative energy transfer into the QDs [246]. The exciton diffusion was described as a 3D random walk on a discrete cubic lattice. First, an exciton is optically created in the organic layer with an initial random position within the organic layer while considering the geometric distribution of the excitons in the organic layer due to the absorption profile in the organic layer. Any created exciton can move a single step of length ε in a random direction after each time interval (Δt) while being confined to the boundaries of the organic layer unless NRET takes place. The maximum number of steps (N_{max}) required for the exciton to travel a distance equal to the diffusion length L_D is given by $N_{max} = g \left(L_D / \varepsilon \right)$, where $g = 6$ is the degree of freedom. The time step (Δt) is related to the donor fluorescence lifetime by the following formula $N_{max} \Delta t = \tau_D$. Then, NRET rate at each time step was calculated by [107], [247]

$$k_{ET} = \frac{1}{\tau_D} \left(\frac{1}{2} \pi \sigma_{QD} \right) \frac{R_0^6}{r^4} \quad (5.1)$$

where r is distance between the exciton position and the QD center, σ_{QD} is the number of QD per unit area, and R_0 is the Förster radius for the organic layer to the QD pair. The distance dependence is r^{-4} due to the two-dimensional construct of the acceptor QDs [107]. Next, we defined the probabilities for energy transfer during the time step Δt as

$$P_{trans} = 1 - \text{Exp}(-k_{ET}t) \quad (5.2)$$

here $t = N \Delta t$ is the time and $N = 0, 1, 2, \dots, N_{max}$ is the step number, P_{ET} is the probability for an exciton to be transfer to the QD. Substitution of (5.1) into (5.2) and using $t = N \Delta t$ and $\Delta t = \tau_D / N_{max}$, we obtain

$$P_{trans} = 1 - \text{Exp} \left(- \left(\frac{N}{N_{max}} \right) \left(\frac{1}{2} \pi \sigma_{QD} \right) \frac{R_0^6}{r^4} \right) \quad (5.3)$$

To determine whether the exciton is transferred or not, we set $P_{trans} > 0.9$. Thus, if $P_{trans} > 0.9$ the exciton is assumed to be transferred and the random walk of the exciton is terminated, if not, the exciton diffusion continues to the next time step. This algorithm continues until either the exciton is transferred or the maximum exciton diffusion length is reached, then the exciton could radiatively recombine in the organic layer as well.

We estimated the NRET efficiencies as a function of the organic layer thickness. The parameters that were used for the model are: diffusion length $L_D = 15.0 \text{ nm}$ [248], random walk step size $\varepsilon = 1 \text{ nm}$, and QD radius $R_{QD} = 3.0 \text{ nm}$ (as measured by TEM images). At 330 nm, the absorption coefficient of TCTA is about $3 \times 10^5 \text{ cm}^{-1}$ whereas it is about 10^5 cm^{-1} for the QDs [249]. For TCTA/QD sample, the Förster radius is estimated to be $R_0 = 4.957 \text{ nm}$. For this, molar extinction coefficient of the QDs is calculated as $4.1 \times 10^5 \text{ M/cm}$, the PL quantum yield of the TCTA is used as 20% [250], [251] and the refractive index of the medium is taken as 1.7 [232]. The fluorescence lifetime of the TCTA was measured as $\tau_D = 3.98 \text{ ns}$. For the TCTA:FIrpic/QD sample, Förster radius was estimated as $R_0 = 6.030 \text{ nm}$. The PL quantum yield of the FIrpic was assumed as 80% [248]. The phosphorescence lifetime FIrpic was measured as $\tau_D = 994 \text{ ns}$. In Figure 5.5b, the modeled NRET efficiencies are plotted as a function of organic layer thickness for the case of TCTA:FIrpic/QD sample. Also, NRET efficiencies are plotted without exciton diffusion assistance to NRET. The exciton diffusion assistance significantly helps for enhanced NRET efficiencies. However, we observed that discrepancy between the exciton diffusion assisted NRET model and the experimental NRET efficiencies increases as the organic layer thickness is increased (see Figure 5.5b). This indicates that even much stronger exciton diffusion assistance might be taking place in the energy transfer process of the excitons from the organic phase into the QDs.

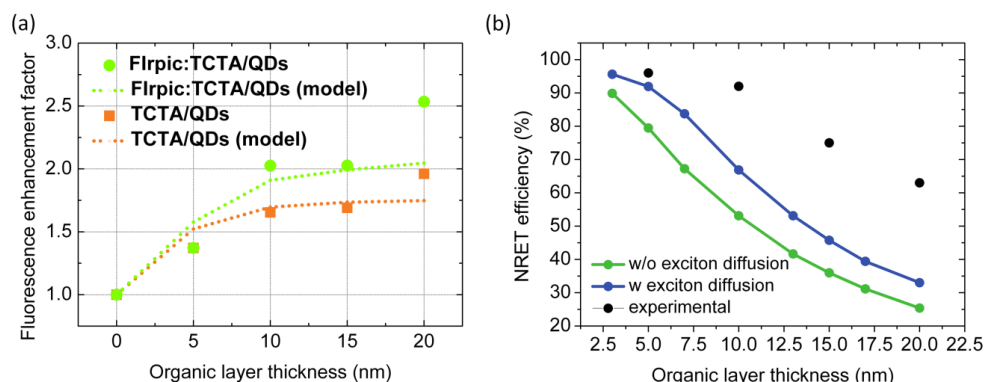


Figure 5.5. (a) Fluorescence enhancement factors of the QD emission in the samples of TCTA/QDs (orange) and FIrpic:TCTA/QDs (green) as a function of the organic film thickness and the modelled enhancement factors plotted in dashed curves. (b) Modelled NRET efficiency in the TCTA:FIrpic/QDs sample as a function of organic layer thickness with and without exciton diffusion assistance together with experimentally measured NRET efficiency from time resolved fluorescence measurements. Reprinted (or Adapted) with permission from [190]. Copyright 2014 American Chemical Society.

Using the modelled NRET efficiencies and the exciton distribution in the organic layer we calculated the fluorescence enhancement factor of the QD emission. These modelled enhancement factors are plotted as a function of the organic film thickness with dashed lines (see Figure 5.5a). As can be seen in Figure 5.5a, exciton diffusion assisted exciton transfer model that we proposed predicts the photoluminescence enhancement of the QDs with a good agreement until 20 nm organic layer thickness. We have a slight deviation in the 20 nm organic layer thickness case, which we believe that the discrepancy at thick organic layer thickness is due to our assumption that exciton diffusion is isotropic in the organic layer. If we were to introduce just a slight anisotropy (tendency of diffusion towards the QD layer is slightly larger than the other directions), then we would have achieved much better agreement (not presented here) in the 20 nm thick organic film. Therefore, exciton diffusion might be anisotropic in these hybrid organic-inorganic films due to an energy gradient towards the interface. These calculated results agree very well with the experimental results.

We also characterized the degree of cross-talk between the emission of QDs and FIrpic, which is important to interpret the results of the time resolved fluorescence spectroscopy. In the hybrid of QD/FIrpic:TCTA, the cross-talk between the emission of QDs and FIrpic is very small and insignificant in all of the samples under consideration. To calculate the degree of cross-talk at 615 nm (peak emission wavelength of the QDs), we measured the relative of emission intensity of FIrpic at 615 nm as compared to its peak emission wavelength at 472 nm. This corresponds to a factor of 1/47. Then, we computed the degree of cross-talk ($I_{\text{QDs}}/I_{\text{FIrpic}}$) at 615 nm for the samples that are excited at 330 nm as shown in Figure 5.6.

In the case of 5, 10 and 15 nm organic layer thicknesses, the degree of cross-talk was 482, 448 and, 97 respectively. Therefore, more than 99% of the emission at 615 nm originated from the QDs. In the case of 20 nm thick organic layer (FIrpic:TCTA), the degree of cross-talk was found to be ~50 corresponding to ~98% QD emission (only 2% FIrpic emission) at 615 nm. Furthermore, time resolved fluorescence measurements were performed using pulsed pump laser at 375 nm, where absorption of FIrpic and TCTA is much weaker (see Figure 5.3b for the PLE of the TCTA and FIrpic). Therefore, the degree of cross-talk is even smaller for the time-resolved fluorescence measurements since picoseconds pump laser at 375 nm was employed. By accounting this change in the excitation wavelength, we achieved 99.3% of the emission at 615 nm coming from the QDs even in the case of 20 nm thick organic layer. Therefore, practically there is no cross-talk problem in these measurements.

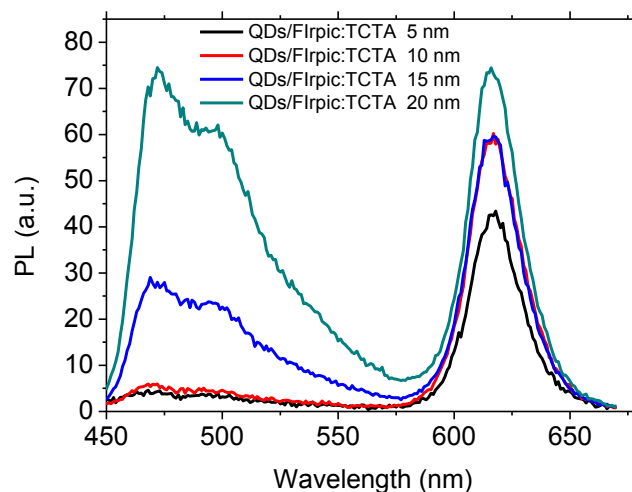


Figure 5.6. Photoluminescence of the QD/FIrpic:TCTA samples when excited at 330 nm. Reprinted (or Adapted) with permission from [190]. Copyright 2014 American Chemical Society.

5.2.3 Summary

In conclusion, we studied exciton transfer in a bilayer nanostructure of QDs interfaced with phosphorescent small organic FIrpic molecules in fluorescent TCTA host via steady state and time resolved fluorescence spectroscopies. We showed that TCTA alone is an efficient exciton donor for the QDs. On the other hand, utilization of FIrpic increases the exciton funneling into the QDs. Overall, the emission of the QDs was increased up to 2.5-fold. These significant enhancements in the fluorescence of the QDs were found to be due to exciton diffusion assistance to NRET. These findings suggest that such hybrid thin films employing phosphorescent molecules are promising for efficient exciton harvesting.

5.3 Excitonic light-emitting diodes: energy transfer enabled electroluminescence from the quantum dots

This section is based on the publication “Colloidal Quantum Dot Light-Emitting Diodes Employing Phosphorescent Small Organic Molecules as Efficient Exciton Harvesters,” E. Mutlugun*, **B. Guzelturk***, A. P. Abiyasa*, Y. Gao, X. W. Sun and H. V. Demir, *The Journal of Physical Chemistry Letters* 5, 2802-2807 (2014). * Equal contribution. Adapted (or “Reproduced in part”) with permission from American Chemical Society. Copyright 2014 American Chemical Society.

5.3.1 Motivation

Colloidal quantum dots are appealing light-emitting materials owing to their favorable optical properties, which make them promising for electroluminescent light-emitting devices (QLEDs) [10], [16], [230]. Excitation of the QDs in these electroluminescent devices occurs via either direct charge injection and/or nonradiative energy transfer from an adjacent charge transport layer [16], [109]. Energy transfer pumping was suspected to be an important mechanism for QLEDs, which employs organic hole and electron transport layers [139]. Energy transfer pumping of the QDs can be facilitated through funneling of excitons, which are initially formed in an adjacent transport layer, into the QDs via near field dipole-dipole coupling. Generally, these organic charge transport layers are comprised of fluorescent small organic molecules or conjugated polymers; therefore, only $\frac{1}{4}$ of the created excitons are singlet states due to spin statistics [231]. Therefore, $\frac{3}{4}$ of the excitons [111], [252] that are formed in these fluorescent charge transport layers will not be transferred into the QDs via NRET since they have zero oscillatory strength (i.e., triplet states). On the other hand, phosphorescent materials are known to have 100% internal quantum efficiency owing to the enhanced spin-orbit coupling and strong inter-system crossing [234], [235]. Hence, utilization of phosphorescent small organic molecules in the adjacent charge

transport layer could boost the energy transfer pumping of the QDs in QLEDs by harvesting all of the excitons (both singlet and triplet states).

Previously, energy transfer [232] and charge transfer [253] from a phosphorescent small organic molecule to a QD was shown via time resolved fluorescence spectroscopy. However, these previous reports did not consider, nor engineer the potential excitonic pumping. Only Zhang *et al.* reported an enhancement of the external quantum efficiency up to 3-folds via employing triplet harvesting phosphorescent molecules, but the color (spectral) purity of QLEDs could not be preserved at high current densities due to the expansion of the exciton recombination zone resulting in an incomplete energy transfer from the phosphorescent molecules into the QDs [233].

5.3.2 Experimental

For the device fabrication; patterned ITO glass (sheet resistance of 25 Ω /sq) was first cleaned using DI water, acetone and isopropanol followed by the oxygen plasma treatment prior to Poly(3,4-ethylenedioxythiophene)-poly(styrenesulfonate) (PEDOT:PSS) spin-coating. The device fabrication steps were all performed inside N₂-filled glove box environment without breaking the vacuum during the deposition of subsequent organic molecules. Spin-coating of PEDOT:PSS and poly[N,N'-bis(4-butylphenyl)-N, N'-bis(phenyl)benzidine] (poly-TPD) (15mg/ml in chlorobenzene) was performed using 4000 rpm for 1 min followed by baking at 100°C. QDs in toluene (10mg/ml) were spin-coated using the same recipe for PEDOT:PSS and poly-TPD with annealing at 80°C for 30 min. After the solution-processing steps were completed, samples were loaded into organic evaporation chamber to deposit organic and metal layers. In general approach, unless otherwise stated, the thicknesses of the organic and metal layers were chosen as follows: 2,2',2''-tris-(N-carbazolyl)-triphenylamine: iridium, tris(2-phenylpyridine) (TCTA:Ir(ppy)₃) was deposited using 10% co-doping of Ir(ppy)₃ into TCTA with a total film thickness of 2.5 nm; un-doped TCTA as 7.5 nm, 1,3,5-tris(N-phenylbenzimidazole-2-yl)benzene (TPBI) as 35 nm, Bathophenanthroline

(BPhen) varied as 1, 1.5 and 2 nm; lithium fluoride (LiF) as 1 nm and aluminum as 150 nm.

For the device measurement; emission spectra of the QLEDs were measured using Photo Research Spectra Scan PR705 spectra photometer and Konica-Minolta LS-100 luminance-meter. The devices were characterized under ambient conditions without any encapsulation.

5.3.3 Results and discussion

In this part, we developed hybrid highly spectrally pure QLEDs, in which the QDs are energy transfer pumped via NRET from the phosphorescent small organic molecule co-doped electron transport layer. Excitonically engineered hybrid QLEDs exhibit substantially enhanced external quantum efficiencies (up to 2.11%) with more than 6-fold enhancement over the conventional QLEDs that do not possess exciton transferring phosphorescent co-doped electron transport layer. These excitonic light emitting diodes can also achieve very high color purity, as high as 99%. Here, we denote the color purity as the fraction of photons emitted by the QDs to the total emitted photons from the overall hybrid QLED. High color purity of the electroluminescence was achieved via exciton formation zone management by introducing a hole blocking layer in between the QDs and the phosphorescent co-doped electron transport layer. To optimize the exciton transfer pumping and exciton harvesting into the QDs, spatial position of the partial co-doping of the phosphorescent molecules in the electron transport layer is fine-tuned. Additionally, time-resolved fluorescence spectroscopy was utilized to experimentally verify the enhanced exciton feeding into the QDs. These excitonic hybrid QLEDs are expected to boost the performance levels of the quantum dots for electroluminescent devices that will be promising for displays and lighting.

As opposed to the previous efforts on optimizing direct charge injection in QLEDs, our design strategy was to achieve high color purity QLEDs that are engineered for the

highly efficient energy transfer pumping by effectively harvesting the singlet and triplet state excitons in the phosphorescent co-doped electron transport layer. Red-emitting core/shell CdSe/ZnS QDs were synthesized [254] and used as an emissive layer for the QLEDs. The red-emitting QDs are highly monodisperse having less than 30 nm full-width at half-maximum and exhibit >20% quantum efficiency in their solid films. As the triplet state harvester and efficient energy transfer donor, phosphorescent molecule co-doped electron transport layer of 2,2',2''-tris-(N-carbazolyl)-triphenylamine: Iridium, tris(2-phenylpyridine) (TCTA:Ir(ppy)₃) was employed. The proposed device architecture of the hybrid QLEDs is illustrated in Figure 5.7a. Figure 5.7b demonstrates the energy band alignments of these hybrid QLEDs.

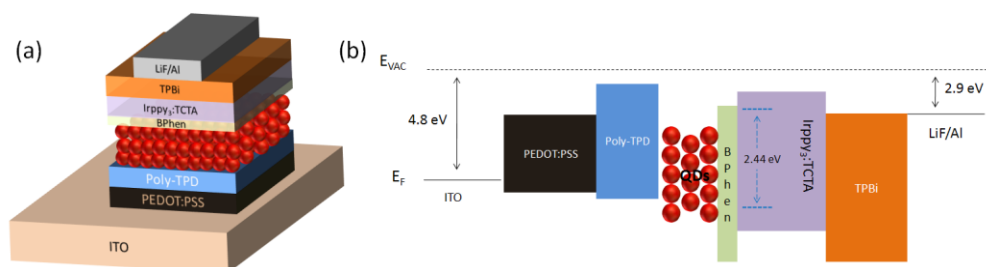


Figure 5.7. (a) 3D schematic of the QLED designed to achieve efficient energy transfer pumping. (b) Energy band alignment of the device in the structure of ITO/PEDOT:PSS/poly-TPD/QD/BPhen/Ir(ppy)₃TCTA/TPBi/LiF/Al. Reprinted (or Adapted) with permission from [21]. Copyright 2014 American Chemical Society.

The devices were fabricated using both solution and vacuum processing techniques (see Experimental). Briefly, on a transparent conductive oxide substrate (i.e., ITO), PEDOT:PSS, poly-TPD and the QDs were consecutively spin-coated. Then, BPhen, TCTA, Ir(ppy)₃, TPBi, LiF were deposited using thermal sublimation under high vacuum conditions ($< 10^{-6}$ Torr). The thickness of the deposited film was monitored using a calibrated quartz crystal microbalance (QCM) thickness gauge having sensitivity of ± 0.03 nm.

In the conventional device structure: ITO/PEDOT:PSS/poly-TPD/QD/TPBi/LiF/Al, the electroluminescence is purely from the QD layer as shown in Figure 5.8a. However, the maximum EQE level is quite low (i.e., 0.58%), due to poor charge

injection balance and poor energy transfer pumping, which the latter could take place either from poly-TPD or TPBi into the QDs. Starting with the conventional structure, we first introduced the phosphorescent emitter co-doped Ir(ppy)₃:TCTA layer (10% doping concentration) (ITO/PEDOT:PSS/poly-TPD/QD/TCTA:Ir(ppy)₃/TPBi/LiF/Al) as the electron transport layer. Although overall EQEs were high (> 5%), we observed insuppressible emission from the phosphorescent co-doping in the electroluminescence spectra as shown in Figure 5.8a. This necessitates the engineering of exciton formation and recombination zones to achieve efficient exciton confinement to the QD layer for superior color purity. To this end, we introduced Bathophenanthroline (BPhen) hole blocking layer, which helps to slow down the leakage of the holes into the phosphorescent co-doped electron transport layer. Thus, BPhen layer became quite handy to keep the electroluminescence spectrally pure whilst optimizing the exciton harvesting through NRET from the adjacent phosphorescent molecules into the QDs. As we introduce the BPhen layer in between the QDs and the co-doped electron transport layer (ITO/PEDOT:PSS/poly-TPD/QD/BPhen/TCTA:Ir(ppy)₃/TPBi/LiF/Al), we observed a significant suppression of the emission from the phosphorescent molecules in the electroluminescence spectrum of these hybrid QLEDs. As we increased the thickness of BPhen from 0.5 to 1.5 nm, the corresponding electroluminescence spectra of the hybrid QLEDs are shown in Figure 5.8b. We realized that color purity can be made as high as 99% (fraction of the photons emitted by QDs to the total number of photons emitted by the hybrid QLED) when the BPhen thickness is optimized for 1.5 nm (Figure 5.8b green curve).

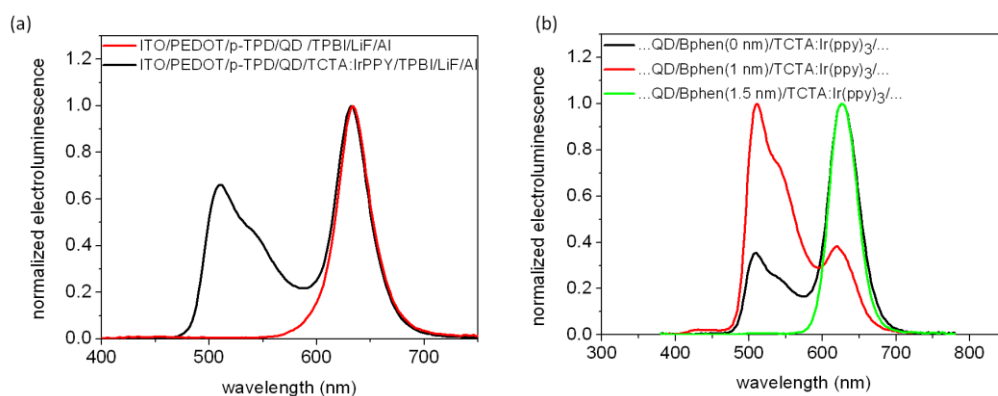


Figure 5.8. (a) Normalized electroluminescence spectra of the ITO/PEDOT:PSS/poly-TPD/QD/TPBi/LiF/Al, ITO/PEDOT:PSS/poly-TPD/QD/TCTA:Ir(ppy)₃/TPBi/LiF/Al.

(b) Normalized electroluminescence spectra of ITO/PEDOT:PSS/poly-TPD/QD/BPhen/TCTA:Ir(ppy)₃/TPBI/LiF/Al with varying the BPhen thickness. Reprinted (or Adapted) with permission from [21]. Copyright 2014 American Chemical Society.

By varying the BPhen layer thickness from 0 to 2 nm, we checked the hybrid QLED performance and found that the optimized device performance is achieved for a BPhen thickness of 1.5 nm. Although very thin BPhen layer (0.5 - 2 nm) slightly increases the turn-on voltage of the hybrid QLEDs due to the impeded hole transport (see Figure 5.9), yet it does not deteriorate the overall electroluminescence performance. Furthermore, we could achieve substantially suppressed emission of the phosphorescent small organic molecules (from 24% for BPhen thickness of 0.5 nm to 1% for BPhen thickness of 1.5 nm), enabling a very high color purity. It is worth noting here that the thickness of BPhen also plays a critical role in determining the overall QLED efficiency since it leads to a separation distance between the phosphorescent donor and the QD acceptor. Thus, while thicker BPhen layer could provide higher color purity, exciton transfer from the phosphorescent molecules into the QDs would decrease. Thus, an optimum thickness for BPhen exists.

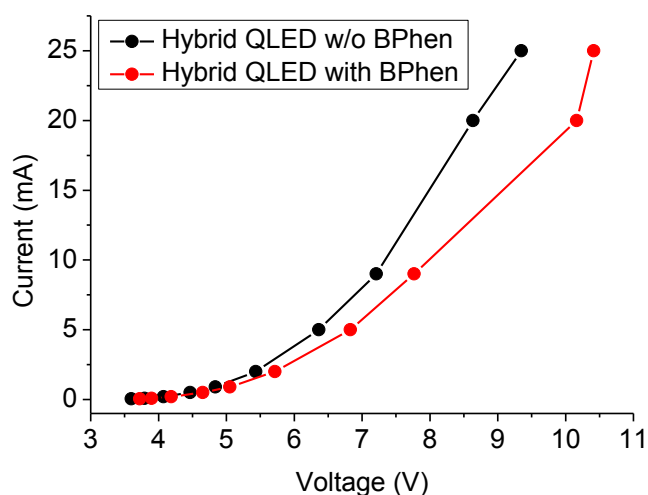


Figure 5.9. The current-voltage profile of the devices: ITO/PEDOT:PSS/poly-TPD/QD/ TCTA:Ir(ppy)₃/TPBI/LiF/Al and ITO/PEDOT:PSS/poly-

TPD/QD/BPhen/TCTA:Ir(ppy)₃/TPBI/LiF/Al. Reprinted (or Adapted) with permission from [21]. Copyright 2014 American Chemical Society.

To understand exciton recycling and pumping in the hybrid QLEDs, we investigated partially co-doped Ir(ppy)₃:TCTA electron transport layers instead of completely co-doped layers while keeping all of the other layers the same. We co-doped Ir(ppy)₃ into TCTA with a thickness of 2.5 nm and the rest of the TCTA was kept undoped (7.5 nm). Figure 5.10 exhibits the representative schematic of these partially co-doped electron transport layers. Then, the spatial position of the co-doped portion inside TCTA layer was varied as shown by position 1 to 4 (see Figure 5.10). This enabled us to probe the effects of the energy transfer pumping on the electroluminescence performance and the external quantum efficiency of these QLEDs. Figure 5.11a shows the absolute electroluminescence spectra of the QLEDs at the same injection current density as we varied the 2.5 nm thick co-doping layer's position in 2.5 nm intervals within 10 nm film thickness of TCTA. As the co-doping is placed closest to the QDs (position 1), we achieved 99% color purity (emission ratio of the QDs to Ir(ppy)₃ is ~100) with the highest overall emission intensity as shown by Figure 5.11a.

Moreover, as we moved the co-doped phosphorescent molecules away from the QDs (position 2 to 4), the color purity becomes inferior (see the inset of Figure 5.11a) and we observed that the color purity quantitatively decreases from 99% to 92%. This is due to the fact that excitonic pumping from the phosphorescent co-doping to the QDs becomes less efficient and the excitons that are generated in the co-doping starts to recombine radiatively instead of being transferred into the QDs.

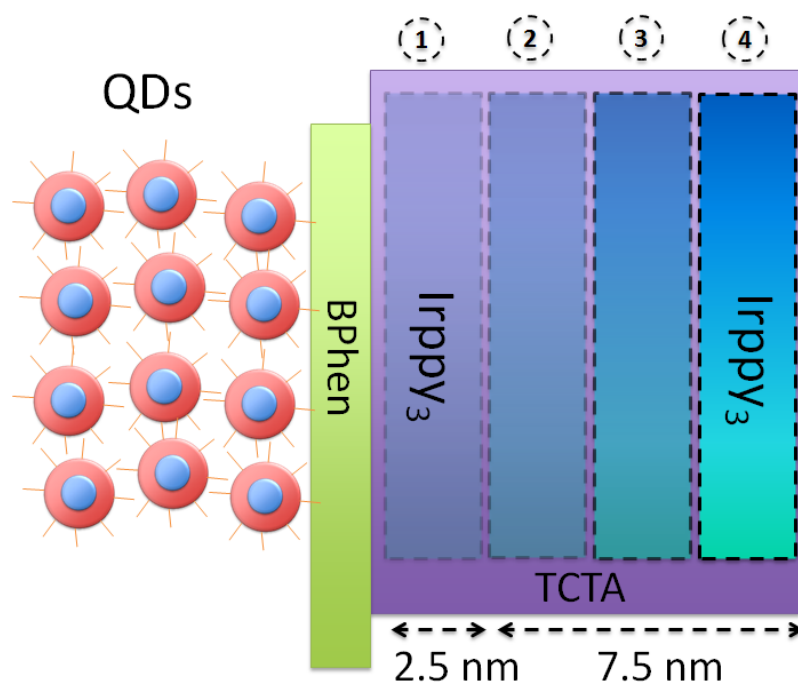


Figure 5.10. Schematic of the partially phosphorescent co-doped electron transport layer of TCTA. The partial co-doping is positioned in four different zones within the TCTA as indicated by positions 1 to 4 above the scheme, where position 1 is the closest to the QDs. NRET is expected to be the strongest for the co-doping located at the position 1. Reprinted (or Adapted) with permission from [21]. Copyright 2014 American Chemical Society.

Figure 5.11b shows the EQE of four different hybrid QLEDs at the same current density (55 mA/cm^2) having varying co-doping position. The closest co-doping leads to the highest EQE levels. The EQEs progressively decrease as the co-doping is moved from position 1 to 4. In the optimized case of co-doping layer being closest to the QDs (position 1 in Figure 5.10) (ITO/PEDOT:PSS/poly-TPD/QD/BPhen (1.5 nm)/TCTA:Ir(ppy)₃ (2.5nm)/TCTA (7.5nm)/TPBI/LiF/Al), the peak the EQE of the device reaches 2.11%, which is 3.6-fold larger than peak EQE of the reference QLED (without phosphorescent co-doping), in which peak EQEs can reach only 0.58% as

shown by Figure 5.11c. Moreover, maximum enhancement factor achieved in EQEs is over 6-folds at a current density of 11 mA/cm^2 . Figure 5.11d shows the electroluminescence spectra of the optimized QLED device at increasing current levels (device area is 9 mm^2). High color purity is always preserved even at high current injection densities. Furthermore, the optimized device results in peak brightness level as high as 1574 cd/m^2 as shown in Figure 5.12.

Table 5.1 summarizes various combinations of the QLED structures with their peak EQE levels.

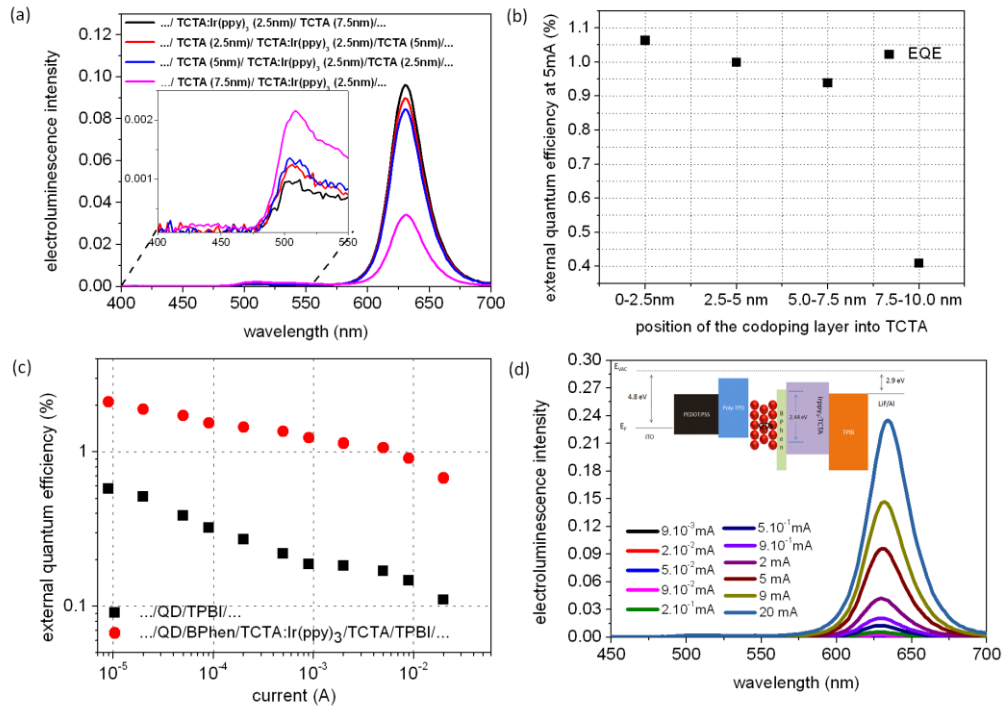


Figure 5.11. (a) Non-normalized electroluminescence spectra of the ITO/PEDOT:PSS/poly-TPD/QD/BPhen/TCTA:Ir(ppy)₃/TPBI/LiF/Al device with varying the position of the co-doped TCTA:Ir(ppy)₃ layer within the TCTA electron transport layer. (b) External quantum efficiencies of the devices at 5 mA injection current as a function of the position of the co-doping layer into TCTA. (c) EQE vs. current density of the devices: energy transfer pumping and color purity optimized ITO/PEDOT:PSS/poly-TPD/QD/BPhen(1.5 nm)/TCTA:Ir(ppy)₃(2.5nm)/TCTA

(7.5nm)/TPBI/LiF/Al and conventional ITO/PEDOT:PSS/poly-TPD/QD/TPBI/LiF/Al. (d) Electroluminescence spectra of the outperforming ITO/PEDOT:PSS/poly-TPD/QD/BPhen/TCTA:Ir(ppy)₃/TPBI/LiF/Al device (Ir(ppy)₃ doping in the first 2.5 nm of the TCTA layer). Reprinted (or Adapted) with permission from [21]. Copyright 2014 American Chemical Society.

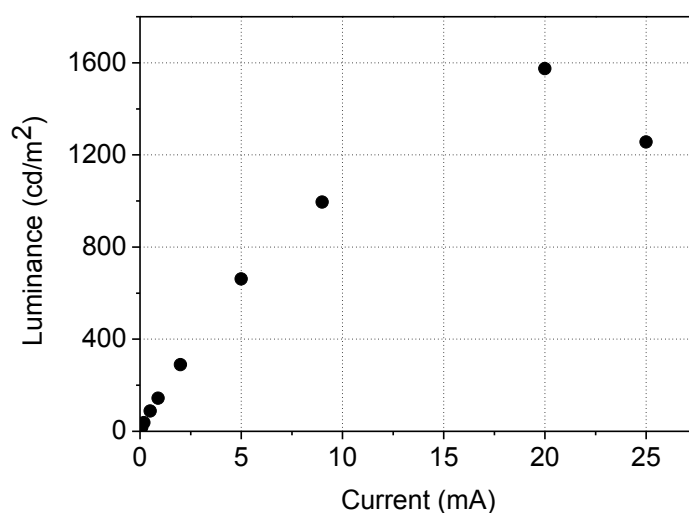


Figure 5.12. The luminance - current profile of the optimized device of ITO/PEDOT:PSS/poly-TPD/QD/BPhen/TCTA:Ir(ppy)₃/TPBI/LiF/Al. (2.5 nm codoped layer is just positioned next to the BPhen layer). Reprinted (or Adapted) with permission from [21]. Copyright 2014 American Chemical Society.

Table 5.1. Peak external quantum efficiency of the excitonic LEDs and also control devices.

Device	Max. EQE (%)
ITO/PEDOT:PSS/poly-TPD/TCTA:Ir(ppy) ₃ /TPBI/LiF/Al	14.66
ITO/PEDOT:PSS/poly-TPD/BPhen/TCTA:Ir(ppy) ₃ /TPBI/LiF/Al	8.28
ITO/PEDOT:PSS/poly-TPD/QD/TPBI/LiF/Al	0.58
ITO/PEDOT:PSS/poly-TPD/QD/TCTA/TPBI/LiF/Al	0.77
ITO/PEDOT:PSS/poly-TPD/QD/BPhen/TPBI/LiF/Al	0.79
ITO/PEDOT:PSS/poly-TPD/QD/BPhen/TCTA/TPBI/LiF/Al	1.81

ITO/PEDOT:PSS/poly-TPD/QD/TCTA:Ir(ppy) ₃ /TPBI/LiF/Al	3.22
ITO/PEDOT:PSS/poly-TPD/QD/BPhen/TCTA:Ir(ppy) ₃ /TPBI/LiF/Al	2.11

To understand the dynamics of the exciton transfer from the phosphorescent co-doped electron transport layer into the QDs in these hybrid QLEDs, we investigated the hybrid thin films via time-resolved fluorescence spectroscopy. Previously, fluorescence of the QDs was shown to be slowed down due to NRET (i.e., the exciton feeding effect) [108], [126], [133]. In our case, NRET increases the electroluminescence performance of the electrically driven QDs. This process should also increase the optically pumped luminescence of the QDs as well. Figure 5.13 shows the fluorescence decay curves measured at the QD peak emission (excited by a pulsed laser at 375 nm) to investigate the fluorescence lifetime variation of the QDs due to NRET from various electron transport layers of that are employed in the QLEDs including BPhen, TCTA, Ir(ppy)₃:TCTA and BPhen/Ir(ppy)₃:TCTA. The collected fluorescence decays were analyzed using bi-exponential decay functions. The amplitude-averaged lifetime in bare QD film was found to be 2.79 ns. When QDs were interfaced with the exciton transferring films, their fluorescence lifetime became longer. Table 5.2 summarizes the fluorescence lifetime of the QDs for the different donor cases. The longest fluorescence lifetime (3.87 ns) of the QDs was achieved when using the QD/BPhen/Ir(ppy)₃:TCTA structure, which also led to the best QLED performance. In this sample, the fluorescence lifetime of the QDs was elongated by 38.7% as compared to that of the bare QDs. The next longest lifetime of the QDs was achieved for the case of QD/Ir(ppy)₃:TCTA sample (3.44 ns). Thus, the presence of BPhen hole blocking interlayer is observed to enhance the NRET to the QDs. We attribute this to the suppression of the interface trapping and nonradiative dissociation of the triplet excitons at the interface between the organic film and the QDs [255]. When BPhen is employed as an interlayer at the interface, trapping and nonradiative dissociation of the triplet excitons may be possibly suppressed. Thus, this allows for more efficient exciton harvesting.

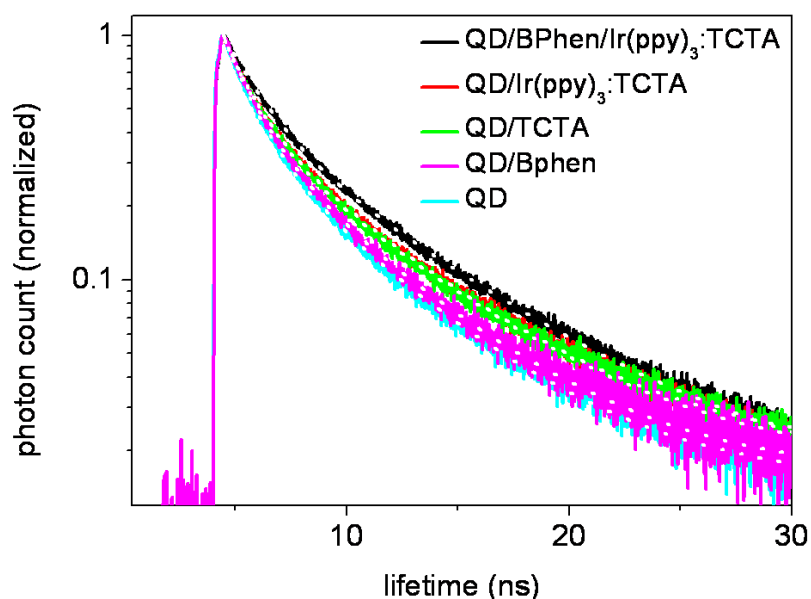


Figure 5.13. Time resolved fluorescence spectra of the quantum dot (QD) layer in the bare and in various architecture samples (QD/BPhen, QD/TCTA, QD/Ir(ppy)₃:TCTA, QD/ BPhen /Ir(ppy)₃:TCTA) along with the bi-exponential fits given with white dots. Reprinted (or Adapted) with permission from [21]. Copyright 2014 American Chemical Society.

Table 5.2. Amplitude-averaged fluorescence lifetimes of the QDs in bare-QD, QD/BPhen, QD/TCTA, QD/Ir(ppy)₃:TCTA and QD/ BPhen /Ir(ppy)₃:TCTA samples.

Sample name	Amplitude weighted lifetime (ns)
Bare-QD	2.79
QD/BPhen	2.94
QD/TCTA	3.26
QD/Ir(ppy) ₃ :TCTA	3.44
QD/BPhen/Ir(ppy) ₃ :TCTA	3.87

5.3.4 Summary

In conclusion, we demonstrated energy transfer pumping of the QDs by NRET from the phosphorescent co-doped electron transport layer, making highly efficient excitonic light-emitting diodes. This energy transfer pumping via exciton harvesting boosted up the efficiency of the QLEDs while maintaining very high color purity (99%) via controlling the exciton formation zone in these engineered hybrid QLEDs. We achieved up to a 6-fold enhancement of the external quantum efficiencies of the QLEDs when the phosphorescent layer is introduced in the optimized device architecture as compared to that of the conventional QLED structures. The utilization of the exciton harvesting in such architectures will pave the way for the superior performance of electroluminescent devices.

5.4 Summary of the chapter

In this chapter, we developed exciton harvesting scheme for quantum dot LEDs to recycle the excitons that have been leaking to the adjacent charge transport layers. For this, we proposed using phosphorescent small organic molecules as exciton capturing and transferring molecules, which can also simultaneously utilize singlet and triplet state excitons. This scheme has resulted ca. 2.5-fold enhancement of the quantum dot emission under optical pumping conditions (i.e., ex-situ studies). More importantly, exciton harvesting in an active LED resulted in ~6-fold enhancement of the electroluminescence efficiency under electrical charge injection conditions (i.e., in-situ studies). Greater enhancement of the electroluminescence efficiency strongly suggests the superiority of using phosphorescent molecule-based exciton donors in the hybrid QLEDs that can effectively harvest spin-forbidden triplet state excitons, which are dominantly formed under electrical injection.

Chapter 6

Optical Gain in Colloidal Semiconductor Nanocrystals

6.1 Introduction to colloidal gain

Colloidal semiconductor nanocrystals are appealing for optical gain and lasing owing to the ease of color tunability in these materials. In principle, a nanocrystal laser could lase at any color in the visible and also in the infrared. Thus, “all color” nanocrystal lasers could overcome the “green gap” problem in laser diodes, which are based on epitaxial semiconductors (e.g., multiple quantum wells of InGaN/GaN or InAlGaAs/AlGaInP/GaAs) grown by gas-phase epitaxy [256]. Furthermore, optical gain in strongly confined nanocrystals is expected to be temperature insensitive since density of states resembles atomic-like discrete states since energy separation between consecutive electronic states become distinct [257]. Also, large density of states at the band edge in strongly confined semiconductors (e.g., quantum dots) was predicted to achieve large and spectrally narrow gain [118]. Because of these, optical gain in

quantum dots is expected to be highly desired for high-speed optical communications and high-power applications [258].

Since the first demonstration of optical gain in the colloidal nanocrystals (i.e., CdSe quantum dots) by Klimov and Bawendi groups in 2000 [6], lasers of these colloidal nanocrystals have been excitedly pursued. However, colloidal nanocrystal lasers still cannot offer a feasible laser technology platform, which could have been an alternative to laser diodes. This mainly arises from the fact that there exist severe practical and fundamental limitations in colloidal nanocrystal gain media against achieving efficient optical gain. These limitations result in large gain thresholds ($\sim 1 \text{ mJ/cm}^2$), small modal gain coefficients ($< 100 \text{ cm}^{-1}$) and ultrashort gain lifetimes ($\ll 100 \text{ ps}$), making these materials impractical for real-life laser applications. As explained in Chapter 2, the underpinning reason behind the limited optical gain performance in the colloidal nanocrystals is the degeneracy of the first excited state in II-VI semiconductors. Therefore, it is required to make the population of nanocrystals having biexcitons larger than the population of the nanocrystals that are in the ground-state. The challenge arises due to ultrafast lifetime of the biexcitons in the conventional nanocrystals due to the dominant nonradiative Auger recombination [11]. Auger recombination leads to ultrafast annihilation of the biexcitons before they could be effectively used for net optical gain.

These limitations of the optical gain in colloidal nanocrystals make it very difficult to achieve lasing using conventional and cheap pump sources such as blue-emitting laser diodes and continuous wave lasers. To date, lasing in nanocrystals could be realized using only expensive and bulky pulsed lasers (e.g., femtosecond Ti:Sapphire regenerative amplifiers pumped with mode-locked lasers). In addition, small modal gain coefficients in the nanocrystals cause the need to employ highly closed-packed nanocrystal solids for optical gain. However, quenching effects become inevitable in these highly closed-packed films due to nanocrystal-to-nanocrystal near-field interactions, such as nonradiative energy transfer. Small gain coefficients, which is inherent to conventional CdSe quantum dots, also obstruct the use of nanocrystal in

their solution-state as the optical gain media [259]. Overall, these practical limitations pose significant challenges against achieving feasible nanocrystal lasers.

To address these aforementioned challenges in the optical gain, there have been efforts in the nanocrystal community to improve their optical gain performance. The most useful strategies so far have been to develop heterostructured nanocrystals having controlled shape and tuned composition to partially (or completely) eliminate Auger recombination and to tailor the electronic structure of the nanocrystals to enable single exciton gain (e.g., Type-II quantum dots). Here we discuss the strategies to overcome the challenges associated with the colloidal gain media. If we only consider the size of the nanocrystals:

- 1) Need for smaller nanocrystals:
 - a. Modal gain coefficients should be increased. This could be achieved by increasing the optical confinement factor (Γ) in the solid films of the nanocrystals by making their size smaller. Thus, smaller nanocrystals would achieve much higher packing densities.
 - b. Stimulated emission cross-section should be increased. This could be achieved by increasing the degree of the quantum confinement in the nanocrystals by having strong confinement at least in one dimension. This would increase the exciton binding, thus the emission oscillator strength.
 - c. Absorption cross-section should be increased. This could be achieved by increasing the oscillator strength via increasing the confinement in small-sized nanocrystals.
- 2) Need for bigger nanocrystals:
 - a. Gain thresholds should be decreased. This could be accomplished by increasing the absorption cross-section of the nanocrystals. Nanocrystals with a larger volume has generally overall a larger absorption cross-section.

- b. Auger recombination rates should be suppressed. This could be achieved by increasing the volume of the nanocrystals so that carrier-carrier interactions would be minimized.

By only tuning the size of the nanocrystals, one cannot overcome the problems of optical gain since both small and large sized nanocrystals have their own advantages and disadvantages. For example, small-sized nanocrystals would achieve larger gain coefficients, but gain itself would be ultrashort-lived due to dominant Auger recombination. Thus, overall gain performance would be quite poor. On the other hand, large nanocrystals would decrease the gain threshold due to their large absorption cross-section and suppressed Auger recombination, but they will severely suffer from very small modal gain coefficients. One possibility is to find an optimum size, where large modal gain coefficients and small gain thresholds could be simultaneously accomplished. However, this is generally quite difficult without sacrificing from high gain performance. The second option is to alter the composition and shape of the nanocrystals so that large size and tight quantum confinement could be realized simultaneously (i.e., nanoplatelets). Alternatively, composition-tuned nanocrystals such as the ones having soft-confinement potential could suppress Auger recombination though having quite small sizes.

Overall, nanocrystals that are the most desired for optical gain should simultaneously have large absorption cross-section, large oscillator strength and high packing densities. To date, various shapes of nanocrystals (spherical quantum dots, nanorods, tetrapods, etc.) have been employed for optical gain. Although nanorods [260], [261] and tetrapods [262] could reduce the gain thresholds owing to their large physical size, they could not achieve large gain coefficients due to their reduced packing densities and smaller stimulated emission cross-sections (since carriers are physically separated from each other, this leads to weak confinement conditions). Similarly, giant-shell quantum dots [43], [263] suffer from the small packing densities and as well as weak-confinement of the carriers. Moreover, nanocrystals with large physical volumes commonly suffer from crystal defects, which start to dominate the optical properties by deteriorating the emission quantum yields.

Alternatively, it has been shown that creation of a gradient core/shell interface in core/shell QDs could suppress the Auger recombination by reducing the available number of spatial frequency components, which would be needed for the momentum matching condition [264]. Thus, core/shell QDs with a gradient core/shell interface, also called as “soft confinement barrier”, have been proposed to considerably suppress nonradiative Auger recombination. This allows to create a feasible strategy to reduce the gain thresholds in smaller nanocrystals by suppressing Auger recombination. However, the gain performance of the nanocrystals having alloyed core/shell interface has not been elucidated to date. Only Dang et al. have demonstrated relatively low threshold gain in quantum dots that might have unintentional alloying at the core/shell interface [10].

In this thesis, we have proposed, designed, developed the nanocrystals that have alloyed core/shell interface that enabled us to realize ultralow threshold optical gain without comprising the gain coefficients. This strategy led us to achieve record low gain thresholds both in blue-emitting and red-emitting quantum dots. Moreover, these high quality quantum dots enabled us to achieve the first all solution-processed colloidal lasers with record low lasing thresholds. More importantly, we have identified a new class of nanocrystals for efficient optical gain, which are atomically-flat colloidal nanoplatelets. The nanoplatelets thanks to their superior properties, including large oscillator strength, large absorption cross-section, suppressed Auger recombination and absence of inhomogenous broadening, allowed us to develop the most efficient colloidal gain system so far. We achieved record-high modal gain coefficients with ultralow gain thresholds among all colloidal nanocrystals. In the near future, these nanoplatelets are expected to pave the way for CW pumped optical gain that is expected to be a game changer for the colloidal gain systems.

6.2 Efficient optical gain in blue-emitting quantum dots

This section is based on the publication “Ultralow threshold one-photon-and two-photon-pumped optical gain media of blue-emitting colloidal quantum dot films,” **B. Guzelturk**, Y. Kelestemur, M. Z. Akgul, V. K. Sharma and H. V. Demir, *The Journal of Physical Chemistry Letters* 5, 2214-2218 (2014). Adapted (or “Reproduced in part”) with permission from American Chemical Society. Copyright 2014 American Chemical Society.

6.2.1 Motivation

Recently, full color lasing has been demonstrated in the QD-based gain media by one-photon absorption (1PA) pumping [10]. Although green and red-emitting QDs have shown low gain thresholds, blue-emitting QDs have always suffered poor optical gain performance. To this date, several reports could realize optical gain using the QDs in the blue region with very high thresholds [10], [265]–[267]. Also, two-photon absorption pumped (2PA) optical gain, which has various advantages for various applications via employing frequency up-conversion schemes [261], [268]–[273], had not been possible using blue-emitting QDs.

The first demonstration of the optical gain in the blue-emitting QDs was realized at cryogenic temperatures since it was not feasible at room temperature [265]. Later, Bawendi *et al.* demonstrated the amplified spontaneous emission (ASE) at room temperature using CdS/ZnS core/shell QDs [266]. However, these QDs suffered from poor stabilities and very high gain thresholds. The best gain performance for the blue-emitting QDs had been achieved by Dang *et al.* with a threshold of $800 \mu\text{J}/\text{cm}^2$. However, this gain thresholds is very high as compared to the best performing red-emitting QDs, which showed ASE thresholds on the order of $50 \mu\text{J}/\text{cm}^2$ [10].

This poor optical gain performance in the blue-emitting QDs mainly arises from their small size. To achieve blue-emission, the size of the QD should be made very small to reach high quantum confinement levels so that high bandgap energies (blue region $\sim 2.55 - 2.90$ eV), where blue emission can be accomplished. However, in such strongly confined QDs strong nonradiative Auger recombination (AR) dominates the biexciton kinetics. Also, very large surface to volume ratio in small QDs leads to stability issues and increases their vulnerability to the ambient environment (i.e., creation of surface traps upon exposure to oxygen and moisture). These effects have before proven that it is challenging to achieve efficient optical gain in the blue-emitting QDs. In addition, the small size of the blue-emitting QDs had restrained their two-photon absorption cross-section and to date it had not been possible to show 2PA-pumped optical gain in these QDs.

6.2.2 Results and discussion

In this part of the thesis, we proposed a strategy to overcome the challenges associated with optical gain in the blue-emitting QDs. We synergistically combined large size, high stability and suppressed Auger recombination in the blue-emitting QDs via developing blue-emitting QDs based on alloyed CdZnS QDs. These alloyed QDs have composition tunable bandgap in the UV-blue region. Blue-emission could be preserved even for QD sizes larger than 5 nm. Moreover, we designed these QDs in a core/shell architecture of ZnCdS/ZnS (see Figure 6.1) to both suppress Auger recombination (via creating soft-confinement potential) and to increase the stability by passivating with a high bandgap material. Therefore, these blue-emitting QDs could simultaneously combine both large size (~ 10 nm) and gradient alloyed core/shell interface.

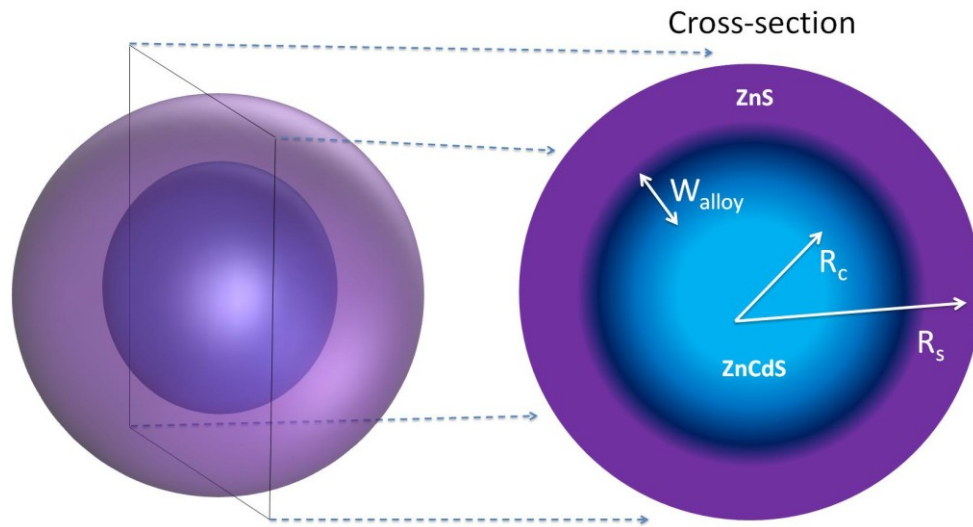


Figure 6.1 Structure of the core/shell ZnCdS/ZnS quantum dots that simultaneously combine large size, high stability and suppressed Auger recombination thanks to the gradient core/shell interface.

We demonstrated low threshold ASE under 1PA- and 2PA-pumping using these blue-emitting QDs. We achieved 1PA-pumped ASE threshold as low as $60 \mu\text{J}/\text{cm}^2$, which represents more than an order of magnitude improvement as compared to that of best reports using blue-emitting QDs before. In addition, we achieved the first time 2PA-pumped ASE in the blue-emitting QDs with a relatively low threshold of $6 \text{ mJ}/\text{cm}^2$, which is comparable to that of the best 2PA-pumped green- or red-emitting QDs [268]. These substantially reduced optical gain thresholds were enabled by the large size of the QDs along with the gradient core-shell interface, which helps to suppress the nonradiative Auger recombination.

Blue-emitting CdZnS/ZnS QDs were synthesized using the slightly modified recipe from the literature [222]. Formation of the core and growth of the shell was carried out in a single step synthesis. During the growth of these colloidal nanocrystals, sulfur injection was performed twice. With the first injection of sulfur precursor, nucleation of CdZnS cores were achieved. These nucleates were allowed to grow for sometime. Then, the shell growth was initiated with the dropwise injection of the second sulfur precursor. As studied before, these structures possess alloyed ZnCdS core, while the

composition of the shell varies gradually from ZnCdS to pure ZnS similar to Bae *et al.*'s one-pot quantum dot recipe [47].

We studied and contrasted the performance of three different blue-emitting QD samples, which have the same CdZnS core, but have different extent of shell. This has been achieved by varying the duration of the shell growth (i.e., 30 min, 120 min and 180 min) on the same core QDs resulting in different shell thickness, thus, different overall size. The size of the QDs were investigated by transmission electron microscopy (TEM) (see Figure 6.2c). By analyzing over 100 QDs, we found the sizes of the QDs were 8.4, 9.2, 10.0 nm (± 1.0 nm) for the 30, 120 and 180 min shell growth durations, respectively. The absorption and the photoluminescence (PL) spectra of the QDs are shown in Figure 6.2a-b. The PL peak of the QDs is located ~ 443 -448 nm. There is a slight blue-shift of the PL peak as the shell growth duration is increased from 30 to 180 min, which is an indication of the inter-diffusion of Zn into the core through the core/shell interface. This also suggest the presence of gradient core/shell interface in these QDs.

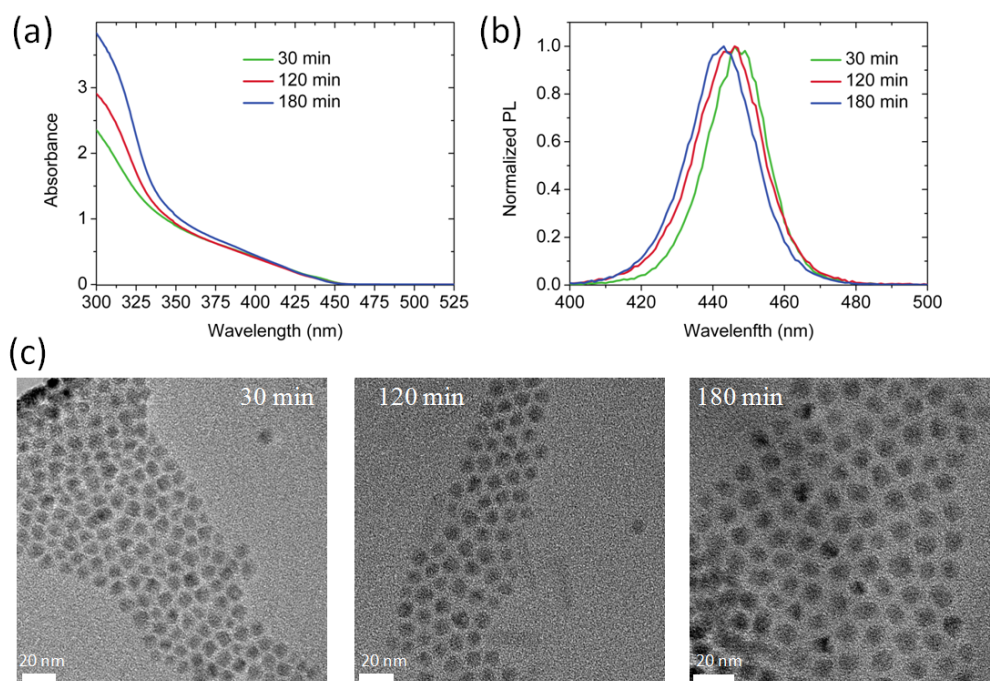


Figure 6.2 (a) Absorbance and (b) photoluminescence of the blue-emitting CdZnS/ZnS QDs having different shell growth time. (c) Transmission electron microscopy images

of the different shell grown QDs. Reprinted (or Adapted) with permission from [274]. Copyright 2014 American Chemical Society.

To show a solid evidence of the gradient core/shell interface in these QDs, we conducted depth profile study using x-ray photoelectron spectroscopy (XPS). We recorded XPS spectra of the QD film (few monolayers thick) after every Ar^+ etching cycle. Figure 6.3 presents the atomic ratio of Zn to Cd (calculated from Zn 2p and Cd 3d peaks in XPS) as a function of etching duration. The gradual change of the Zn/Cd ratio, which is first a decrease then followed by an increase, suggests that there should be a gradient interface in these QDs instead of an abrupt core/shell interface. All of the three QDs exhibit this type of gradient alloying. Among these samples, we observed the gradient interface is the most prominent for the QDs with 180 min grown shell, since the largest change of Zn/Cd ratio is observed.

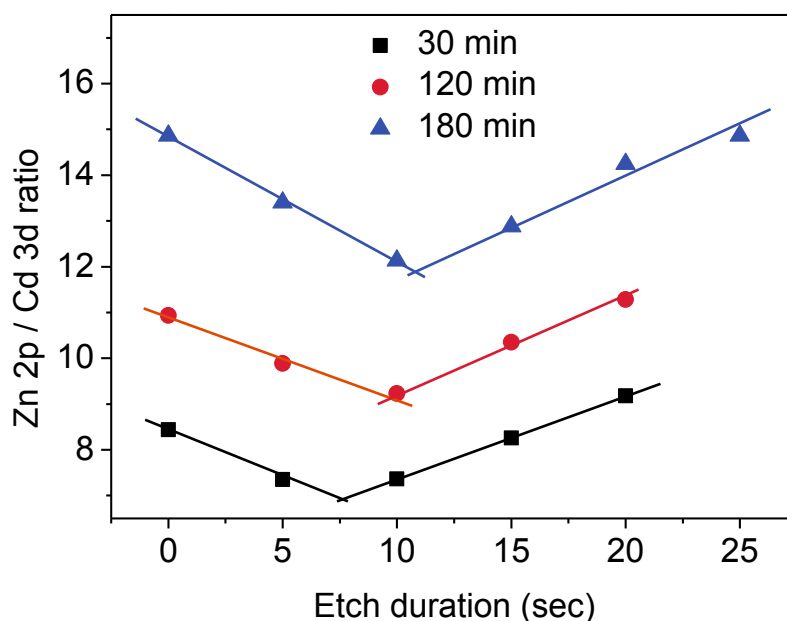


Figure 6.3 Zn/Cd ratio of the graded QDs with shells grown in 30, 120, and 180 min measured with XPS as a function of etching time. Linear fits are presented to guide the eye. Reprinted (or Adapted) with permission from [274]. Copyright 2014 American Chemical Society

Next, we studied the optical gain performance in the solid films of the blue-emitting QDs that were spin-coated on quartz substrates at a high concentration (50-60 mg/mL in hexane). As the pump source, we utilized Spectra Physics – Spitfire Pro XP regenerative amplifier having 120 fs pulse width at 800 nm with 1 kHz repetition rate. Using a cylindrical lens (20 cm focus), we excited the samples with a stripe geometry. Emission spectra was measured as the pump-intensity was gradually increased via collecting the emitted photons along the stripe using a fiber coupled to a spectrometer. For the 1PA-pumping, we frequency doubled the pump source using a nonlinear BBO crystal and filtering out the residual 800 nm. Figure 6.4a-c show the emission spectra of the three different QD samples under 1PA pumping while the pump intensity is gradually increased. In all of the QDs, we observed the transition from spontaneous emission (fwhm 20-25 nm) to amplified spontaneous emission (fwhm ~6-9 nm). The ASE peaks are slightly red-shifted with respect to the spontaneous emission peaks of the samples in 30 and 120 min shell grown QDs. In the case of the QD with 180 min shell grown, the ASE peak is almost at the spontaneous emission peak (~450 nm).

Figure 6.4d plots the emission intensity vs. pump intensity (the so-called input-output curve for the ASE experiment) for the three different QDs. Here, 180 min shell grown QDs exhibit the lowest ASE threshold, which is $58.9 \mu\text{J}/\text{cm}^2$. For the 120 min and 30 min shell grown QDs, the ASE thresholds are $74 \mu\text{J}/\text{cm}^2$ and $193.5 \mu\text{J}/\text{cm}^2$, respectively. The ASE threshold achieved using the QDs having 180 min grown shell is at least an order of magnitude lower than the previously best reported gain threshold in the blue-emitting QDs ($\sim 800 \mu\text{J}/\text{cm}^2$ [10]). Furthermore, our 1PA pumped ASE threshold is comparable to the state-of-the-art green- and red-emitting QD-based gain media [10]. These ZnCdS/ZnS QDs also recently showed high efficiency in their light-emitting diodes, attributed to their high emission quantum yields and suppressed nonradiative Auger recombination and reduced inter-QD nonradiative energy transfer due to the large size [222]. This further shows the great potential of these QDs for optoelectronic applications.

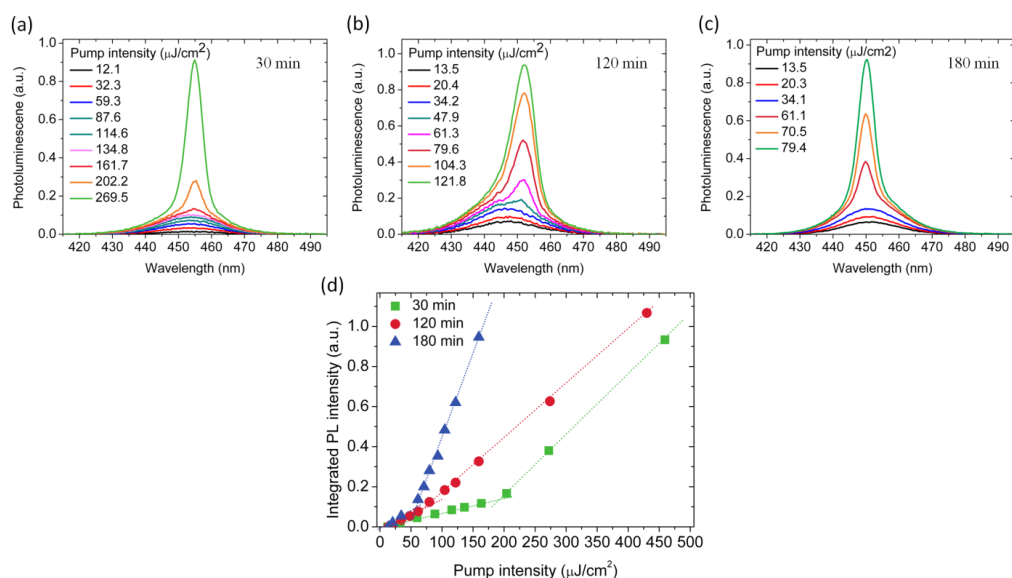


Figure 6.4 Pump intensity dependent PL of (a) 30 min, (b) 120 min and (c) 180 min shell grown CdZnS/ZnS QDs under 1PA pumping. (d) Luminescence vs. pump intensity curve of the 180 min shell grown QDs with 1PA pumping. Reprinted (or Adapted) with permission from [274]. Copyright 2014 American Chemical Society.

In the case of 2PA-pumping (at 800 nm), emission spectra are shown for 30, 120 and 180 min shell grown CdZnS/ZnS QDs in Figure 6.5a-c, respectively. As the pump intensity was gradually increased, ASE peak builds up as a narrower emission feature (with a fwhm of 4.5-6.5 nm). For the 30 min shell grown QDs, the position of the ASE peak is almost at the same position of the spontaneous emission peak. For the 120 and 180 min shell grown QDs, ASE is red shifted by 2 and 2.3 nm as compared to their corresponding spontaneous emission peak, respectively. As compared to the 1PA pumped ASE peaks, there are slight spectral difference under 2PA pumping. This could be attributed to the fact that 2PA pumping may cause extra heating that could red-shift the emission features. Another possibility is that the gain dynamics might be changing due to the use of 2PA process. Also, ASE peak might also spectrally shift due to surface trapping and/or multiexciton effects [273], [275].

Figure 6.5d demonstrates the integrated emission intensity vs. pump intensity for three different QD samples having different shell thicknesses. The threshold for the

2PA-pumped ASE is 6.25 mJ/cm^2 , 8.44 mJ/cm^2 and 15.45 mJ/cm^2 for the 180 min, 120 min and 30 min shell grown QDs, respectively. Our achievement represents the first frequency up-converted optical gain in the blue-emitting QDs. The 2PA-pumped ASE threshold is comparable to the best reported threshold achieved when using the red-emitting QDs and even better than that of the green-emitting QDs [269], [270], [273]. We observed that 2PA pumped gain thresholds decrease as the shell thickness is increased, which is attributed to the increasing size of the QDs that also increases the 2PA cross-section and also reduces the nonradiative AR [222], [264], [276].

Previously, it was shown that QDs having soft confinement potential, or gradient core/shell interface, could suppress the AR to a greater extent when compared to QDs having abrupt core/shell interface [264]. Before, with the combination of larger size and gradient core/shell interfaces, suppressed AR and superior optical gain performances have been demonstrated in CdSe/CdS core/shell QDs [18], [43], [273]. However, these type of QDs could only emit in the red spectral range due to their energy band levels. Previously, it was not possible to achieve blue-emitting QDs from the gradient-shell QDs.

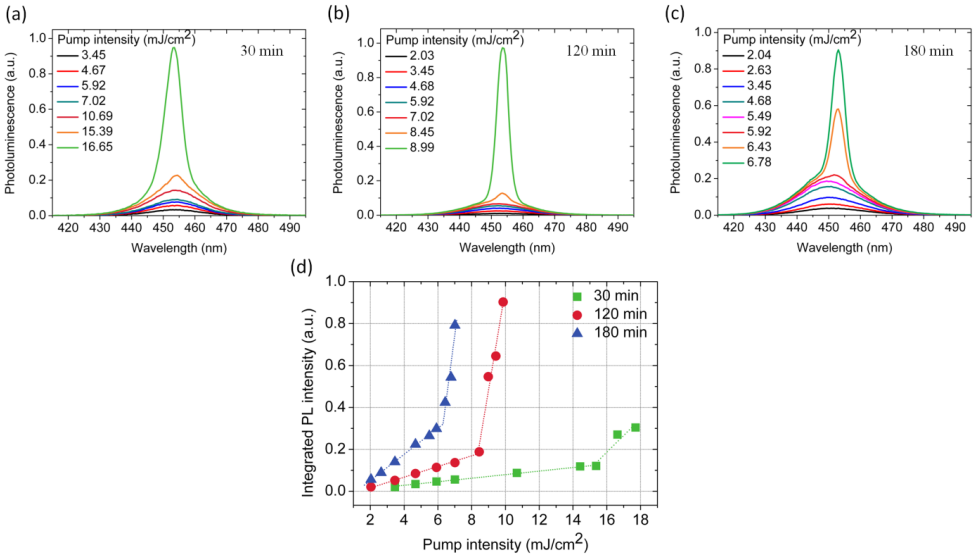


Figure 6.5 Pump intensity dependent PL of (a) 30 min, (b) 120 min and (c) 180 min shell grown CdZnS/ZnS QDs under 2PA pumping. (d) Luminescence vs. pump

intensity curve of the 30 min, 120 min and 180 min shell grown QDs with 2PA pumping. Reprinted (or Adapted) with permission from [274]. Copyright 2014 American Chemical Society.

Finally, we investigated the emission of our QDs at elevated pump intensities (much larger than the ASE threshold) to anticipate the utilization of the higher order excitonic states for the optical gain. Higher order excitonic gain can be only expected from the QDs with highly suppressed Auger recombination. For the exemplary case of 30 min grown QDs, as shown in Figure 6.6a, a new ASE emission peak can be seen at the higher energy side of the spontaneous emission peak (110 meV blue shifted as compared to the spontaneous emission peak) for pump intensities above $400 \mu\text{J}/\text{cm}^2$ (which is 2.5-fold greater than the ASE threshold). This newly emerging peak intensity increases at a faster rate than that of the regular ASE peak. We attribute this new ASE peak to be originating from higher order excitonic states (i.e., $1P_e-1P_{3/2}$) in these QDs. This observation of higher order excitonic ASE supports the existence of the long-lived multiexcitons in our QDs, which is also a clear indication of the suppressed nonradiative AR. Otherwise, higher order excitons would not be sustained in these QDs. This type of multi-excitonic ASE was not shown for the blue-emitting QDs before. Furthermore, ASE originating from high order excitons could be very rarely observed in the colloidal nanocrystals. Previously, only giant-shell CdSe/CdS QDs [43], [277] or very large nanorods [262] could achieve such higher order excitonic optical gain. Thus, this makes the first time observation of higher order excitonic gain in the blue-emitting QDs.

We also characterized the modal gain coefficients in our blue-emitting QDs using variable stripe length method [124]. The integrated emission intensity as a function of the stripe length is plotted in Figure 6.6b. The VSL data is fitted according to the reference [278]. The net modal gain coefficient is found to be 78 cm^{-1} , which is comparable to the highest reported gain coefficient of 150 cm^{-1} in the red-emitting QDs [279].

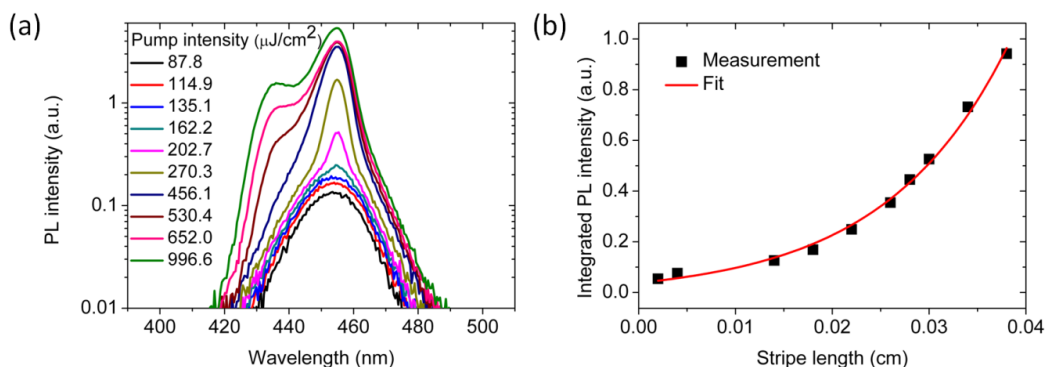


Figure 6.6 (a) PL intensity of the 30 min shell grown QDs under 1PA pumping as a function of pump intensity. At higher pump intensities higher-order multiexcitonic ASE is observed in addition to the regular ASE. (b) Variable stripe length measurement of the gain coefficient of the 180 min shell grown QDs pumped by 1PA. Reprinted (or Adapted) with permission from [274]. Copyright 2014 American Chemical Society.

6.2.3 Summary

As a summary, we synthesized and studied optical gain performance of blue-emitting CdZnS/ZnS QDs that combine both large size and gradient core/shell interface. These QDs are the first blue-emitting QDs having gradient core/shell interface, which showed a great potential for ultralow threshold optical gain. For the first time, we achieved 2PA pumped ASE in the blue-emitting QDs with a threshold as low as $\sim 6 \text{ mJ}/\text{cm}^2$. Furthermore, we showed record low gain thresholds ($\sim 60 \mu\text{J}/\text{cm}^2$) under single photon pumping with moderately high gain coefficients ($\sim 80 \text{ cm}^{-1}$). These QDs will be expected to be highly promising optical gain media for colloidal lasers that emit in the near UV-blue range.

6.3 All-colloidal quantum dot lasers

This section is based on the publication “Stable and Low-Threshold Optical Gain in CdSe/CdS Quantum Dots: An All-Colloidal Frequency Up-Converted Laser,” **B. Guzelturk**, Y. Kelestemur, K. Gungor, A. Yeltik, M. Z. Akgul, Y. Wang, R. Chen, C. Dang, H. Sun, and H. V. Demir, *Advanced Materials* 27, 2741-2746 (2015). Adapted (or “Reproduced in part”) with permission from John Wiley and Sons. Copyright 2015 Wiley-VCH Verlag GmbH & Co. KGaA, Weinheim.

6.3.1 Motivation

Current semiconductor lasers are experiencing technological challenges to access the green and yellow regions of the spectrum [256]. With quantum confinement effects, colloidal QDs are artificial atoms whose optical properties can be widely tuned via shape, size and composition during a colloidal synthesis process [238]. The QD based optical gain media can be precisely controlled to make a laser at any wavelength in the entire visible spectrum [10], [17], [42], [280], [281] and further in the near infrared region [282]. Besides the advantages of colour tunability and chemical process-ability, the QDs promise temperature insensitive optical gain because of well-separated energy levels, the atomic-like states [6], [257]. To date, optical gain has been shown with various colloidal core/shell QDs [10], [260], [274], [277], [283]. However, the small volume of nanometer-sized QDs substantially increases the nonradiative multiexciton Auger recombination, creating a significantly large nonradiative channel for depleting exciton energy into heat [119], [120].

The single exciton gain in type-I QDs is an advantageous mechanism to eliminate the multiexciton AR process and therefore to enable low threshold QD gain media [10], [281]. Yet, the gain performance would still be limited by the extremely fast AR rate when working at higher pump intensities. Reducing the wave function overlap of the electron and hole was demonstrated to reduce the AR rate through tailoring the energy levels and the size of the core and the shell [43], [44]. This led to a lowered

gain thresholds [284], but the reduction of electron-hole wave function overlap in these type-II or quasi type-II structures of quantum rods [44], or giant QDs [43] dramatically decreases the optical oscillator strength and, thus, the gain coefficient. In addition, the optical gain coefficient suffers from the low particle density per volume because of the giant size of these particles [43].

6.3.2 Experimental

CdSe-core/CdS-shell QDs were synthesized in two steps; synthesizing CdSe cores and the coating of the CdS shell. In the CdSe core synthesis, cadmium myristate and selenium dioxide were used as cadmium precursor and selenium precursor, respectively. They were dissolved in octadecene and evacuated at room temperature for 10-15 min. After evacuating, the solution was heated to 240 °C within 10 min. When the temperature reached 220 – 240°C, the nucleation of CdSe cores was initiated and observed with the change of solution color to yellowish. Then, the temperature of the solution was kept at 240°C for the growth of CdSe cores until the desired size of CdSe cores was reached. Following that, we stopped the reaction by decreasing the temperature. Finally, as-synthesized CdSe cores were precipitated by using acetone and dissolved in hexane.

For the coating of CdS shell, a certain amount of CdSe cores (100 nmol) dissolved in hexane was loaded to four-neck flask containing 3 mL octadecene and 3 mL oleylamine. Then, the solution was taken under vacuum at around 100°C to remove hexane and any other organic residuals. After that, the temperature of the reaction solution was set to 310°C for the coating of CdS shell under argon atmosphere. When the temperature reached around 240°C, injection of calculated amount of cadmium precursor (cadmium oleate diluted in octadecene) and sulfur precursor (octanethiol diluted in octadecene) was started at the rate of 3mL/hr. After complete injection of shell precursors within two hours at 310°C, the reaction was stopped with decreasing the temperature. As-synthesized CdSe-core/CdS-shell QDs were precipitated with acetone and dispersed in hexane.

For the ASE and lasing measurements; we employed an amplified femtosecond Ti:Sapphire laser system (Spitfire Pro XP, Spectra Physics) having 120 fs pulse width, 1kHz repetition rate at 800 nm wavelength for 2PA experiments. For the 1PA experiments, BBO crystal was used to generate second harmonic frequency (400 nm wavelength) from 800 nm laser beam. The pump laser beam was focused onto the sample via a cylindrical lens of 20 cm focal length. For the ASE measurements, the stripe area is ~ 11.3 and 2.6 mm^2 for 2PA and 1PA pumping experiments, respectively as measured by a beam profiler.

For the thin-film sample preparation; we spin-coated the QDs (60-80 mg/mL) on pre-cleaned quartz substrates. The resulting film thickness was measured as ~ 430 nm.

For the all-colloidal vertical-cavity surface-emitting lasers; SiO_2 nanoparticle solution (Aldrich Ludox TMA 30w%, water) and TiO_2 nanoparticle solution (Nanoamor Rutile TiO_2 nanoparticles 15w%, water) were diluted with methanol to have final concentrations of 3.5 w% and 5 w%, respectively. To fabricate the DBRs, we alternatively spin coated the nanoparticles at 4000 rpm for 1 min and annealed at 200°C at each spin coating step. To accomplish the QD film in the Fabry-Perot cavity, we deposited PMMA (PMMA 950 A9, 4000 rpm, 45 s) on top of the DBRs, deposited the QDs (60-80 mg/mL) via drop casting on one of the DBRs then placed the other DBR on top. Using epoxy, we fixed two DBRs to form the all-colloidal vertical-cavity surface-emitting lasers.

For the calculation of average number of excitons per QD at the ASE threshold; first we assumed that the absorption cross-section of the zinc-blende CdSe QDs is the same with their wurtzite counterparts at 3.54 eV and calculated their absorption cross-section by using the equation given by Leatherdale *et al.* [285]. For the shell growth, we used 100 nM of the CdSe core QDs as the seed. By knowing the initial concentration and final volume of the as-synthesized core/shell QDs, we prepared solutions with known concentration for both core-only and core/shell QDs and measured their absorption spectra. Then, we employed Lambert-Beer's law to calculate the absorption cross section of the as-synthesized core/shell QDs. For this, we assumed

that all of the core QDs were coated by CdS and there is no homo-nucleation of CdS QDs. We justified this since we did not observe any absorption or emission from CdS QDs.

To calculate the average number excitons per QD, we utilize $\langle N_{1PA} \rangle = f \times \sigma_{1PA}$ and $\langle N_{2PA} \rangle = \frac{f^2 \times \sigma_{2PA}}{\tau_{pulse}}$ for the 1PA and 2PA, respectively. f is the pump intensity; σ_{1PA} and σ_{2PA} are the 1PA and 2PA cross-sections, respectively; and τ_{pulse} is the pulse width of the excitation source. For the core/shell QDs, σ_{1PA} is $3.536 \times 10^{-14} \text{ cm}^2$ and σ_{2PA} is measured as 41,885 GM by the open aperture z-scan measurement, the value is close to the 2PA cross-section previously reported to be 45,000 GM for CdSe/ZnS QDs [269], [273]. For the core-only QDs, σ_{1PA} is measured as $5.463 \times 10^{-15} \text{ cm}^2$. The $\langle N \rangle$ values at the threshold for 1PA and 2PA pumping are very close to each other (1.43 and 1.24), indicating that the ASE mechanisms are the same.

6.3.3 Results and discussion

In this part of the thesis, we achieved very high performance and extremely stable optical gain media using tailor-made CdSe-core/CdS-shell QDs via both single- and two-photon absorption pumping. We synthesized high quality zinc-blende CdSe nanocrystals followed by slow CdS-shell growth at high temperature to improve crystal quality. The relatively thin CdS shell (approx. 6 monolayers) greatly helped to advantageously combine the small size (i.e., larger number of particles per volume), high photoluminescence quantum yield and the high performance optical gain. This resulted in a low gain threshold of $29 \mu\text{J}/\text{cm}^2$ and extremely high gain stability while preserving the initial stimulated emission intensity even after 1.8×10^7 laser shots (> 5 hours of continuous excitation) under 1PA. The high performance QD gain medium was further demonstrated in an all-colloidal vertical-cavity surface-emitting laser (AC – VCSEL), for the first time, using simple and solution processed distributed Bragg reflectors (DBR) of 96% reflectivity. With the solution processed DBRs and the tailored core/shell QDs, we have achieved a record low frequency up-converted lasing threshold of $764 \mu\text{J}/\text{cm}^2$, which surpass that of the previous best reports in the colloidal

QDs (5-10 mJ/cm² [270], [286]) and the colloidal nanorods (910 μJ/cm² [261]). All solution processed QD-laser represents one of the most cost effective approaches toward high-performance full-color nanocrystal lasers based on a single material technology.

CdSe-core/CdS-shell QDs having 6 monolayer CdS-shell were synthesized with a modified recipe by Bawendi group Ref. [287] (see Experimental). High temperature synthesis with slow crystal growth and small lattice mismatch allowed precise control of the shell growth. Figure 6.7a and its inset show the transmission electron microscopy images of the highly single-crystalline quality QDs with monodispersed size distribution resulting in excellently self-assembly on TEM grids. The crystal structure of the QDs was investigated by X-ray diffraction (XRD) patterns in Figure 6.7b. While the CdSe core exhibit pure zinc-blende (ZB) crystal structure, CdSe/CdS core/shell QDs seem to show diffraction peaks from both zinc-blende and wurtzite (W) phases. The result suggests that these QDs exhibit ZB-W polytypism, where wurtzite and zinc-blende domains can be retained within each nanocrystal and can be attributed to the high temperature CdS shell coating in the presence of primary amines [288]. XRD diffractogram in Figure 6.7b also demonstrates the enhanced crystal structure after high temperature CdS shell growth as observed by the sharper diffraction peaks. The core/shell QD solution shows well-defined excitonic absorption peak (at 615 nm) and excellent photoluminescence (PL) emission (FWHM 20-25 nm) with a quantum yield of as high as 90% in solution-state (see Figure 6.7c). In their solid films, quantum yield was also measured to be as high as 50% using an integrating sphere.

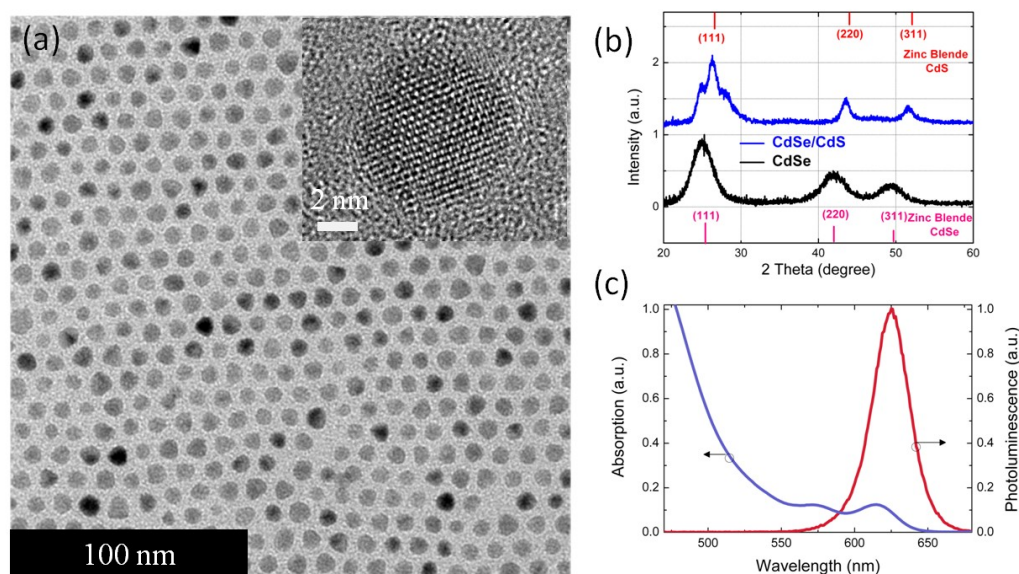


Figure 6.7 (a) Transmission electron microscopy image of the CdSe/CdS QDs having CdSe core of 2.2 nm radius and 6 monolayer CdS shell. Inset shows the high resolution TEM image of a CdSe/CdS QD with diameter of ~ 8 nm. (b) XRD patterns of CdSe core (bottom) and CdSe/CdS QDs (top). The CdSe core shows zinc-blende structure with matched XRD pattern to its bulk counterpart. After CdS shell growth, diffraction peaks are shifted to higher angles and become narrower, indicating the increased crystalline quality and alloying at the core/shell interface. (c) Photoluminescence (red, solid) and absorbance (blue, dotted) spectrum of the core/shell QD. Emission line width is less than 30 nm (full width at half maximum – FWHM) suggesting the small size distribution. Reprinted by permission from Wiley [18], Copyright 2015 Wiley-VCH Verlag GmbH & Co. KGaA, Weinheim.

The exciton recombination kinetics were studied by time-resolved PL spectroscopy using a streak camera while increasing excitation intensity levels as presented in Figure 6.8 for both core-only and core/shell QDs. At the low excitation intensities (resulting in average number of excitons per QD as $\langle N \rangle \ll 0.1$), slow exponential decay is associated with fluorescence lifetime of the single exciton state (τ_x), which is about 35 ns for CdSe-core/CdS-shell structures (Figure 6.8a) and ~ 22 ns for CdSe QDs (Figure 6.8b). For the core-only CdSe QD structure, there is a small contribution from a fast decay component with a time constant τ_{ss} of 1.3-1.8 ns even at extremely low

excitation levels. This is attributed to active surface trap states in the core-only CdSe QD, which also deplete excitons via nonradiative pathway [289]. This also explains the low quantum yield (<10%) in the core-only CdSe QDs. Growth of the CdS shell passivates the surface states effectively, resulting in a much higher quantum yield (~90%) and the disappearance of such fast trap related decay (τ_{ss}). As the pump intensity was increased (as more excitons per QD is created), we started to observe the buildup of a faster decay component, which is attributed to the decay of the multiexciton (τ_{XX}) where the nonradiative AR has generally a dominant contribution [6].

Table 6.1 and

Table 6.2 summarize the lifetime components at different excitation intensities. To calculate the biexciton population in the ensemble for given excitation fluence, we employ the following: $\langle N \rangle = f \times \sigma$ (see Experimental part for the calculation of the absorption cross-section σ). In the core-only QDs, for $\langle N \rangle = 1.40$, where ~40.5% of the QD population has multiexcitons (biexciton and higher order excitons), very fast multiexciton lifetime of ~90 ps is observed (Figure 6.8b-inset). This indicates the occurrence of a very fast AR process in the core-only QDs. In the case of the core/shell QDs, for $\langle N \rangle = 1.23$, where ~35.0% of the QD population has multiexcitons, much slower multiexciton lifetime of ~1.25 ns is observed (Figure 6.8a).

We calculated Auger time constant by $\tau_{AR}^{-1} = \tau_{XX}^{-1} - 4\tau_X^{-1}$, where $4\tau_X^{-1}$ is the radiative recombination rate of biexciton, the factor 4 indicates the number of recombination pathways of 2 electron-hole pairs. We calculated the Auger time constants τ_{AR} of 91.6 ps and 1480 ps for the core-only and the core/shell QDs, respectively. The Auger time constant (1480 ps) of the CdSe-core/CdS-shell QD structure implies a significant suppression, up to an order of magnitude, in comparison to that of the core-only QDs [119], [120], [263]. Furthermore, this slow Auger lifetime compares well with that of the recent reports using excitonically engineered giant core/shell QDs [290], [291]. This substantial AR suppression is also consistent with recent suppressed blinking observation in similar QDs by [287] and suggests a

potential solution for the fundamentally challenging problem of using QDs for optical amplification.

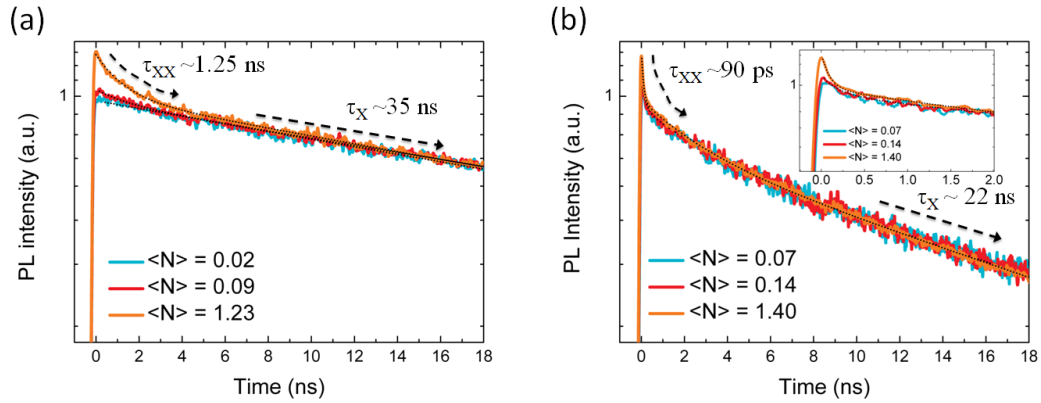


Figure 6.8 Transient PL intensity measured at the peak emission wavelength at three different excitation levels for (a) CdSe-core/CdS-shell and (b) core-only CdSe QDs. τ_{XX} is the multi-exciton lifetime, τ_X is the single exciton lifetime of the QDs. The average number of excitons per QD ($\langle N \rangle$) was calculated from the excitation levels. (b) Inset shows the decay of the CdSe QDs at an early time window. Reprinted by permission from Wiley [18], Copyright 2015 Wiley-VCH Verlag GmbH & Co. KGaA, Weinheim.

Table 6.1 Fluorescence lifetime components and the corresponding amplitudes for the CdSe/CdS QDs at different pump intensities measured at peak emission wavelength of 626 nm.

$\langle N \rangle$	A_x	τ_x (ns)	A_{xx}	τ_{xx} (ns)
0.023	0.86	35.00		
0.092	0.90	35.18		
1.234	0.92	35.20	0.31	1.27

Table 6.2 Fluorescence lifetime components and the corresponding amplitudes for the zinc-blende CdSe QDs at different pump intensities measured at peak emission wavelength of 567 nm.

$\langle N \rangle$	A_x	τ_x (ns)	A_{ss}	τ_{ss} (ns)	A_{xx}	τ_{xx} (ns)
0.07	0.70	21.7	0.22	2.67		
0.14	0.68	22.1	0.20	3.52		
1.40	0.71	21.0	0.25	2.66	0.37	0.09

The nature of crystal structure should not be accounted for the Auger recombination suppression as our zinc-blende CdSe core-only QDs show a similar Auger time constant with their wurtzite counterparts. The CdS shell is relatively thin, thus, this slightly reduces the overlap of the electron and hole wave functions. This would be one of the reasons for the Auger suppression as also previously demonstrated in other QD heterostructures [284]. Such electron-hole overlap reduction usually lowers the optical oscillator strength, i.e. reduces radiative recombination rate, and therefore comes with a decreased quantum yield because of the competition with the nonradiative recombination channels. In our core/shell heterostructure, a very high quantum yield is achieved using a relatively thin CdS shell (~6 monolayers). This suggests that not only an excellent passivation of surface is achieved but also optical oscillator strength is still high.

Another reason for the Auger suppression might be the smooth confinement barrier between the core and the shell, which was also shown to suppresses the blinking in the QDs [264], [292], [293]. In QDs with abrupt interface between the core and the shell, the relaxation of the momentum conservation requirement increases AR rate significantly [294]. Alloying at the core/shell interface was demonstrated for various heterostructured QD systems including CdSeS/ZnS [295] and wurtzite CdSe/CdSeS/CdS QDs [43]. In our QDs, the CdS shell was grown at an exceptionally high temperature of 310°C and at a very slow rate (6 monolayers in 3 hours). Thus, a

smooth CdSeS interfaced layer might be created due to enhanced inter-diffusion of the core and the shell material. Furthermore, our detailed XPS measurements and analysis strongly suggest the presence of the gradient alloying with an extent of 2-4 monolayers at the core/shell interface.

In order to explore the core/shell interface in the CdSe/CdS QDs, we performed x-ray photoelectron spectroscopy on the thin film sample of the core/shell QDs. We recorded XPS spectra of the sample as we performed an etch depth study by slowly etching the sample with Ar^+ ions (Thermo, K-Alpha Monochromated high-performance XPS spectrometer). Figure 6.9a shows the etch depth profile analysis of the atomic ratio of S to Se, where atomic percentages of S and Se are constructed from the XPS signal collected at S (2p) and Se (3d) peaks, respectively. In the initial etch depth region (etch depth step of 0-10 as shadowed by orange color), we observed a gradual change of the S/Se ratio, which is first a decrease then followed by an increase. The signal in this region came from the top QDs as shown in Figure 6.9b. Then, in the further etches (etch depth steps of 10-40 as shadowed by green color in Figure 6.9b), we achieved almost constant ratio (S/Se) of $\sim 7-9$. This indicates that after etching the top QDs, etching converges to an ensemble atomic ratio. Considering the size of the QDs having core radius of 2.2 nm and CdS shell thickness of 1.8 nm (6 monolayer CdS), the expected S/Se ratio from the volume of the core and shell region would be 5.01. The difference observed between the XPS measurement and the volume calculation is due to the fact that photoelectrons are exposed attenuation in the core and the shell region of the QDs.

As previously reported by [296]–[298], XPS can be used to precisely measure the thicknesses of core and shell in core/multi-shell nanocrystals by considering the mean free path of the emitted photoelectrons. For this, the intensity attenuation of a photoelectron created away from the surface, within the material, should be considered. This attenuation is given as,

$$dI = I_0 \exp\left(\frac{-Z}{\lambda}\right) dV \quad (6.1)$$

where dI is the infinitesimal intensity contribution from infinitesimal volume dV . z is the distance between the surface and the position of the emitted photoelectron and λ is the mean free path of the electron. I_0 is a constant that depends on the physical material properties and instrumental factors. In the case of core/shell QDs, the instrumental factors will be the same except the material properties given by,

$$\frac{I_0^{CdS}}{I_0^{CdSe}} = \frac{\rho^{CdS}}{M^{CdS}} \frac{M^{CdSe}}{\rho^{CdSe}} \quad (6.2)$$

where ρ and M are the density and the molecular weight of each material.

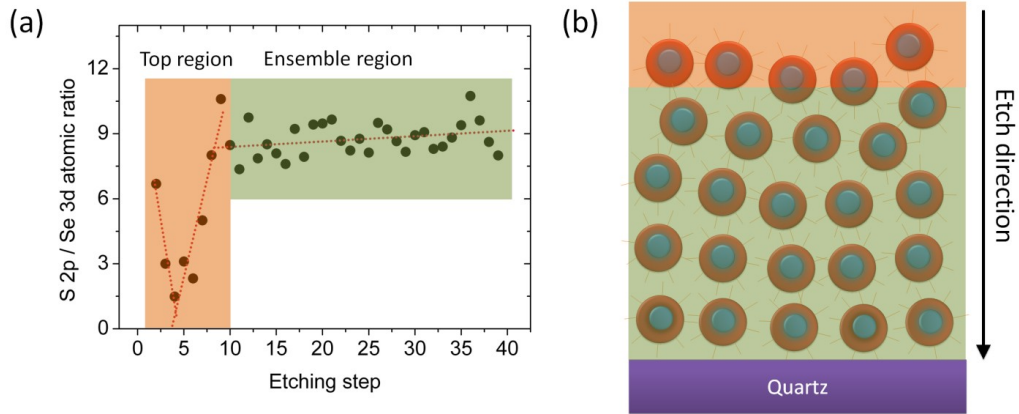


Figure 6.9 (a) Etch depth profile analysis of the atomic ratio of S to Se. (b) Initial etched part (i.e., top QDs) and deeper etched part (i.e., ensemble region). Reprinted by permission from Wiley [18], Copyright 2015 Wiley-VCH Verlag GmbH & Co. KGaA, Weinheim.

Then, measured intensities of emitted photoelectrons from the core and the shell in the XPS measurement can be calculated by employing the following equation [296]

$$I = I_0 \int_{R1}^{R2} \int_0^\pi \int_0^{2\pi} \exp\left(-\frac{f(r, \theta)}{\lambda}\right) r^2 dr \sin(\theta) d\theta d\phi \quad (6.3)$$

where $f(r, \theta) = (R^2 - r^2 \sin^2(\theta))^{\frac{1}{2}} - r \cos(\theta)$. Using spherical symmetry, the intensity ratio of the emitted photoelectrons from the shell (CdS) and the core (CdSe) is calculated by the following assuming that there is an abrupt core/shell interface (see Figure 6.10);

$$\frac{I_{Shell}}{I_{Core}} = \frac{I_0^{Shell} \int_{R_c}^{R_s} \int_0^\pi \exp\left(-\frac{f(r, \theta)}{\lambda}\right) r^2 dr \sin(\theta) d\theta d\phi}{I_0^{Core} \int_0^{R_c} \int_0^\pi \exp\left(-\frac{f(r, \theta)}{\lambda}\right) r^2 dr \sin(\theta) d\theta d\phi} \quad (6.4)$$

where R_c and R_s are the radius of the core and the width of the shell, respectively. In our QDs, R_c is measured as 2.2 nm and R_s is 1.8 nm (6 monolayer of CdS) and mean free path (λ) is 1.8 nm for CdS 2p peak [296], [297]. Using these parameters, we calculated $\frac{I_{CdS}}{I_{CdSe}}$ ratio to be 12.90 assuming an abrupt core/shell interface. However, the measured $\frac{I_{CdS}}{I_{CdSe}}$ ratio by the XPS data is between 7 and 9 (see Figure 6.9a ensemble region). Therefore, there is a discrepancy for the S to Se ratio when assuming abrupt core/shell interface. Here, diffusion of the Se atoms into the shell region would potentially result in lower $\frac{I_{CdS}}{I_{CdSe}}$ ratios. Therefore, we consider the presence of a gradient alloyed interface in our QDs (see Figure 6.10). We introduced an alloyed region having a width (w_{alloy}), where the atomic composition of Se and S changes linearly (i.e., linear gradient alloy of selenium and sulfur) as shown by the atomic composition in Figure 6.10. The $\frac{I_{CdS}}{I_{CdSe}}$ ratio is defined for the alloy case as follows:

$$\frac{I_{Shell}}{I_{Core}} = \frac{I_0^{Shell} \int_{R_c - w_{alloy}}^{R_s} \int_0^\pi c(r)^S \exp\left(-\frac{f(r, \theta)}{\lambda}\right) r^2 dr \sin(\theta) d\theta d\phi}{I_0^{Core} \int_0^{R_c + w_{alloy}} \int_0^\pi c(r)^{Se} \exp\left(-\frac{f(r, \theta)}{\lambda}\right) r^2 dr \sin(\theta) d\theta d\phi} \quad (6.5)$$

where:

$$c(r)^S = 0, \text{ if } r < R_c - \frac{w_{alloy}}{2} \quad (6.6)$$

$$c(r)^S = \frac{r - \left(R_c - \frac{w_{\text{alloy}}}{2}\right)}{w_{\text{alloy}}}, \text{ if } R_c - \frac{w_{\text{alloy}}}{2} < r < R_c + \frac{w_{\text{alloy}}}{2} \quad (6.7)$$

$$c(r)^S = 1, \text{ if } R_c + \frac{w_{\text{alloy}}}{2} < r < R_s \quad (6.8)$$

$$c(r)^{\text{Se}} = 1 - c(r)^S \quad (6.9)$$

Here, $c(r)^S$ is the atomic percentage of the sulfur atoms throughout the QD and $c(r)^{\text{Se}}$ is the atomic percentage of the selenium atoms. As shown in Table 6.3, we found that when alloyed region thickness w_{alloy} varies for 0.6, 0.9 and 1.2 nm (corresponding to 2, 3 and 4 monolayers), $\frac{I_{\text{CdS}}}{I_{\text{CdSe}}}$ ratio become 8.97, 7.91 and 7.10, respectively. This observation strongly suggests that our QDs possess a gradient alloy CdSeS layer at the core/shell interface. Also, the width of the alloyed layer is expected to be between two and four monolayers of CdSe and CdS lattice (i.e., 0.6 to 1.2 nm).

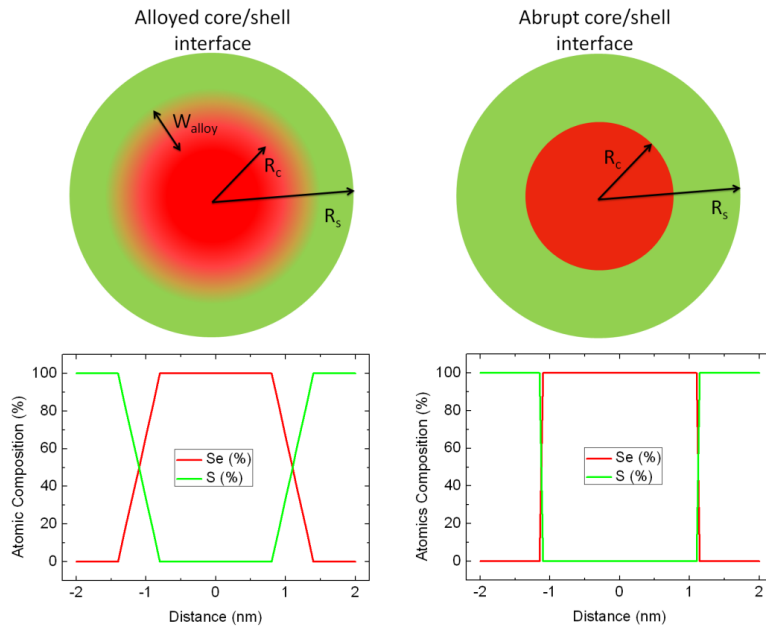


Figure 6.10 Alloyed vs. abrupt core/shell interface in CdSe/CdS QDs along with their atomic composition throughout the QD. Reprinted by permission from Wiley [18], Copyright 2015 Wiley-VCH Verlag GmbH & Co. KGaA, Weinheim.

Table 6.3 Sulfur to Selenium ratio calculated by the volumes of the core and the shell, measured by XPS and calculated by (6.4) assuming abrupt core/shell interface and calculated by (6.5) assuming alloyed core/shell interface with varying alloy width.

	I_S/I_{Se} ratio
Volume ratio (V_{CdS}/V_{CdSe})	5.01
Measurement (XPS data)	7.0 – 9.0
Calc. (abrupt core/shell interface, $w_{alloy} = 0$ nm)	12.90
Calc. (gradient alloy, $w_{alloy} = 0.6$ nm)	8.97
Calc. (gradient alloy, $w_{alloy} = 0.9$ nm)	7.91
Calc. (gradient alloy, $w_{alloy} = 1.2$ nm)	7.10

Amplified spontaneous emission (ASE) in the spin-coated core/shell QD films is presented in Figure 6.11a and Figure 6.11b for 1PA and 2PA pumping, respectively. The onset of amplified spontaneous emission in the QD films is clearly shown with the abrupt rise of the output emission intensity (ASE peak at ~639 nm) and the narrowing of the emission spectrum (fwhm ~7-9 nm) when pumped over the threshold pumping intensity. The red shift (8-10 nm) of the ASE peak in comparison to the PL peak (see Figure 6.11a-b) is a strong indicator of biexcitonic gain mechanism in our type-I QDs due to the presence of thin CdS shell [273], [284]. Biexcitonic gain has been further suggested by the calculated average number of excitons per QD ($\langle N \rangle$) at the ASE threshold, which are 1.43 and 1.24 under 1PA and 2PA pumping, respectively. These values are in good agreement with biexciton gain mechanism in our core/shell QD structure which is similar to type-I QDs. Slow Auger rate in our core/shell QDs largely helps to reduce the biexcitonic gain threshold owing to the suppressing the most competitive pathway of biexciton annihilation. The spin-coated QD films realized 1PA pumped ASE with a threshold of 29 $\mu\text{J}/\text{cm}^2$ (Figure 6.11a-inset), one of the lowest thresholds reported among all QDs (previous best reports were 30-100 $\mu\text{J}/\text{cm}^2$ [10], [43], [262], [274]), and while maintaining high modal gain coefficients as high as 120 cm^{-1} , measured using variable stripe length technique (see Figure 6.12). Optical gain coefficient of the core/shell QDs was characterized by performing variable stripe length measurement on the spin coated solid film of the QDs on quartz. Pump intensity

was chosen to be four times of the 1PA-pumped ASE threshold corresponding to $\langle N \rangle \sim 5$. Fitting of the data is performed according to the references [278], [279].

For the case of frequency up-converted, 2PA, pumping, the threshold for ASE is $\sim 5.02 \text{ mJ/cm}^2$ (Figure 6.11b-inset), which is the lowest threshold among red-emitting spherical QDs so far [269], [270]. Our 2PA pumped gain threshold is slightly larger than the threshold for the CdSe/CdS nanorods, which have ~ 5 -fold larger volumes than our QDs [261]. Overall, achievement of low threshold gain using 2PA pumping in the red spectral range, also considering our previous demonstrations using green-emitting colloidal nanoplatelets [17] and blue-emitting alloyed-core/shell QDs [274], makes the colloidal semiconductor nanocrystal a highly promising class of materials for frequency up-converted lasers. We used open aperture z-scan measurements to find the 2PA cross-section. We employed amplified femtosecond Ti:Sapphire laser system (Spitfire Pro XP, Spectra Physics) having 120 fs pulse width at 800 nm with 1 kHz repetition rate. We placed the QDs in a quartz cuvette having 1 mm optical path length. The sample is translated along the focus of the fs Gaussian beam. The following (6.10) is used to fit the measured open aperture z-scan transmission measurements [299]:

$$T(z) = \frac{1}{1 + \frac{I_0 \times \beta \times l}{1 + \left(\frac{z}{z_0}\right)^2}} \quad (6.10)$$

$T(z)$ is the normalized transmitted intensity as a function of sample position on z . I_0 is the peak on-axis irradiance at the focus. β is the two-photon absorption coefficient. l is the cuvette length (1 mm). z_0 is the Rayleigh range (6 mm). Excitation per pulse energy was attenuated to 3.12 μJ , which yields $I_0 \sim 1.399 \times 10^{16} \text{ W/m}^2$. Fitting of the measured transmission curve yielded β as $4.16 \times 10^{-15} \text{ m/W}$. Then, using (6.11), we calculated two photon absorption (2PA) cross-section.

$$\sigma_{2PA} = \frac{h\nu \times \beta}{N_A \times d_0 \times 10^{-3}} \quad (6.11)$$

Here $h\nu$ is the energy of the excitation photons, N_A is the Avagadro's number and d_0 is the molar concentration of the QDs. For CdSe-core/CdS-shell and CdSe QDs, σ_{2PA} was found to be 42,000 and 11,000 GM, respectively. Figure 6.13 shows the open aperture z-scan measurement of the CdSe/CdS QDs along with the fit. The measurement of the

bare solvent hexane is also shown at the same experimental conditions, where there is no nonlinear absorption observed.

Recently, colloidal nanoplatelets have emerged as alternative competitors for the optical gain exhibiting low ASE thresholds ($\sim 10 \mu\text{J}/\text{cm}^2$) and high gain coefficients (650 cm^{-1}) [17], [59], [75]. Although nanoplatelets are expected to be highly advantageous for optical gain, the stability of ASE in the nanoplatelets has been quite limited (after 10^4 - 10^5 laser shots, the ASE intensity drops to half of the initial intensity) [17]. We showed that our CdSe/CdS QDs exhibit an excellent ASE stability even for laser shots $\sim 1.8 \times 10^7$ (5 hours of continuous pumping) under pump intensity of $35 \mu\text{J}/\text{cm}^2$ (see Figure 6.11c). As shown in Figure 6.11c, the ASE intensity also exhibits an enhancement in the early time window (up to 1×10^6 laser shots), which is attributed to reaching the thermal equilibrium with partial removal of oxygen and moisture from the solid film sample. Therefore, the stability of our core/shell QDs represents more than two orders of magnitude enhancement over the stability of ASE observed in the nanoplatelets [17]. As compared the other type of colloidal nanocrystals (i.e., nanorods and tetrapods), which have shown stabilities up to 6×10^6 laser shots [261], our core/shell QDs also stand out as an exceptionally stable material for lasing.

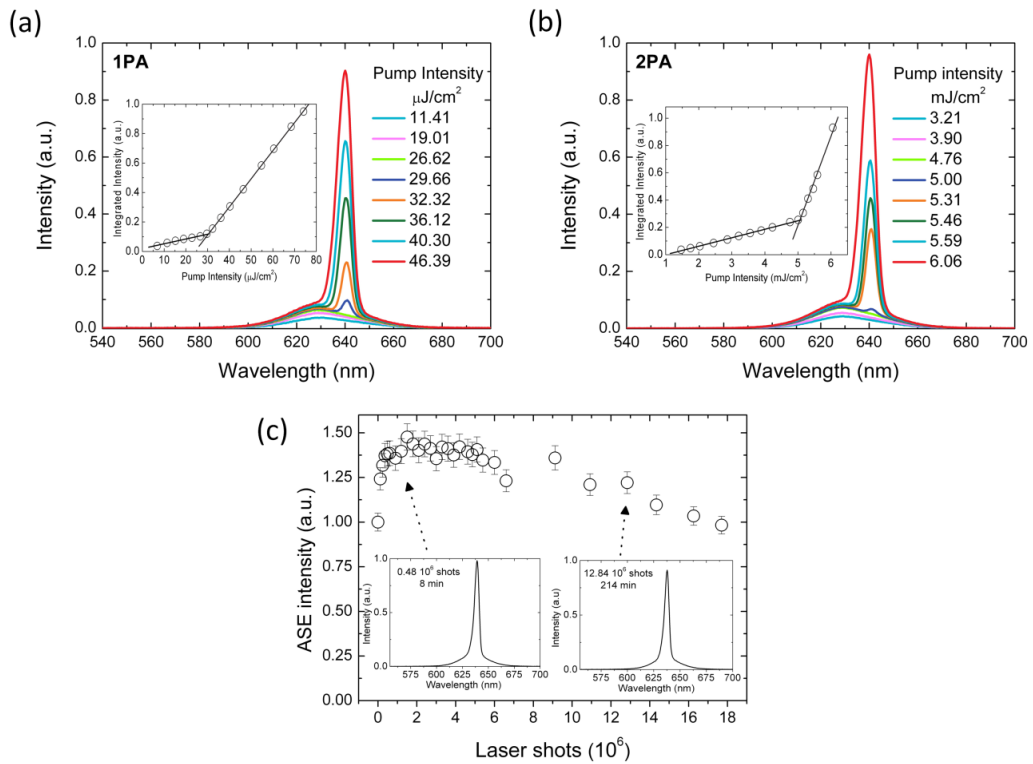


Figure 6.11 (a) The emission spectra of the core/shell QD film under 1PA stripe excitation pumping. The inset shows the integrated emission intensity as a function of 1PA pumping energy intensity. (b) 2PA pumped emission spectra of the QDs at various pump intensities. Inset shows the integrated intensity of the emission as a function of 2PA pump intensity. The narrow ASE peak with a FWHM of 5 nm kicks off at the red-tail of the spontaneous emission spectrum (FWHM of ~ 29 nm). (c) Laser shot dependent ASE intensity under pump laser shots up to 1.8×10^7 indicating the exceptional stability of the QDs. Reprinted by permission from Wiley [18], Copyright 2015 Wiley-VCH Verlag GmbH & Co. KGaA, Weinheim.

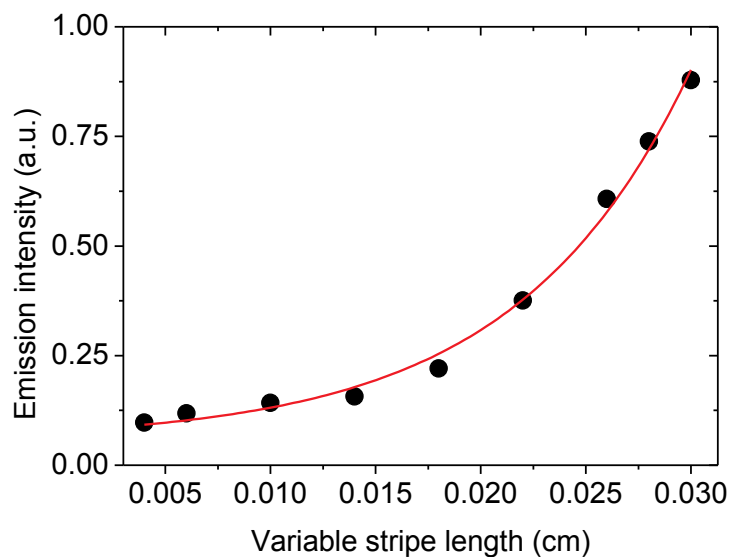


Figure 6.12 Variable stripe length technique based measurement of the net modal gain coefficient and the fit to the experimental data. Reprinted by permission from Wiley [18], Copyright 2015 Wiley-VCH Verlag GmbH & Co. KGaA, Weinheim.

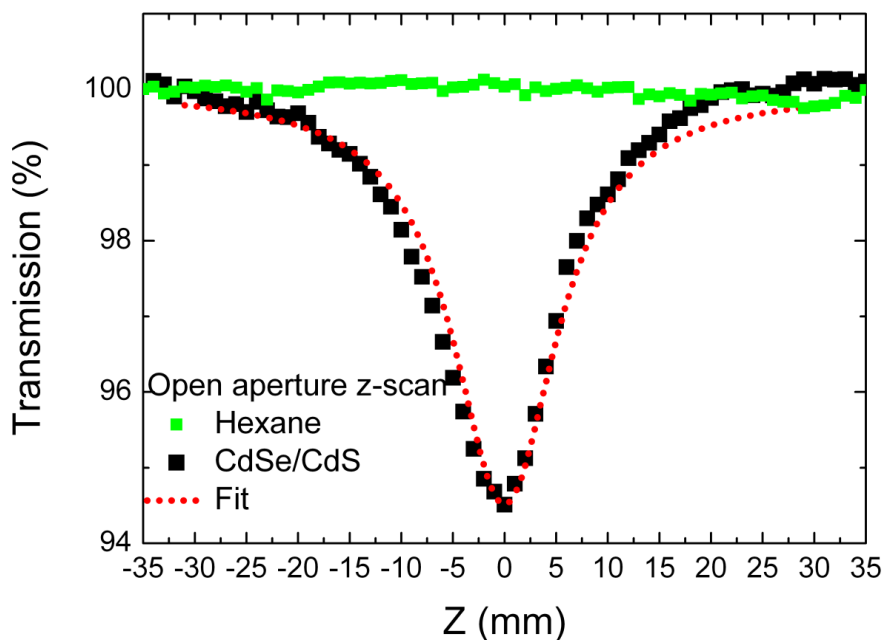


Figure 6.13 Open aperture z-scan measurement reveals the 2PA cross-section of the QDs as 41,885 GM. Although this is not the highest reported 2PA cross-section for the QDs, the threshold for amplified spontaneous emission is the lowest among 2PA

pumped QD gain media. This is only possible by the high gain performance of QD materials. Reprinted by permission from Wiley [18], Copyright 2015 Wiley-VCH Verlag GmbH & Co. KGaA, Weinheim.

With highly efficient optical gain performance, we proposed and developed an all-colloidal laser using these CdSe/CdS QDs as the active gain media. The most challenging laser configuration – vertical cavity surface emitting laser (VCSEL) – was fully enabled by the most cost-effective technology: solution processing. Two distributed Bragg reflectors (DBR) were fabricated by using only spin coating of the alternating layers of silicon dioxide and titanium dioxide nanoparticles on quartz substrates [300], [301]. The densely packed dielectric nanoparticles form multilayered films (see Figure 6.15 for the cross-section of the Bragg stack imaged with scanning electron microscopy) with a considerable refractive index contrast (i.e., ~ 1.31 and ~ 1.95 for SiO_2 and TiO_2 layers at 630 nm, respectively). We have checked the refractive index of SiO_2 and TiO_2 nanoparticles using ellipsometer. Figure 6.14 shows the n and k values of these nanoparticles. In addition, absorption of the TiO_2 nanoparticles was measured as shown by Figure 6.14.

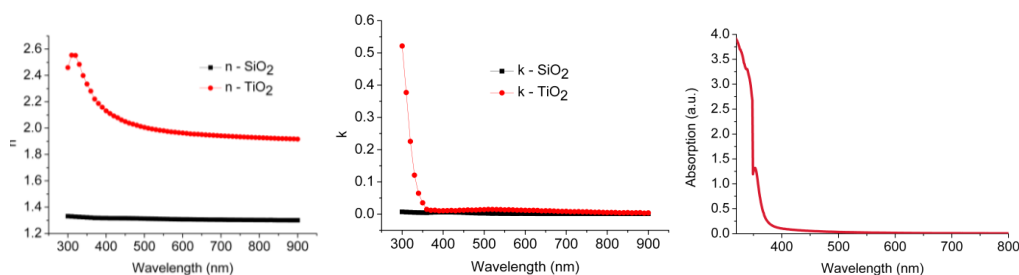


Figure 6.14 Optical constants of SiO_2 and TiO_2 nanoparticle films and absorption of TiO_2 nanoparticles. Reprinted by permission from Wiley [18], Copyright 2016 Wiley-VCH Verlag GmbH & Co. KGaA, Weinheim.

The thickness of each oxide nanoparticles layer was controlled to be a quarter of wavelength at the ASE peak, and the reflectance reaches the maximum of 96% with 10-bilayers (see Figure 6.15a). The PMMA was then deposited on top of the DBR as the final layer ($\sim 3 \mu\text{m}$ thickness) for protection and creating an optical distance. Then, the core/shell QDs were drop casted on one of the DBRs and the other DBR was used

to sandwich the QD layer so that an all-solution processed and all-colloidal VCSEL (AC-VCSEL) was completed. Epoxy was applied at the edges to fix the structure together. PL emission spectrum of the QDs inside the AC-VCSEL is shown in Figure 6.15b, exhibiting the resonant cavity modes corresponding to an optical thickness of about 15 μm .

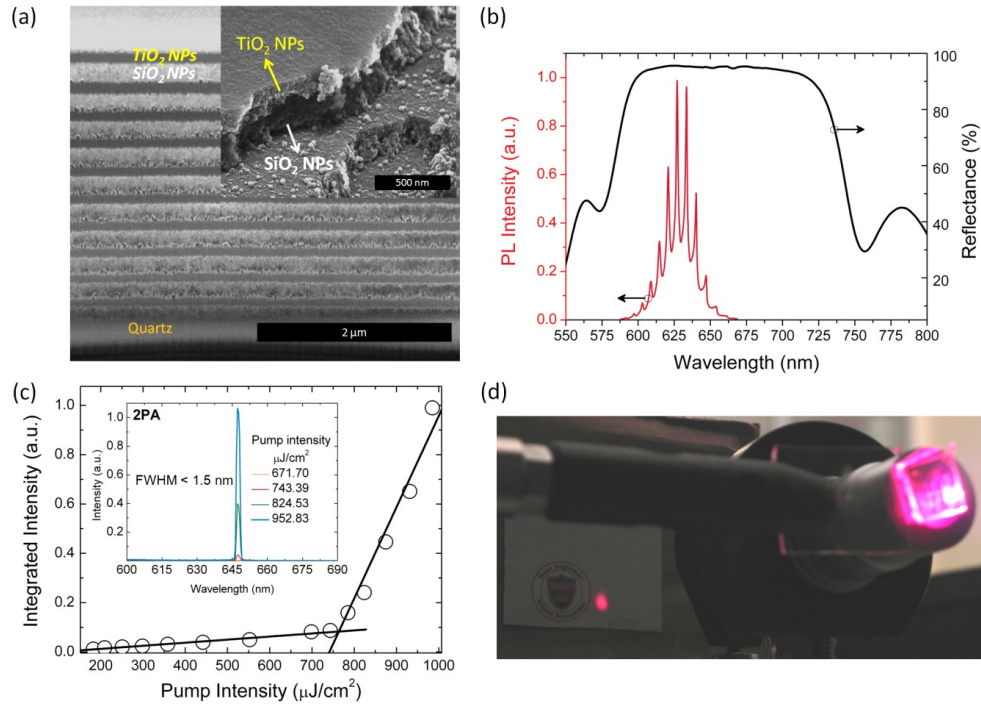


Figure 6.15 (a) Scanning electron microscopy cross-sectional image of the all-colloidal DBR shows alternating stacks as the results of different spin-casted nanoparticles (SiO_2 and TiO_2). Focused ion beam was used to create cross section of the colloidal DBR. Inset shows the close-up of the layered stacks of TiO_2 and SiO_2 nanoparticles at the cleaved edge of a DBR. (b) Surface normal reflectance of the DBR stack with 10-bilayer of TiO_2 and SiO_2 nanoparticles along with the PL of the QDs in the cavity having optical thickness of about 15 μm . (c) Emission intensity as a function of pump intensity for frequency up-converted all-colloidal VCSEL clearly shows the threshold behavior of the AC-VCSEL. Inset shows the emission spectrum of the laser under different excitation pump density. Single mode lasing is achieved with a Q-factor greater than 430. Lasing peak is narrower than 1.5 nm (limited by the spectral resolution of our measurement system). (d) Photographic image of the lasing spot from

the all-colloidal VCSEL. The spectrally and spatially coherent lasing beam is visible as a bright spot on the screen. Reprinted by permission from Wiley [18], Copyright 2015 Wiley-VCH Verlag GmbH & Co. KGaA, Weinheim.

Here, the highly performed QD gain medium with relatively large thickness enabled a frequency up-converted AC-VCSEL with single mode and sharp laser output (Figure 6.15c-inset) at 647 nm with a fwhm less than 1.5 nm (limited by the resolution of the spectrometer, which is also ~ 1.5 nm). Lasing was observed throughout the whole sample with a small variation of the threshold due to slightly different thickness of the gain medium over the large area of the sample. The average threshold of the AC-VCSEL is as low as $764 \mu\text{J}/\text{cm}^2$ under 2PA pumping as shown in Figure 6.15c. This is the lowest threshold for a frequency up-converted laser reported to date even compared to the thresholds achieved by colloidal nanorods and organic semiconductors [261], [302]. Depending on the thickness of the drop casted QD film, multi-mode lasing in the spectral window of optical gain medium was also possible as shown in Figure 6.16.

Figure 6.16 demonstrates the single- and multi-mode lasing from the AC-VCSELs. Depending on the location of the pump spot on the AC-VCSEL, either single-mode or multi-mode lasing was observed when the pump intensity was above the threshold. This is attributed to the local thicknesses variation of the QD layer and varying local wedge angle. However, the threshold variation throughout the AC-VCSELs was minimal. The stability of the AC-VCSEL was also tested; the laser could operate without degradation for duration on the order of tens of minutes corresponding to $>10^6$ pump pulses.

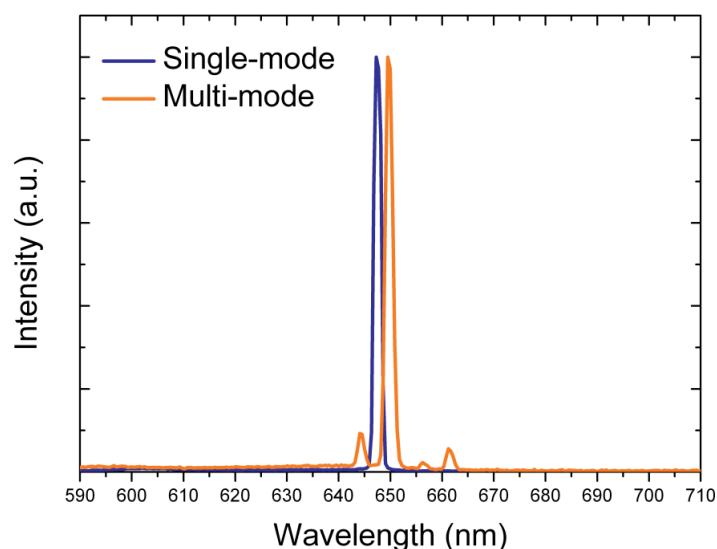


Figure 6.16 Single- and multi-mode lasing in AC-VCSELs. Depending on the location of the pump spot on the AC-VCSEL, either single-mode or multi-mode lasing is observed when the pump intensity is above the threshold. Reprinted by permission from Wiley [18], Copyright 2015 Wiley-VCH Verlag GmbH & Co. KGaA, Weinheim.

Given the relatively low reflectivity of our colloidal DBRs, the ultralow threshold of the VCSEL structure emphasizes the high optical gain capability of our core/shell QDs with the help of the suppressed AR. Unlike alternating polymer-based DBRs [303], the spectrally and spatially coherent emission of a well-defined laser beam was observed with a bright spot at the screen behind the sample (Figure 6.15d). However, the AC-VCSEL did not lase under 400 nm pumping due to finite absorption and scattering caused by the TiO₂ nanoparticles (see Figure 6.14 for the optical constants). This highlights the advantage of 2PA pumping mechanism, which avoids unwanted scattering and absorption losses due to the use of a longer wavelength pump.

6.3.4 Summary

In conclusion, tailored CdSe-core/CdS-shell QDs were demonstrated as very efficient and highly stable optical gain media thanks to high volume packing density and substantial AR suppression. The ASE performance of the QDs showed very low

optical gain thresholds with relatively high gain coefficient, enabling an all-colloidal VCSEL with solution processed DBRs. For the first time, the spatially and spectrally coherent, well-defined laser beam emission from an all-colloidal laser was presented especially at a record low threshold in frequency up-converted regime. Our results would certainly extend to other sizes of QDs for different colors, representing a promising future for QD lasers as well as all-solution processed lasers: the most cost effective approach for single-material full-color lasers. Frequency up-converted QD-based AC-VCSELs might be promising for sensing and biological applications in the future where the increasing penetration depth and reducing destructive effects of the excitation light are critical.

6.4 Optical gain and lasing in colloidal nanoplatelets

This section is based on the publication “Amplified spontaneous emission and lasing in colloidal nanoplatelets,” **B. Guzelturk**, Y. Kelestemur, M. Olutas, S. Delikanli and H. V. Demir, *ACS Nano* 8, 6599-6605 (2014). Adapted (or “Reproduced in part”) with permission from American Chemical Society. Copyright 2014 American Chemical Society.

6.4.1 Motivation

Colloidal quantum dots have been considered as versatile and promising light-emitting materials towards achieving full color lasers [10], [11]. However, optical gain is severely limited in these colloidal nanocrystals due to the nonradiative Auger recombination [119], [304]. Alternatively, various shaped nanocrystals including nanorods and tetrapods were developed and have shown to enhance the optical gain performance as compared to that of the QDs [116], [257], [262], [305]–[307]. Yet, the maximum reachable gain was still limited in these materials [116].

Recently, colloidal nanoplatelets, which are also known as colloidal quantum wells, have been introduced [56], [57], [308]. The NPLs exhibit superior optical and electronic properties as compared to the QDs including their narrower spontaneous emission spectra, suppressed inhomogeneous emission broadening and giant oscillator strength, which are highly desired for optical gain and lasing applications [58], [78], [138]. In addition, with the great efforts within last years, the synthesis of NPLs having different thicknesses are optimized [308] and the NPLs having assorted structures such as core/crown (laterally grown shell) [77], [78] and core/shell (vertically grown shell) have been successfully synthesized that realize high quantum yields and stabilities together with larger absorption cross-sections [79].

Among these CdSe/CdS core/crown NPLs (or also denoted as CdSe/CdS nanoheteroplatelets with a CdS wing) are highly attractive owing to their favorable photophysical properties. First, the peak emission wavelength of the core/crown NPLs do not change (except a few nm red-shift) as compared to their core-only counterparts owing to the strong confinement of the excitons in the core. Second, the core/crown NPLs preserve their narrow spontaneous emission width as in the case of the core-only NPLs, while the absorption cross-section of the NPL is being boosted owing to the exciton funneling from the crown into the core [77], [78]. Third, with the growth CdS-crown, the quantum yield and ambient stability of the NPLs could be significantly enhanced [77]. With these attractive properties, core/crown NPLs were proposed to be promising for photovoltaic devices [78]. Furthermore, light-emitting diodes of the NPLs were demonstrated [83]. To date, however, optical gain in the NPLs has not been investigated nor considered. Neither two-photon absorption pumped amplified spontaneous emission nor lasing have been reported in the newly emerging NPLs.

6.4.2 Experimental

The synthesis of 4 ML thick CdSe core-only NPL having emission at 513 nm was performed according to the recipe from the literature [77]. For a typical synthesis, 170 mg of cadmium myristate, 12 mg of selenium and 15 mL of octadecene (ODE) were loaded into a three-neck flask. After evacuation of solution at room temperature, the solution was heated to 240⁰C under inert atmosphere. When the temperature reached 195⁰C, the color of solution became yellowish. Then, 80 mg of cadmium acetate dihydrate was introduced. After 10 minutes growth of CdSe NPLs at 240⁰C, the reaction was stopped and cooled down to room temperature with the injection of 0.5 mL of oleic acid (OA). 4 ML CdSe NPLs were separated by other reaction products with the successive purification steps.

The synthesis of the CdSe/CdS core/crown NPL was performed with the injection of cadmium and sulfur precursors which were prepared according to recipe from the literature.[77] For a typical synthesis, certain amount of CdSe NPLs that was dissolved

in hexane and 5 mL of ODE were loaded into a three-neck flask. The solution was degassed to remove all hexane, water and oxygen inside the solution. Then, under the inert atmosphere, the solution was heated to 240 °C. When temperature reached 240 °C, cadmium and sulfur precursors were injected with the rate of 4 mL/hr. According to desired CdS-crown size, injection amount can be changed. After the injection of cadmium and sulfur precursors, the reaction was stopped with the injection of 0.5 mL of OA and the system was cooled down to room temperature. The CdSe/CdS core/crown NPLs were purified with successive purification steps.

For the fabrication of the VCSELs of the core/crown NPLs; SiO₂ nanoparticle solution (Aldrich Ludox TMA 30 w%, water) and TiO₂ nanoparticle solution (Nanoamor Rutile TiO₂ nanoparticles 15 w%, water) were diluted with methanol to have final concentrations of 2.2 w% and 5 w%, respectively. To fabricate the DBRs, we alternatively deposited the nanoparticles via spin coating them at 4000 rpm for 1 min on piranha cleaned quartz substrates. Between each deposition step, the samples were annealed at 200°C. To create an optical path and realize multiple available longitudinal modes, we deposited PMMA (PMMA 950 A9) with a spin rate of 4000 rpm for 45 s on top of one of the DBR. Then, we drop coated the NPLs (30-40 mg/mL) on the DBR that was not deposited with PMMA. We brought the two DBRs together, applied slight pressure and using an epoxy we fixed the formed cavity.

6.4.3 Results and discussion

In this part of the thesis, we studied one- and two-photon absorption pumped amplified spontaneous emission in the core-only and the core/crown NPLs for the first time. The core/crown NPLs demonstrated substantially enhanced 1PA and 2PA pumped ASE performance as compared to the core-only NPLs. Among the varying lateral size of the core/crown NPLs, the NPLs with larger crown size exhibits better ASE performance (i.e., lower gain threshold) as compared to the smaller ones. However, as the crown thickness is further increased, the shape of the NPLs becomes irregular; thus, ASE

performance is observed to deteriorate possibly due to the increased number of defects in these larger NPLs.

We found 2PA and 1PA pumped ASE thresholds as low as 4.5 mJ/cm^2 and 41 uJ/cm^2 , respectively. The ASE performance of the NPLs surpasses that of the best reported QDs and other shaped nanocrystals emitting in the same spectral range. The net modal gain coefficient of the core/crown NPLs was measured to be as high as 650 cm^{-1} that is at least 4-fold larger than that of the best reported QD-based gain media and also outperforms that of the any other shaped nanocrystals so far. The superior performance of the NPLs was attributed to advantageous properties including the inter-exciton funneling from the CdS-crown into the CdSe-core and suppressed Auger recombination due to the anisotropic nature of the excitons in these quasi 2D nanostructures [58], [78]. Finally, we demonstrated the first lasers of the NPLs in a vertical cavity surface emitting architecture with a frequency up-converted lasing threshold of $\sim 2.49 \text{ mJ/cm}^2$.

We synthesized four monolayer (4 ML) thick CdSe core-only and CdSe/CdS core/crown NPLs layer having different lateral extent of the crown with the modified recipe from the literature [77]. Briefly, CdSe/CdS core/crown NPLs were synthesized at two steps. As compared to single step synthesis of core/crown NPLs, two step synthesis results in highly uniform NPLs with reproducible results. First, 4 ML CdSe NPLs were synthesized having peak emission at 513 nm. Second, after purification of the 4 ML CdSe NPLs, CdS-crown layer was grown with the injection of the cadmium and sulfur precursors at higher temperature (see Experimental for the details of the synthesis). Figure 6.17 depicts high-angle annular dark-field transmission electron microscopy (HAADF-TEM) images of the core-only and three different crown-size core/crown NPLs. The core-only NPL has a shape varying between square and rectangle with average long-edge length of 16.8 nm (Figure 6.17a) with a standard deviation of 2.28 nm. For the core/crown NPLs, simply by changing the injection amount of cadmium and sulfur precursors, we were able to tune the size of the crown layer. Therefore, by changing the injection amounts, we achieved core/crown NPLs having the average size of 20.6, 25.3, and 31.9 nm with standard deviations of 4.29,

5.00 and 5.27 nm as shown in Figure 6.17b, c and d, respectively. In the case of core/crown NPLs, the vertical thickness is the same thickness as the initial CdSe NPLs due to only lateral growth of the CdS crown. It is also worth mentioning that as the crown layer is grown larger, the shape of the NPLs starts to become more irregular and non-uniform as can be seen for 25.3 and 31.9 nm size core/crown NPLs (see Figure 6.17c and d) [77].

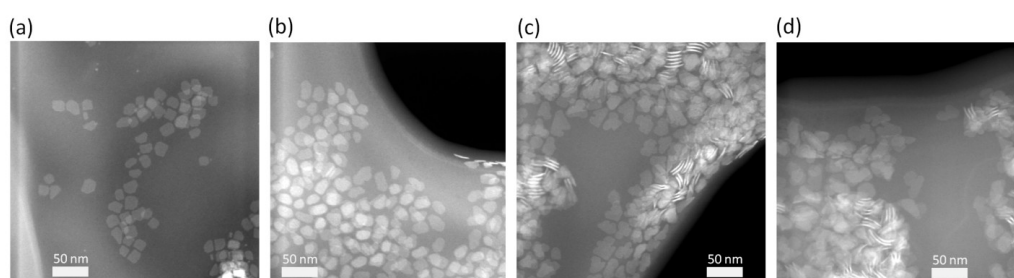


Figure 6.17 High-angle annular dark-field transmission electron microscopy (HAADF-TEM) images of (a) the core-only and core/crown NPLs having a size of (b) 21, (c) 25 and 32 nm. Reprinted (or Adapted) with permission from [17]. Copyright 2014 American Chemical Society.

Figure 6.18a shows the absorbance and photoluminescence spectra of the core and the varying crown-size core/crown NPLs. The core/crown NPLs are denoted by their average long-axis length as 21, 25 and 32 nm. As shown in Figure 6.18a, the spontaneous emission peak of the NPLs is at 515 and 517 nm for the core-only and the core/crown NPLs, respectively. The slight red-shift of the spontaneous emission by 2 nm in the case of core/crown NPLs is possibly due to the change of the dielectric medium of the excitons and induced strain by the CdS-crown layer. The absorbance of the core-only and core/crown exhibits the heavy- and light-hole transitions at 513 and 480 nm, respectively. In the case of core-only NPLs, the absorption around 400 nm is flat. However, a new absorption peak at 407 nm starts to arise and becomes more prominent as the CdS-crown is grown larger. This peak is due to the first exciton peak of the CdS layer having 4 ML thickness, which also supports the formation of the CdS-crown [78].

Figure 6.18b shows the photoluminescence excitation spectra of these NPLs that were measured for their peak emission wavelength at 515 nm (core-only) and 517 nm (core/crown). The PLE spectrum of the NPLs resembles to their absorption spectrum. In the case of core/crown NPLs, CdS's first exciton absorption peak at 407 nm also emerges in the PLE spectrum, which indicates that CdS-crown strongly transfers their exciton to the CdSe core [78]. This type of efficient exciton funneling, which substantially enhances the absorbance of the nanocrystals, was previously observed in the core/shell QDs and nanorods [309]–[312]. In our case, inter-NPL exciton funneling is expected to boost the absorbance of the NPLs in the spectral range that covers the first exciton absorption peak of the 4 ML CdS-crown ($\lambda < 407$ nm) [77], [78]. Pump lasers, which are generally mode-locked femtosecond lasers of Ti:sapphire crystals, generally operate at around 800 nm (or ~ 400 nm when frequency doubled). Therefore, enhancing the optical absorption at the wavelength of the common femtosecond pump lasers is expected to result in increased exciton density in the core/crown NPLs reducing the threshold for the population inversion condition.

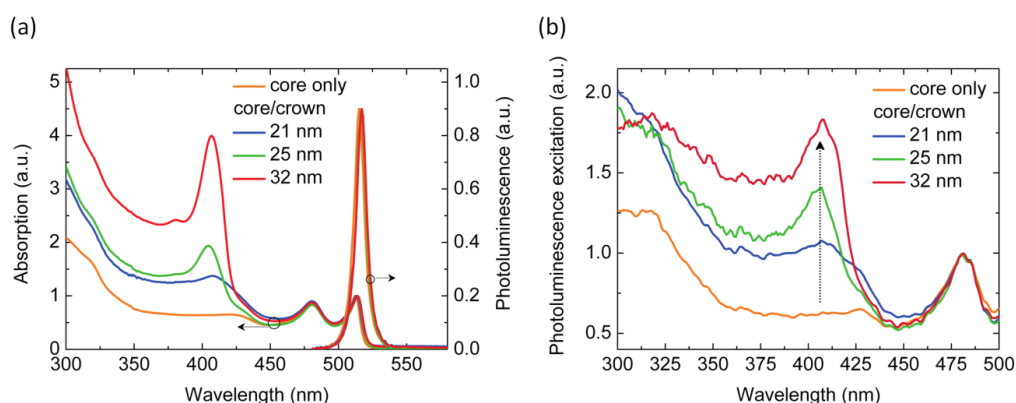


Figure 6.18 Absorbance and photoluminescence of the NPLs: core-only (orange), core/crown NPL having size of 21 nm (blue), 25 nm (green) and 32 nm (red). (b) Photoluminescence excitation spectra of the core-only and core/crown NPLs. Reprinted (or Adapted) with permission from [17]. Copyright 2014 American Chemical Society.

To study the amplified spontaneous emission in these NPLs, we prepared close-packed solid-films by drop casting them on pre-cleaned glass substrates. In the case of

2PA pumped ASE ($\lambda_{\text{exc}} = 800 \text{ nm}$), luminescence spectra of the $\sim 21 \text{ nm}$ sized core/crown NPLs is shown as an exemplary case in Figure 6.19a for increasing pump intensity (see Figure 6.20 for the other NPL samples). At low pump intensities, spontaneous emission dominates the PL spectra of the NPLs with a fwhm of 18-20 nm in solid-films of the NPLs. As the pump intensity is increased further, an ASE peak arises in the emission spectrum at $\sim 534 \text{ nm}$ having a narrower fwhm of $\sim 5 \text{ nm}$. For the NPLs investigated here the position of the ASE peak is red shifted by 12-13 nm as compared to the spontaneous emission peak. This highly red-shifted ASE peak indicates the existence of multi-exciton gain which was shown to be common for Type-I like QDs [284]. Moreover, owing to very small Stokes shift (3 nm) of these NPLs, the red-shifted ASE in these materials is highly desired that contributes to decreased self-absorption; thus, enhanced optical gain performance.

Figure 6.19b demonstrates the integrated emission intensity vs. pump intensity for the core-only and the varying crown-size core/crown NPLs. The ASE thresholds for 2PA-pumped were 8.21 mJ/cm^2 , 5.81 mJ/cm^2 , 4.48 mJ/cm^2 and 4.63 mJ/cm^2 for the core-only, 21, 25 and 32 nm core/crown NPLs, respectively. The core/crown NPLs demonstrated substantially lowered ASE thresholds as compared to the core-only NPLs. We interpreted the substantial reduction of the ASE threshold in the core/crown NPLs owing to the enhanced absorption cross-section of the NPLs due to the CdS crown layer, which acts as an exciton transferring antenna.

Among the core/crown NPLs, 25 nm sized exhibits the best 2PA pumped ASE performance. The rise of the ASE threshold in the 32 nm core/crown NPLs is possibly attributed to the increased defects (indented NPLs in Figure 6.17d) that may quench the inter-energy transfer from the crown to the core. The achieved lowest threshold of 4.4 mJ/cm^2 is a record low for the spectral range of green emission and it is ~ 5 -fold smaller than the best reported 2PA pumped ASE threshold of the QDs that emit in the same spectral range [269], [286]. Overall, the core/crown NPLs are promising candidates for frequency up-converted lasers.

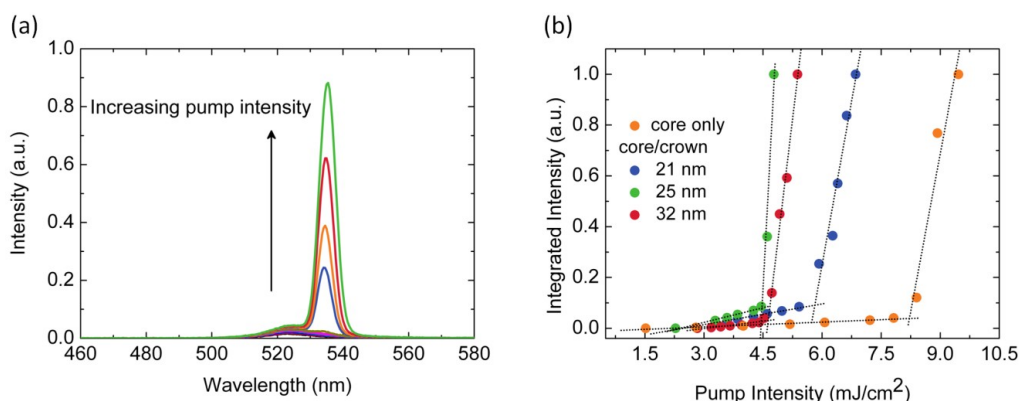


Figure 6.19 (a) 2PA pumped ASE of the 21 nm size core/crown NPLs. (b) 2PA pumped luminescence vs. pump intensity of the core-only and core/crown NPLs having a size of 21, 25 and 32 nm. Reprinted (or Adapted) with permission from [17]. Copyright 2014 American Chemical Society.

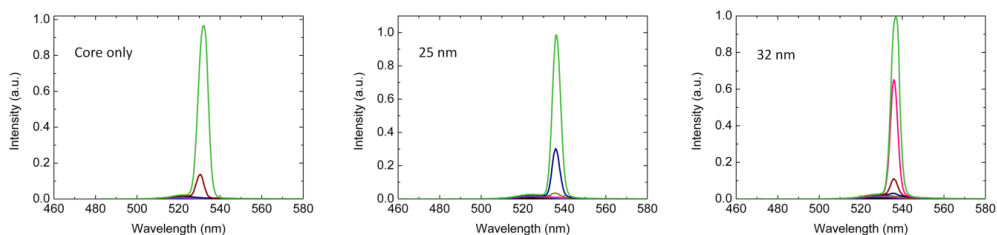


Figure 6.20 2PA pumped ASE of the core-only and core/crown NPLs having size of 25 and 32 nm. Reprinted (or Adapted) with permission from [17]. Copyright 2014 American Chemical Society.

Next, we investigated the 1PA pumped ASE of the NPLs ($\lambda_{\text{exc}} = 400 \text{ nm}$). Luminescence spectra are plotted in Figure 6.21a for the 21 nm sized core/crown NPLs as an exemplary case measured for increasing pump intensities (see Figure 6.22 for the other NPL samples). The rise of the ASE peak is clear for the pump intensities above the 1PA pumped ASE threshold. The ASE peak is again red shifted by 10-11 nm as compared to the spontaneous emission peak. The amount of the red-shift is slightly less ($\sim 2 \text{ nm}$) in 1PA pumped ASE as compared to the shift observed in the 2PA pumped ASE. Therefore, the ASE peaks are slightly blue shifted in the case of 1PA pumped ASE as compared to that of the 2PA pumped case. This could be due to heating caused

by 800 nm pump or due to some other excitonic effects. Figure 6.22b depicts the luminescence intensity vs. pump intensity curves for the NPLs. The 1PA pumped ASE thresholds are 214, 85, 41 and 71 $\mu\text{J}/\text{cm}^2$ for the core-only, 21, 25 and 32 nm core/crown NPLs, respectively. Here, 25 nm sized core/crown NPLs again exhibited the best 1PA pumped ASE performance as compared to the other samples. The largest crown size NPL of 32 nm performed worse than the 25 nm NPLs, whereas their 2PA pumped ASE performances were comparable. The reason of this observation might be due to the greater two-photon absorption cross-section of the 32 nm NPLs as compared to the 25 nm NPLs. The increase of the 1PA pumped ASE threshold of the 32 nm size NPLs is possibly due to the induced shape irregularities causing increased number of defects that may quench the inter-NPL energy transfer from the crown to the cores. The best 1PA pumped ASE threshold of 41 $\mu\text{J}/\text{cm}^2$ is an important achievement for the purpose of realizing lasing with green-emitting colloidal materials. Previously, best reported 1PA pumped ASE threshold for the green-emitting QDs was as low as 150 $\mu\text{J}/\text{cm}^2$ [10]. Therefore, these NPLs with their record low ASE threshold levels in green spectral emission range will be essential for achieving to the multi-color lasing (i.e., R-G-B) with the colloidal materials.

In addition, we performed variable stripe length measurements to quantify the net modal gain coefficients in the NPLs [278], [279]. Figure 6.22c depicts the VSL measurement of the 25 nm core/crown NPLs that had achieved the best ASE performance both with 1PA and 2PA pumping. Surprisingly, the net modal gain coefficient is found to be exceptionally high (650 cm^{-1}). This ultrahigh gain coefficient is much larger than the best reported gain coefficients in the QDs and the nanorods [116], [279]. Previously, the best reported gain coefficient was shown to be 150 cm^{-1} in the QDs [279] while in nanorods it was shown to be as high as 350 cm^{-1} [116]. However, this gain coefficient in nanorods could be measured only at temperatures below 120 K. Here we achieved this ultra-high gain coefficient at room temperature. Therefore, the NPLs prove them to be excellent colloidal gain media for lasers.

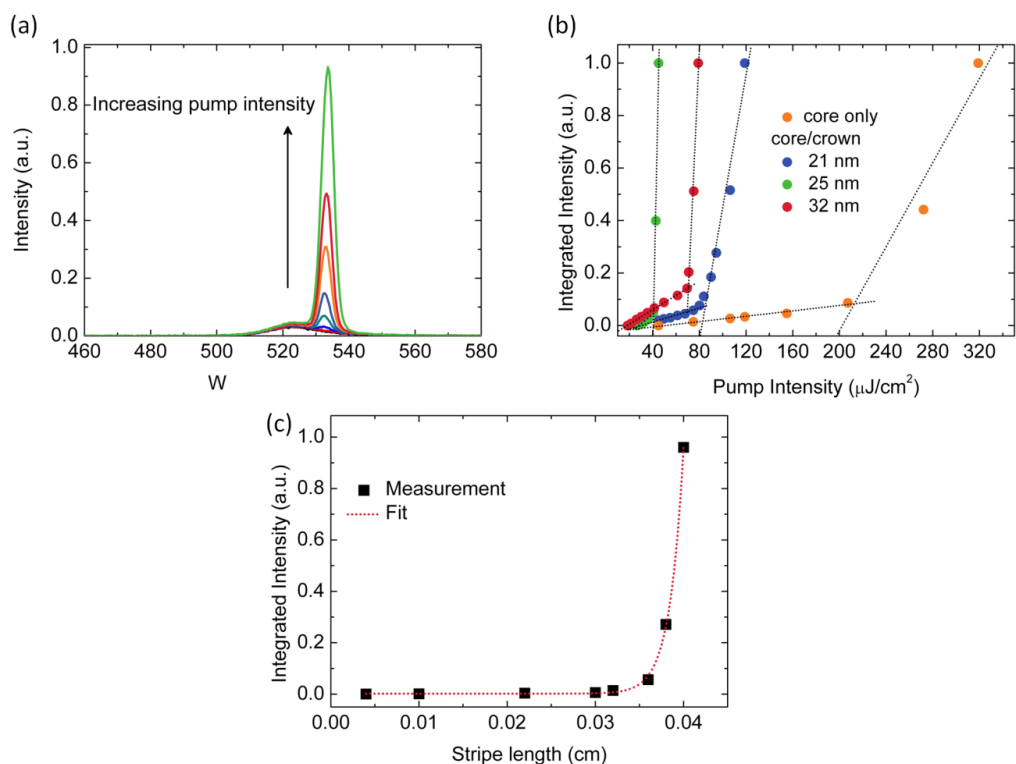


Figure 6.21 (a) 1PA pumped ASE of the 21 nm size core/crown NPLs. (b) 1PA pumped luminescence vs. pump intensity of the core-only and core/crown NPLs having a size of 21, 25 and 32 nm. (c) Variable stripe length measurement of the gain coefficient. Reprinted (or Adapted) with permission from [17]. Copyright 2014 American Chemical Society.

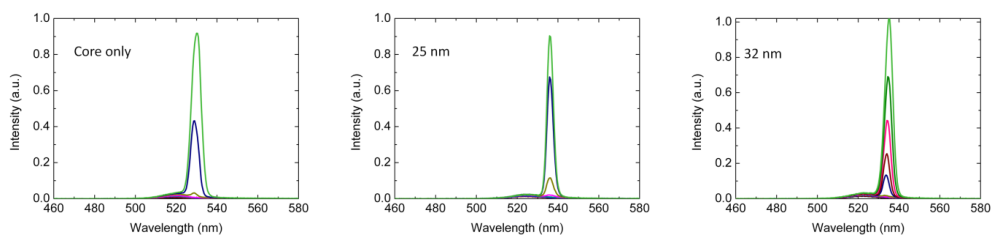


Figure 6.22 1PA pumped ASE of the core-only and core/crown NPLs having size of 25 and 32 nm. Reprinted (or Adapted) with permission from [17]. Copyright 2014 American Chemical Society.

Finally, we developed the proof-of-concept laser of the NPLs using all solution processed distributed Bragg reflectors made out of alternatively stacked SiO_2 and TiO_2 nanoparticles [18], [301], [313]. Employing 6-bilayers of the $\text{SiO}_2/\text{TiO}_2$, we realized DBRs with peak reflectivity as high as 91-93% at the spectral range where ASE emerges (~ 535 nm). Then, we sandwiched 25 nm size core/crown NPL film (film thickness ~ 3 - 5 μm) in between two DBRs such that we realized vertical-cavity surface-emitting laser of the NPLs (see Experimental part). Figure 6.23a illustrates the architecture of the VCSEL of the NPLs. Figure 6.23b shows the emission spectra of VCSELs under 2PA pumping as the pump intensity is progressively increased. After the lasing threshold, lasing peak at 535 nm emerged with a FWHM of 2 nm that corresponds to a Q-factor of ~ 270 . We observed both spectrally and spatially coherent emission from the VCSELs after the laser threshold. Figure 6.23c showed the luminescence intensity vs. pump intensity plot. The threshold for the lasing is ~ 2.49 mJ/cm^2 . The lasing threshold was better than the 2PA pumped ASE threshold of the drop-casted 25 nm core/crown NPLs owing to the energy storage in the cavity.

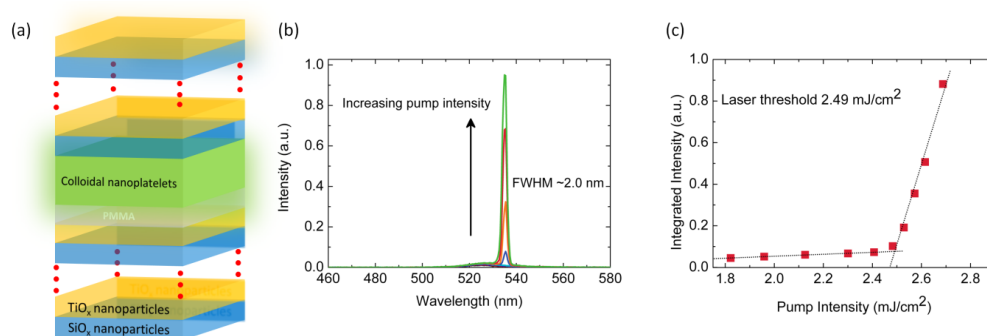


Figure 6.23 (a) Schematic of the VCSEL of the NPLs that employ DBRs having 6-bilayers stack of SiO_2 and TiO_2 nanoparticles each. (b) Emission spectrum of the VCSEL is plotted as the pump intensity is progressively increased. (c) Integrated emission intensity vs. pump intensity measurement and the linear fits indicating the 2PA pumped lasing threshold of 2.49 mJ/cm^2 . Reprinted (or Adapted) with permission from [17]. Copyright 2014 American Chemical Society.

6.4.4 Summary

In summary, we demonstrated that colloidal nanoplatets are promising for both 1PA and 2PA pumped optical gain and lasing. Here for the first time, we investigated and revealed the ASE performance of the core-only and core/crown NPLs having varying crown size. These NPLs exhibited superior performance as compared to the other colloidal counterparts including QDs, nanorods and other shaped nanocrystals. 1PA and 2PA pumped ASE thresholds of the NPLs reached record low levels as $41 \mu\text{J}/\text{cm}^2$ and $4.48 \text{ mJ}/\text{cm}^2$ for the green spectral emission region, respectively. The net modal gain coefficient of the NPLs was measured as high as 650 cm^{-1} that remarkably represents a 4-fold enhancement over the best reported gain coefficient of the colloidal QDs. Finally, we developed vertical cavity surface emitting laser of the core/crown NPLs that exhibited 2PA pumped laser with low threshold of $2.49 \text{ mJ}/\text{cm}^2$. These results clearly demonstrated that the NPLs are excellent materials for optical gain and lasing.

6.5 Lateral area dependent spontaneous and stimulated emission properties in colloidal nanoplatelets

This section is based on the publication “Lateral Size-Dependent Spontaneous and Stimulated Emission Properties in Colloidal CdSe Nanoplatelets,” M. Olutas*, **B. Guzelturk***, Y. Kelestemur, A. Yeltik, S. Delikanli and H. V. Demir, ACS Nano 9, 5041-5050 (2015). * Equal contribution. Adapted (or “Reproduced in part”) with permission from American Chemical Society. Copyright 2015 American Chemical Society.

6.5.1 Motivation

Since the first synthesis of colloidal semiconductor nanocrystals [28] there is an ever increasing interest in colloidal nanomaterials owing to their unique optical and electronic features that enable advanced optoelectronic devices [6], [15], [33], [314], [315]. The physical properties of the colloidal semiconductors can be engineered by tailoring their size and shape in addition to composition. There are previous reports that studied strongly size dependent optical properties in colloidal quantum dots including extinction coefficient, photoluminescence quantum efficiency (PL-QE) and multi-exciton kinetics in relation to nonradiative Auger recombination [120], [121], [316]–[322].

Recently, a new type of atomically flat nanocrystalline colloids known as solution-processed nanoplatelets has been introduced [56]. The NPLs have lateral dimensions that are much larger than the exciton Bohr radius of the material (*i.e.*, CdSe, CdTe, CdS, *etc.*) and also than their well-defined and well-controlled vertical thicknesses, typically of several monolayers (MLs) [56], [57]. Therefore, there exists strong quasi-1D quantum confinement in these NPLs.

Although vertical thickness dependent optical properties have been commonly investigated, the lateral size dependency of spontaneous emission kinetics and efficiency or optical gain performance in CdSe NPLs have not been studied nor elucidated yet. Although the strong quantum confinement in these NPLs is only in the vertical direction, it has thus far remained unknown to what extent the lateral dimensions would affect the optical and excitonic properties in the NPLs and how critical the lateral size is in spontaneous and stimulated emission processes, which are crucial for high performance in light-generating device applications.

6.5.2 Experimental

For the synthesis of the 4 ML CdSe NPLs; 170 mg of cadmium myristate, 12 mg of selenium (Se) and 15 mL of octadecene (ODE) were loaded into a three-neck flask. After evacuation of the mixed solution at room temperature for 1h, it was heated to 240°C under argon (Ar) atmosphere. When the temperature reaches 195°C, the color of solution becomes yellowish, 55 mg of cadmium acetate dihydrate was introduced swiftly into the reaction. After 2, 4, 6 and 8 min of growth of CdSe NPLs for NPL-1, NPL-2, NPL-3 and NPL-4 at 240°C, respectively, the reaction was stopped and cooled down to room temperature with the injection of 0.5 mL of oleic acid (OA). The resulting 4 ML CdSe NPLs were separated by other reaction products with successive purification steps. First, the resulting mixture is centrifuged at 14500 rpm for 10 min, and the supernatant is removed from the centrifuge tube. The precipitate is dried under nitrogen and dissolved in hexane and centrifuged again at 4500 rpm for 5 min. In the second step, the supernatant is separated into another centrifuge tubes and ethanol is added into supernatant solution until it becomes turbid. In the last step, after the turbid solution is centrifuged at 4500 rpm for 5 min, the precipitate is dissolved in hexane and filtered with 0.20 micrometer filter.

Two photon absorption (2PA) cross-sections of two different NPL ensembles having different lateral size were measured by open-aperture z-scan technique. For this, the excitation source was a Ti:Sapphire laser system (Spitfire Pro XP, Spectra Physics) having 120 fs pulse width at 800 nm with 1 kHz repetition rate. 1 mm quartz cuvette was used as the container. We dissolved 0.497 μM (NPL-2) and 0.299 μM

(NPL-4) solutions of the NPL ensembles in hexane in a 1 mm quartz cuvette. The concentration of the NPL solution was determined via analysis of the concentration by the elemental analysis using inductively coupled plasma optical emission spectroscopy (ICP-OES). In our z-scan setup, we separately monitored the excitation beam (using a beam splitter) for the possible changes in the excitation intensity. Then, we measured the transmitted intensity of the excitation beam through the sample (1 mm cuvette), which was mounted on a translation stage (total translation of ± 14 cm). σ_{2PA} of NPL-2 and NPL-4 are found to be 0.537×10^6 GM and 2.247×10^6 GM, respectively.

6.5.3 Results and discussion

In this part of the thesis, we systematically studied the effects of the lateral size on the optical and excitonic properties of CdSe NPLs in the weak lateral confinement regime for both spontaneous and stimulated emissions. We synthesized CdSe NPLs having different lateral sizes. We observed that the spontaneous emission spectra of the NPLs do not exhibit any significant spectral shift as their lateral size is extended. However, the photoluminescence decay rate was found to strongly accelerate and PL-QE of these NPLs was observed to considerably decrease with increasing lateral size. These observations strongly suggest the increasing overall nonradiative decay with increasing lateral area. To explain these observations, we have analyzed the PL decay kinetics *via* considering defected and non-defected NPL sub-populations revealing that defected NPL population fraction increases more than 2-folds as the lateral area is increased. With this understanding, we systematically studied both single- and two-photon absorption pumped optical gain for the NPL samples with varying lateral size. The NPL ensembles having fewer defected NPL fraction (i.e., ensembles with smaller lateral area) exhibited lower amplified spontaneous emission threshold under single-photon absorption pumping, whereas the NPLs with the larger lateral size achieved the lower threshold for two-photon absorption pumping owing to their giant nonlinear absorption cross-sections, which could be as high as 2×10^6 GM.

The synthesis of CdSe core-only NPLs having zinc-blende crystal structure was carried out using a modified recipe [77]. CdSe NPLs having different lateral sizes were synthesized using the same recipe with different growth times (see Experimental part). The vertical thickness and the mean lateral size of the NPLs were extracted from the transmission electron microscopy images (see Figure 6.24). The synthesized CdSe NPLs have the same vertical thickness (~ 1.2 nm) corresponding to 4 MLs. This is consistent with the photoluminescence and absorbance peaks in Figure 6.25 [136], [159]. The lateral sizes of the NPLs were found to be 170.0 ± 22.5 nm² (NPL-1), 269.6 ± 38.6 nm² (NPL-2), 377.6 ± 56.4 nm² (NPL-3), and 391.9 ± 65.7 nm² (NPL-4).

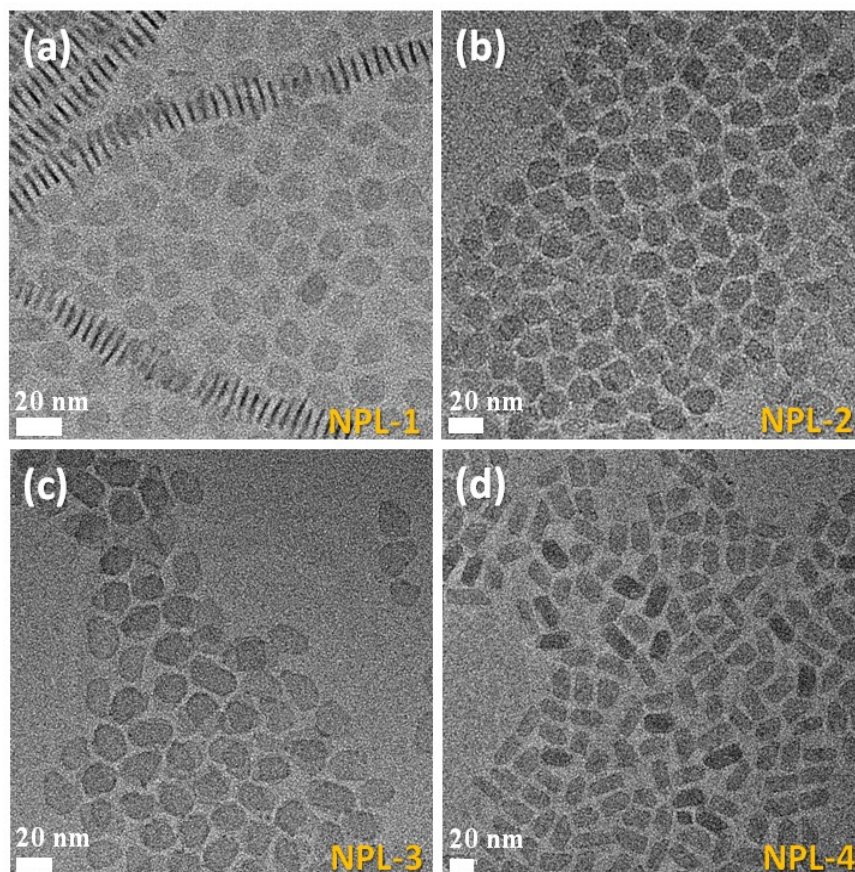


Figure 6.24 Transmission electron microscopy (TEM) images of the 4 ML CdSe NPLs having different lateral sizes: (a) 170.0 ± 22.5 nm² (NPL-1), (b) 269.6 ± 38.6 nm² (NPL-2), (c) 377.6 ± 56.4 nm² (NPL-3) and (d) 391.9 ± 65.7 nm² (NPL-4), grown using different growth times. Reprinted (or Adapted) with permission from [66]. Copyright 2015 American Chemical Society.

Figure 6.25 shows the absorbance and steady state photoluminescence spectra of the NPLs in hexane at room temperature. For each NPL, the absorbance spectrum exhibits two peaks: a sharp peak at 512 nm and the slightly broader peak at 480 nm, corresponding to the electron-heavy hole (e-hh) and the electron-light hole (e-lh) transitions, respectively. The photoluminescence spectra show a single narrow peak at 513 nm, resulting from the radiative recombination at the electron-heavy hole transition [57], with a very small Stokes shift (~ 1 nm). As the lateral size of the NPLs grows larger, the photoluminescence emission peak does not change its spectral position. Also, the fwhm of the photoluminescence emission peak remains unchanged (~ 8 nm). The spectral positions of the absorption and photoluminescence features are summarized in Table 6.4. Having the same features in the UV-Vis and the photoluminescence spectra with growing lateral size suggests weak quantum confinement in the lateral plane owing to the fact that the lateral dimensions are much larger than the exciton Bohr radius of CdSe [58], [69].

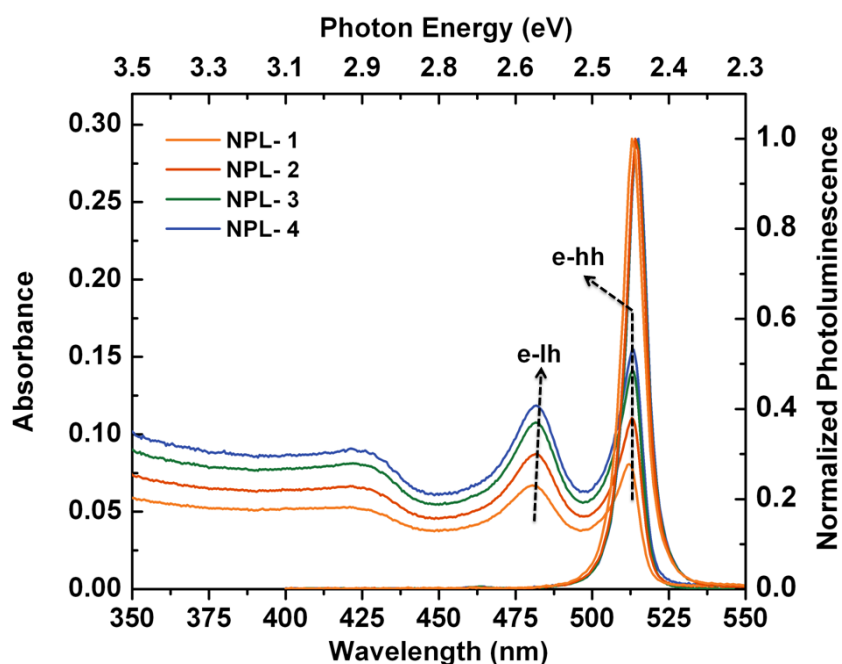


Figure 6.25 Absorbance and photoluminescence spectra of the 4ML CdSe NPLs grown in lateral direction with different growth times. The peaks labeled as e-lh and e-hh in the absorbance spectrum correspond to the electron-light hole and the electron-heavy

hole transitions, respectively. Reprinted (or Adapted) with permission from [66]. Copyright 2015 American Chemical Society.

Table 6.4 Analysis of UV-Vis and photoluminescence spectra for the 4 ML CdSe NPLs grown using different growth times.

Sample	TEM	PL Spectroscopy		Absorption Spectroscopy		QE Measurements
	Lateral size (nm ²)	λ_{Peak} of PL (nm)	FWHM of PL (nm)	$\lambda_{\text{e-lh}}$ of Abs (nm)	$\lambda_{\text{e-hh}}$ of Abs (nm)	PL-QE (%)
NPL-1	170.0 ± 22.5	512.9	8.1	480.8	512.1	76.8
NPL-2	269.6 ± 38.6	514.0	8.1	481.6	513.0	61.5
NPL-3	377.6 ± 56.4	514.1	8.0	481.9	513.0	35.3
NPL-4	391.9 ± 65.7	514.6	7.9	481.8	513.5	33.3

To understand the fluorescence decay kinetics of the NPLs as a function of the changing lateral size, time-resolved fluorescence spectroscopy using time-correlated single photon counting (TCSPC) system was performed (Figure 6.26). Here we used a pulsed pump laser (375 nm, 2.5 MHz repetition rate, < 100 ps pulse width) to excite the diluted NPL solutions in hexane. The exciton density per NPL is very small ($\langle N \rangle \ll 1$) due to very low intensity of the pump laser. Figure 6.26a shows the fluorescence decay curves measured at the peak emission wavelength (~513 nm) of the NPLs for four different samples. The fluorescence decay curves of the NPLs were numerically fitted with multi-exponential decay functions indicating the presence of multiple decay channels in the ensemble of the NPLs. The fitting parameters are given in Table 6.5. The multi-exponential decay behavior in both a single NPL and ensemble of NPLs were previously reported [58], [61], [137]. Tessier *et al.* have performed single NPL based time-resolved fluorescence spectroscopy and measured PL decay curves that could be fitted by three exponential decay functions [58]. This indicates that individual NPLs exhibit complex decay dynamics possibly due to the presence of more than one radiative channels (*i.e.*, direct radiative recombination and trap-related radiative recombination) in addition to nonradiative (*i.e.*, electron and hole traps) channels present in the NPL ensembles.

Figure 6.26b presents the fluorescence lifetime components of the measure in different NPL ensembles of varying mean lateral size. These four exponential decay components have distinct lifetimes: ~ 90 ns, ~ 16 ns, ~ 4 ns and ~ 0.5 ns. Amplitude-averaged photoluminescence lifetime τ_{av} of the NPL ensembles with increasing lateral size is presented in Figure 6.26c showing that the τ_{av} decreases from 7.61 to 2.73 ns as the mean lateral size of the NPLs is increased. This shortening in the photoluminescence lifetime was previously reported in epitaxial quantum wells that was studied as a function of well thickness [74]. In the colloidal NPLs, photoluminescence lifetime has been studied as a function of temperature revealing the giant oscillator strength transition in these materials, although lateral size dependence has not been understood to date [57], [58], [69].

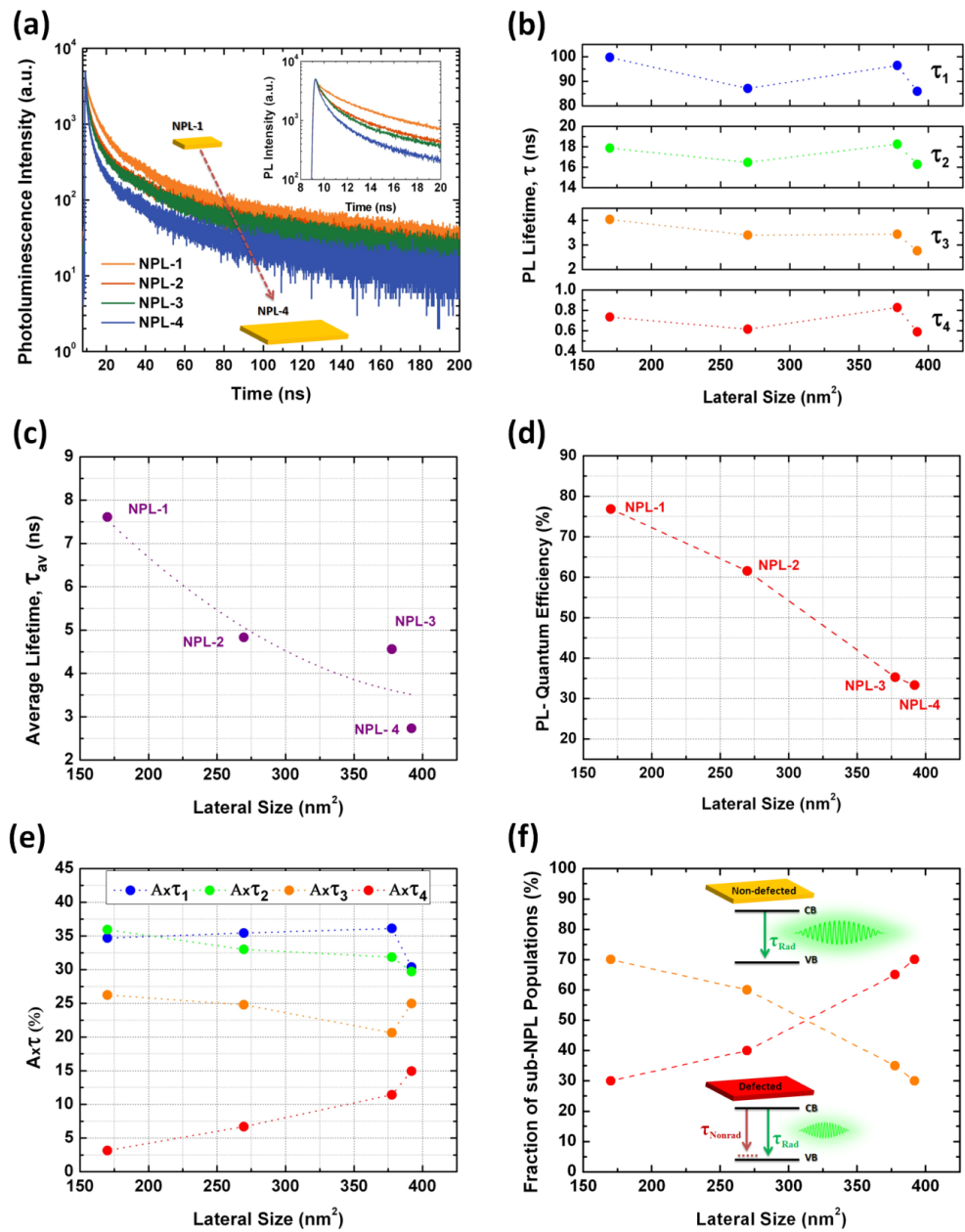


Figure 6.26 (a) Time-resolved fluorescence decays of the NPLs having different lateral sizes. The inset shows the zoom-in of the same TRF decay. Evolution of (b) the lifetime components of fluorescence decays, (c) the amplitude-averaged photoluminescence lifetimes, (d) photoluminescence quantum efficiency (PL-QE) (e) the percentage steady state contribution from each decay component of the NPLs and (f) calculated fraction of NPL sub-populations as a function of the lateral size. The

dotted lines are a guide for eyes. Reprinted (or Adapted) with permission from [66].
Copyright 2015 American Chemical Society.

Table 6.5 Fluorescence decay components and the fractional emission contributions of the 4 ML CdSe NPLs grown using different growth times (i.e., different lateral areas).

Sample	TRF Decay Components								Amplitude- average Lifetimes ($\frac{\sum A_i \times \tau_i}{\sum A_i}$)
	τ_1 (ns)	τ_2 (ns)	τ_3 (ns)	τ_4 (ns)	A_1	A_2	A_3	A_4	τ_{av} (ns)
NPL-1	99.76	17.88	4.04	0.74	130.18	752.3	2431.8	1605	7.61
NPL-2	87.07	16.48	3.39	0.62	99.26	488.5	1780.2	2686	4.83
NPL-3	96.46	18.26	3.44	0.83	86.53	403.1	1388.1	3189	4.56
NPL-4	85.93	16.28	2.76	0.59	49.99	258.1	1279.8	3583	2.73

Sample	Fractional Emission Contributions ($\frac{A_i \times \tau_i}{\sum A_i \times \tau_i}$)			
	$A_1 \times \tau_1$ (%)	$A_2 \times \tau_2$ (%)	$A_3 \times \tau_3$ (%)	$A_4 \times \tau_4$ (%)
NPL-1	34.69	35.93	26.23	3.15
NPL-2	35.43	33.00	24.79	6.70
NPL-3	36.11	31.85	20.63	11.42
NPL-4	30.38	29.71	24.96	14.94

One possible hypothesis to explain the accelerated photoluminescence decay rates with extended lateral size is the increasing radiative rates due to increasing oscillator strength. To check this hypothesis, photoluminescence quantum efficiency of different NPL ensembles was measured using a reference dye Rhodamine 6G (Rh6G) having 95% PL-QE in its highly diluted ethanol solution at room temperature (see Figure 6.27). Previously in the core-only NPLs, PL-QE was reported to be 30-50% [56], [57], [63], [75], [308]. However, the relation between the PL-QE and the lateral size of the NPLs has not been studied. Here, we found that the PL-QE substantially decreases from 76.8% to 33.3% as the lateral size of the NPLs increases (see Figure 6.26d). This shows that the hypothesis concerning increasing radiative rates cannot be correct. Thus, the observed strong decrease of the PL-QE in the larger lateral size NPLs cannot be accounted for the increasing oscillator strength. The decrease in the PL-QE of the

NPLs together with the accelerated photoluminescence decay rates strongly suggests the increased overall nonradiative recombination in these NPLs. A simple calculation ($PL\text{-}QE = \gamma_{\text{Rad}} / (\gamma_{\text{Rad}} + \gamma_{\text{Nonrad}})$) indicates that effective nonradiative decay rate increases by 8-folds in the larger lateral area NPLs (*i.e.*, NPL-4) as compared to the smaller ones (*i.e.*, NPL-1), whereas the radiative decay rate (and, thus, the oscillator strength) increases only by 1.2-folds.

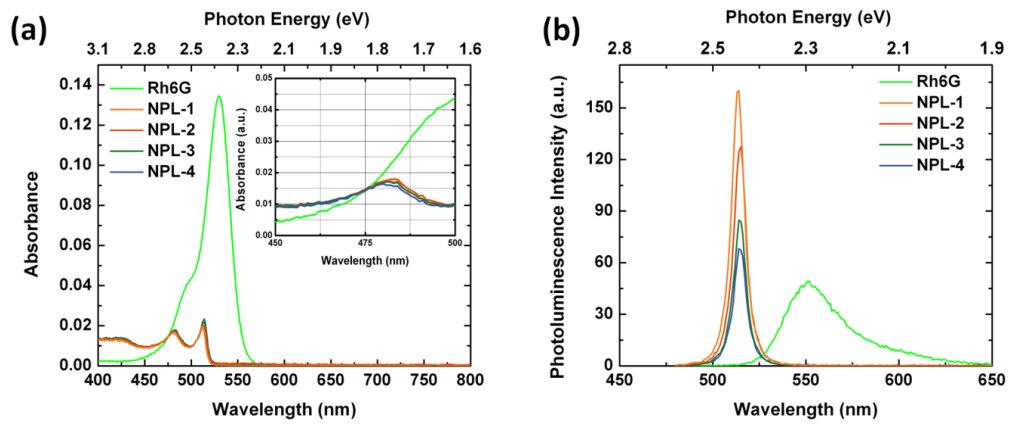


Figure 6.27 Photoluminescence quantum efficiency (PL-QE) measurements of the 4ML CdSe NPLs grown in lateral direction using different growth times, in comparison to the reference dye of Rhodamine 6G (Rh6G) with 95% PL-QE. Reprinted (or Adapted) with permission from [66]. Copyright 2015 American Chemical Society.

To understand the effect of nonradiative recombination channels in the NPLs, we looked into the exponential photoluminescence decay components and their steady state contributions, which are quantified with $A_i \times \tau_i$ products ($i = 1$ to 4) where A_i represents the amplitude of the exponential decay and τ_i is its characteristic lifetime, extracted from numerical fits to the photoluminescence decay curves using the relation:

$$PL(t) = \sum_i A_i e^{-\frac{t}{\tau_i}} \quad (6.12)$$

$$A_i \times \tau_i = \int A_i e^{-\frac{t}{\tau_i}} \quad (6.13)$$

Each $A_i \times \tau_i$ term corresponds to the area under the corresponding exponential decay curve giving its specific steady state contribution within the total emission. Figure 6.26e exhibits the fractional change of the steady state contribution of each lifetime component for four different NPL samples being studied here. As the size of the NPLs is increased, the relative contribution of $A_4 \times \tau_4$ term increases from 3.15% to 14.94%. The fractional contributions of other lifetime components (*i.e.*, $A_1 \times \tau_1$, $A_2 \times \tau_2$, and $A_3 \times \tau_3$) are observed to decrease with increasing lateral size. Increasing contribution from $A_4 \times \tau_4$ term as the PL-QE decreases would strongly imply that τ_4 component, which is the fastest lifetime, is related to a nonradiative decay channel within the NPL population. For example, fast hole-trapping is widely observed in Cd-based NCs especially due to poor surface passivation and Cd-vacancies [143], [154], [155]. Recently, Kunneman *et al.* have also shown that large fraction of the NPL populations contain NPLs with hole traps exhibiting lifetimes on the order of 10s or 100s of picoseconds [62]. As the lateral size of an NPL is increased, the probability of finding a hole trap state such as a Cd-vacancy within that NPL would be increasing. Therefore, the population fraction of the NPLs having hole traps would be higher in an NPL ensemble having a larger mean lateral size, which would in turn strongly decrease the ensemble PL-QE.

Recently, we have shown that such defected NPLs can strongly quench the photoluminescence emission of the stacked NPLs due to ultra-fast exciton transport within the stacked NPLs through Förster resonance energy transfer [19]. The lateral size dependent photoluminescence decay components (τ_i) and fractional emission contributions ($\frac{A_i \times \tau_i}{\sum A_i \times \tau_i}$), which are listed in Table 6.5, indicate that while the lifetime components do not change significantly as a function of the lateral size (see Figure 6.26b), the fractional emission contributions do (see Figure 6.26e). Therefore, the amplitude average lifetimes change considerably with the lateral size. The shortening in the amplitude average lifetimes might be explained by changing relative contributions of the lifetime components due to the changing population fractions of

the defected and non-defected NPLs in the ensemble. With increasing lateral size, the number of defected NPLs grows larger. As a result, the overall nonradiative channels in the NPL ensembles are increased with the increased lateral size. Similarly, such complex PL decay kinetics have been previously observed in the CdSe QDs [323], [324] and in CdSe NPLs [19], [62] arising due to dynamic surface trapping. Furthermore, the surface trapping in the NCs has been shown to be highly sensitive to temperature and time since these can excitonically alter the heterogeneity of the nanocrystal populations. We also observed exactly the same lateral size dependent behavior in the NPL populations synthesized using the core-seeded approach.

To develop a better insight, we quantitatively calculated the change of the NPL sub-populations for the different NPL ensembles. Here, we assumed that the NPL population consists of two types of NPLs: non-defected and defected (*i.e.*, having rapid nonradiative recombination) [19], [62]. Previously, Dubertret group has observed the presence of three distinct fluorescence lifetime components in emissive NPLs *via* single particle measurements [58]. These lifetime components match very well with τ_1 (80-100 ns), τ_2 (15-18 ns), τ_3 (1-3 ns) lifetime components that we found using our NPLs. Therefore, we related these lifetime components (τ_1 , τ_2 and τ_3) as the distinct radiative states in non-defected NPLs. In the case of defected NPLs, the fastest lifetime component τ_4 (0.6-0.8 ns) was attributed to as the nonradiative channel (*i.e.*, hole trapping) since its contribution significantly increases (from 3% to 15%) as the PL-QE of the NPLs decreases. We assumed that x% of the NPL population consists of non-defected NPLs and the rest (1-x)% consists of defected NPLs (see Figure 6.28). Non-defected NPLs are assumed to have a PL-QE of 100% and exhibit only τ_1 , τ_2 and τ_3 lifetime components. On the other hand, defected NPLs have the fast nonradiative lifetime of τ_4 in addition to three distinct radiative lifetime components. The PL-QE in the defected NPLs was found by considering that the nonradiative channel (τ_4) would compete with each of the radiative channels (τ_1 , τ_2 and τ_3) individually. Therefore, τ_1 - τ_4 , τ_2 - τ_4 and τ_3 - τ_4 combinations (see Figure 6.28) would result in PL-QEs ($\text{PL-QE} = \gamma_{\text{Rad}} / (\gamma_{\text{Rad}} + \gamma_{\text{Nonrad}})$) of ~0.7%, ~3.5%, and ~18%, respectively.

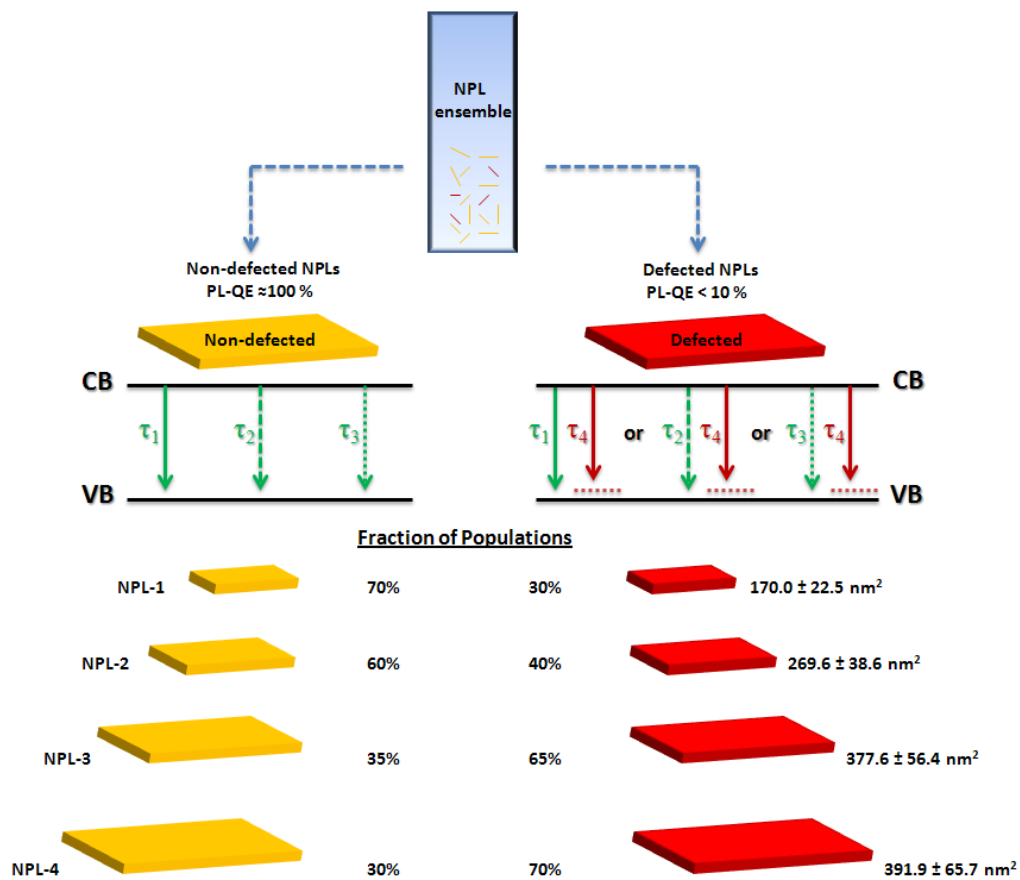


Figure 6.28 The schematic representation of the non-defected (yellow) and defected (red) NPLs within the NPL ensembles. The relative change of the fraction of these two different NPL populations as a function of lateral area is shown to match the experimental PL QEs. Reprinted (or Adapted) with permission from [66]. Copyright 2015 American Chemical Society.

Considering that these three distinct radiative emission channels have almost equal contribution to the total radiative emission, which can be justified by considering their almost equal fractional emission contributions as shown in Table 6.5, the average PL-QE of a defected NPL would be calculated to be ~8%. We matched the calculated PL-QEs to experimentally measured PL-QEs for the different NPL samples (NPL-1, -2, -3 and -4) *via* choosing the population fraction ($x\%$) of the non-defected and $((1-x)\%$) defected NPLs properly ($\text{PL-QE} = 100\% \times x + 8\% \times (1-x)$) (see Figure 6.28). We observed that NPL-1 has the lowest defected NPL population fraction (~30%) since it

has the highest PL-QE. As the lateral area of the NPL samples increases, the defected NPL population fraction increases up to 70% (for the NPL-4) (see Figure 6.26f and Figure 6.28). This explains the significantly reduced the PL-QEs in the larger lateral area NPLs.

Furthermore, to check the consistency of the calculated defected and non-defected NPL sub-population fractions with the time-resolved fluorescence measurements, we calculated the contribution of the fluorescence lifetime components to the total emission of the NPL ensemble (see Table 6.6) for the two NPL sub-populations. In this calculation, we assumed the contributions of the radiative channels τ_1 , τ_2 and τ_3 to the total emission to be almost equal (*i.e.*, 35, 35 and 30%, respectively). We justify this by the observation of the fractional contributions of the τ_1 , τ_2 and τ_3 lifetime components to the experimental data in Table 6.5. In the case of the contribution of the lifetime components to the total emission in the defected NPLs, the presence of the fast nonradiative τ_4 component and the low PL-QE (~8%) were considered. In Table 6.6, we summarize the calculated emission contributions of all lifetime components for the four different NPL ensembles and the calculated values were compared to the experimental ones. The calculated emission contributions exhibit a very good match with the experimental ones. Therefore, the change of the population fraction of the defected NPLs causes the reduced PL-QEs in the increased lateral area NPLs. This good agreement between the calculated and the experiment data for each NPL ensembles (NPL-1, -2, -3 and -4) exhibits a strong support for the hypothesis that the nonradiative decay pathways dictate the decreasing trend in the PL-QE due to poorly passivated surfaces (acting as fast hole traps) becoming dominantly stronger with increasing lateral size.

Table 6.6 Calculated contribution of the fluorescence lifetime components to the total emission of the NPL samples.

Non-defected NPLs (PL-QE = 100%)						
Sample	Population Fraction (%)	Contribution to total emission	Contribution of lifetime component to total emission ($A_i \times \tau_i$)			
			$A_1 \times \tau_1$	$A_2 \times \tau_2$	$A_3 \times \tau_3$	$A_4 \times \tau_4$
NPL-1	70	70	25	25	20	0
NPL-2	60	60	22	22	16	0
NPL-3	35	35	13	13	9	0
NPL-4	30	30	11	11	8	0

Defected NPLs (PL-QE = 8%)						
Sample	Population Fraction (%)	Contribution to total emission	Contribution of lifetime component to total emission ($A_i \times \tau_i$)			
			$A_1 \times \tau_1$	$A_2 \times \tau_2$	$A_3 \times \tau_3$	$A_4 \times \tau_4$
NPL-1	30	2.4	0.005	0.025	0.119	2.25
NPL-2	40	3.2	0.007	0.033	0.159	3.00
NPL-3	65	5.2	0.011	0.054	0.258	4.90
NPL-4	70	5.6	0.012	0.058	0.278	5.25

Table 6.7 Calculated and experimental fractions emission contributions of the lifetime components are compared, exhibiting a very well match with the calculation and the experiment.

Sample	Calculated fractional emission contributions ($\frac{A_i \times \tau_i}{\sum A_i \times \tau_i}$)					Experimental fractional emission contributions ($\frac{A_i \times \tau_i}{\sum A_i \times \tau_i}$)				
	Calculated PL-QE (%)	$A_1 \times \tau_1$ (%)	$A_2 \times \tau_2$ (%)	$A_3 \times \tau_3$ (%)	$A_4 \times \tau_4$ (%)	Experimental PL-QE (%)	$A_1 \times \tau_1$ (%)	$A_2 \times \tau_2$ (%)	$A_3 \times \tau_3$ (%)	$A_4 \times \tau_4$ (%)
NPL-1	72.4	34.54	34.56	27.79	3.11	76.8	34.69	35.93	26.23	3.15
NPL-2	63.2	34.82	34.86	25.57	4.75	61.5	35.43	33.00	24.79	6.70
NPL-3	40.2	32.37	32.47	23.03	12.19	35.3	36.11	31.85	20.63	11.42
NPL-4	35.6	30.93	31.06	23.25	14.75	33.3	30.38	29.71	24.96	14.94

Recently, optical gain has been shown in the colloidal NPLs independently by She *et al.* [59] using core/shell architecture and Guzelurk *et al.* [17] (see Chapter 6.4) using core/crown architecture. A record high optical gain coefficient among all colloidal optical gain media, which is as high as 650 cm^{-1} , has been achieved using the core/crown NPLs [17]. Most recently, Grim *et al.* have shown that continuous-wave

pumped optical gain is possible in the NPL based gain media [75]. These recent works strongly suggest that colloidal NPLs are extremely promising materials for lasers [17], [75]. However, the dependency of the optical gain threshold, at which pump intensity the amplified spontaneous emission (ASE) can be initiated, on the lateral area of the NPLs has not previously been elucidated. Thus, we studied the optical gain performance of the CdSe NPLs having varying lateral sizes. To this end, we investigated both single- and two-photon absorption pumped ASE (1PA- and 2PA-ASE) in the NPL samples mentioned above. We prepared solid film samples of the NPLs (*i.e.*, NPL-1, NPL-2, NPL-3 and NPL-4) on glass substrates *via* drop-casting from concentrated solutions.

Single-photon absorption pumped (400 nm, 120 fs, 1kHz) ASE measurements were performed *via* using stripe excitation configuration to excite the samples through a cylindrical lens ($f = 20$ cm). We used a variable neutral density filter before the cylindrical lens to adjust the excitation intensity. The pump intensity dependent emission spectra are presented in Figure 6.29a for the exemplary case of NPL-1. In 4 ML thick CdSe NPLs, the ASE peak was observed at ~ 532 nm arising due to the biexcitonic optical gain [17], [75]. Here, in accordance with the previous reports, we observed a red-shifted ASE peak that has a FWHM as narrow as 6 nm at room temperature. The transition from the spontaneous emission to the amplified spontaneous emission is visible for the excitation intensities higher than $45 \mu\text{J}/\text{cm}^2$. The emission intensity vs. single-photon pump intensity measurements are shown in Figure 6.29b for all of the NPLs. The single-photon pumped ASE threshold is the lowest for the NPL-1, which has the smallest lateral size. As the lateral size is increased, the ASE threshold becomes progressively larger (see Figure 6.29c). This indicates that for single-photon absorption pumping, there is a strong correlation between the PL-QEs of the NPLs and the stimulated emission thresholds. As the NPL lateral size is increased, the defected NPL (*i.e.*, NPL with a fast nonradiative trap channel) population also increases in number. Therefore, in the dense solid-state films of the NPLs, which are required for the optical gain purposes, strong nonradiative energy transfer among the same type of NPLs can quench the emission considerably

[19]. Therefore, NPL populations having lower defected NPL fraction will be favorable for optical gain and light-generation application.

We also performed two-photon absorption pumping (800 nm, 120 fs, 1 kHz) to realize frequency up-converted ASE in the NPLs, which is interesting for nonlinear optical applications including frequency up-converted lasers and bio-imaging. However, the lateral size dependency of the frequency up-converted optical gain has not been considered before. In the nonlinear processes such as two-photon absorption, the physical volume becomes critical [18], [260], [273], [274]. Therefore, one might expect to observe different trends for the two-photon pumped optical gain performance of the NPLs as compared to single-photon pumping. Figure 6.29d shows the emission spectra of the exemplary case NPL-4 for different pump intensities revealing the transition from spontaneous to stimulated emission. The emission intensity vs. two-photon pump intensity measurements are depicted for all four NPLs in Figure 6.29e. The 2PA-ASE threshold is found to be the lowest for NPL-4, which has the largest lateral size. As the lateral size is decreased, the threshold for ASE increases (see Figure 6.29f). This shows an opposite trend to that of 1PA-ASE. Increasing the lateral size of the NPLs is important for boosting the nonlinear optical response. Therefore, larger area NPLs offer better response in terms of optical gain threshold despite the increasing overall nonradiative decay channels in the ensemble.

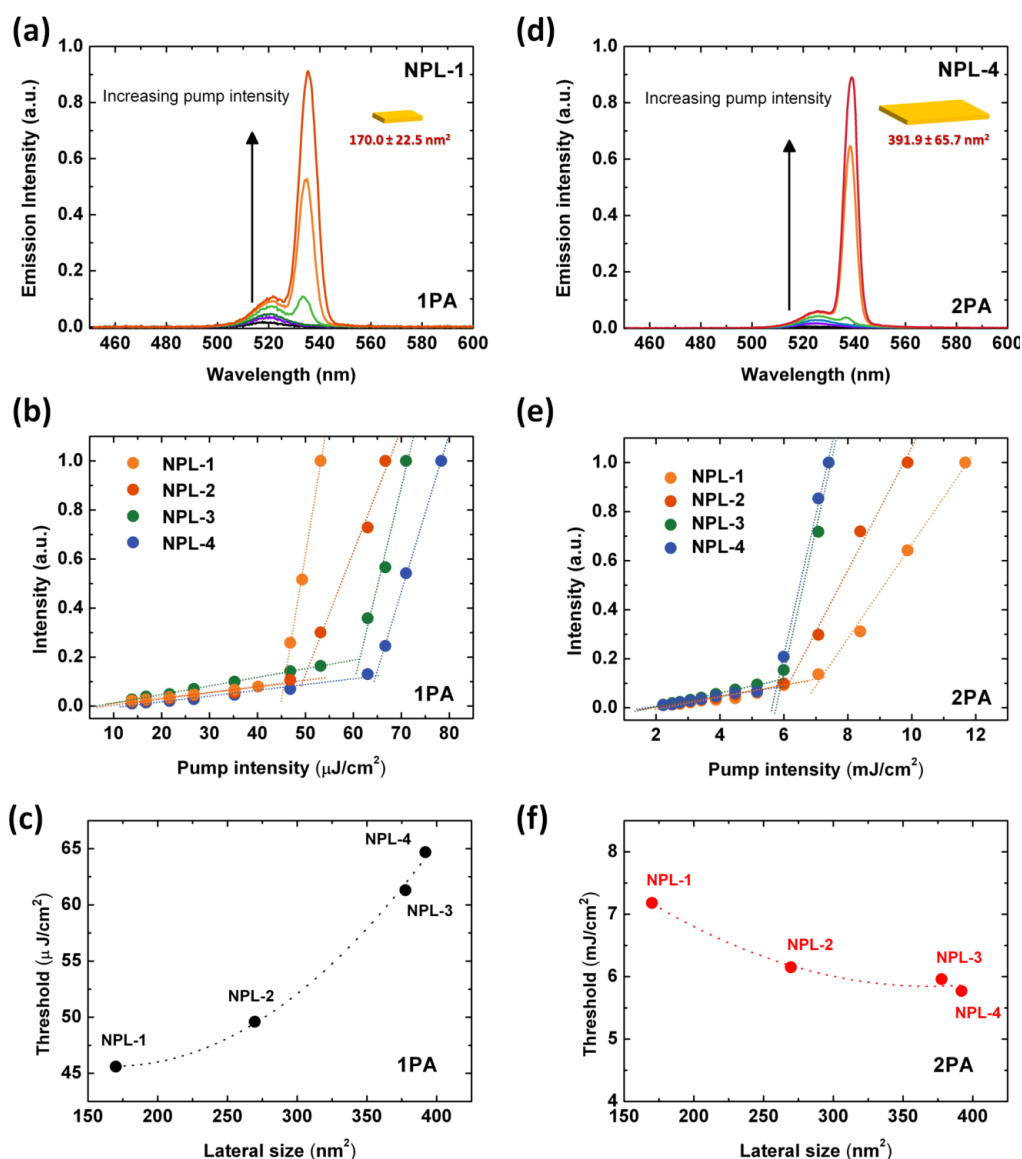


Figure 6.29 (a) Single-photon absorption (1PA) pumped ASE of the 4ML CdSe NPLs (NPL-1) having a lateral size of 170.0 nm^2 . (b) 1PA pumped luminescence vs. pump intensity of the NPLs having different lateral size. (c) Evolution of the 1PA pumped ASE thresholds with lateral size. (d) Two-photon absorption (2PA) pumped ASE of the NPL-4 having a lateral size of 391.9 nm^2 . (e) 2PA pumped luminescence vs. pump intensity of the NPLs having different lateral size. (f) Evolution of the 2PA pumped ASE thresholds with lateral size. The dotted lines are a guide for eyes. The 1PA- and 2PA-ASE thresholds exhibit opposite trends over for varying lateral size. Reprinted (or Adapted) with permission from [66]. Copyright 2015 American Chemical Society.

Table 6.8 Single- (1PA) and two-photon absorption (2PA) pumped of ASE thresholds of the 4ML CdSe NPLs having different lateral size.

Sample	Lateral size (nm ²)	1PA pumped ASE threshold ($\mu\text{J}/\text{cm}^2$)	2PA pumped ASE threshold (mJ/cm^2)
NPL-1	170.0 \pm 22.5	45.6	7.18
NPL-2	269.6 \pm 38.6	49.6	6.15
NPL-3	377.6 \pm 56.4	61.3	5.96
NPL-4	391.9 \pm 65.7	64.7	5.77

To understand the trend of decreasing 2PA-ASE threshold with increasing lateral size, we measured the two photon absorption (2PA) cross-section of the NPL ensembles by open-aperture z-scan technique. We dissolved 0.497 μM (NPL-2) and 0.299 μM (NPL-4) solutions of the NPL ensembles in hexane in a 1 mm quartz cuvette. The concentration of the NPL solutions were determined *via* analysis of the concentration by the elemental analysis using inductively coupled plasma optical emission spectroscopy. We fit the normalized transmittance data using (6.10) and (6.11). Two-photon absorption cross-section of the smaller NPL ensemble (NPL-2) was found to be 0.537×10^6 GM (1 GM = $10^{-58} \text{ m}^4 \times \text{s} \times \text{photon}^{-1}$), while 2.247×10^6 GM was measured for the largest NPL ensemble (NPL-4). This comparative measurement showed that 2PA cross-section grows overwhelmingly stronger with increasing lateral size and reaches extraordinarily high levels. To the best of our knowledge, this “giant” two-photon absorption cross-section measured in our largest NPL ensemble is the highest reported nonlinear absorption cross-section in all colloidal semiconductor NCs. Previously, in the case of colloidal quantum dots, two-photon absorption cross-section was measured to be up to 50,000 GM [18]. In the case of colloidal nanorods, two-photon absorption cross-section was found as high as 2.3×10^5 GM [261]. In the organic semiconductors, the maximum two-photon absorption cross-section was reported up to 10^6 GM [325]. Therefore, this giant two-photon absorption cross-section makes colloidal NPLs highly attractive and suitable materials for bio-imaging in deep tissues *via* using near-infrared (NIR) sources.

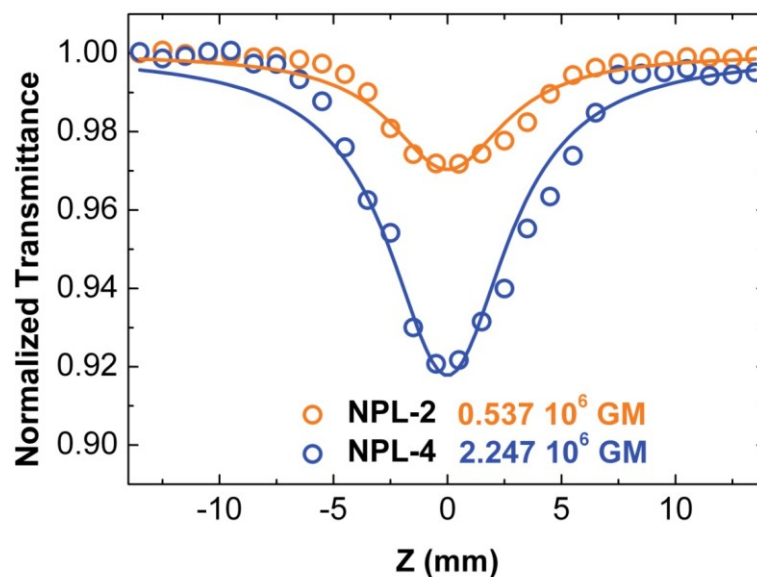


Figure 6.30 Comparative open aperture z-scan measurement of the NPL ensembles having lateral area of 269.6 nm^2 (NPL-2) and 391.9 nm^2 (NPL-4). The fit of the z-scan measurement gives a giant two-photon absorption cross-section of $0.537 \times 10^6 \text{ GM}$ and $2.247 \times 10^6 \text{ GM}$ for the NPL-2 and NPL-4, respectively. Reprinted (or Adapted) with permission from [66]. Copyright 2015 American Chemical Society.

6.5.4 Summary

We have investigated the effect of lateral size variation on the optical and excitonic properties of the colloidal CdSe NPLs having 4 ML of thickness both for spontaneous and stimulated emissions. In the spontaneous emission, we found accelerating photoluminescence decay rate and decreasing PL-QE at room temperature with increasing lateral size. Contrary to expectations, this revealed that the nonradiative channels dictate the observed trend due to increasing fraction of the defected NPL sub-population with extended lateral size. In the case of stimulated emission, both the single- (1PA) and two-photon absorption (2PA) pumping ASE measurements exhibited size-dependent behavior. However, their ASE threshold trends over varying laterals size were completely opposite. The NPLs with a larger lateral size showed a higher threshold in 1PA-pumped ASE due to their decreased quantum efficiency, as compared

to the smaller ones. On the other hand, the larger NPLs enabled a lower threshold in 2PA-pumped ASE owing to their strongly increased nonlinear absorption cross-section. This increase was so large that the nonlinear absorption cross-section reaches record high levels above 10^6 GM.

Lateral size control of the NPLs, therefore, proves to be critical in the resulting optical and excitonic properties. The vertical dimension of the NPLs, though leading to the strong quantum confinement, does not alone set the properties of spontaneous and stimulated emissions. In particular, a careful selection of the NPL lateral size is essential to low-threshold 1PA- and 2PA-ASE. Also, the “giant” nonlinear absorption cross-section observed in the NPLs, measured here as high as 2.25×10^6 GM for a lateral size of ~ 392 nm², is at least an order of magnitude stronger than those of colloidal quantum dots and rods ever reported to date. We believe that these new findings will help to realize high-performance solution-processed NPL devices.

6.6 Summary of the chapter

In this part of the thesis, we pushed the limits of the optical gain in the colloidal beyond the state of the art. For that we proposed, developed and demonstrated highly efficient colloidal gain media. Our achievements are as follows:

- 1) We developed blue-emitting core/shell quantum dots of ZnCdS/ZnS that have alloying at the core/shell interface. These QDs combine large size, high quantum yields and suppressed Auger recombination.
 - a. We achieved record low gain threshold among all blue-emitting QDs.
 - b. We realized for the first time two-photon absorption pumped optical gain in blue-emitting QDs.
- 2) We developed red-emitting core/shell quantum dots of CdSe/CdS that exhibit alloying at the core/shell interface thanks to the high temperature shell growth. These QDs have optimum size that can simultaneously attain suppressed Auger recombination, low gain thresholds and large gain coefficients at the same time.

- a. We achieved ultralow threshold gain both under single- and two-photon absorption pumping.
 - b. We developed the first all-colloidal vertical-cavity surface-emitting nanocrystal lasers.
 - c. We accomplished record low lasing thresholds using these all-colloidal nanocrystal lasers under frequency up-converted pumping region.
- 3) We introduced colloidal nanoplatelets, which make the most promising colloidal gain media and has a great potential to surpass the long standing challenges of the colloidal gain systems. The nanoplatelets can simultaneously offer large oscillator strength, large absorption cross-section, suppressed Auger recombination and do not have inhomogeneous broadening.
- a. We realized the first lasing action in the colloidal nanoplatelets.
 - b. We accomplished record high modal gain coefficients among all solution-processed semiconductors.
 - c. We uncovered giant two-photon absorption cross-sections in the nanoplatelets.

Chapter 7

Conclusions and Perspectives

7.1 General conclusions

In this thesis, we have investigated excitonic properties in colloidal semiconductor nanocrystals and their hybrids to accomplish energy-efficient optoelectronics. To this end, we have proposed, designed and demonstrated new-generation of colloidal nanocrystals, including atomically-flat nanoplatelets, heterostructured gradient-shell quantum dots and their hybrids, to overcome the long-standing fundamental limitations and practical challenges in light-harvesting and light-emitting devices of conventional nanocrystals. Particular challenges that we have addressed here encompass poor optical gain performance of the conventional nanocrystals and limited exciton transport in the nanocrystal solids. The former challenge has hampered the use of colloidal nanocrystals in practical lasers, while the latter one has been causing undesirably low performance levels in photovoltaics and light-emitting diodes of the nanocrystals. Therefore, these challenges have been restraining the potential of nanocrystals for energy-efficient optoelectronics.

Our main strategy in this thesis has been the exploitation of new-generation nanocrystals that offer superior optical and material attributes in contrast to those of the conventional nanocrystals. To this end, we have aimed to gain control over the collective excitonic processes (e.g., exciton transfer, diffusion, radiative recombination, trapping, etc.) through advancing tailor-made heterostructures of these nanocrystals and developing their assembly-controlled hybrid films, in addition to extensive optical spectroscopy and material characterizations. Our key achievements include the accomplishment of record high modal gain coefficients among all solution-processed semiconductors. This has been enabled by developing and harnessing heterostructured nanoplatelets that can simultaneously combine Auger recombination suppression and large stimulated emission cross-section while avoiding inhomogeneous broadening.

In these nanoplatelets, we have also uncovered “giant” nonlinear absorption cross-section that can be more than an order of magnitude larger than the highest reported cross-sections in the colloidal nanocrystals to date. This feature is expected to make nanoplatelets exciting for bio-imaging and nonlinear optics. Furthermore, we have achieved frequency up-converted nanocrystal lasers that exhibit record low lasing thresholds. These up-converted lasers are fabricated by using only solution-processing and offer the most cost effective approach for single-material all-color semiconductor lasers.

We have also unveiled ultrafast exciton transfer in self-assembled nanoplatelet films that can conceivably facilitate ultralong exciton transport, which has been missing in conventional nanocrystals. Therefore, designer nanoplatelet solids with long exciton transport are expected to impact solar cells, photodetectors and sensors. Additionally, we have introduced the concept of exciton-driven light-emitting diodes that can actively capture and harvest excitons within an electroluminescent device based on organic-inorganic hybrids. Our prototype excitonic LEDs gave a significant boost to their external quantum efficiencies, which underscores the importance of exciton pumping as a promising alternative to conventional charge injection pumping.

Overall, the findings of this thesis advance the current understanding of the photophysical properties in colloidal semiconductors and present beyond the-state-of-the-art performance in nanocrystal photonic devices. Furthermore, we believe that these findings will strongly help to establish a bridge between the fields of excitonics and optoelectronics using colloidal nanocrystals to attain the overarching goal: energy-efficient nanocrystal devices. This technology platform empowered by innovative nanomaterial processing and optical physics discoveries will be deployed in numerous applications ranging from displays to bio-imaging, sensing and lighting. Furthermore, nanocrystal optoelectronics will help to combat the global challenges of the world such as sustainable energy generation, efficient lighting and versatile healthcare technologies.

7.2 Future outlook

After more than two decades of research and development, extensive efforts are still today needed to uncover and unleash the potential of the colloidal semiconductor nanocrystals for diverse applications. Thanks to extremely rich opportunities and possibilities at the nanoscale at the crossing point of various disciplines including physics, chemistry, biology, materials science and electronics, nanocrystals and their hybrid systems are expected to continue to surprise the scientific community with unexpected and extraordinary properties. In this section, we highlight some of the future challenges that are needed to be tackled towards practical nanocrystal lasers and ultraefficient light-harvesting and light-emitting devices. Also, we will give a perspective for possible future research directions.

7.2.1 Optical gain and lasing

Gain using affordable optical pump sources or electrical injection: Colloidal nanocrystal lasers commonly employ femtosecond or nanosecond pulsed lasers as the pump source. However, practical nanocrystal lasers would require using conventional and affordable pump sources such as continuous-wave (CW) lasers, blue laser diodes

or using electrical injection from an external power supply. In conventional nanocrystals, these pumping sources are not feasible to achieve gain since it is extremely short-lived due to dominant Auger recombination.

The CW-pumped lasing threshold can be calculated using the following relation $P_{th} = \langle N \rangle_{th} \frac{h\nu}{\sigma\tau_X}$, where $\langle N \rangle_{th}$ is the average number of excitons per particle at the net gain threshold, σ is the absorption cross-section and τ_X is the exciton lifetime. Assuming a biexciton gain model ($\langle N \rangle_{th} \approx 1.15$), physically attainable σ (10^{-13} cm²) and τ_X (1 ns), the CW-pumped lasing threshold would be 8 kW/cm². Nevertheless, pump intensities above kW/cm² can cause considerable heating that would lead to the destruction of the material before it can deliver net gain. Therefore, CW-pumped lasing thresholds should be further decreased. As we have shown recently in the nanoplatelets [67], it is possible to increase σ ($\sim 5 \times 10^{-13}$ cm²) by controlling the vertical thickness and the lateral area of the nanoplatelets. Also, longer exciton lifetimes ($\tau_X \approx 5$ ns) can be attained using nanoplatelets in core/shell structure. Thus, CW-pumped lasing threshold could be made as low as 300 W/cm², which can be readily achieved using commercially available laser diodes. Here, the practical challenge remains accommodating large absorption cross-sections in the nanoplatelets without degrading their high quality optical properties. As we have shown recently, larger nanoplatelets tend to suffer from higher probability of having defects on their surfaces [66]. Additionally, poor film packing density in the nanoplatelets with large lateral area may lead to reduced optical confinement factor (Γ), overall decreasing the effective modal gain.

These practical problems can be circumvented by developing post-synthetic chemical processing to increase surface passivation of the nanoplatelets. Also, controlled self-assembly of the nanoplatelets would allow for the formation of highly close-packed films. Recently, Moreels group have reported a proof-of-concept CW-pumped nanoplatelet laser [75]. Although it has not been possible to reproduce the results of this paper, this report highlights the potential of the nanoplatelets for CW-pumped lasing. Moreover, complex heterostructures of the nanoplatelets such as core/crown and core/shell with a composition tuning (e.g., alloying and/or doping) are

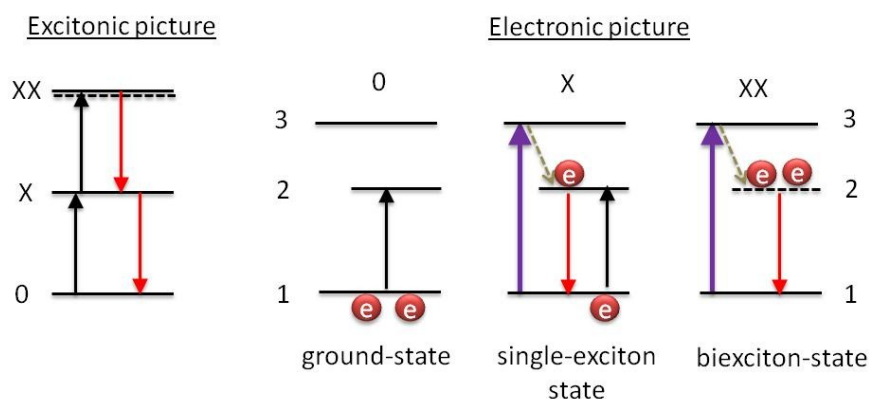
expected to help further reducing the lasing thresholds towards feasible and robust CW lasing.

Electrically injected nanocrystal lasers are also highly desired, but it has never been attained before. These have been the Holy Grail for all soft semiconductor material systems including organic semiconductors. The calculations show that the required threshold current density to reach net optical gain is larger than 1 kA/cm^2 that corresponds to carrier densities $\gg 10^{18} \text{ cm}^{-3}$ [326]. The challenge is that film thicknesses required for optical gain are generally $100 - 500 \text{ nm}$, where poor charge mobilities ($\ll 1 \text{ cm}^2 \text{ V}^{-1} \text{ s}^{-1}$) together with poor heat conductivity in the colloidal nanocrystal films cause the breakdown of these films before they could reach the threshold carrier injection levels. To overcome this, the best strategy would be to employ nanocrystals with large gain potential (i.e., nanoplatelets). Thus, thinner nanocrystal films ($\ll 100 \text{ nm}$) could be sufficient to generate net gain. Furthermore, recently introduced inorganic ligands, which lead to large mobilities ($>1 \text{ cm}^2 \text{ V}^{-1} \text{ s}^{-1}$) in nanocrystal films [49], could be employed by replacing the original organic ligands that are believed to impede the charge injection and transport. Here, the challenge would be to preserve the high quality optical properties of the nanoplatelets after inorganic ligand exchange process. This problem may possibly be circumvented by using platelet-in-a-box type structures, where surface states do not affect the excitonic emission from the inner-core of the nanoplatelets; hence, the efficient emission can be still preserved [80].

Advancing alternative gain systems: Another fundamental challenge in conventional nanocrystal-based gain media is the gain mechanism itself. As explained in Chapter 2, in conventional nanocrystals optical gain arises from the biexcitons. To achieve net gain, the biexciton population should overcome the ground-state population. Thus, gain in the conventional nanocrystals effectively resembles a three-level gain system, which dictates the gain dynamics (see Figure 7.1a). To date, more efficient gain systems such as four-level gain have remained elusive in nanocrystals. We propose that through tailoring the exciton-exciton, exciton-charge and exciton-phonon interactions, it would be possible to shift the energy of the biexciton state so that competition between the

biexciton and ground-state populations can be eliminated. Therefore, one could effectively generate “thresholdless” nanocrystal lasers, relying on a four-level gain system.

(a) 3-level gain in conventional nanocrystals



(b) 4-level gain in excitonically engineered nanocrystals

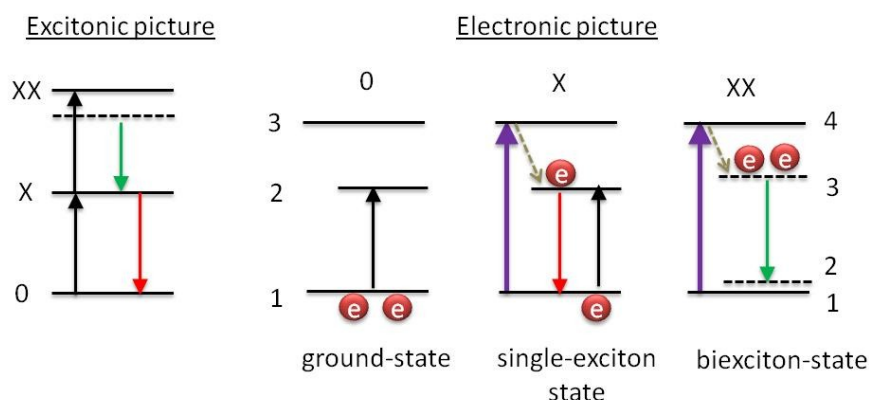


Figure 7.1. (a) Three-level optical gain in conventional nanocrystals. (b) Prospect of four-level optical gain in excitonically engineered next-generation nanocrystals.

Our preliminary results suggest that core/crown nanoplatelets having Type-II electronic structure could allow for the realization of a four-level gain (Guzelturk et al., 2016 unpublished). This has been possible through electronic coupling between the exciton in the crown and the charge transfer state at the Type-II interface, which red-shifts the energy of the coupled biexciton state (see Figure 7.1b). In these nanoplatelets, pump intensity dependent modal gain coefficients (see Figure 7.2)

strongly support the prevailing “thresholdless” gain system, which exhibits linearly increasing gain coefficients as a function of the pump intensity, a characteristic response of a four-level gain system.

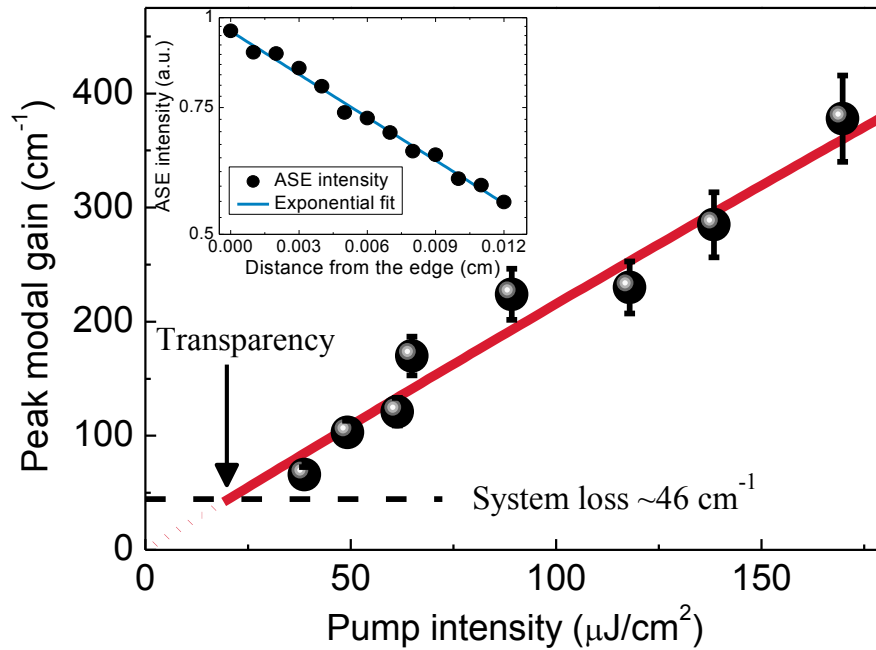


Figure 7.2. Peak modal gain coefficients as a function of pump intensity in heterostructured nanoplatelets having Type-II electronic structure. (Guzelturk et al., unpublished data.)

Single exciton gain: In 2007, Klimov group have shown that single-exciton gain in colloidal nanocrystals having Type-II electronic structure would be the most efficient process for nanocrystal lasers [284]. Since then, however, single-exciton gain could not be easily achieved except few cases, where the nanocrystals had controversially a Type-I electronic structure [10]. Therefore, it has not been fully understood nor systematically studied how single-exciton gain prevails in the colloidal nanocrystals. Potentially, single-exciton gain might be triggered by the strong exciton-phonon coupling in the nanocrystals that lead to large Stokes-shifted emission. Also, doped nanocrystals having mid-gap states might offer single-exciton gain.

Solution-state lasing: Colloidal nanocrystals are very bright emitters in their solution-state. When they are transferred to their close-packed films, their optical properties start to deteriorate due to particle-particle interactions at the nanoscale leading to charge and exciton trapping. Also, surfaces of the nanocrystals are more prone to oxidation in their solid films. Thus, solution-state lasing is quite interesting and can overcome the limitations of solid film-based lasing [283]. Moreover, solution-state nanocrystal lasers can provide the versatility of continuously refreshing the gain media that can empower for continuously color tunable lasers. However, a typical difficulty was the low gain coefficients in the conventional nanocrystals that obstructs the achievement of net gain in nanocrystal in their solutions. To this end, nanoplatelets with extremely large gain coefficients can defeat this difficulty and conveniently achieve net gain in solution state [327].

Improving stability: One of the least considered aspects of the nanocrystal gain media is their stability. Generally, nanocrystal gain starts to decrease after continuous excitation of a pulsed laser. Considering a repetition rate of 1 kHz, the gain is generally completely diminished after 10^5 - 10^6 pump laser shots. This generally happens due to the existing nonradiative channels in the nanocrystals creating significant heating and also oxidation of the surfaces creating additional traps that compete with optical gain. Therefore, to make practical nanocrystal lasers, the operation lifetime of a nanocrystal gain medium should be considerably prolonged. Our achievement of $>10^7$ pump laser shot stability in well-passivated core/shell quantum dots [18] and core/crown/shell nanoplatelets [80] suggest that epitaxial passivation of the nanocrystals greatly helps to improve their gain stability. Furthermore, encapsulation of the films is expected to further increase the stability.

7.2.2 Nanocrystals for light-harvesting and light-generation

Self-assembly of the nanoplatelets: In recent years, self-assembly of the nanocrystals has created a great interest for practical devices [328], [329]. Using self-assembly, it

becomes possible to create large-scale ordered solid films of the nanocrystals. Self-assembly of the nanoplatelets is also possible as we have performed preliminary experiments in this thesis. For example, face-to-face stacked needle-like superstructures (Figure 7.3a) of CdSe nanoplatelets can be achieved using air/liquid self-assembly. These stacked nanoplatelet assemblies will be highly promising for long-range exciton transport. Also, completely flat-lying nanoplatelet assemblies (Figure 7.3b) can be achieved, which are expected to be exciting for light-emitting devices.

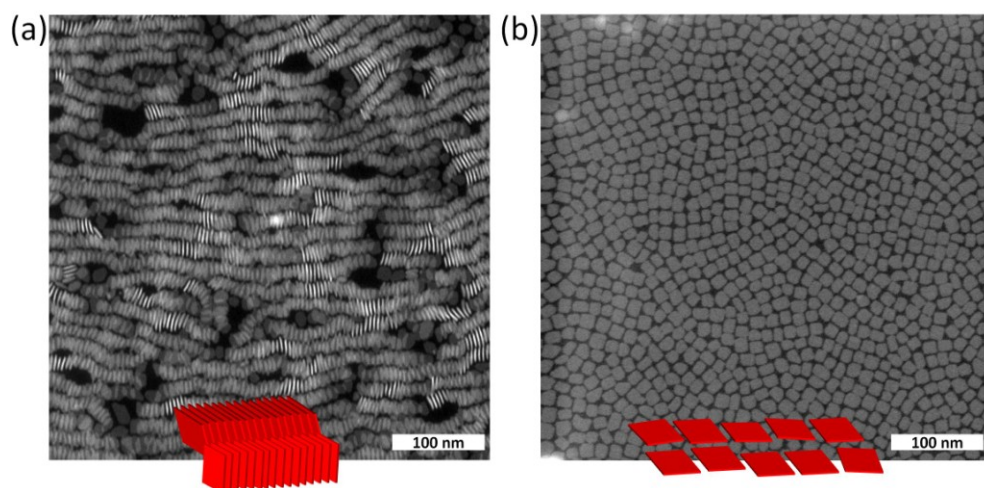


Figure 7.3. HAADF-STEM images of the self-assembled CdSe nanoplatelets: (a) face-to-face stacked perpendicular-lying nanoplatelets on a substrate, (b) side-by-side oriented flat-lying nanoplatelets on a substrate. (Guzelturk et al., unpublished data.)

Limited hole transfer: Previously, organic-inorganic hybrids that comprise colloidal nanocrystals and organic semiconductors have been considered to be promising for solar cells [12]. However, hole transfer from the nanocrystal into the organic semiconductor has been found to be quite limited due to very slow transfer rates. This has been restricting the performance of such hybrid solar cells. In our recent work based on nanoplatelet – conjugated polymer hybrids [185], we have observed strong quenching of the photoluminescence of the nanoplatelets as attributed to the dominant exciton dissociation at the hybrid interfaces. With their atomically-flat surfaces and large extension of their lateral surface, the nanoplatelets may overcome the limited

hole transfer rates in organic-inorganic hybrids. These hybrids employing nanoplatelets are expected to initiate further studies using ultrafast optical probes such as pump-probe transient absorption spectroscopy to understand the potential of the nanoplatelets for hybrid solar cells.

Harvesting triplet-state excitons via Dexter energy transfer: In this thesis, we have demonstrated exciton recycling using phosphorescent emitters in active nanocrystal LEDs. The limitation of the phosphorescent organic materials is the slow rate of exciton transfer due to their intrinsic slow exciton recombination rates. Recently, Baldo and Friend groups have shown that exciton transfer from an organic semiconductor into a colloidal nanocrystal is also possible via Dexter energy transfer [330], [331], which commonly takes place for separation distances on the order of a nanometer or less. To date, this type of energy transfer has been only shown for the infrared-emitting quantum dots. It will be also very exciting to harness triplet excitons in conjugated polymer – colloidal nanocrystal hybrids that emit in the visible. This would boost hybrid excitonic LEDs to reach the theoretical efficiency levels.

Control of surface chemistry to eliminate surface traps: Although colloidal nanoplatelets could in principle attain large exciton transport lengths, the presence of defected non-emissive nanoplatelets, which are believed to have Cd-vacancies at their surfaces, can effectively trap freely diffusing excitons at an ultrafast rate. Thus, this process would limit exciton diffusion lengths and would also limit their power conversion efficiencies in the case of solar cell operation. Similarly, exciton trapping leads to decreased performance in the light-emitting diodes, which can be detrimental for the emission efficiency. To this end, it will be crucial to develop means to control the surface chemistry of the nanoplatelets in order to passivate the surface trap sites. For this, small inorganic ligands (e.g., Cl) could be utilized.

7.3 Contributions of this thesis to the literature and patents

First-authored publications:

- 1) **B. Guzelturk**, Y. Kelestemur, K. Gungor, A. Yeltik, M. Z. Akgul, W. Yue, R. Chen, H. D. Sun, C. Dang, H. V. Demir, "Stable and Low Threshold Optical Gain in CdSe/CdS Quantum Dots: All-Colloidal Frequency Up-Converted Laser" *Advanced Materials* 27, 2741 (2015). Selected as Inside Front Cover.
- 2) **B. Guzelturk**, F. Menk, K. Philipps, Y. Kelestemur, M. Olutas, R. Zentel, H. V. Demir, "Colloidal Nanoplatelet/Conducting Polymer Hybrids: Excitonic and Material Properties," *J. Phys. Chem. C* 120, 3573 (2016).
- 3) M. Olutas*, **B. Guzelturk***, Y. Kelestemur, A. Yeltik, S. Delikanli, H. V. Demir, "Lateral Size-Dependent Spontaneous and Stimulated Emission Properties in Colloidal CdSe Nanoplatelets" *ACS Nano* 9, 5041 (2015). * Equal contribution
- 4) **B. Guzelturk**, H. V. Demir, "Organic-Inorganic Composites of Semiconductor Nanocrystals For Efficient Excitonics" *J. Phys. Chem. Lett.* 6, 2206 (2015). Invited Perspective Letter, also selected as Front Cover.
- 5) **B. Guzelturk**, M. Olutas, S. Delikanli, Y. Kelestemur, O. Erdem, H. V. Demir, "Nonradiative energy transfer in colloidal CdSe nanoplatelet films," *Nanoscale* 7, 2345 (2015).
- 6) **B. Guzelturk**, A. L. Kanibolotsky, C. Orofino-Pena, N. Laurand, M. D. Dawson, P. J. Skabara, H. V. Demir, "Ultralow-Threshold Up-Converted Lasing in Oligofluorenes with Tailored Strong Nonlinear Absorption," *J. Mater. Chem. C* 3, 12018 (2015). Selected as Front Cover.
- 7) **B. Guzelturk**, O. Erdem, M. Olutas, Y. Kelestemur, H. V. Demir, "Stacking in Colloidal Nanoplatelets: Excitonic Properties," *ACS Nano* 8, 12524 (2014).
- 8) **B. Guzelturk**, Y. Kelestemur, M. Olutas, S. Delikanli, H. V. Demir, "Amplified Spontaneous Emission and Lasing in Colloidal Nanoplatelets," *ACS Nano* 8, 6599 (2014).
- 9) **B. Guzelturk**, P. L. H. Martinez, Q. Zhang, Q. Xiong, H. Sun, X. W. Sun, A. O. Govorov and H. V. Demir, "Excitonics of semiconductor quantum dots and wires for

lighting and displays," *Laser & Photonics Reviews* 8, 73 (2014). Selected as Front Cover.

10) **B. Guzelturk**, P. L. H. Martinez, V.K. Sharma, Y. Coskun, V. Ibrahimova, D. Tuncel, A. O. Govorov, X. W. Sun, Q. Xiong, H. V. Demir, "Study of exciton transfer in dense quantum dot nanocomposites," *Nanoscale* 6, 11387 (2014).

11) E. Mutlugun*, **B Guzelturk***, A. P. Abiyasa*, Y. Gao, X. W. Sun, H. V. Demir, "Colloidal Quantum Dot Light-Emitting Diodes Employing Phosphorescent Small Organic Molecules as Efficient Exciton Harvesters," *J. Phys. Chem. Lett.* 5, 2802 (2014). * Equal contribution

12) **B. Guzelturk**, Y. Kelestemur, M. Z. Akgul, V. K. Sharma, H. V. Demir, "Ultralow Threshold One-Photon and Two-Photon Pumped Optical Gain Media of Blue-Emitting Colloidal Quantum Dot Films," *J. Phys. Chem. Lett.* 5, 2214 (2014).

13) **B. Guzelturk**, P. L. H. Martinez, D. Zhao, X. W. Sun, H. V. Demir, "Singlet and Triplet Exciton Harvesting in the Thin Films of Colloidal Quantum Dots Interfacing Phosphorescent Small Organic Molecules," *J. Phys. Chem. C* 118, 25964 (2014).

14) A.Yeltik*, **B. Guzelturk***, P. L. H. Martinez, A. O. Govorov, H.V.Demir, "Phonon assisted nonradiative energy transfer into silicon from colloidal quantum dots," *ACS Nano* 7, 10492 (2013). * Equal contribution

15) **B. Guzelturk**, E. Mutlugun, X. Wang, K. L. Pey, H. V. Demir, "Enhancement of photovoltaic radial junction nanopillar architecture integrating semiconductor quantum dot nanocrystals as light harvesters," *Appl. Phys. Lett.* 97, 093111 (2010).

Co-authored publications:

1) Y. Kelestemur, **B. Guzelturk**, O. Erdem, M. Olutas, K. Gungor, H. V. Demir, "Platelet-in-Box Colloidal Quantum Wells: CdSe/CdS@CdS Core/Crown@Shell Heteronanoplatelets" *Adv. Funct. Mater.* (2016). DOI: 10.1002/adfm.201600588

2) M. Olutas, **B. Guzelturk**, Y. Kelestemur, K. Gungor, H. V. Demir, "Highly Efficient Nonradiative Energy Transfer from Colloidal Semiconductor Quantum Dots to Wells for Sensitive Non-contact Temperature Probing" *Adv. Funct. Mater.* (2016). DOI: 10.1002/adfm.201505108

- 3) O. Erdem, M. Olutas, **B. Guzelturk**, Y. Kelestemur, H. V. Demir, "Temperature-Dependent Emission Kinetics of Colloidal Semiconductor Nanoplatelets Strongly Modified by Stacking," *J. Phys. Chem. Lett.* 7, 548 (2016).
- 4) S. Delikanli, **B. Guzelturk**, P. L. Hernandez-Martinez, T. Erdem, Y. Kelestemur, M. Olutas, M. Z. Akgul, H. V. Demir, "Continuously Tunable Emission in Inverted Type-I CdS/CdSe Core/Crown Semiconductor Nanoplatelets," *Adv. Funct. Mater.* 25, 4282 (2015).
- 5) H. Keita, **B. Guzelturk**, J. Pennakalathil, T. Erdem, H. V. Demir, D. Tuncel, "Construction of multi-layered white emitting organic nanoparticles by clicking polymers," *J. Mater. Chem. C* 3, 10277 (2015).
- 6) Y. Kelestemur, M. Olutas, S. Delikanli, **B. Guzelturk**, M. Z. Akgul, H. V. Demir, "Type-II Colloidal Quantum Wells: CdSe/CdTe Core/Crown Heteronanoplatelets," *J. Phys. Chem. C* 119, 2177-2185 (2015).
- 7) A. Yeltik, S. Delikanli, M. Olutas, Y. Kelestemur, **B. Guzelturk**, H. V. Demir, "Experimental Determination of the Absorption Cross-Section and Molar Extinction Coefficient of Colloidal CdSe Nanoplatelets," *J. Phys. Chem. C* (2015). DOI: 10.1021/acs.jpcc.5b09275
- 8) V. K. Sharma, **B. Guzelturk**, T. Erdem, Y. Kelestemur, H. V. Demir, "Tunable White-Light-Emitting Mn-Doped ZnSe Nanocrystals," *ACS Applied Materials & Interfaces* 6, 3654 (2014).
- 9) Y. Kelestemur, A. F. Cihan, **B. Guzelturk**, H. V. Demir, "Type-Tunable Amplified Spontaneous Emission from Core-Seeded CdSe/CdS Nanorods Controlled by Exciton-Exciton Interaction" *Nanoscale* 6, 8509 (2014).
- 10) C. Uran, T. Erdem, **B. Guzelturk**, N. K. Perkgoz, S. Jun, E. Jang, H. V. Demir, "Highly polarized light emission by isotropic quantum dots integrated with magnetically aligned segmented nanowires," *Appl. Phys. Lett.* 105, 141116 (2014).
- 11) A. Yeltik, **B. Guzelturk**, P. L. Hernandez-Martinez, S. Akhavan, H. V. Demir, "Excitonic enhancement of nonradiative energy transfer to bulk silicon with the hybridization of cascaded quantum dots," *Appl. Phys. Lett.* 103, 261103 (2013).
- 12) A. Yeltik, G. Kucukayan-Dogu, **B. Guzelturk**, S. Fardindoost, Y. Kelestemur, H. V. Demir, "Evidence for Nonradiative Energy Transfer in Graphene-Oxide-Based Hybrid Structures," *J. Phys. Chem. C* 117, 25298 (2013).

- 13) A. F. Cihan, Y. Kelestemur, **B. Guzelturk**, O. Yerli, U. Kurum, H. G. Yaglioglu, A. Elmali, and H. V. Demir, "Attractive versus Repulsive Excitonic Interactions of Colloidal Quantum Dots Control Blue-to Red-Shifting (and Non-shifting) Amplified Spontaneous Emission," *J. Phys. Chem. Lett.* 4, 4146 (2013).
- 14) S. Akhavan, **B. Guzelturk**, V. K. Sharma, H. V. Demir, "Large-area semi-transparent light-sensitive nanocrystal skins," *Optics Express* 20, 25255 (2012).
- 15) S. Nizamoglu, **B. Guzelturk**, D. - W. Jeon, I. -H. Lee, H. V. Demir, "Efficient exciton migration from InGaN/GaN nanopillars to CdSe/ZnS core/shell nanocrystals," *Appl. Phys. Lett.* 98, 163108 (2011).

Patents:

- 1) **B. Guzelturk**, J. Bae, J. Park, S. Jeon, "Textile based stretchable energy generator," US patent 20,140,111,063.
- 2) **B. Guzelturk**, J. Bae, J. Park, S. Jeon, "Textile based stretchable energy generator," S. Korea patent KR20140050393.
- 3) **B. Guzelturk**, J. Bae, J. Park, S. Jeon, "Textile-based energy generator having stacked structure," S. Korea patent KR20140055150.
- 4) **B. Guzelturk**, S. Akhavan, H. V. Demir, "Large and Photosensitive Nanocrystal Skin and Manufacturing Method," TR patent 2012/02,559.
- 5) **B. Guzelturk**, H. V. Demir, C. Uran, T. Erdem, K. Gungor, S. Jun, E. J. Jang, "Optical elements and electronic devices including the same regarding polarized light emitting display using nanocrystal composites," US patent 20,160,027,963.
- 6) **B. Guzelturk**, H. V. Demir, C. Uran, T. Erdem, K. Gungor, S. Jun, E. J. Jang, "Optical elements and electronic devices including the same regarding polarized light emitting display using nanocrystal composites," S. Korea patent pending.

Bibliography

- [1] “Towards 2020 – Photonics driving economic growth in Europe Multiannual Strategic Roadmap 2014 – 2020,” 2013.
- [2] “Nanocrystals in their prime,” *Nat. Nanotechnol.*, vol. 9, no. 5, pp. 325–325, May 2014.
- [3] K. Bourzac, “Quantum dots go on display,” *Nature*, vol. 493, no. 7432, pp. 283–283, Jan. 2013.
- [4] A. Sandhu, “Quantum dots: A bright future,” *Nat. Nanotechnol.*, Nov. 2007.
- [5] J. Wallace, “Quantum-dot market to grow at CAGR of 29.9% between 2014 and 2020,” *LaserFocusWorld*. [Online]. Available: <http://www.laserfocusworld.com/articles/2014/04/quantum-dot-market-to-grow-at-cagr-of-29-9-between-2014-and-2020.html>. [Accessed: 29-Apr-2016].
- [6] V. I. Klimov, A. A. Mikhailovsky, S. Xu, A. Malko, H. J. A. C. A. Leatherdale, H. J. Eisler, and M. G. Bawendi, “Optical Gain and Stimulated Emission in Nanocrystal Quantum Dots,” *Science (80-.)*, vol. 290, no. 5490, pp. 314–317, Oct. 2000.
- [7] E. H. Sargent, “Colloidal quantum dot solar cells,” *Nat. Photonics*, vol. 6, no. 3, pp. 133–135, Feb. 2012.
- [8] D. V Talapin and C. B. Murray, “PbSe nanocrystal solids for n- and p-channel thin film field-effect transistors,” *Science*, vol. 310, no. 5745, pp. 86–9, Oct. 2005.
- [9] R. C. Somers, M. G. Bawendi, and D. G. Nocera, “CdSe nanocrystal based chem-/bio- sensors,” *Chem. Soc. Rev.*, vol. 36, no. 4, pp. 579–91, Apr. 2007.
- [10] C. Dang, J. Lee, C. Breen, J. S. Steckel, S. Coe-Sullivan, and A. Nurmikko, “Red, green and blue lasing enabled by single-exciton gain in colloidal quantum dot films,” *Nat. Nanotechnol.*, vol. 7, no. 5, pp. 335–339, May 2012.
- [11] V. I. Klimov, A. A. Mikhailovsky, S. Xu, A. Malko, J. A. Hollingsworth, C. A. Leatherdale, H. Eisler, and M. G. Bawendi, “Quantization of Multiparticle Auger Rates in Semiconductor Quantum Dots,” *Science (80-.)*, vol. 290, no.

5490, pp. 314–317, Feb. 2000.

- [12] W. U. Huynh, J. J. Dittmer, and A. P. Alivisatos, “Hybrid nanorod-polymer solar cells,” *Science*, vol. 295, no. 5564, pp. 2425–7, Mar. 2002.
- [13] J. B. Asbury, E. Hao, Y. Wang, H. N. Ghosh, and T. Lian, “Ultrafast Electron Transfer Dynamics from Molecular Adsorbates to Semiconductor Nanocrystalline Thin Films,” *J. Phys. Chem. B*, vol. 105, no. 20, pp. 4545–4557, May 2001.
- [14] G. M. Akselrod, F. Prins, L. V Poulidakos, E. M. Y. Lee, M. C. Weidman, A. J. Mork, A. P. Willard, V. Bulović, and W. A. Tisdale, “Subdiffusive exciton transport in quantum dot solids,” *Nano Lett.*, vol. 14, no. 6, pp. 3556–62, Jun. 2014.
- [15] X. Dai, Z. Zhang, Y. Jin, Y. Niu, H. Cao, X. Liang, L. Chen, J. Wang, and X. Peng, “Solution-processed, high-performance light-emitting diodes based on quantum dots,” *Nature*, vol. 515, no. 7525, pp. 96–99, Oct. 2014.
- [16] Y. Shirasaki, G. J. Supran, M. G. Bawendi, and V. Bulović, “Emergence of colloidal quantum-dot light-emitting technologies,” *Nat. Photonics*, vol. 7, no. 12, pp. 933–933, Nov. 2013.
- [17] B. Guzelturk, Y. Kelestemur, M. Olutas, S. Delikanli, and H. V. Demir, “Amplified Spontaneous Emission and Lasing in Colloidal Nanoplatelets,” *ACS Nano*, vol. 8, no. 7, pp. 6599–6605, Jun. 2014.
- [18] B. Guzelturk, Y. Kelestemur, K. Gungor, A. Yeltik, M. Z. Akgul, Y. Wang, R. Chen, C. Dang, H. Sun, and H. V. Demir, “Stable and Low-Threshold Optical Gain in CdSe/CdS Quantum Dots: An All-Colloidal Frequency Up-Converted Laser,” *Adv. Mater.*, vol. 27, no. 17, pp. 2741–2746, Mar. 2015.
- [19] B. Guzelturk, O. Erdem, M. Olutas, Y. Kelestemur, and H. V. Demir, “Stacking in colloidal nanoplatelets: tuning excitonic properties,” *ACS Nano*, vol. 8, no. 12, pp. 12524–33, Dec. 2014.
- [20] B. Guzelturk and H. V. Demir, “Organic-Inorganic Composites of Semiconductor Nanocrystals for Efficient Excitonics,” *J. Phys. Chem. Lett.*, vol. 6, no. 12, pp. 2206–15, Jun. 2015.
- [21] E. Mutlugun, B. Guzelturk, A. P. Abiyasa, Y. Gao, X. W. Sun, and H. V. Demir, “Colloidal Quantum Dot Light-Emitting Diodes Employing

- Phosphorescent Small Organic Molecules as Efficient Exciton Harvesters,” *J. Phys. Chem. Lett.*, vol. 5, no. 16, pp. 2802–2807, Aug. 2014.
- [22] A. I. Ekimov, A. L. Efros, and A. A. Onushchenko, “Quantum size effect in semiconductor microcrystals,” *Solid State Commun.*, vol. 56, no. 11, pp. 921–924, Dec. 1985.
- [23] L. E. Brus, “Electron–electron and electron-hole interactions in small semiconductor crystallites: The size dependence of the lowest excited electronic state,” *J. Chem. Phys.*, vol. 80, no. 9, p. 4403, May 1984.
- [24] M. L. Steigerwald, A. P. Alivisatos, J. M. Gibson, T. D. Harris, R. Kortan, A. J. Muller, A. M. Thayer, T. M. Duncan, D. C. Douglass, and L. E. Brus, “Surface derivatization and isolation of semiconductor cluster molecules,” *J. Am. Chem. Soc.*, vol. 110, no. 10, pp. 3046–3050, May 1988.
- [25] A. P. Alivisatos, A. L. Harris, N. J. Levinos, M. L. Steigerwald, and L. E. Brus, “Electronic states of semiconductor clusters: Homogeneous and inhomogeneous broadening of the optical spectrum,” *J. Chem. Phys.*, vol. 89, no. 7, p. 4001, Oct. 1988.
- [26] M. G. Bawendi, W. L. Wilson, L. Rothberg, P. J. Carroll, T. M. Jedju, M. L. Steigerwald, and L. E. Brus, “Electronic structure and photoexcited-carrier dynamics in nanometer-size CdSe clusters,” *Phys. Rev. Lett.*, vol. 65, no. 13, pp. 1623–1626, Sep. 1990.
- [27] M. G. Bawendi, M. L. Steigerwald, and L. E. Brus, “The Quantum Mechanics of Larger Semiconductor Clusters (‘Quantum Dots’),” *Annu. Rev. Phys. Chem.*, vol. 41, no. 1, pp. 477–496, Oct. 1990.
- [28] C. B. Murray, D. J. Norris, and M. G. Bawendi, “Synthesis and characterization of nearly monodisperse CdE (E = S, Se, Te) semiconductor nanocrystallites,” *J. Am. Chem. Soc.*, vol. 115, pp. 8706–8715, 1993.
- [29] A. Eychmüller, A. Mews, and H. Weller, “A quantum dot quantum well: CdS/HgS/CdS,” *Chem. Phys. Lett.*, vol. 208, no. 1–2, pp. 59–62, Jun. 1993.
- [30] A. P. Alivisatos, “Semiconductor Clusters, Nanocrystals, and Quantum Dots,” *Science (80-.)*, vol. 271, no. 5251, pp. 933–937, Feb. 1996.
- [31] D. V Talapin, J.-S. Lee, M. V Kovalenko, and E. V Shevchenko, “Prospects of colloidal nanocrystals for electronic and optoelectronic applications,” *Chem.*

- Rev.*, vol. 110, no. 1, pp. 389–458, Jan. 2010.
- [32] M. Bruchez Jr., “Semiconductor Nanocrystals as Fluorescent Biological Labels,” *Science (80-.)*, vol. 281, no. 5385, pp. 2013–2016, Sep. 1998.
- [33] V. L. Colvin, M. C. Schlamp, and A. P. Alivisatos, “Light-emitting diodes made from cadmium selenide nanocrystals and a semiconducting polymer,” *Nature*, vol. 370, no. 6488, pp. 354–357, Aug. 1994.
- [34] M. A. Hines and P. Guyot-Sionnest, “Synthesis and Characterization of Strongly Luminescing ZnS-Capped CdSe Nanocrystals,” *J. Phys. Chem.*, vol. 100, no. 2, pp. 468–471, Jan. 1996.
- [35] B. O. Dabbousi, J. Rodriguez-Viejo, F. V. Mikulec, J. R. Heine, H. Mattoussi, R. Ober, K. F. Jensen, and M. G. Bawendi, “(CdSe)ZnS Core–Shell Quantum Dots: Synthesis and Characterization of a Size Series of Highly Luminescent Nanocrystallites,” *J. Phys. Chem. B*, vol. 101, no. 46, pp. 9463–9475, Nov. 1997.
- [36] X. Peng, M. C. Schlamp, A. V. Kadavanich, and A. P. Alivisatos, “Epitaxial Growth of Highly Luminescent CdSe/CdS Core/Shell Nanocrystals with Photostability and Electronic Accessibility,” *J. Am. Chem. Soc.*, vol. 119, no. 30, pp. 7019–7029, Jul. 1997.
- [37] D. V. Talapin, I. Mekis, S. Götzinger, A. Kornowski, O. Benson, and H. Weller, “CdSe/CdS/ZnS and CdSe/ZnSe/ZnS Core–Shell–Shell Nanocrystals,” *J. Phys. Chem. B*, vol. 108, no. 49, pp. 18826–18831, Dec. 2004.
- [38] X. Peng, L. Manna, W. Yang, J. J. Wickham, E. Scher, A. Kadavanich, and A. P. Alivisatos, “Shape control of CdSe nanocrystals,” *Nature*, vol. 404, no. 6773, pp. 59–61, Mar. 2000.
- [39] L. Manna, E. C. Scher, and a. P. Alivisatos, “Synthesis of Soluble and Processable Rod-, Arrow-, Teardrop-, and Tetrapod-Shaped CdSe Nanocrystals,” *J. Am. Chem. Soc.*, vol. 122, no. 51, pp. 12700–12706, Dec. 2000.
- [40] W. C. Chan, “Quantum Dot Bioconjugates for Ultrasensitive Nonisotopic Detection,” *Science (80-.)*, vol. 281, no. 5385, pp. 2016–2018, Sep. 1998.
- [41] M. C. Schlamp, X. Peng, and A. P. Alivisatos, “Improved efficiencies in light emitting diodes made with CdSe(CdS) core/shell type nanocrystals and a

- semiconducting polymer,” *J. Appl. Phys.*, vol. 82, no. 11, p. 5837, Dec. 1997.
- [42] M. Kazes, D. Y. D. Y. Lewis, Y. Ebenstein, T. Mokari, and U. Banin, “Lasing from Semiconductor Quantum Rods in a Cylindrical Microcavity,” *Adv. Mater.*, vol. 14, no. 4, pp. 317–321, Feb. 2002.
- [43] F. García-Santamaría, Y. Chen, J. Vela, R. D. Schaller, J. a Hollingsworth, and V. I. Klimov, “Suppressed Auger recombination in ‘giant’ nanocrystals boosts optical gain performance,” *Nano Lett.*, vol. 9, no. 10, pp. 3482–3488, 2009.
- [44] M. Zavelani-Rossi, M. G. Lupo, F. Tassone, L. Manna, and G. Lanzani, “Suppression of biexciton auger recombination in CdSe/CdS dot/rods: role of the electronic structure in the carrier dynamics,” *Nano Lett.*, vol. 10, no. 8, pp. 3142–3150, Aug. 2010.
- [45] S. C. Erwin, L. Zu, M. I. Haftel, A. L. Efros, T. A. Kennedy, and D. J. Norris, “Doping semiconductor nanocrystals,” *Nature*, vol. 436, no. 7047, pp. 91–4, Jul. 2005.
- [46] R. E. Bailey and S. Nie, “Alloyed semiconductor quantum dots: tuning the optical properties without changing the particle size,” *J. Am. Chem. Soc.*, vol. 125, no. 23, pp. 7100–6, Jun. 2003.
- [47] W. K. Bae, K. Char, H. Hur, and S. Lee, “Single-Step Synthesis of Quantum Dots with Chemical Composition Gradients,” *Chem. Mater.*, vol. 20, no. 2, pp. 531–539, Jan. 2008.
- [48] W. K. Bae, Y.-S. Park, J. Lim, D. Lee, L. a Padilha, H. McDaniel, I. Robel, C. Lee, J. M. Pietryga, and V. I. Klimov, “Controlling the influence of Auger recombination on the performance of quantum-dot light-emitting diodes,” *Nat. Commun.*, vol. 4, p. 2661, Jan. 2013.
- [49] M. V Kovalenko, M. Scheele, and D. V Talapin, “Colloidal nanocrystals with molecular metal chalcogenide surface ligands,” *Science*, vol. 324, no. 5933, pp. 1417–20, Jun. 2009.
- [50] H. Zhang, J. Jang, W. Liu, and D. V Talapin, “Colloidal nanocrystals with inorganic halide, pseudohalide, and halometallate ligands,” *ACS Nano*, vol. 8, no. 7, pp. 7359–69, Jul. 2014.
- [51] D. K. Kim, Y. Lai, B. T. Diroll, C. B. Murray, and C. R. Kagan, “Flexible and low-voltage integrated circuits constructed from high-performance nanocrystal

- transistors,” *Nat. Commun.*, vol. 3, p. 1216, Jan. 2012.
- [52] D. H. Son, S. M. Hughes, Y. Yin, and A. Paul Alivisatos, “Cation exchange reactions in ionic nanocrystals,” *Science*, vol. 306, no. 5698, pp. 1009–12, Nov. 2004.
- [53] S. Ithurria and D. V Talapin, “Colloidal atomic layer deposition (c-ALD) using self-limiting reactions at nanocrystal surface coupled to phase transfer between polar and nonpolar media,” *J. Am. Chem. Soc.*, vol. 134, no. 45, pp. 18585–90, Nov. 2012.
- [54] D. V. Talapin and J. Steckel, “Quantum dot light-emitting devices,” *MRS Bull.*, vol. 38, no. 09, pp. 685–691, Sep. 2013.
- [55] A. Nurmikko, “What future for quantum dot-based light emitters?,” *Nat. Nanotechnol.*, vol. 10, no. 12, pp. 1001–4, Dec. 2015.
- [56] S. Ithurria and B. Dubertret, “Quasi 2D Colloidal CdSe Platelets with Thicknesses Controlled at the Atomic Level,” *J. Am. Chem. Soc.*, vol. 130, no. 49, pp. 16504–16505, Dec. 2008.
- [57] S. Ithurria, M. D. Tessier, B. Mahler, R. P. S. M. Lobo, B. Dubertret, and A. L. Efros, “Colloidal nanoplatelets with two-dimensional electronic structure,” *Nat. Mater.*, vol. 10, no. 12, pp. 936–41, Dec. 2011.
- [58] M. D. Tessier, C. Javaux, I. Maksimovic, V. Lorientte, and B. Dubertret, “Spectroscopy of Single CdSe Nanoplatelets,” *ACS Nano*, vol. 6, no. 8, pp. 6751–6758, Aug. 2012.
- [59] C. She, I. Fedin, D. S. Dolzhenkov, A. Demortière, R. D. Schaller, M. Pelton, D. V Talapin, and D. Richard, “Low-threshold stimulated emission using colloidal quantum wells,” *Nano Lett.*, vol. 14, no. 5, pp. 2772–7, May 2014.
- [60] D. A. B. Miller, *Quantum Mechanics for Scientists and Engineers*. Cambridge University Press, 2008.
- [61] M. D. Tessier, B. Mahler, B. Nadal, H. Heuclin, S. Pedetti, and B. Dubertret, “Spectroscopy of colloidal semiconductor core/shell nanoplatelets with high quantum yield,” *Nano Lett.*, vol. 13, no. 7, pp. 3321–8, Jul. 2013.
- [62] L. T. Kunneman, J. M. Schins, S. Pedetti, H. Heuclin, F. C. Grozema, A. J. Houtepen, B. Dubertret, and L. D. A. Siebbeles, “Nature and decay pathways of photoexcited states in CdSe and CdSe/CdS nanoplatelets,” *Nano Lett.*, p.

doi:10.1021/nl503406a, Nov. 2014.

- [63] M. D. Tessier, L. Biadala, C. Bouet, S. Ithurria, B. Abecassis, and B. Dubertret, “Phonon line emission revealed by self-assembly of colloidal nanoplatelets,” *ACS Nano*, vol. 7, no. 4, pp. 3332–40, Apr. 2013.
- [64] E. Baghani, S. K. O. Leary, I. Fedin, D. V Talapin, and M. Pelton, “Auger-Limited Carrier Recombination and Relaxation in CdSe Colloidal Quantum Wells,” 2015.
- [65] M. Pelton, S. Ithurria, R. D. Schaller, D. S. Dolzhenkov, and D. V Talapin, “Carrier cooling in colloidal quantum wells,” *Nano Lett.*, vol. 12, no. 12, pp. 6158–63, Dec. 2012.
- [66] M. Olutas, B. Guzelturk, Y. Kelestemur, A. Yeltik, S. Delikanli, and H. V. Demir, “Lateral Size-Dependent Spontaneous and Stimulated Emission Properties in Colloidal CdSe Nanoplatelets,” *ACS Nano*, vol. 9, no. 5, pp. 5041–5050, May 2015.
- [67] A. Yeltik, S. Delikanli, M. Olutas, Y. Kelestemur, B. Guzelturk, and H. V. Demir, “Experimental Determination of the Absorption Cross-Section and Molar Extinction Coefficient of Colloidal CdSe Nanoplatelets,” *J. Phys. Chem. C*, vol. 119, no. 47, pp. 26768–26775, Nov. 2015.
- [68] B. Guzelturk, M. Olutas, S. Delikanli, Y. Kelestemur, O. Erdem, and H. V. Demir, “Nonradiative Energy Transfer in Colloidal CdSe Nanoplatelet Films,” *Nanoscale*, vol. 7, no. 6, pp. 2545–2551, 2015.
- [69] A. Naeem, F. Masia, S. Christodoulou, I. Moreels, P. Borri, and W. Langbein, “Evidence of giant oscillator strength in the exciton dephasing of CdSe nanoplatelets measured by resonant four-wave mixing,” *Arxiv*, p. arXiv:1403.7798, Mar. 2014.
- [70] K. Wu, Q. Li, Y. Du, Z. Chen, and T. Lian, “Ultrafast exciton quenching by energy and electron transfer in colloidal CdSe nanosheet–Pt heterostructures,” *Chem. Sci.*, vol. 6, no. 2, pp. 1049–1054, Jan. 2015.
- [71] A. W. Achtstein, A. V Prudnikau, M. V Ermolenko, L. I. Gurinovich, S. V Gaponenko, U. Woggon, A. V Baranov, M. Y. Leonov, I. D. Rukhlenko, A. V Federov, and M. V Artemyev, “Electroabsorption by 0D, 1D, and 2D Nanocrystals: A Comparative Study of CdSe Colloidal Quantum Dots,

- Nanorods and Nanoplatelets,” *ACS Nano*, no. 8, pp. 7678–7686, 2014.
- [72] R. Benchamekh, N. a. Gippius, J. Even, M. O. Nestoklon, J.-M. Jancu, S. Ithurria, B. Dubertret, A. L. Efros, and P. Voisin, “Tight-binding calculations of image-charge effects in colloidal nanoscale platelets of CdSe,” *Phys. Rev. B*, vol. 89, no. 3, p. 035307, Jan. 2014.
- [73] T. Cheiwchanchamnangij and W. R. L. Lambrecht, “Quasiparticle band structure calculation of monolayer, bilayer, and bulk MoS₂,” *Phys. Rev. B*, vol. 85, no. 20, p. 205302, May 2012.
- [74] J. Feldmann, G. Peter, and E. O. Gobel, “Linewidth Dependence of Radiative Exciton Lifetimes in Quantum Wells,” *Phys. Rev. Lett.*, vol. 59, no. 20, pp. 2337–2340, 1987.
- [75] J. Q. Grim, S. Christodoulou, F. Di Stasio, R. Krahne, R. Cingolani, L. Manna, and I. Moreels, “Continuous-wave biexciton lasing at room temperature using solution-processed quantum wells,” *Nat. Nanotechnol.*, vol. 9, no. 11, pp. 891–5, Nov. 2014.
- [76] C. She, I. Fedin, D. S. Dolzhenkov, P. D. Dahlberg, G. S. Engel, R. D. Schaller, and D. V. Talapin, “Red, Yellow, Green, and Blue Amplified Spontaneous Emission and Lasing Using Colloidal CdSe Nanoplatelets,” *ACS Nano*, no. Xx, p. 150909085400003, Sep. 2015.
- [77] M. D. Tessier, P. Spinicelli, D. Dupont, G. Patriarche, S. Ithurria, and B. Dubertret, “Efficient exciton concentrators built from colloidal core/crown CdSe/CdS semiconductor nanoplatelets,” *Nano Lett.*, vol. 14, no. 1, pp. 207–13, Jan. 2014.
- [78] A. Prudnikau, A. Chuvilin, and M. Artemyev, “CdSe-CdS nanoheteroplatelets with efficient photoexcitation of central CdSe region through epitaxially grown CdS wings,” *J. Am. Chem. Soc.*, vol. 135, no. 39, pp. 14476–9, Oct. 2013.
- [79] B. Mahler, B. Nadal, C. Bouet, G. Patriarche, and B. Dubertret, “Core/shell colloidal semiconductor nanoplatelets,” *J. Am. Chem. Soc.*, vol. 134, no. 45, pp. 18591–8, Nov. 2012.
- [80] Y. Kelestemur, B. Guzel Turk, O. Erdem, M. Olutas, K. Gungor, and H. V. Demir, “Platelet-in-Box Colloidal Quantum Wells: CdSe/CdS@CdS Core/Crown@Shell Heteronoplatelets,” *Adv. Funct. Mater.*, Apr. 2016.

- [81] S. Pedetti, S. Ithurria, H. Heuclin, G. Patriarche, and B. Dubertret, “Type-II Core/Crown CdSe/CdTe Semiconductor Nanoplatelets,” *J. Am. Chem. Soc.*, vol. 136, no. 46, pp. 16430–16438, 2014.
- [82] Y. Kelestemur, M. Olutas, S. Delikanli, B. Guzelturk, M. Z. Akgul, and H. V. Demir, “Type-II Colloidal Quantum Wells: CdSe/CdTe Core/Crown Heteronanoplatelets,” *J. Phys. Chem. C*, vol. 119, pp. 2177–2185, 2015.
- [83] Z. Chen, B. Nadal, B. Mahler, H. Aubin, and B. Dubertret, “Quasi-2D Colloidal Semiconductor Nanoplatelets for Narrow Electroluminescence,” *Adv. Funct. Mater.*, vol. 24, no. 3, pp. 295–302, Jan. 2014.
- [84] F. Fan, P. Kanjanaboos, M. Saravanapavanantham, E. Beauregard, G. Ingram, E. Yassitepe, M. M. Adachi, O. Voznyy, A. K. Johnston, G. Walters, G.-H. Kim, Z.-H. Lu, and E. H. Sargent, “Colloidal CdSe(1-x)S(x) Nanoplatelets with Narrow and Continuously-Tunable Electroluminescence,” *Nano Lett.*, vol. 15, no. 7, pp. 4611–5, Jul. 2015.
- [85] E. Lhuillier, J.-F. Dayen, D. O. Thomas, A. Robin, B. Doudin, and B. Dubertret, “Nanoplatelets bridging a nanotrench: a new architecture for photodetectors with increased sensitivity,” *Nano Lett.*, vol. 15, no. 3, pp. 1736–42, Mar. 2015.
- [86] F. Federspiel, G. Froehlicher, M. Nasilowski, S. Pedetti, A. Mahmood, B. Doudin, S. Park, J.-O. Lee, D. Halley, B. Dubertret, P. Gilliot, and S. Berciaud, “Distance Dependence of the Energy Transfer Rate from a Single Semiconductor Nanostructure to Graphene,” *Nano Lett.*, vol. 15, pp. 1252–1258, 2015.
- [87] C. E. Rowland, I. Fedin, H. Zhang, S. K. Gray, A. O. Govorov, D. V. Talapin, and R. D. Schaller, “Picosecond energy transfer and multiexciton transfer outpaces Auger recombination in binary CdSe nanoplatelet solids,” *Nat. Mater.*, vol. 14, pp. 484–489, 2015.
- [88] N. W. Ashcroft and N. D. Mermin, *Solid State Physics*. 1976.
- [89] V. I. Klimov, *Nanocrystal Quantum Dots, Second Edition*. CRC Press, 2010.
- [90] D. J. Norris, A. L. Efros, M. Rosen, and M. G. Bawendi, “Size dependence of exciton fine structure in CdSe quantum dots,” *Phys. Rev. B*, vol. 53, no. 24, pp. 16347–16354, Jun. 1996.

- [91] M. Nirmal, D. Norris, M. Kuno, M. Bawendi, A. Efros, and M. Rosen, "Observation of the 'Dark exciton' in CdSe quantum dots," *Phys. Rev. Lett.*, vol. 75, no. 20, pp. 3728–3731, Nov. 1995.
- [92] A. L. Rogach, *Semiconductor Nanocrystal Quantum Dots: Synthesis, Assembly, Spectroscopy and Applications*. Springer, 2008.
- [93] J. Cui, A. P. Beyler, I. Coropceanu, L. Cleary, T. R. Avila, Y. Chen, J. M. Cordero, S. L. Heathcote, D. K. Harris, O. Chen, J. Cao, and M. G. Bawendi, "Evolution of the Single-Nanocrystal Photoluminescence Linewidth with Size and Shell: Implications for Exciton-Phonon Coupling and the Optimization of Spectral Linewidths," *Nano Lett.*, vol. 16, no. 1, pp. 289–96, Jan. 2016.
- [94] E. Collini and G. D. Scholes, "Coherent intrachain energy migration in a conjugated polymer at room temperature," *Science*, vol. 323, no. 5912, pp. 369–73, Jan. 2009.
- [95] D. Beljonne, G. Pourtois, C. Silva, E. Hennebicq, L. M. Herz, R. H. Friend, G. D. Scholes, S. Setayesh, K. Mullen, and J. L. Bredas, "Interchain vs. intrachain energy transfer in acceptor-capped conjugated polymers," *Proc. Natl. Acad. Sci. U. S. A.*, vol. 99, no. 17, pp. 10982–7, Aug. 2002.
- [96] J.-L. Brédas, D. Beljonne, V. Coropceanu, and J. Cornil, "Charge-transfer and energy-transfer processes in pi-conjugated oligomers and polymers: a molecular picture," *Chem. Rev.*, vol. 104, no. 11, pp. 4971–5004, Nov. 2004.
- [97] C. Kagan, C. Murray, M. Nirmal, and M. Bawendi, "Electronic Energy Transfer in CdSe Quantum Dot Solids," *Phys. Rev. Lett.*, vol. 76, no. 9, pp. 1517–1520, Feb. 1996.
- [98] S. Crooker, J. Hollingsworth, S. Tretiak, and V. Klimov, "Spectrally Resolved Dynamics of Energy Transfer in Quantum-Dot Assemblies: Towards Engineered Energy Flows in Artificial Materials," *Phys. Rev. Lett.*, vol. 89, no. 18, p. 186802, Oct. 2002.
- [99] S. Günes, H. Neugebauer, and N. S. Sariciftci, "Conjugated polymer-based organic solar cells," *Chem. Rev.*, vol. 107, no. 4, pp. 1324–38, Apr. 2007.
- [100] G. Xing, N. Mathews, S. Sun, S. S. Lim, Y. M. Lam, M. Grätzel, S. Mhaisalkar, and T. C. Sum, "Long-range balanced electron- and hole-transport lengths in organic-inorganic CH₃NH₃PbI₃," *Science*, vol. 342, no. 6156, pp. 344–7, Oct.

2013.

- [101] T. Förster, “Zwischenmolekulare Energiewanderung und Fluoreszenz,” *Ann. Phys.*, vol. 437, no. 1–2, pp. 55–75, 1948.
- [102] D. L. Dexter, “A Theory of Sensitized Luminescence in Solids,” *J. Chem. Phys.*, vol. 21, no. 5, p. 836, Dec. 1953.
- [103] J. R. Lakowicz, *Principles of Fluorescence Spectroscopy*, vol. 13, no. 2. Boston, MA: Springer US, 2006.
- [104] V. M. Agranovich, Y. N. Gartstein, and M. Litinskaya, “Hybrid resonant organic-inorganic nanostructures for optoelectronic applications,” *Chem. Rev.*, vol. 111, no. 9, pp. 5179–214, Sep. 2011.
- [105] T. W. J. Gadella, *FRET and FLIM Techniques*, vol. 33. Elsevier, 2009.
- [106] L. Stryer and R. P. Haugland, “Energy transfer: a spectroscopic ruler,” *Proc. Natl. Acad. Sci. U. S. A.*, vol. 58, no. 2, pp. 719–26, Aug. 1967.
- [107] P. L. Hernández-Martínez, A. O. Govorov, and H. V. Demir, “Förster-Type Nonradiative Energy Transfer for Assemblies of Arrayed Nanostructures: Confinement Dimension vs Stacking Dimension,” *J. Phys. Chem. C*, vol. 118, no. 9, pp. 4951–4958, Mar. 2014.
- [108] S. Nizamoglu, B. Guzelturk, D.-W. Jeon, I.-H. Lee, and H. V. Demir, “Efficient nonradiative energy transfer from InGaN/GaN nanopillars to CdSe/ZnS core/shell nanocrystals,” *Appl. Phys. Lett.*, vol. 98, no. 16, p. 163108, Apr. 2011.
- [109] B. Guzelturk, P. L. Hernandez Martinez, V. K. Sharma, Y. Coskun, V. Ibrahimova, D. Tuncel, A. O. Govorov, X. W. Sun, Q. Xiong, H. V. Demir, and P. L. Hernandez-Martinez, “Study of Exciton Transfer in Dense Quantum Dot Nanocomposites,” *Nanoscale*, vol. 6, no. 19, pp. 11387–94, Jul. 2014.
- [110] M. Olutas, B. Guzelturk, Y. Kelestemur, K. Gungor, and H. V. Demir, “Highly Efficient Nonradiative Energy Transfer from Colloidal Semiconductor Quantum Dots to Wells for Sensitive Noncontact Temperature Probing,” *Adv. Funct. Mater.*, vol. 26, no. 17, pp. 2891–2899, May 2016.
- [111] A. Köhler and H. Bässler, “Triplet states in organic semiconductors,” *Mater. Sci. Eng. R Reports*, vol. 66, no. 4–6, pp. 71–109, Nov. 2009.
- [112] N. S. Sariciftci, L. Smilowitz, A. J. Heeger, and F. Wudl, “Photoinduced

- electron transfer from a conducting polymer to buckminsterfullerene,” *Science*, vol. 258, no. 5087, pp. 1474–6, Nov. 1992.
- [113] J.-L. Bredas and R. Silbey, “CHEMISTRY: Excitons Surf Along Conjugated Polymer Chains,” *Science (80-.)*, vol. 323, no. 5912, pp. 348–349, Jan. 2009.
- [114] L. Novotny and B. Hecht, *Principles of Nano-Optics*. Cambridge University Press, 2012.
- [115] M. C. Beard, K. P. Knutsen, P. Yu, J. M. Luther, Q. Song, W. K. Metzger, R. J. Ellingson, and A. J. Nozik, “Multiple exciton generation in colloidal silicon nanocrystals,” *Nano Lett.*, vol. 7, no. 8, pp. 2506–12, Aug. 2007.
- [116] M. Kazes, D. Oron, I. Shweky, and U. Banin, “Temperature Dependence of Optical Gain in CdSe/ZnS Quantum Rods,” *J. Phys. Chem. C*, vol. 111, no. 22, pp. 7898–7905, Jun. 2007.
- [117] E. a. Dias, J. I. Saari, P. Tyagi, and P. Kambhampati, “Improving Optical Gain Performance in Semiconductor Quantum Dots via Coupled Quantum Shells,” *J. Phys. Chem. C*, vol. 116, no. 9, pp. 5407–5413, 2012.
- [118] M. Asada, Y. Miyamoto, and Y. Suematsu, “Gain and the threshold of three-dimensional quantum-box lasers,” *IEEE J. Quantum Electron.*, vol. 22, no. 9, pp. 1915–1921, Sep. 1986.
- [119] V. I. Klimov, “Quantization of Multiparticle Auger Rates in Semiconductor Quantum Dots,” *Science (80-.)*, vol. 287, no. 5455, pp. 1011–1013, Feb. 2000.
- [120] I. Robel, R. Gresback, U. Kortshagen, R. Schaller, and V. Klimov, “Universal Size-Dependent Trend in Auger Recombination in Direct-Gap and Indirect-Gap Semiconductor Nanocrystals,” *Phys. Rev. Lett.*, vol. 102, no. 17, p. 177404, May 2009.
- [121] P. Kambhampati, “Hot Exciton Relaxation Dynamics in Semiconductor Quantum Dots: Radiationless Transitions on the Nanoscale,” *J. Phys. Chem. C*, vol. 115, no. 45, pp. 22089–22109, Nov. 2011.
- [122] A. J. Cross and G. R. Fleming, “Analysis of time-resolved fluorescence anisotropy decays,” *Biophys. J.*, vol. 46, no. 1, pp. 45–56, Jul. 1984.
- [123] F. Wang, G. Dukovic, L. E. Brus, and T. F. Heinz, “Time-resolved fluorescence of carbon nanotubes and its implication for radiative lifetimes,” *Phys. Rev. Lett.*, vol. 92, no. 17, p. 177401, Apr. 2004.

- [124] K. L. Shaklee, R. E. Nahory, and R. F. Leheny, "Optical gain in semiconductors," *J. Lumin.*, vol. 7, no. C, pp. 284–309, 1973.
- [125] A. J. Hoff and J. Deisenhofer, "Photophysics of photosynthesis. Structure and spectroscopy of reaction centers of purple bacteria," *Phys. Rep.*, vol. 287, no. 1–2, pp. 1–247, Aug. 1997.
- [126] B. Guzelturk, P. L. H. Martinez, Q. Zhang, Q. Xiong, H. Sun, X. W. Sun, A. O. Govorov, and H. V. Demir, "Excitonics of semiconductor quantum dots and wires for lighting and displays," *Laser Photon. Rev.*, vol. 8, no. 1, pp. 73–93, Jan. 2014.
- [127] A. L. Rogach, T. A. Klar, J. M. Lupton, A. Meijerink, and J. Feldmann, "Energy transfer with semiconductor nanocrystals," *J. Mater. Chem.*, vol. 19, no. 9, p. 1208, Feb. 2009.
- [128] A. Yeltik, B. Guzelturk, P. L. Hernandez-Martinez, A. O. Govorov, and H. V. Demir, "Phonon-assisted exciton transfer into silicon using nanoemitters: the role of phonons and temperature effects in Förster resonance energy transfer.," *ACS Nano*, vol. 7, no. 12, pp. 10492–501, Dec. 2013.
- [129] B. Guzelturk, E. Mutlugun, X. Wang, K. L. Pey, and H. V. Demir, "Photovoltaic nanopillar radial junction diode architecture enhanced by integrating semiconductor quantum dot nanocrystals as light harvesters," *Appl. Phys. Lett.*, vol. 97, no. 9, p. 093111, Sep. 2010.
- [130] S. Lu, Z. Lingley, T. Asano, D. Harris, T. Barwicz, S. Guha, and A. Madhukar, "Photocurrent induced by nonradiative energy transfer from nanocrystal quantum dots to adjacent silicon nanowire conducting channels: toward a new solar cell paradigm.," *Nano Lett.*, vol. 9, no. 12, pp. 4548–52, Dec. 2009.
- [131] A. Yeltik, G. Kucukayan-Dogu, B. Guzelturk, S. Fardindoost, Y. Kelestemur, and H. V. Demir, "Evidence for nonradiative energy transfer in graphene-oxide-based hybrid structures," *J. Phys. Chem. C*, vol. 117, pp. 25298–25304, 2013.
- [132] G. Konstantatos, M. Badioli, L. Gaudreau, J. Osmond, M. Bernechea, F. P. Garcia de Arquer, F. Gatti, and F. H. L. Koppens, "Hybrid graphene-quantum dot phototransistors with ultrahigh gain," *Nat. Nanotechnol.*, vol. 7, no. 6, pp. 363–8, Jun. 2012.
- [133] M. Achermann, M. A. Petruska, S. Kos, D. L. Smith, D. D. Koleske, and V. I.

- Klimov, “Energy-transfer pumping of semiconductor nanocrystals using an epitaxial quantum well,” *Nature*, vol. 429, no. 6992, pp. 642–6, Jun. 2004.
- [134] V. Bulovi, V. Bulovic, V. G. Kozlov, V. B. Khalfin, and S. R. Forrest, “Transform-Limited, Narrow-Linewidth Lasing Action in Organic Semiconductor Microcavities,” *Science (80-.)*, vol. 279, no. January, pp. 553–555, 1998.
- [135] G. M. Akselrod, P. B. Deotare, N. J. Thompson, J. Lee, W. A. Tisdale, M. A. Baldo, V. M. Menon, and V. Bulović, “Visualization of exciton transport in ordered and disordered molecular solids,” *Nat. Commun.*, vol. 5, p. 3646, Jan. 2014.
- [136] B. Abécassis, M. D. Tessier, P. Davidson, and B. Dubertret, “Self-assembly of CdSe nanoplatelets into giant micrometer-scale needles emitting polarized light,” *Nano Lett.*, vol. 14, no. 2, pp. 710–5, Feb. 2014.
- [137] A. W. Achtstein, A. Schliwa, A. Prudnikau, M. Hardzei, M. V Artemyev, C. Thomsen, and U. Woggon, “Electronic structure and exciton-phonon interaction in two-dimensional colloidal CdSe nanosheets,” *Nano Lett.*, vol. 12, no. 6, pp. 3151–7, Jun. 2012.
- [138] M. D. M. D. Tessier, C. Javaux, I. Maksimovic, V. Lorientte, B. Dubertret, L. T. Kunneman, H. Heuclin, Y. V. Aulin, F. C. Grozema, J. M. Schins, and L. D. A. Siebbeles, “Spectroscopy of single CdSe nanoplatelets,” *J. Phys. Chem. Lett.*, vol. 4, no. 21, pp. 3574–3578, Nov. 2013.
- [139] P. Anikeeva, C. Madigan, J. Halpert, M. Bawendi, and V. Bulović, “Electronic and excitonic processes in light-emitting devices based on organic materials and colloidal quantum dots,” *Phys. Rev. B*, vol. 78, no. 8, p. 085434, Aug. 2008.
- [140] B. N. Pal, Y. Ghosh, S. Brovelli, R. Laocharoensuk, V. I. Klimov, J. A. Hollingsworth, and H. Htoon, “‘Giant’ CdSe/CdS core/shell nanocrystal quantum dots as efficient electroluminescent materials: strong influence of shell thickness on light-emitting diode performance,” *Nano Lett.*, vol. 12, no. 1, pp. 331–6, Jan. 2012.
- [141] C. Kagan, C. Murray, and M. Bawendi, “Long-range resonance transfer of electronic excitations in close-packed CdSe quantum-dot solids,” *Phys. Rev. B*, vol. 54, no. 12, pp. 8633–8643, Sep. 1996.

- [142] S. M. Thon, A. H. Ip, O. Voznyy, L. Levina, K. W. Kemp, G. H. Carey, S. Masala, and E. H. Sargent, "Role of bond adaptability in the passivation of colloidal quantum dot solids.," *ACS Nano*, vol. 7, no. 9, pp. 7680–8, Sep. 2013.
- [143] D. A. Hines and P. V. Kamat, "Quantum Dot Surface Chemistry: Ligand Effects and Electron Transfer Reactions," *J. Phys. Chem. C*, vol. 117, no. 27, pp. 14418–14426, Jul. 2013.
- [144] T. Stoferle, U. Scherf, and R. F. Mahrt, "Energy Transfer in Hybrid Organic/Inorganic Nanocomposites," *Nano Lett.*, vol. 9, no. 1, pp. 453–456, Jan. 2009.
- [145] N. Greenham, X. Peng, and A. Alivisatos, "Charge separation and transport in conjugated-polymer/semiconductor-nanocrystal composites studied by photoluminescence quenching and photoconductivity," *Phys. Rev. B*, vol. 54, no. 24, pp. 17628–17637, Dec. 1996.
- [146] D. R. Lutz, K. A. Nelson, C. R. Gochanour, and M. D. Fayer, "Electronic excited state energy transfer, trapping by dimers and fluorescence quenching in concentrated dye solutions: Picosecond transient grating exp," *Chem. Phys.*, vol. 58, no. 3, pp. 325–334, Jan. 1981.
- [147] L. Kułak and C. Bojarski, "Forward and reverse electronic energy transport and trapping in solution. I. Theory," *Chem. Phys.*, vol. 191, no. 1–3, pp. 43–66, Feb. 1995.
- [148] R. F. Loring, H. C. Andersen, and M. D. Fayer, "Electronic excited state transport and trapping in solution," *J. Chem. Phys.*, vol. 76, no. 4, pp. 2015–2027, Feb. 1982.
- [149] S. M. Menke, W. A. Luhman, and R. J. Holmes, "Tailored exciton diffusion in organic photovoltaic cells for enhanced power conversion efficiency.," *Nat. Mater.*, vol. 12, no. 2, pp. 152–7, Feb. 2013.
- [150] C. Galland, Y. Ghosh, A. Steinbrück, M. Sykora, J. A. Hollingsworth, V. I. Klimov, and H. Htoon, "Two types of luminescence blinking revealed by spectroelectrochemistry of single quantum dots," *Nature*, vol. 479, no. 7372, pp. 203–7, Nov. 2011.
- [151] S. Rosen, O. Schwartz, and D. Oron, "Transient Fluorescence of the Off State in Blinking CdSe/CdS/ZnS Semiconductor Nanocrystals Is Not Governed by

- Auger Recombination,” *Phys. Rev. Lett.*, vol. 104, no. 15, p. 157404, Apr. 2010.
- [152] P. Frantsuzov, M. Kuno, B. Jankó, and R. A. Marcus, “Universal emission intermittency in quantum dots, nanorods and nanowires,” *Nat. Phys.*, vol. 4, no. 5, pp. 519–522, Jul. 2008.
- [153] X. Brokmann, L. Coolen, M. Dahan, and J. Hermier, “Measurement of the Radiative and Nonradiative Decay Rates of Single CdSe Nanocrystals through a Controlled Modification of their Spontaneous Emission,” *Phys. Rev. Lett.*, vol. 93, no. 10, p. 107403, Sep. 2004.
- [154] F. Vietmeyer, T. Tchelidze, V. Tsou, B. Janko, and M. Kuno, “Electric field-induced emission enhancement and modulation in individual CdSe nanowires,” *ACS Nano*, vol. 6, no. 10, pp. 9133–40, Oct. 2012.
- [155] K. E. Knowles, E. A. McArthur, and E. A. Weiss, “A multi-timescale map of radiative and nonradiative decay pathways for excitons in CdSe quantum dots,” *ACS Nano*, vol. 5, no. 3, pp. 2026–35, Mar. 2011.
- [156] R. C. Powell and Z. G. Soos, “Singlet exciton energy transfer in organic solids,” *J. Lumin.*, vol. 11, no. 1–2, pp. 1–45, Sep. 1975.
- [157] C. Bouet, M. D. Tessier, S. Ithurria, B. Mahler, B. Nadal, and B. Dubertret, “Flat Colloidal Semiconductor Nanoplatelets,” *Chem. Mater.*, vol. 25, no. 8, pp. 1262–1271, Apr. 2013.
- [158] L. T. Kunneman, M. D. Tessier, H. Heuclin, B. Dubertret, Y. V. Aulin, F. C. Grozema, J. M. Schins, L. D. A. Siebbeles, D. Cdse, C. Cdzn, and C. Shell, “Bimolecular Auger Recombination of Electron–Hole Pairs in Two-Dimensional CdSe and CdSe/CdZnS Core/Shell Nanoplatelets,” *J. Phys. Chem. Lett.*, vol. 4, no. 21, pp. 3574–3578, Nov. 2013.
- [159] L. Biadala, F. Liu, M. D. Tessier, D. R. Yakovlev, B. Dubertret, and M. Bayer, “Recombination dynamics of band edge excitons in quasi-two-dimensional CdSe nanoplatelets,” *Nano Lett.*, vol. 14, no. 3, pp. 1134–9, Mar. 2014.
- [160] A. L. Rogach, “Fluorescence energy transfer in hybrid structures of semiconductor nanocrystals,” *Nano Today*, vol. 6, no. 4, pp. 355–365, Aug. 2011.
- [161] A. R. Clapp, I. L. Medintz, and H. Mattoussi, “Förster resonance energy transfer investigations using quantum-dot fluorophores,” *Chemphyschem*, vol.

- 7, no. 1, pp. 47–57, Jan. 2006.
- [162] M. He, F. Qiu, and Z. Lin, “Toward High-Performance Organic–Inorganic Hybrid Solar Cells: Bringing Conjugated Polymers and Inorganic Nanocrystals in Close Contact,” *J. Phys. Chem. Lett.*, vol. 4, no. 11, pp. 1788–1796, Jun. 2013.
- [163] P. Reiss, E. Couderc, J. De Girolamo, and A. Pron, “Conjugated polymers/semiconductor nanocrystals hybrid materials--preparation, electrical transport properties and applications.,” *Nanoscale*, vol. 3, no. 2, pp. 446–89, Mar. 2011.
- [164] M. Wright and A. Uddin, “Organic–inorganic hybrid solar cells: A comparative review,” *Sol. Energy Mater. Sol. Cells*, vol. 107, pp. 87–111, Dec. 2012.
- [165] J. Kwak, W. K. Bae, M. Zorn, H. Woo, H. Yoon, J. Lim, S. W. Kang, S. Weber, H.-J. H.-J. Butt, R. Zentel, S. Lee, K. Char, and C. Lee, “Characterization of quantum dot/conducting polymer hybrid films and their application to light-emitting diodes.,” *Adv. Mater.*, vol. 21, no. 48, pp. 5022–6, Dec. 2009.
- [166] M. Zorn, W. K. Bae, J. Kwak, H. Lee, C. Lee, R. Zentel, and K. Char, “Quantum dot-block copolymer hybrids with improved properties and their application to quantum dot light-emitting devices.,” *ACS Nano*, vol. 3, no. 5, pp. 1063–8, May 2009.
- [167] P. T. K. Chin, R. A. M. Hikmet, and R. A. J. Janssen, “Energy transfer in hybrid quantum dot light-emitting diodes,” *J. Appl. Phys.*, vol. 104, no. 1, p. 013108, Jul. 2008.
- [168] E. Holder, N. Tessler, and A. L. Rogach, “Hybrid nanocomposite materials with organic and inorganic components for opto-electronic devices,” *J. Mater. Chem.*, vol. 18, no. 10, p. 1064, Feb. 2008.
- [169] R. Zhou, R. Stalder, D. Xie, W. Cao, Y. Zheng, Y. Yang, M. Plaisant, P. H. Holloway, K. S. Schanze, J. R. Reynolds, and J. Xue, “Enhancing the Efficiency of Solution-Processed Polymer:Colloidal Nanocrystal Hybrid Photovoltaic Cells Using Ethanedithiol Treatment,” *ACS Nano*, vol. 7, no. 6, pp. 4846–4854, Jun. 2013.
- [170] Z. Liu, Y. Sun, J. Yuan, H. Wei, X. Huang, L. Han, W. Wang, H. Wang, and

- W. Ma, "High-efficiency hybrid solar cells based on polymer/PbSx Se_{1-x} nanocrystals benefiting from vertical phase segregation.," *Adv. Mater.*, vol. 25, no. 40, pp. 5772–8, Oct. 2013.
- [171] M. C. Scharber, D. Mühlbacher, M. Koppe, P. Denk, C. Waldauf, A. J. Heeger, and C. J. Brabec, "Design Rules for Donors in Bulk-Heterojunction Solar Cells—Towards 10 % Energy-Conversion Efficiency," *Adv. Mater.*, vol. 18, no. 6, pp. 789–794, Mar. 2006.
- [172] M. J. Greaney and R. L. Brutchey, "Ligand engineering in hybrid polymer:nanocrystal solar cells," *Mater. Today*, vol. 18, no. 1, pp. 31–38, Jan. 2015.
- [173] E. Martínez-Ferrero, J. Albero, and E. Palomares, "Materials, Nanomorphology, and Interfacial Charge Transfer Reactions in Quantum Dot/Polymer Solar Cell Devices," *J. Phys. Chem. Lett.*, vol. 1, no. 20, pp. 3039–3045, Oct. 2010.
- [174] J. Tang, K. W. Kemp, S. Hoogland, K. S. Jeong, H. Liu, L. Levina, M. Furukawa, X. Wang, R. Debnath, D. Cha, K. W. Chou, A. Fischer, A. Amassian, J. B. Asbury, and E. H. Sargent, "Colloidal-quantum-dot photovoltaics using atomic-ligand passivation," *Nat. Mater.*, vol. 10, no. 10, pp. 765–71, Oct. 2011.
- [175] N. Tomczak, D. Jańczewski, M. Han, and G. J. Vancso, "Designer polymer–quantum dot architectures," *Prog. Polym. Sci.*, vol. 34, no. 5, pp. 393–430, May 2009.
- [176] M. Soreni-Harari, N. Yaacobi-Gross, D. Steiner, A. Aharoni, U. Banin, O. Millo, and N. Tessler, "Tuning Energetic Levels in Nanocrystal Quantum Dots through Surface Manipulations," *Nano Lett.*, vol. 8, no. 2, pp. 678–684, Feb. 2008.
- [177] A. M. Munro, B. Zacher, A. Graham, and N. R. Armstrong, "Photoemission spectroscopy of tethered CdSe nanocrystals: shifts in ionization potential and local vacuum level as a function of nanocrystal capping ligand.," *ACS Appl. Mater. Interfaces*, vol. 2, no. 3, pp. 863–9, Mar. 2010.
- [178] F. Mathias, A. Fokina, K. Landfester, W. Tremel, F. Schmid, K. Char, and R. Zentel, "Morphology control in biphasic hybrid systems of semiconducting

- materials.," *Macromol. Rapid Commun.*, vol. 36, no. 11, pp. 959–83, Jun. 2015.
- [179] A. M. Munro, I. Jen-LaPlante, M. S. Ng, and D. S. Ginger, "Quantitative Study of the Effects of Surface Ligand Concentration on CdSe Nanocrystal Photoluminescence," *J. Phys. Chem. C*, vol. 111, no. 17, pp. 6220–6227, May 2007.
- [180] K. E. Knowles, D. B. Tice, E. A. McArthur, G. C. Solomon, and E. A. Weiss, "Chemical Control of the Photoluminescence of CdSe Quantum Dot–Organic Complexes with a Series of Para-Substituted Aniline Ligands," *J. Am. Chem. Soc.*, vol. 132, no. 3, pp. 1041–1050, Jan. 2010.
- [181] S. Ren, L.-Y. Chang, S.-K. Lim, J. Zhao, M. Smith, N. Zhao, V. Bulović, M. Bawendi, and S. Gradecak, "Inorganic-organic hybrid solar cell: bridging quantum dots to conjugated polymer nanowires.," *Nano Lett.*, vol. 11, no. 9, pp. 3998–4002, Sep. 2011.
- [182] E. Lhuillier, S. Pedetti, S. Ithurria, B. Nadal, H. Heuclin, and B. Dubertret, "Two-Dimensional Colloidal Metal Chalcogenides Semiconductors: Synthesis, Spectroscopy, and Applications.," *Acc. Chem. Res.*, vol. 48, no. 1, pp. 22–30, Jan. 2015.
- [183] E. Lhuillier, A. Robin, S. Ithurria, H. Aubin, and B. Dubertret, "Electrolyte-gated colloidal nanoplatelets-based phototransistor and its use for bicolor detection," *Nano Lett.*, vol. 14, pp. 2715–2719, 2014.
- [184] L. zur Borg, A. L. Domanski, R. Berger, and R. Zentel, "Photoinduced Charge Separation of Self-Organized Semiconducting Superstructures Composed of a Functional Polymer-TiO₂ Hybrid," *Macromol. Chem. Phys.*, vol. 214, no. 9, pp. 975–984, May 2013.
- [185] B. Guzelturk, F. Menk, K. Philipps, Y. Kelestemur, M. Olutas, R. Zentel, and H. V. Demir, "Colloidal Nanoplatelet/Conducting Polymer Hybrids: Excitonic and Material Properties," *J. Phys. Chem. C*, vol. 120, no. 6, pp. 3573–3582, Feb. 2016.
- [186] H. Sirringhaus, P. J. Brown, R. H. Friend, M. M. Nielsen, K. Bechgaard, B. M. W. Langeveld-Voss, A. J. H. Spiering, R. A. J. Janssen, E. W. Meijer, P. Herwig, and D. M. de Leeuw, "Two-dimensional charge transport in self-organized, high-mobility conjugated polymers," *Nature*, vol. 401, no. 6754, pp.

685–688, Oct. 1999.

- [187] T. Rajh, L. X. Chen, K. Lukas, T. Liu, M. C. Thurnauer, and D. M. Tiede, “Surface Restructuring of Nanoparticles: An Efficient Route for Ligand–Metal Oxide Crosstalk,” *J. Phys. Chem. B*, vol. 106, no. 41, pp. 10543–10552, Oct. 2002.
- [188] F. Mathias, M. N. Tahir, W. Tremel, and R. Zentel, “Functionalization of TiO₂ Nanoparticles with Semiconducting Polymers Containing a Photocleavable Anchor Group and Separation via Irradiation Afterward,” *Macromol. Chem. Phys.*, vol. 215, no. 7, pp. 604–613, Apr. 2014.
- [189] F. Menk, M. Mondeshki, D. Dudenko, S. Shin, D. Schollmeyer, O. Ceyhun, T.-L. Choi, and R. Zentel, “Reactivity Studies of Alkoxy-Substituted [2.2]Paracyclophane-1,9-dienes and Specific Coordination of the Monomer Repeating Unit during ROMP,” *Macromolecules*, vol. 48, no. 20, pp. 7435–7445, Oct. 2015.
- [190] B. Guzelturk, P. L. Hernandez Martinez, D. Zhao, X. W. Sun, and H. V. Demir, “Singlet and Triplet Exciton Harvesting in the Thin Films of Colloidal Quantum Dots Interfacing Phosphorescent Small Organic Molecules,” *J. Phys. Chem. C*, vol. 118, no. 45, pp. 25964–25969, Nov. 2014.
- [191] M. H. van der Veen, B. de Boer, U. Stalmach, K. I. van de Wetering, and G. Hadziioannou, “Donor–Acceptor Diblock Copolymers Based on PPV and C₆₀: Synthesis, Thermal Properties, and Morphology,” *Macromolecules*, vol. 37, no. 10, pp. 3673–3684, May 2004.
- [192] B. C. Thompson, Y.-G. Kim, T. D. McCarley, and J. R. Reynolds, “Soluble narrow band gap and blue propylenedioxythiophene-cyanovinylene polymers as multifunctional materials for photovoltaic and electrochromic applications,” *J. Am. Chem. Soc.*, vol. 128, no. 39, pp. 12714–25, Oct. 2006.
- [193] A. E. Colbert, E. M. Janke, S. T. Hsieh, S. Subramanian, C. W. Schlenker, S. A. Jenekhe, and D. S. Ginger, “Hole Transfer from Low Band Gap Quantum Dots to Conjugated Polymers in Organic/Inorganic Hybrid Photovoltaics,” *J. Phys. Chem. Lett.*, vol. 4, no. 2, pp. 280–4, Jan. 2013.
- [194] F. S. F. Morgenstern, A. Rao, M. L. Böhm, R. J. P. Kist, Y. Vaynzof, and N. C. Greenham, “Ultrafast Charge- and Energy-Transfer Dynamics in Conjugated

- Polymer: Cadmium Selenide Nanocrystal Blends,” *ACS Nano*, vol. 8, no. 2, pp. 1647–1654, Feb. 2014.
- [195] X. Qiu, N. Hildebrandt, E. Fondamentale, and O. Cedex, “Rapid and Multiplexed MicroRNA Diagnostic Assay Using Quantum Dot-Based Förster Resonance Energy,” no. 8, pp. 8449–8457, 2015.
- [196] D. Geissler, S. Linden, K. Liermann, K. D. Wegner, L. J. Charbonniere, and N. Hildebrandt, “Lanthanides and quantum dots as Förster resonance energy transfer agents for diagnostics and cellular imaging,” *Inorg Chem*, vol. 53, pp. 1824–1838, 2014.
- [197] Y. Xiao, F. Shu, K. Y. Wong, and Z. Liu, “Förster resonance energy transfer-based biosensing platform with ultrasmall silver nanoclusters as energy acceptors,” *Anal. Chem.*, vol. 85, pp. 8493–8497, 2013.
- [198] A. B. Descalzo, C. Somoza, M. C. Moreno-Bondi, and G. Orellana, “Luminescent core-shell imprinted nanoparticles engineered for targeted Förster resonance energy transfer-based sensing,” *Anal. Chem.*, vol. 85, pp. 5316–5320, 2013.
- [199] D. J. Farrell and N. J. Ekins-Daukes, “Photovoltaic technology: Relay dye boosts efficiency,” *Nat. Photonics*, vol. 3, no. 7, pp. 373–374, 2009.
- [200] N. Cicek, S. Nizamoglu, T. Ozel, E. Mutlugun, D. U. Karatay, V. Lesnyak, T. Otto, N. Gaponik, A. Eychmüller, and H. V. Demir, “Structural tuning of color chromaticity through nonradiative energy transfer by interspacing CdTe nanocrystal monolayers,” *Appl. Phys. Lett.*, vol. 94, no. 6, p. 061105, Feb. 2009.
- [201] V. Vohra, G. Calzaferri, S. Destri, M. Pasini, W. Porzio, and C. Botta, “Supporting information Towards white light emission through efficient two steps energy transfer in hybrid nanofibers,” vol. 4, no. 3, p. 350, 2010.
- [202] E. Mutlugun, O. Samarskaya, T. Ozel, N. Cicek, N. Gaponik, A. Eychmüller, and H. V. Demir, “Highly efficient nonradiative energy transfer mediated light harvesting in water using aqueous CdTe quantum dot antennas,” *Opt. Express*, vol. 18, no. 10, pp. 10720–10730, 2010.
- [203] S. Buhbut, S. Itzhakov, E. Tauber, M. Shalom, I. Hod, T. Geiger, K. Y. Garini, D. Oron, and A. Zaban, “Built-in Quantum Dot Antennas in Dye-Sensitized Solar Cells,” *ACS Nano*, vol. 4, no. 3, pp. 1293–1298, 2010.

- [204] S. Chanyawadee, R. T. Harley, M. Henini, D. V. Talapin, and P. G. Lagoudakis, "Photocurrent enhancement in hybrid nanocrystal quantum-dot p-i-n photovoltaic devices," *Phys. Rev. Lett.*, vol. 102, no. February, pp. 1–4, 2009.
- [205] E. Mutlugün, S. Nizamoğlu, and H. V. Demir, "Highly efficient nonradiative energy transfer using charged CdSe/ZnS nanocrystals for light-harvesting in solution," *Appl. Phys. Lett.*, vol. 95, pp. 95–97, 2009.
- [206] S. Nizamoglu and H. V. Demir, "Förster resonance energy transfer enhanced color-conversion using colloidal semiconductor quantum dots for solid state lighting," *Appl. Phys. Lett.*, vol. 95, pp. 95–97, 2009.
- [207] M. Baldo, M. Thompson, and S. Forrest, "High-efficiency fluorescent organic light-emitting devices using a phosphorescent sensitizer," *Nature*, vol. 403, no. 6771, pp. 750–3, Feb. 2000.
- [208] X. Liu and J. Qiu, "Recent advances in energy transfer in bulk and nanoscale luminescent materials: from spectroscopy to applications," *Chem. Soc. Rev.*, vol. 44, pp. 8714–8746, 2015.
- [209] M. Artemyev, E. Ustinovich, and I. Nabiev, "Efficiency of Energy Transfer from Organic Dye Molecules to CdSe - ZnS Nanocrystals: Nanorods versus Nanodots," no. 17, pp. 8061–8065, 2009.
- [210] M. Hardzei, M. Artemyev, M. Molinari, M. Troyon, A. Sukhanova, and I. Nabiev, "Comparative efficiency of energy transfer from CdSe-ZnS quantum dots or nanorods to organic dye molecules," *ChemPhysChem*, vol. 13, pp. 330–335, 2012.
- [211] N. À. Dye, "ARTICLE Effect of Nanoparticle Dimensionality on Fluorescence Resonance Energy," no. 3, pp. 2758–2765, 2012.
- [212] A. Sitt, N. Even-Dar, S. Halivni, A. Faust, L. Yedidya, and U. Banin, "Analysis of Shape and Dimensionality Effects on Fluorescence Resonance Energy Transfer from Nanocrystals to Multiple Acceptors," *J. Phys. Chem. C*, p. 130204084921001, 2013.
- [213] P. L. Hernández-Martínez, A. O. Govorov, and H. V. Demir, "Generalized Theory of Förster-Type Nonradiative Energy Transfer in Nanostructures with Mixed Dimensionality," *J. Phys. Chem. C*, vol. 117, no. 19, pp. 10203–10212, May 2013.

- [214] J. Lee, A. O. Govorov, and N. a. Kotov, “Bioconjugated superstructures of CdTe nanowires and nanoparticles: Multistep cascade Förster resonance energy transfer and energy channeling,” *Nano Lett.*, vol. 5, pp. 2063–2069, 2005.
- [215] J. B. Hoffman, H. Choi, and P. V Kamat, “Size-Dependent Energy Transfer Pathways in CdSe Quantum-Squaraine, Dot Fo, Light-harvesting Assemblies: Förster versus Dexter,” *J. Phys. Chem. C*, vol. 118, pp. 18453–18461, 2014.
- [216] X. Zhang, C. a. Marocico, M. Lunz, V. a. Gerard, Y. K. Gun’Ko, V. Lesnyak, N. Gaponik, A. S. Susha, A. L. Rogach, and a. L. Bradley, “Wavelength, concentration, and distance dependence of nonradiative energy transfer to a plane of gold nanoparticles,” *ACS Nano*, vol. 6, no. 10, pp. 9283–9290, 2012.
- [217] D. Prasai, A. R. Klots, A. Newaz, J. S. Niezgod, N. J. Orfield, C. a. Escobar, A. Wynn, A. Efimov, G. K. Jennings, S. J. Rosenthal, and K. I. Bolotin, “Electrical Control of near-Field Energy Transfer between Quantum Dots and Two-Dimensional Semiconductors,” *Nano Lett.*, p. 150603085419002, 2015.
- [218] S. Nizamoglu, E. Sari, J. H. Baek, I. H. Lee, and H. V. Demir, “Nonradiative resonance energy transfer directed from colloidal CdSe/ZnS quantum dots to epitaxial ingan/gan quantum wells for solar cells,” *Phys. Status Solidi - Rapid Res. Lett.*, vol. 4, pp. 178–180, 2010.
- [219] C. Higgins, M. Lunz, a L. Bradley, V. a Gerard, S. Byrne, Y. K. Gun’ko, V. Lesnyak, and N. Gaponik, “Energy transfer in colloidal CdTe quantum dot nanoclusters,” *Opt. Express*, vol. 18, no. 24, pp. 24486–24494, 2010.
- [220] S. Nizamoglu, P. Ludwig Hernández-Martínez, E. Mutlugun, D. Ugur Karatay, and H. Volkan Demir, “Excitonic enhancement of nonradiative energy transfer from a quantum well in the optical near field of energy gradient quantum dots,” *Appl. Phys. Lett.*, vol. 100, no. 24, p. 241109, Jun. 2012.
- [221] J. C. de Mello, H. F. Wittmann, and R. H. Friend, “An Improved Experimental Determination of External Photoluminescence Quantum Efficiency,” *Adv. Mater.*, vol. 9, no. 3, pp. 230–232, 1997.
- [222] K.-H. Lee, J.-H. Lee, W. Song, H. Ko, C. Lee, J. Lee, and H. Yang, “Highly efficient, color-pure, color-stable blue quantum dot light-emitting devices,” *ACS Nano*, vol. 7, no. 8, pp. 7295–302, Aug. 2013.
- [223] N. Durisic, A. G. Godin, D. Walters, P. Grütter, P. W. Wiseman, and C. D.

- Heyes, "Probing the 'dark' fraction of core-shell quantum dots by ensemble and single particle pH-dependent spectroscopy," *ACS Nano*, vol. 5, no. 11, pp. 9062–9073, 2011.
- [224] T. Franzl, A. Shavel, A. Rogach, N. Gaponik, T. A. Klar, A. Eychmüller, and J. Feldmann, "High-Rate Unidirectional Energy Transfer in Directly Assembled CdTe Nanocrystal Bilayers," *Small*, vol. 1, no. 4, pp. 392–395, 2005.
- [225] M. Lorenzon, S. Christodoulou, G. Vaccaro, J. Pedrini, F. Meinardi, I. Moreels, and S. Brovelli, "Reversed oxygen sensing using colloidal quantum wells towards highly emissive photoresponsive varnishes," *Nat. Commun.*, vol. 6, p. 6434, 2015.
- [226] J. Feng, K. Tian, D. Hu, S. Wang, S. Li, Y. Zeng, Y. Li, and G. Yang, "A Triarylboron-Based Fluorescent Thermometer: Sensitive Over a Wide Temperature Range," *Angew. Chemie - Int. Ed.*, vol. 50, pp. 8072–8076, 2011.
- [227] E. J. McLaurin, V. A. Vlaskin, and D. R. Gamelin, "Water-soluble dual-emitting nanocrystals for ratiometric optical thermometry," *J. Am. Chem. Soc.*, vol. 133, pp. 14978–14980, 2011.
- [228] X. Rao, T. Song, J. Gao, Y. Cui, Y. Yang, C. Wu, B. Chen, and G. Qian, "A highly sensitive mixed lanthanide metal-organic framework self-calibrated luminescent thermometer," *J. Am. Chem. Soc.*, vol. 135, pp. 15559–15564, 2013.
- [229] S. Zheng, W. Chen, D. Tan, J. Zhou, Q. Guo, W. Jiang, C. Xu, X. Liu, and J. Qiu, "Lanthanide-doped NaGdF₄ core-shell nanoparticles for non-contact self-referencing temperature sensors," *Nanoscale*, vol. 6, pp. 5675–5679, 2014.
- [230] S. Coe, W.-K. Woo, M. Bawendi, and V. Bulović, "Electroluminescence from single monolayers of nanocrystals in molecular organic devices," *Nature*, vol. 420, no. 6917, pp. 800–3, Jan. 2002.
- [231] M. A. Baldo, D. F. O'Brien, and S. R. Forrest, "Excitonic singlet-triplet ratio in a semiconducting organic thin film," *Phys. Rev. B*, vol. 60, no. 20, pp. 14422–14428, Nov. 1999.
- [232] P. O. Anikeeva, C. F. Madigan, S. A. Coe-Sullivan, J. S. Steckel, M. G. Bawendi, and V. Bulović, "Photoluminescence of CdSe/ZnS core/shell quantum dots enhanced by energy transfer from a phosphorescent donor,"

- Chem. Phys. Lett.*, vol. 424, no. 1–3, pp. 120–125, Jun. 2006.
- [233] Y. Q. Zhang and X. A. Cao, “Electroluminescence of green CdSe/ZnS quantum dots enhanced by harvesting excitons from phosphorescent molecules,” *Appl. Phys. Lett.*, vol. 97, no. 25, p. 253115, Dec. 2010.
- [234] M. A. Baldo, D. F. O’Brien, Y. You, A. Shoustikov, S. Sibley, M. E. Thompson, and S. R. Forrest, “Highly efficient phosphorescent emission from organic electroluminescent devices,” *Nature*, vol. 395, no. 6698, pp. 151–154, Sep. 1998.
- [235] C. Adachi, M. A. Baldo, M. E. Thompson, and S. R. Forrest, “Nearly 100% internal phosphorescence efficiency in an organic light-emitting device,” *J. Appl. Phys.*, vol. 90, no. 10, p. 5048, Nov. 2001.
- [236] B. D’Andrade, “Lighting: White phosphorescent LEDs offer efficient answer,” *Nat. Photonics*, vol. 1, no. 1, pp. 33–34, Jan. 2007.
- [237] S. Reineke, F. Lindner, G. Schwartz, N. Seidler, K. Walzer, B. Lüssem, and K. Leo, “White organic light-emitting diodes with fluorescent tube efficiency,” *Nature*, vol. 459, no. 7244, pp. 234–8, May 2009.
- [238] C. B. Murray, D. J. Norris, and M. G. Bawendi, “Synthesis and characterization of nearly monodisperse CdE (E = sulfur, selenium, tellurium) semiconductor nanocrystallites,” *J. Am. Chem. Soc.*, vol. 115, no. 19, pp. 8706–8715, Sep. 1993.
- [239] H. V. Demir, S. Nizamoglu, T. Erdem, E. Mutlugun, N. Gaponik, and A. Eychmüller, “Quantum dot integrated LEDs using photonic and excitonic color conversion,” *Nano Today*, vol. 6, no. 6, pp. 632–647, Dec. 2011.
- [240] G. Cheng, M. Mazzeo, A. Rizzo, Y. Li, Y. Duan, and G. Gigli, “White light-emitting devices based on the combined emission from red CdSe/ZnS quantum dots, green phosphorescent, and blue fluorescent organic molecules,” *Appl. Phys. Lett.*, vol. 94, no. 24, p. 243506, Jun. 2009.
- [241] G. Cheng, W. Lu, Y. Chen, and C.-M. Che, “Hybrid light-emitting devices based on phosphorescent platinum(II) complex sensitized CdSe/ZnS quantum dots,” *Opt. Lett.*, vol. 37, no. 6, pp. 1109–11, Mar. 2012.
- [242] J. Lim, W. K. Bae, J. Kwak, S. Lee, C. Lee, and K. Char, “Perspective on synthesis, device structures, and printing processes for quantum dot displays,”

- Opt. Mater. Express*, vol. 2, no. 5, p. 594, Apr. 2012.
- [243] C. Adachi, R. C. Kwong, P. Djurovich, V. Adamovich, M. A. Baldo, M. E. Thompson, and S. R. Forrest, “Endothermic energy transfer: A mechanism for generating very efficient high-energy phosphorescent emission in organic materials,” *Appl. Phys. Lett.*, vol. 79, no. 13, p. 2082, Sep. 2001.
- [244] T. Tsuboi, H. Murayama, and A. Penzkofer, “Energy transfer in a thin film of TPD fluorescent molecules doped with PtOEP and Ir(ppy)₃ phosphorescent molecules,” *Appl. Phys. B*, vol. 81, no. 1, pp. 93–99, Jun. 2005.
- [245] X. Yuan, J. Zhao, P. Jing, W. Zhang, H. Li, L. Zhang, X. Zhong, and Y. Masumoto, “Size- and Composition-Dependent Energy Transfer from Charge Transporting Materials to ZnCuInS Quantum Dots,” *J. Phys. Chem. C*, vol. 116, no. 22, pp. 11973–11979, Jun. 2012.
- [246] C. Wu, Y. Zheng, C. Szymanski, and J. McNeill, “Energy Transfer in a Nanoscale Multichromophoric System: Fluorescent Dye-Doped Conjugated Polymer Nanoparticles,” *J. Phys. Chem. C. Nanomater. Interfaces*, vol. 112, no. 6, pp. 1772–1781, Feb. 2008.
- [247] D. Kim, S. Okahara, M. Nakayama, and Y. Shim, “Experimental verification of Förster energy transfer between semiconductor quantum dots,” *Phys. Rev. B*, vol. 78, no. 15, p. 153301, Oct. 2008.
- [248] R. R. Lunt, N. C. Giebink, A. A. Belak, J. B. Benziger, and S. R. Forrest, “Exciton diffusion lengths of organic semiconductor thin films measured by spectrally resolved photoluminescence quenching,” *J. Appl. Phys.*, vol. 105, no. 5, p. 053711, Mar. 2009.
- [249] N. C. Giebink, Y. Sun, and S. R. Forrest, “Transient analysis of triplet exciton dynamics in amorphous organic semiconductor thin films,” *Org. Electron.*, vol. 7, no. 5, pp. 375–386, Oct. 2006.
- [250] Y. Kawamura, K. Goushi, J. Brooks, J. J. Brown, H. Sasabe, and C. Adachi, “100% phosphorescence quantum efficiency of Ir(III) complexes in organic semiconductor films,” *Appl. Phys. Lett.*, vol. 86, no. 7, p. 071104, Feb. 2005.
- [251] P. Jing, X. Yuan, W. Ji, M. Ikezawa, X. Liu, L. Zhang, J. Zhao, and Y. Masumoto, “Efficient energy transfer from hole transporting materials to CdSe-core CdS/ZnCdS/ZnS-multishell quantum dots in type II aligned blend films,”

- Appl. Phys. Lett.*, vol. 99, no. 9, p. 093106, Sep. 2011.
- [252] S. Reineke, M. Thomschke, B. Lüssem, and K. Leo, “White organic light-emitting diodes: Status and perspective,” *Rev. Mod. Phys.*, vol. 85, no. 3, pp. 1245–1293, Jul. 2013.
- [253] Y. Wang, S. Li, S. V Kershaw, F. Hetsch, A. Y. Y. Tam, G. Shan, A. S. Susha, C.-C. Ko, V. Wing-Wah Yam, K. K. W. Lo, and A. L. Rogach, “Design of a water-soluble hybrid nanocomposite of CdTe quantum dots and an iridium complex for photoinduced charge transfer,” *Chemphyschem*, vol. 13, no. 10, pp. 2589–95, Jul. 2012.
- [254] W. K. Bae, J. Kwak, J. Lim, D. Lee, M. K. Nam, K. Char, C. Lee, and S. Lee, “Multicolored light-emitting diodes based on all-quantum-dot multilayer films using layer-by-layer assembly method,” *Nano Lett.*, vol. 10, no. 7, pp. 2368–73, Jul. 2010.
- [255] J. Ribierre, A. Ruseckas, K. Knights, S. Staton, N. Cumpstey, P. Burn, and I. Samuel, “Triplet Exciton Diffusion and Phosphorescence Quenching in Iridium(III)-Centered Dendrimers,” *Phys. Rev. Lett.*, vol. 100, no. 1, p. 017402, Jan. 2008.
- [256] S. P. and Fasol, Shuji Nakamura, *The Blue Laser Diode: The Complete Story*, 2nd update. Springer, 2000.
- [257] I. Moreels, G. Rainò, R. Gomes, Z. Hens, T. Stöferle, and R. F. Mahrt, “Nearly Temperature-Independent Threshold for Amplified Spontaneous Emission in Colloidal CdSe/CdS Quantum Dot-in-Rods,” *Adv. Mater.*, vol. 24, no. 35, pp. OP231–OP235, Sep. 2012.
- [258] P. Kambhampati, Z. Mi, and R. R. Cooney, *Comprehensive Nanoscience and Technology*. Elsevier, 2011.
- [259] *Dye Lasers*. 1973.
- [260] Y. Kelestemur, A. F. Cihan, B. Guzelturk, and H. V. Demir, “Type-tunable amplified spontaneous emission from core-seeded CdSe/CdS nanorods controlled by exciton-exciton interaction,” *Nanoscale*, vol. 6, no. 15, pp. 8509–14, Jul. 2014.
- [261] G. Xing, Y. Liao, X. Wu, S. Chakraborty, X. Liu, E. K. L. Yeow, Y. Chan, and T. C. Sum, “Ultralow-threshold two-photon pumped amplified spontaneous

- emission and lasing from seeded CdSe/CdS nanorod heterostructures.,” *ACS Nano*, vol. 6, no. 12, pp. 10835–44, Dec. 2012.
- [262] Y. Liao, G. Xing, N. Mishra, T. C. Sum, and Y. Chan, “Low Threshold , Amplified Spontaneous Emission from Core-Seeded Semiconductor Nanotetrapods Incorporated into a Sol – Gel Matrix,” *Adv. Mater.*, vol. 24, no. 23, pp. 159–164, Jun. 2012.
- [263] F. García-Santamaría, S. Brovelli, R. Viswanatha, J. A. Hollingsworth, H. Htoon, S. A. Crooker, and V. I. Klimov, “Breakdown of volume scaling in Auger recombination in CdSe/CdS heteronanocrystals: the role of the core-shell interface.,” *Nano Lett.*, vol. 11, no. 2, pp. 687–93, Feb. 2011.
- [264] G. E. Cragg and A. L. Efros, “Suppression of Auger processes in confined structures,” *Nano Lett.*, vol. 10, no. 1, pp. 313–7, Jan. 2010.
- [265] S. a Ivanov, J. Nanda, A. Piryatinski, M. Achermann, L. P. Balet, I. V Bezel, P. O. Anikeeva, S. Tretiak, and V. I. Klimov, “Light Amplification Using Inverted Core/Shell Nanocrystals: Towards Lasing in the Single-Exciton Regime,” *J. Phys. Chem. B*, vol. 108, no. 30, pp. 10625–10630, 2004.
- [266] Y. Chan, J. S. Steckel, P. T. Snee, J.-M. Caruge, J. M. Hodgkiss, D. G. Nocera, and M. G. Bawendi, “Blue semiconductor nanocrystal laser,” *Appl. Phys. Lett.*, vol. 86, no. 7, p. 073102, 2005.
- [267] Q. Darugar, W. Qian, and M. a. El-Sayed, “Observation of optical gain in solutions of CdS quantum dots at room temperature in the blue region,” *Appl. Phys. Lett.*, vol. 88, no. 26, p. 261108, 2006.
- [268] J. Jasieniak, J. Pacifico, R. Signorini, A. Chiasera, M. Ferrari, A. Martucci, and P. Mulvaney, “Luminescence and amplified stimulated emission in CdSe–ZnS-nanocrystal-doped TiO₂ and ZrO₂ waveguides,” *Adv. Funct. Mater.*, vol. 17, no. 10, pp. 1654–1662, Jul. 2007.
- [269] J. J. J. Jasieniak, I. Fortunati, S. Gardin, R. Signorini, R. Bozio, A. Martucci, and P. Mulvaney, “Highly efficient amplified stimulated emission from CdSe–CdS–ZnS quantum dot doped waveguides with two-photon infrared optical pumping,” *Adv. Mater.*, vol. 20, no. 1, pp. 69–73, Jan. 2008.
- [270] R. Signorini, I. Fortunati, F. Todescato, S. Gardin, R. Bozio, J. J. Jasieniak, A. Martucci, G. Della Giustina, G. Brusatin, M. Guglielmi, and D. Giustina,

- “Facile production of up-converted quantum dot lasers,” *Nanoscale*, vol. 3, no. 10, pp. 4109–13, Oct. 2011.
- [271] I. Fortunati, R. Signorini, R. Bozio, J. J. Jasieniak, A. Antonello, A. Martucci, G. Della Giustina, G. Brusatin, and M. Guglielmi, “CdSe Core–Shell Nanoparticles as Active Materials for Up-Converted Emission,” *J. Phys. Chem. C*, vol. 115, no. 10, pp. 3840–3846, Mar. 2011.
- [272] C. Zhang, F. Zhang, A. Cheng, B. Kimball, and A. Y. Wang, “Frequency upconverted lasing of nanocrystal quantum dots in microbeads Frequency upconverted lasing of nanocrystal quantum dots in microbeads,” vol. 183109, no. May 2013, pp. 18–21, 2009.
- [273] A. F. Cihan, Y. Kelestemur, B. GuzelTURK, O. Yerli, U. Kurum, H. G. Yaglioglu, A. Elmali, and H. V. Demir, “Attractive versus repulsive excitonic interactions of colloidal quantum dots control blue- to red-shifting (and non-shifting) amplified spontaneous emission,” *J. Phys. Chem. Lett.*, vol. 4, no. 23, pp. 4146–4152, Dec. 2013.
- [274] B. GuzelTURK, Y. Kelestemur, M. Z. Akgul, V. K. Sharma, and H. V. Demir, “Ultralow Threshold One-Photon- and Two-Photon-Pumped Optical Gain Media of Blue-Emitting Colloidal Quantum Dot Films,” *J. Phys. Chem. Lett.*, vol. 5, no. 13, pp. 2214–2218, Jul. 2014.
- [275] R. R. Cooney, S. L. Sewall, D. M. Sagar, and P. Kambhampati, “State-resolved manipulations of optical gain in semiconductor quantum dots: Size universality, gain tailoring, and surface effects,” *J. Chem. Phys.*, vol. 131, no. 16, p. 164706, Oct. 2009.
- [276] W. K. Bae, L. a Padilha, Y.-S. Park, H. McDaniel, I. Robel, J. M. Pietryga, and V. I. Klimov, “Controlled alloying of the core-shell interface in CdSe/CdS quantum dots for suppression of Auger recombination,” *ACS Nano*, vol. 7, no. 4, pp. 3411–9, Apr. 2013.
- [277] Y. Chan, J.-M. Caruge, P. T. Snee, and M. G. Bawendi, “Multiexcitonic two-state lasing in a CdSe nanocrystal laser,” *Appl. Phys. Lett.*, vol. 85, no. 13, p. 2460, 2004.
- [278] I. D. W. Samuel and G. A. Turnbull, “Organic semiconductor lasers.,” *Chem. Rev.*, vol. 107, no. 4, pp. 1272–95, Apr. 2007.

- [279] A. V. Malko, A. A. Mikhailovsky, M. A. Petruska, J. A. Hollingsworth, H. Htoon, M. G. Bawendi, and V. I. Klimov, “From amplified spontaneous emission to microring lasing using nanocrystal quantum dot solids,” *Appl. Phys. Lett.*, vol. 81, no. 7, p. 1303, 2002.
- [280] C. Grivas, C. Li, P. Andreakou, P. Wang, M. Ding, G. Brambilla, L. Manna, and P. Lagoudakis, “Single-mode tunable laser emission in the single-exciton regime from colloidal nanocrystals,” *Nat. Commun.*, vol. 4, no. May, p. 2376, Jan. 2013.
- [281] C. Dang, J. Lee, K. Roh, H. Kim, S. Ahn, H. Jeon, C. Breen, J. S. Steckel, S. Coe-Sullivan, and a. Nurmikko, “Highly efficient, spatially coherent distributed feedback lasers from dense colloidal quantum dot films,” *Appl. Phys. Lett.*, vol. 103, no. 17, p. 171104, Oct. 2013.
- [282] C. Dang and A. Nurmikko, “Beyond quantum dot LEDs: Optical gain and laser action in red, green, and blue colors,” *MRS Bull.*, vol. 38, no. 09, pp. 737–742, Sep. 2013.
- [283] Y. Wang, V. D. Ta, Y. Gao, T. C. He, R. Chen, E. Mutlugun, H. V. Demir, and H. D. Sun, “Stimulated Emission and Lasing from CdSe/CdS/ZnS Core-Multi-Shell Quantum Dots by Simultaneous Three-Photon Absorption,” *Adv. Mater.*, vol. 26, no. 18, pp. 2954–2961, May 2014.
- [284] V. I. Klimov, S. A. Ivanov, J. Nanda, M. Achermann, I. Bezel, J. A. McGuire, and A. Piryatinski, “Single-exciton optical gain in semiconductor nanocrystals,” *Nature*, vol. 447, no. 7143, pp. 441–446, May 2007.
- [285] C. A. Leatherdale, W.-K. Woo, F. V. Mikulec, and M. G. Bawendi, “On the Absorption Cross Section of CdSe Nanocrystal Quantum Dots,” *J. Phys. Chem. B*, vol. 106, no. 31, pp. 7619–7622, Aug. 2002.
- [286] C. Zhang, F. Zhang, T. Zhu, A. Cheng, J. Xu, Q. Zhang, S. E. Mohny, R. H. Henderson, and Y. A. Wang, “Two-photon-pumped lasing from colloidal nanocrystal quantum dots,” *Opt. Lett.*, vol. 33, no. 21, p. 2437, Oct. 2008.
- [287] O. Chen, J. Zhao, V. P. Chauhan, J. Cui, C. Wong, D. K. Harris, H. Wei, H.-S. Han, D. Fukumura, R. K. Jain, and M. G. Bawendi, “Compact high-quality CdSe-CdS core-shell nanocrystals with narrow emission linewidths and suppressed blinking,” *Nat. Mater.*, vol. 12, no. 5, pp. 445–51, May 2013.

- [288] B. Mahler, N. Lequeux, and B. Dubertret, “Ligand-controlled polytypism of thick-shell CdSe/CdS nanocrystals,” *J. Am. Chem. Soc.*, vol. 132, no. 3, pp. 953–9, Jan. 2010.
- [289] M. Califano, A. Franceschetti, and A. Zunger, “Temperature dependence of excitonic radiative decay in CdSe quantum dots: the role of surface hole traps,” *Nano Lett.*, vol. 5, no. 12, pp. 2360–4, Dec. 2005.
- [290] Y.-S. Park, W. K. Bae, L. A. Padilha, J. M. Pietryga, and V. I. Klimov, “Effect of the core/shell interface on auger recombination evaluated by single-quantum-dot spectroscopy,” *Nano Lett.*, vol. 14, no. 2, pp. 396–402, Feb. 2014.
- [291] J. Zhao, O. Chen, D. B. Strasfeld, and M. G. Bawendi, “Biexciton quantum yield heterogeneities in single CdSe (CdS) core (shell) nanocrystals and its correlation to exciton blinking,” *Nano Lett.*, vol. 12, no. 9, pp. 4477–83, Sep. 2012.
- [292] X. Wang, X. Ren, K. Kahen, M. a Hahn, M. Rajeswaran, S. Maccagnano-Zacher, J. Silcox, G. E. Cragg, A. L. Efros, and T. D. Krauss, “Non-blinking semiconductor nanocrystals,” *Nature*, vol. 459, no. 7247, pp. 686–9, Jun. 2009.
- [293] J. I. Climente, J. L. Movilla, and J. Planelles, “Auger recombination suppression in nanocrystals with asymmetric electron-hole confinement,” *Small*, vol. 8, no. 5, pp. 754–9, Mar. 2012.
- [294] D. I. Chepic, A. L. Efros, A. I. Ekimov, M. G. Ivanov, V. A. Kharchenko, I. A. Kudriavtsev, and T. V. Yazeva, “Auger ionization of semiconductor quantum drops in a glass matrix,” *J. Lumin.*, vol. 47, no. 3, pp. 113–127, Oct. 1990.
- [295] W. Qin, R. A. Shah, and P. Guyot-Sionnest, “CdSeS/ZnS Alloyed Nanocrystal Lifetime and Blinking Studies under Electrochemical Control,” *ACS Nano*, vol. 6, no. 1, pp. 912–918, Jan. 2012.
- [296] J. Nanda, B. Kuruvilla, and D. Sarma, “Photoelectron spectroscopic study of CdS nanocrystallites,” *Phys. Rev. B*, vol. 59, no. 11, pp. 7473–7479, Mar. 1999.
- [297] P. K. Santra, R. Viswanatha, S. M. Daniels, N. L. Pickett, J. M. Smith, P. O’Brien, and D. D. Sarma, “Investigation of the internal heterostructure of highly luminescent quantum dot-quantum well nanocrystals,” *J. Am. Chem. Soc.*, vol. 131, no. 2, pp. 470–7, Jan. 2009.
- [298] D. D. Sarma, A. Nag, P. K. Santra, A. Kumar, S. Sapra, and P. Mahadevan,

- “Origin of the Enhanced Photoluminescence from Semiconductor CdSeS Nanocrystals,” *J. Phys. Chem. Lett.*, vol. 1, no. 14, pp. 2149–2153, Jul. 2010.
- [299] M. Sheik-Bahae, A. A. Said, T.-H. Wei, D. J. Hagan, and E. W. Van Stryland, “Sensitive measurement of optical nonlinearities using a single beam,” *IEEE J. Quantum Electron.*, vol. 26, no. 4, pp. 760–769, Apr. 1990.
- [300] D. P. Puzzo, L. D. Bonifacio, J. Oreopoulos, C. M. Yip, I. Manners, and G. A. Ozin, “Color from colorless nanomaterials: Bragg reflectors made of nanoparticles,” *J. Mater. Chem.*, vol. 19, no. 21, p. 3500, May 2009.
- [301] S. Colodrero, M. Ocaña, and H. Míguez, “Nanoparticle-based one-dimensional photonic crystals,” *Langmuir*, vol. 24, no. 9, pp. 4430–4, May 2008.
- [302] C. Bauer, B. Schnabel, E.-B. Kley, U. Scherf, H. Giessen, and R. F. Mahrt, “Two-Photon Pumped Lasing from a Two-Dimensional Photonic Bandgap Structure with Polymeric Gain Material,” *Adv. Mater.*, vol. 14, no. 9, pp. 673–676, May 2002.
- [303] V. M. Menon, M. Luberto, N. V. Valappil, and S. Chatterjee, “Lasing from InGaP quantum dots in a spin-coated flexible microcavity,” *Opt. Express*, vol. 16, no. 24, pp. 19535–40, Nov. 2008.
- [304] V. I. Klimov, “Spectral and dynamical properties of multiexcitons in semiconductor nanocrystals,” *Annu. Rev. Phys. Chem.*, vol. 58, pp. 635–73, Jan. 2007.
- [305] H. Htoon, J. A. Hollingworth, A. V. Malko, R. Dickerson, and V. I. Klimov, “Light amplification in semiconductor nanocrystals: Quantum rods versus quantum dots,” *Appl. Phys. Lett.*, vol. 82, no. 26, p. 4776, Jun. 2003.
- [306] J. Haase, S. Shinohara, P. Mundra, G. Risse, V. G. Lyssenko, H. Frob, M. Hentschel, A. Eychmuller, and K. Leo, “Hemispherical resonators with embedded nanocrystal quantum rod emitters,” *Appl. Phys. Lett.*, vol. 97, no. 21, p. 211101, 2010.
- [307] M. Zavelani-Rossi, M. G. Lupo, R. Krahne, L. Manna, and G. Lanzani, “Lasing in self-assembled microcavities of CdSe/CdS core/shell colloidal quantum rods,” *Nanoscale*, vol. 2, no. 6, pp. 931–935, Jun. 2010.
- [308] S. Ithurria, G. Bousquet, and B. Dubertret, “Continuous transition from 3D to 1D confinement observed during the formation of CdSe nanoplatelets,” *J. Am.*

Chem. Soc., vol. 133, no. 9, pp. 3070–7, Mar. 2011.

- [309] J. Kundu, Y. Ghosh, A. M. Dennis, H. Htoon, and J. a Hollingsworth, “Giant nanocrystal quantum dots: stable down-conversion phosphors that exploit a large stokes shift and efficient shell-to-core energy relaxation.,” *Nano Lett.*, vol. 12, no. 6, pp. 3031–7, Jun. 2012.
- [310] D. V Talapin, J. H. Nelson, E. V Shevchenko, S. Aloni, B. Sadtler, and A. P. Alivisatos, “Seeded growth of highly luminescent CdSe/CdS nanoheterostructures with rod and tetrapod morphologies.,” *Nano Lett.*, vol. 7, no. 10, pp. 2951–9, Oct. 2007.
- [311] D. V. Talapin, R. Koeppel, S. Götzinger, A. Kornowski, J. M. Lupton, A. L. Rogach, O. Benson, J. Feldmann, and H. Weller, “Highly Emissive Colloidal CdSe/CdS Heterostructures of Mixed Dimensionality,” *Nano Lett.*, vol. 3, no. 12, pp. 1677–1681, Dec. 2003.
- [312] N. J. Borys, M. J. Walter, J. Huang, D. V Talapin, and J. M. Lupton, “The role of particle morphology in interfacial energy transfer in CdSe/CdS heterostructure nanocrystals,” *Science*, vol. 330, no. 6009, pp. 1371–4, Dec. 2010.
- [313] D. P. Puzzo, F. Scotognella, M. Zavelani-Rossi, M. Sebastian, A. J. Lough, I. Manners, G. Lanzani, R. Tubino, and G. A. Ozin, “Distributed feedback lasing from a composite poly(phenylene vinylene)-nanoparticle one-dimensional photonic crystal.,” *Nano Lett.*, vol. 9, no. 12, pp. 4273–8, Dec. 2009.
- [314] O. E. Semonin, J. M. Luther, S. Choi, H.-Y. Chen, J. Gao, A. J. Nozik, and M. C. Beard, “Peak external photocurrent quantum efficiency exceeding 100% via MEG in a quantum dot solar cell.,” *Science*, vol. 334, no. 6062, pp. 1530–3, Dec. 2011.
- [315] J. Lim, B. G. Jeong, M. Park, J. K. Kim, J. M. Pietryga, Y.-S. Park, V. I. Klimov, C. Lee, D. C. Lee, and W. K. Bae, “Influence of Shell Thickness on the Performance of Light-Emitting Devices Based on CdSe/Zn_{1-X} Cd_X S Core/Shell Heterostructured Quantum Dots.,” *Adv. Mater.*, vol. 26, pp. 8034–8040, Nov. 2014.
- [316] D. Norris and M. Bawendi, “Measurement and assignment of the size-dependent optical spectrum in CdSe quantum dots,” *Phys. Rev. B*, vol. 53, no.

- 24, pp. 16338–16346, Jun. 1996.
- [317] W. W. Yu, L. Qu, W. Guo, and X. Peng, “Experimental Determination of the Extinction Coefficient of CdTe, CdSe, and CdS Nanocrystals,” *Chem. Mater.*, vol. 15, no. 14, pp. 2854–2860, Jul. 2003.
- [318] J. Jasieniak, L. Smith, J. Van Embden, P. Mulvaney, and M. Califano, “Re-examination of the Size-Dependent Absorption Properties of CdSe Quantum Dots,” *J. Phys. Chem. C*, vol. 113, no. 45, pp. 19468–19474, Nov. 2009.
- [319] M. Leistikow, J. Johansen, a. Kettelarij, P. Lodahl, and W. Vos, “Size-dependent oscillator strength and quantum efficiency of CdSe quantum dots controlled via the local density of states,” *Phys. Rev. B*, vol. 79, no. 4, p. 045301, Jan. 2009.
- [320] K. Gong, Y. Zeng, and D. F. Kelley, “Extinction Coefficients, Oscillator Strengths, and Radiative Lifetimes of CdSe, CdTe, and CdTe/CdSe Nanocrystals,” *J. Phys. Chem. C*, vol. 117, pp. 20268–20279, 2013.
- [321] P. Kambhampati, “Multiexcitons in semiconductor nanocrystals: a platform for optoelectronics at high carrier concentration,” *J. Phys. Chem. Lett.*, vol. 3, no. 9, pp. 1182–1190, May 2012.
- [322] P. Kambhampati, “Unraveling the structure and dynamics of excitons in semiconductor quantum dots,” *Acc. Chem. Res.*, vol. 44, no. 1, pp. 1–13, Jan. 2011.
- [323] P. Kambhampati, “On the Kinetics and Thermodynamics of Excitons at the Surface of Semiconductor Nanocrystals: Are There Surface Excitons?,” *Chem. Phys.*, vol. 446, pp. 92–107, 2015.
- [324] J. Mooney, M. M. Krause, and P. Kambhampati, “Connecting the Dots: The Kinetics and Thermodynamics of Hot, Cold, and Surface-Trapped Excitons in Semiconductor Nanocrystals,” *J. Phys. Chem. C*, vol. 118, pp. 7730–7739, 2014.
- [325] J. E. Raymond, A. Bhaskar, T. Goodson, N. Makiuchi, K. Ogawa, and Y. Kobuke, “Synthesis and two-photon absorption enhancement of porphyrin macrocycles,” *J. Am. Chem. Soc.*, vol. 130, no. 51, pp. 17212–3, Dec. 2008.
- [326] B. R. Sutherland and E. H. Sargent, “Perovskite photonic sources,” *Nat. Photonics*, vol. 10, no. 5, pp. 295–302, Apr. 2016.

- [327] M. Li, M. Zhi, H. Zhu, W.-Y. Wu, Q.-H. Xu, M. H. Jhon, and Y. Chan, “Ultralow-threshold multiphoton-pumped lasing from colloidal nanoplatelets in solution,” *Nat. Commun.*, vol. 6, p. 8513, Jan. 2015.
- [328] C. B. Murray, C. R. Kagan, and M. G. Bawendi, “Self-Organization of CdSe Nanocrystallites into Three-Dimensional Quantum Dot Superlattices,” *Science (80-.)*, vol. 270, no. 5240, pp. 1335–1338, Nov. 1995.
- [329] E. V Shevchenko, D. V Talapin, N. A. Kotov, S. O’Brien, and C. B. Murray, “Structural diversity in binary nanoparticle superlattices,” *Nature*, vol. 439, no. 7072, pp. 55–9, Jan. 2006.
- [330] N. J. Thompson, M. W. B. Wilson, D. N. Congreve, P. R. Brown, J. M. Scherer, T. S. Bischof, M. Wu, N. Geva, M. Welborn, T. Van Voorhis, V. Bulović, M. G. Bawendi, and M. A. Baldo, “Energy harvesting of non-emissive triplet excitons in tetracene by emissive PbS nanocrystals,” *Nat. Mater.*, vol. 13, no. 11, pp. 1039–43, Nov. 2014.
- [331] M. Tabachnyk, B. Ehrler, S. Gélinas, M. L. Böhm, B. J. Walker, K. P. Musselman, N. C. Greenham, R. H. Friend, and A. Rao, “Resonant energy transfer of triplet excitons from pentacene to PbSe nanocrystals,” *Nat. Mater.*, vol. 13, no. 11, pp. 1033–8, Nov. 2014.